Electrically tunable Hybrid-2D Metasurfaces

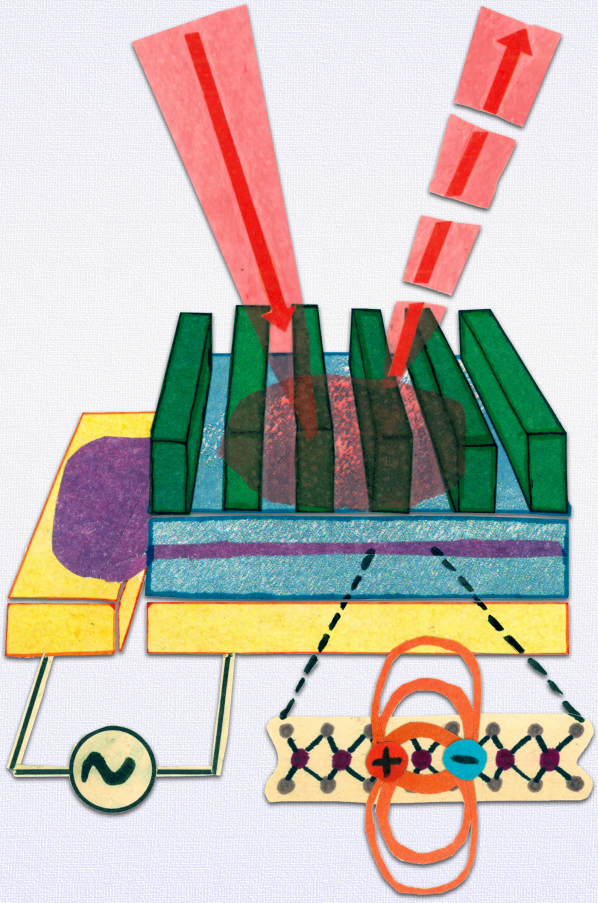

Tom Hoekstra

Electrically tunable hybrid-2D metasurfaces

PhD thesis, University of Amsterdam, June 2026

ELECTRICALLY TUNABLE HYBRID-2D METASURFACES

Tom Hoekstra

Cover: artistic impression of a hybrid-2D metasurface. Handcrafted and digitally edited collage by Mathilda van Breest Smallenburg and Tom Hoekstra.

ISBN 978-94-93539-26-6

The work described in this thesis was carried out at the Van der Waals–Zeeman Institute, Institute of Physics, University of Amsterdam, 1098 XH, Amsterdam, the Netherlands.

This work was financially supported by a Vidi grant (VI.Vidi.203.027) from the Dutch Research Council (NWO).

An electronic version of this dissertation is available via the Digital Academic Repository of the University of Amsterdam.

Electrically tunable hybrid-2D metasurfaces

ACADEMISCH PROEFSCHRIFT

ter verkrijging van de graad van doctor
aan de Universiteit van Amsterdam
op gezag van de Rector Magnificus
prof. dr. ir. P.P.C.C. Verbeek
ten overstaan van een door het College voor Promoties ingestelde commissie,
in het openbaar te verdedigen in de Agnietenkapel
op donderdag 11 juni 2026, te 10.00 uur

door

Tom Hoekstra

geboren te Sneek

Promotiecommissie

Promotor:	dr. J. van de Groep	Universiteit van Amsterdam
Copromotor:	prof. dr. P. Schall	Universiteit van Amsterdam
Overige leden:	prof. dr. M. S. Golden	Universiteit van Amsterdam
	prof. dr. E. Alarcon Llado	Universiteit van Amsterdam
	prof. dr. A.F. Koenderink	Universiteit van Amsterdam
	dr. R. Stabile	TU Eindhoven
	prof. dr. G. Soavi	Friedrich-Schiller University Jena

Faculteit der Natuurwetenschappen, Wiskunde en Informatica

To be an effective scientist
one must be more than a scientist.
For the analytic measurement of nature tells us nothing
if we cannot see nature in any other way.

Alan Watts

Contents

Preface

This thesis is the culmination of my academic journey, which unfolded over more than a decade at the University of Amsterdam. When I first arrived on campus, I knew essentially no one and, though I carried a broad curiosity, I had little certainty about where it might lead me. Fortunately, in the Natural and Social Sciences program I found myself among kindred spirits, and it was there, amid new friendships and a shared sense of directionlessness, that I discovered a natural affinity for mathematics. This provided the much-needed direction and, combined with a deep-rooted fascination for Nature, led me to pursue a major in physics.

Several years later, having committed myself to this direction through further specialization in Advanced Matter and Energy Physics, the rhythm of life was abruptly interrupted by the COVID-19 pandemic. While its effects on wider society were undeniably disruptive, it also proved to be a turning point in my own trajectory. As preventive measures restricted access to training opportunities, the internship I had initially planned could not proceed. It was in this moment of redirection that I first met Jorik van de Groep. That meeting set the course for the years to come, as I soon joined his group for a year-long research project, followed by another four years on the path toward a Doctor of Philosophy.

In the following chapters, I discuss our original contributions to the field of nanophotonics—an interdisciplinary science at the juncture of nanotechnology, materials science, optics, and quantum physics. Before diving in at the deep end, it is worth placing this work in perspective by briefly tracing the road that led us here. Because, as Sir Isaac Newton famously put it, "if I have seen further, it is by standing on the shoulders of giants."

Tom Hoekstra
Amsterdam, March 2026

1

Introduction

1.1 A brief history of optics

The origins of optical technology can be traced back to ancient history.[i] The earliest mirrors were produced by polishing naturally reflective materials, first obsidian and later also metals like bronze and silver.[7,8] Discovered in an underground tomb at Lahun, Egypt, the Mirror of Princess Sithathoriunet (Fig. 1.1a) is one striking specimen from the 19th century BCE. Although polished transparent crystals resembling lenses were often used as ornaments instead of optically (Fig. 1.1b),[9,10] the principle of refraction was certainly known in antiquity. For instance, the burning glass—a positive lens used for concentrating sunlight to start fires—was already mentioned in a play by Aristophanes in the 5th century BCE. Another noteworthy example is the 4th century Roman Lycurgus Cup (Fig. 1.1c), which glows vividly red when held up to the light. Remarkably, this optical effect is due to resonant light scattering from nanometer-sized silver and gold particles dispersed throughout the glass.[11]

The systematic study of optics emerged in the 3rd century BCE, when Euclid enunciated his geometrical treatment of vision.[4–6] From there, the field flourished for several centuries in the Greco-Roman world until the fall of the Western Roman Empire in 476 CE. In the Middle Ages, the center of scholarship shifted to the Islamic world, where the work of Ibn al-Haytham was particularly influential. Contrary to the then-dominant extramission theory—which states that vision occurs through rays emitted from the eye—he correctly argued that vision occurs when light enters the eye.

The primary focus of optics only shifted from sight to light around the 17th century, marking the turn from ancient toward modern optics.[2,3] In this early stage, one of the first major achievements was Willebrord Snellius' formalization of the law of refraction in 1621. Four decades later, motivated by observations of light diffraction

[i] This introduction is necessarily selective and focuses primarily on developments that contextualize the topics discussed in this thesis. For a more comprehensive overview, the reader may consult refs. [1–6].

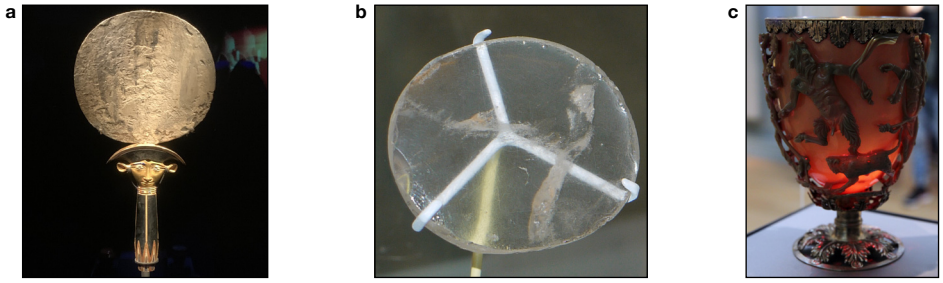

Figure 1.1: Ancient optical technology. **(a)** The silver Mirror of Princess Sithathoriunet, ca. 1900 BCE. **(b)** The Nimrud lens, which could have been used as a burning glass, ca. 750 BCE. **(c)** The Lycurgus Cup, appearing bright red due to nanoparticles embedded in the glass, ca. 300 CE. Photos by DCHNwam (Flickr, public domain), Geni (Wikimedia Commons, CC BY-SA 4.0), and Vassil (Wikimedia Commons, public domain).

by small objects and apertures, Robert Hooke argued that light could be understood as a rapid vibration—that is, as a wave-like disturbance. It was Christiaan Huygens who greatly expanded this point of view, formulating the well-known principle that "each point on a wavefront is itself the source of secondary wavelets", and using wave theory to successfully derive the laws of reflection and refraction. Despite these early successes, the theory was widely rejected by contemporaries including Isaac Newton, who instead favored the corpuscular theory, in which light is regarded as a stream of particles. The corpuscular theory remained the dominant view for more than a century, until the work of Thomas Young and Augustin-Jean Fresnel in the early 1800s. They showed that a wide range of optical phenomena could be understood as a consequence of wave interference, and that polarization is naturally explained if light is treated as a transverse wave—a point that had eluded both Newton and Huygens. Building on these ideas, Fresnel ultimately derived his celebrated formulas for the reflection and transmission coefficients at material interfaces.

Almost independent of optics was the study of electric and magnetic phenomena. In the 11$^{\text{th}}$ century, Chinese polymath Shen Kuo was among the first to document the magnetic compass, a tool which only emerged in Europe about a century later. That an electric current can deflect a compass needle was demonstrated by Hans Christian Ørsted in 1820, providing the first direct link between magnetic and electric phenomena. Not long after, in 1845, master experimentalist Michael Faraday established a link between electromagnetism and light when he discovered that a strong magnetic field can influence the polarization of light. These discoveries were theoretically synthesized by James Clerk Maxwell between 1864 and 1873, when he unified the phenomena of light with those of electricity and magnetism. His crowning achievement was the theory of electromagnetism, which elegantly captured the subject in a single set of equations and led him to predict that light is an electromagnetic

wave. Within a few decades, Heinrich Hertz validated Maxwell's theory by generating radio waves in his laboratory, seemingly settling the particle–wave debate.

In 1905, Albert Einstein introduced two landmark theories. The first was his special theory of relativity, which established the invariance of physical laws in inertial frames and treated light as an electromagnetic wave propagating in vacuum at a universal speed.[12] Then, building on Max Planck's quantization of radiation, Einstein proposed his theory of the photoelectric effect, in which light exchanges energy in discrete quanta.[13] Puzzlingly, this reintroduced a particle-like description of light, treating it as localized packets of energy. At first, these interpretations appeared impossible to reconcile, but over time it became clear that light (and matter) can manifest both as particle and as wave. By 1927, this particle–wave duality was placed on a firmer footing when Paul Dirac developed his quantum theory of light emission and absorption,[14] in which light appears as quantized excitations of the electromagnetic field: photons.[15] Although early quantum electrodynamics was plagued by inconsistencies that cast doubt on its foundations, by the late 1940s these issues were resolved. What emerged was a complete microscopic theory of light–matter interactions with an unprecedented predictive power.[16,17]

1.2 THE NANOTECHNOLOGY REVOLUTION

Around the time that the problems with quantum theory were being worked out, a new experimental paradigm emerged in which electromagnetic waves are manipulated using structures much smaller than a single wavelength. While this had been demonstrated previously,[18] it was Winston Kock who formalized the notion that carefully arranged subwavelength elements can produce an *effective* refractive index that is altogether different from the intrinsic index of the constituent material(s).[19,20] Kock constructed lenses from arrays of metal plates that behaved effectively as a dielectric medium, focusing radio and microwaves in much the same way as ordinary glass lenses focus visible light (Fig. 1.2a). These metal-plate lenses are widely regarded as early precursors of *metamaterials*[21–24]—artificial materials with an engineered electromagnetic response arising from the geometrical arrangement rather than the chemical composition of the constituent materials.[i]

As solutions to Maxwell's equations are scalable across length scales, it was tempting to ask whether metamaterials could be miniaturized to function at optical frequencies. However, producing subwavelength elements for visible light implied that structures had to shrink by several orders of magnitude, down to the nanometer scale. While, in concept, the manipulation of matter with nanoscale precision was

[i] Technically, the term "metamaterials" was coined around 1999 to describe man-made materials with electromagnetic properties *beyond* those found in nature. However, today, the term is often understood more loosely and is also used in other physical domains, including acoustic and mechanical systems.

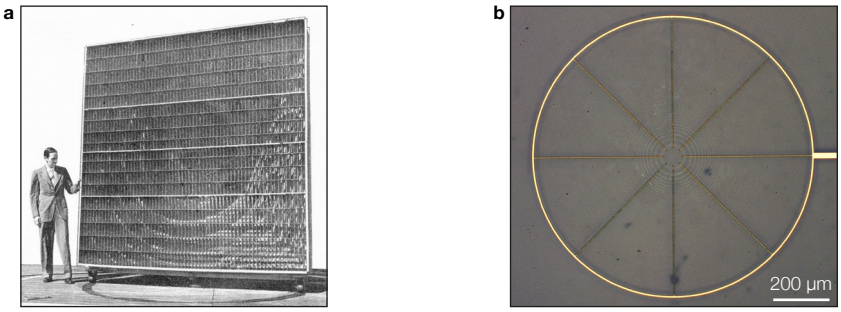

Figure 1.2: The nanotechnology revolution in action. (a) Proto-metamaterial lens comprising subwavelength metal plates that focus microwaves at a wavelength of 7.5 cm, developed by Winston Kock in 1946 (adapted from Ref. [19]). **(b)** Zone-plate lens patterned in an atomically thin semiconductor, designed to modulate the focal intensity at a visible wavelength of 620 nm, demonstrated by Jorik van de Groep in 2020 (adapted from Ref. [25]).

already being envisioned by Richard Feynman in his 1959 lecture, "There's Plenty of Room at the Bottom", such control would have appeared far beyond practical reach at the time. Remarkably, though, over the next few decades, this engineering feat would become a reality owing to several key technical innovations (Fig. 1.2b).

The first crucial step came in the following year, when Theodore Maiman successfully fired the first ruby laser.[26] This invention came with the exciting prospect of intense, highly directional and coherent radiation, ushering in a new era for light-based science and technologies. Around the same time, the silicon integrated circuit was invented at Fairchild Semiconductor. Within a few years, these chips were brought into production by demand from the aerospace and defense sectors, after which they entered mass markets through the first memory chips and microprocessors. In 1982, to meet the semiconductor industry's growing demand for tools that provided faster throughput and higher resolution, a new form of photolithography using excimer lasers was proposed at IBM. These lasers soon became the primary tool in semiconductor manufacturing, enabling a rapid decrease in physical feature sizes from around a micrometer in the late 1980s down to around 200 nanometers[i] within a decade.[27,28]

The rapid advances in nanofabrication were further complemented by the development and refinement of scanning electron and probe-based microscopy techniques. This increasingly enabled the visualization and characterization of structures down to the level of atoms—a length scale that had hitherto been largely inaccessible due to the diffraction limit in optical microscopy. Altogether, by the mid-1990s, the nanotechnology revolution was in full swing, with far-reaching consequences for optics that would ultimately crystallize in the formation of a new discipline known

[i]Today, feature sizes have been pushed to the single-digit nanometer regime using extreme-ultraviolet lithography.

as *nanophotonics*: studying light–matter interactions at the nanoscale in order to control the generation, propagation, manipulation, and detection of light from the near-infrared to the near-ultraviolet.

1.3 EARLY NANOPHOTONICS

In the 1990s, subwavelength gratings were among the first optical metamaterials to arrive on the scene.[29–33] Implemented as a non-resonant artificial-index grating, a wave incident on such a subwavelength structure simply experiences an *effective* refractive index governed by the local filling fraction, much like Winston Kock's metallic delay lenses. Owing to their tailorable permittivity, artificial-index gratings provided a uniquely versatile building block in the creation of diffractive optics. By arraying these gratings on the superwavelength scale, the *local* scattering response could be precisely engineered to realize optical elements such as beam splitters and polarizers.[34]

In contrast, subwavelength gratings could also be operated in the resonant regime, *i.e.* when the periodicity was designed to enable coupling of an incident wave to a guided mode supported by the structure, to harness their *nonlocal* response.[35] Although nonlocality is common in natural materials (*e.g.* charge density waves in conductors), these effects are typically weak.[36–38] However, in metamaterials, nonlocal effects can be very strong and engineered at will, even if all constituent materials are purely local, and can be strategically implemented to realize new functionalities or overcome limitations of conventional refractive and diffractive optics. Researchers soon demonstrated that nonlocal guided-mode resonances in subwavelength gratings were ideally suited for applications requiring enhanced spectral or angular selectivity, such as high-contrast filters.[39]

Two-dimensional (2D) photonic crystals emerged as another promising nonlocal metamaterial.[40,41] Instead of the shallow-etched pattern of guided-mode resonant gratings, 2D photonic crystals feature a waveguide slab that is completely perforated. This can be leveraged to create a photonic bandgap, where no modes exist in a range of frequencies,[42] or extraordinary optical transmission, where light can essentially "squeeze" through holes much smaller than its wavelength.[43,44] In the latter case, the periodic hole array facilitates coupling of photons to surface plasmons—collective oscillations of bound electrons at a metal–dielectric interface—which then hybridize to form surface plasmon polaritons.[45–47] These nonlocal polariton states can be leveraged to generate strong electromagnetic field enhancements at the surface despite the intrinsically lossy nature of metals at optical frequencies, enabling applications such as molecular sensing,[48] or (quantum) light sources.[49,50]

In the early days of nanophotonics, a number of other wavefront-shaping strate-

gies were introduced. For instance, it was shown that light could be controlled through propagation in (and optical coupling between) nanopillars acting as tiny truncated waveguides.[51–54] Later, it was demonstrated that the Pancharatnam–Berry (geometric) phase can be engineered using nanorods functioning as small half-wave plates.[55–58] However, when it was pointed out that metamaterials could be engineered with a *negative* effective index—with the unusual implications of negative refraction and perfect lensing—this rapidly became a driving force within the nascent field.[59–62] Despite the fact that no naturally occurring material has a magnetic response at optical frequencies, negative-index materials were soon pushed into the visible by creating metamaterials that capitalize on local current loops to induce the missing magnetism.[63–65]

1.4 THE ADVENT OF METASURFACES

The field of nanophotonics was truly ignited with the emergence of deeply subwavelength, optically resonant antennas.[66] Light incident on a metallic[67] or dielectric[68] nano-antenna induces a local dipole moment by displacing charges from their equilibrium positions, temporarily storing electromagnetic energy in the antenna before it is re-radiated as scattered light. The Coulombic restoring force experienced by the oscillating charges gives rise to a resonance condition that sensitively depends on the antenna material, its geometry, as well as the dielectric environment.[69] At resonance, the light–matter interaction is unusually strong, and the extinction and scattering cross-sections can even be an order of magnitude larger than the antenna's physical size (*i.e.* its geometrical cross-section).[70,71]

Two distinct physical mechanisms can be distinguished based on the resonator material. In metallic nanostructures, light drives a collective oscillation of the free-electron gas, giving rise to a localized surface plasmon.[72] In contrast, in dielectric and semiconductor nano-antennas, light induces displacement currents of bound electrons, giving rise to so-called Mie resonances.[73] The difference in physical origin—free versus bound charges—has several important consequences. Plasmonic resonances, arising from the collective motion of free electrons, strongly screen electric fields inside the metal, confining the optical fields to incredibly small volumes at the surface.[66,67,74] However, electron scattering in metals inevitably leads to Ohmic losses (Joule heating), which limit the resonant lifetime and render the optical response intrinsically broadband. In contrast, Mie resonances can be lossless in principle, with optical fields predominantly confined inside the antenna and organized into electric and magnetic multipolar modes.[68,75–77] While this richer modal landscape and low material absorption offer opportunities for nanophotonic design, isolated Mie scatterers typically feature large radiative losses and therefore also exhibit a broadband spectral response.

To overcome the lossy nature of subwavelength antennas, they can be carefully arranged in planar arrays known as optical *metasurfaces*.[78–81] From a library of antennas, or meta-atoms, with different scattering responses, in principle any wavefront can be created by discretizing the desired phase distribution and matching each discrete "pixel" with the corresponding antenna in the library. When the inter-antenna spacing is sufficiently large, diffractive optical elements can be constructed in which the wavefront is shaped through the far-field interference of all the separate resonances. This is leveraged in, for instance, Huygens' metasurfaces, which in analogy to Huygens' principle, achieve highly directional scattering from arrays of dielectric nano-antennas with spectrally overlapping electric and magnetic dipole resonances.[76] On the other hand, when antennas are placed in close proximity, prohibitively high losses can be mitigated through evanescent[82] and radiative[83] coupling between adjacent antennas.[84–86] When this is combined with a diffraction condition such as a Rayleigh anomaly, this can give rise to hybridization of the individual resonator modes into a new collective state known as a surface lattice resonance.[87–90] By inheriting properties from the resonator as well as the lattice, this nonlocal effect further enriches the metasurface design toolbox.

Today, metasurfaces offer a uniquely versatile platform to shape optical wavefronts not only through bulk refraction and diffraction, but also at the nanoscale using a wide variety of local and nonlocal resonant effects. Already, metasurfaces have enabled new applications and improved existing ones, including photovoltaics,[91–93] anti-reflection coatings,[94,95] image processing,[96–98] multifunctional optics,[99–101] holography,[102,103] and cloaking,[104–106] to name but a few. Aside from the technological impact, the invention of metasurfaces has also led to new theoretical insights. For instance, because a wave impinging on a metasurface experiences an abrupt phase shift that is not ordinarily captured by Snell's law, the laws of reflection and refraction were further generalized to account for phase discontinuities—nearly four centuries after Snell's original formulation.[107–109]

1.5 ACTIVE METASURFACES

Despite the extraordinary advances over the past few decades, the functionality of optical elements—conventional or metasurface—has remained almost exclusively *passive*. Thus, much like the 19$^{\text{th}}$ century BCE Mirror of Sithathoriunet, the optical response of a typical metasurface is fixed from the moment of fabrication. This lack of post-fabrication tunability stems from the weak variation of most materials' optical properties in response to external stimuli,[110] and is problematic for a wide variety of emerging application areas that require *active* control over optical fields. These include analog computation,[97] dynamic wavefront shaping,[111–113] electro-optic modulation,[114,115] nonlinear and quantum optics,[116–118] thermal emission man-

agement,[119,120] mixed-reality displays,[101,121] and environmental sensing.[122–125]

The drive to realize adaptive, dynamic, and reconfigurable metasurfaces has set the nanophotonics community on a quest to find materials and mechanisms that can be leveraged to achieve active tunability.[208–211] So far, many ingenious approaches have been explored to dynamically induce changes in a material's optical properties or the nanostructural geometry, each with its own strengths and weaknesses. Table 1.1 provides an overview of the chemical, electrical, magnetic, mechanical, optical, phase-transition, and thermal mechanisms that have been employed so far, with a particular focus on free-space meta-optics operating at or near visible wavelengths.[i]

Whereas each application area prioritizes a different set of performance metrics and comes with unique conditions and constraints, most applications stand to benefit from efficient, rapid, and strong modulation capabilities. This often goes hand-in-hand with high quality (Q)-factor resonances (*i.e.* low optical losses) to achieve the strongest possible light–matter interactions. The constituent materials should ideally also be lightweight, stackable, easy to handle and pattern at large scales, as well as chemically stable, sustainable, and earth-abundant. In practice, the likelihood that any platform will find widespread adoption in the near future depends largely on its technological maturity and compatibility with existing back-end manufacturing routines.

Among the most technologically mature routes to reconfigurable meta-optics are liquid crystals[157] and micro-electromechanical systems[169] (MEMS), both of which benefit from well-established silicon-foundry compatibility. Other widely explored contenders include transparent conducting oxides[151] (*e.g.* indium tin oxide) and chalcogenide-based phase-change materials[196] (PCMs; *e.g.* germanium antimony telluride), which have long been deployed in display technologies and non-volatile memory, respectively. More recently, electrostatic gating of 2D semiconductors has emerged as a compelling alternative, combining potential back-end-of-line compatibility with highly efficient and ultrafast control of optical resonances.[25,110,144–148,209,212–214] To understand why this low-dimensional material platform is particularly well suited for active metasurfaces, we briefly step back to consider the rise of 2D semiconductors.

[i] Of course, these stimuli are largely interdependent. For instance, an electrical impulse may heat up a material, which in turn causes it to deform mechanically. Nevertheless, the line must be drawn somewhere, and meaningful distinctions can be made by considering the primary physical parameter that is responsible for the tunability.

Type	Tuning mechanism	Material platform
Chemical	Hydrogenation	Metal hydrides[126–129]
	Changing dielectric environment	Microfluidics[130,131]
	Swelling/deswelling	Conductive polymers[132]
	Electrodeposition	Metals[126]
	Electrochromism	Electrochromic polymers[133,134], Electrochromic oxides[135–138]
	Ion intercalation	2D materials[139–141]
Electrical	Junction biasing (free carrier effects)	Semiconductors[142]
	Electrostatic gating	2D materials[25,143–149], Conductive oxides[150–155]
	Second-order nonlinearities/$\chi^{(2)}$	Electro-optic polymers[114], Ferroelectrics[115,156]
	Liquid crystal reorientation	Nematic liquid crystals[157–160]
	Quantum-confined Stark effect	Multi-quantum wells[161]
Magnetic	Faraday/Kerr effects	Magneto-optical garnets[162,163]
Mechanical	Displacement (period, gap)	Polymers[164–167], MEMS[168–170]
	Deformation (shape, orientation)	Kirigami[171,172], Liquid crystal networks[173]
	Acousto-optic	Piezoelectric crystals[174,175], Chalcogenide glasses[176]
	Strain-tuning	2D materials[177–180]
Optical	Third-order nonlinearities/$\chi^{(3)}$	Conductive oxides[181], Semiconductors[182–186]
	Photogeneration (free carrier effects)	Semiconductors[187,188]
	Photogeneration (exciton bleaching)	2D semiconductors[189–191]
Phase transition	Insulator-metal	Correlated transition metal oxides[192–195]
	Amorphous-crystalline	Chalcogenide PCMs[196–199]
	Nematic-isotropic	Liquid crystals[200,201]
Thermal	Thermal free-carrier effects	Semiconductors[202]
	Thermo-optic effect	Semiconductors[203–205]
	Thermal gradient (phoresis, osmosis)	Microfluidics[206,207]

Table 1.1: Overview of external stimuli utilized to dynamically manipulate free-space optical waves (spanning the spectral region from near-ultraviolet to near-infrared), categorized by tuning mechanisms and relevant material platforms. MEMS = micro-electromechanical systems; PCMs = phase change materials

1.6 2D SEMICONDUCTORS

Reducing the dimensionality of a crystal can profoundly reshape its electronic and optical properties. Indeed, materials can exhibit dramatically different behavior when they manifest in 0D (quantum dot), 1D (nanotube), or 2D (monolayer) forms compared to their bulk counterparts, as quantum confinement modifies the available electronic states. In this context, *low-dimensional* refers to the regime where at least one structural dimension becomes comparable to, or smaller than, the characteristic extent of the electron wavefunction.

However, starting in the 1930s, it was argued that strictly 2D crystals cannot be thermodynamically stable, because thermal fluctuations would induce long-wavelength lattice vibrations that destroy crystalline order at any non-zero temperature.[215] Over the following decades, this notion came to be supported by experimental observations: ultrathin films typically exhibited strongly reduced melting temperatures and chemical or morphological instabilities as their thickness approached the atomic scale. This all changed in 2004, when Andre Geim and Konstantin Novoselov isolated graphene, the two-dimensional form of graphite.[216] The apparent contradiction was resolved when it was pointed out that crystalline membranes are never truly two-dimensional, because the coupling between out-of-plane flexural and in-plane stretching modes intrinsically induces nanoscale ripples which suppress the thermodynamic instability.[215]

Remarkably, the technique that was used to prepare one-atom-thick graphene from a bulk graphite crystal[i] relied solely on common adhesive tape. Because the individual layers in these crystals are held together by relatively weak van der Waals forces, sticking the crystal between two strips of tape and subsequently peeling it causes the bulk crystal to fracture and delaminate into smaller and thinner crystalline flakes. This *mechanical exfoliation* process only had to be repeated a handful of times to create micrometer-sized, atomically thin flakes with exquisite crystal quality. Soon after the discovery of the 2D semimetal graphene, this technique was applied to prepare free-standing monolayers of other layered materials, ranging from metals (niobium diselenide) to semiconductors (molybdenum disulfide, MoS_2) and insulators (hexagonal boron nitride, hBN).[217] By now, more than ten thousand different van der Waals materials have been discovered,[218–220] collectively covering the full gamut of materials, including those with desirable optical properties.

In this regard, semiconducting transition metal dichalcogenides (TMDCs) stand out for their high refractive indices and tightly bound excitons. The most widely studied TMDC monolayers are based on group-VI transition metals molybdenum (Mo) and tungsten (W) combined with chalcogens sulfur (S) and selenium (Se):

[i] More specifically, highly oriented pyrolytic graphite.

MoS_2, $MoSe_2$, WS_2, and WSe_2. These materials are typically prepared in the thermodynamically stable trigonal prismatic (2H) phase and feature covalently bonded chalcogen–metal–chalcogen planes held together primarily by weak out-of-plane van der Waals forces.[221–223] While they feature an indirect bandgap in the multilayer form, the band structure changes to a direct bandgap in the monolayer limit.[i] The direct gap enables efficient fluorescence from the radiative recombination of excitons—electron–hole pairs bound by the Coulomb interaction.[224,225] In conventional bulk semiconductors, excitons tend to be unstable at room temperature because their binding energies are often comparable to or smaller than the thermal energy. In contrast, excitons in atomically thin TMDCs exhibit unusually large binding energies due to reduced dielectric screening and quantum confinement within the sub-nanometer-thick layer.[226,227] As a result, neutral excitons[ii] as well as charged excitons (trions) feature prominently in room-temperature optical spectra, while additional many-body complexes such as bi-excitons and excited-state excitons can be resolved at cryogenic temperatures.[213,226,229,230]

The exceptionally rich exciton physics present in atomically thin semiconductors is further complemented by their remarkable tunability, arising from sensitivity to the local dielectric landscape and crystal structure. This opens up a multitude of ways to manipulate these resonances, including electric and magnetic fields,[231,232] free charges (induced optically, thermally, or electrically),[233] surface chemistry,[234] and mechanical strain.[235] Among these mechanisms, active exciton tuning by electrostatic gating has emerged as particularly technologically relevant due to its compatibility with electronic devices and its potential for highly efficient and ultrafast modulation. These developments have positioned monolayer semiconductors as a promising material platform for electrically tunable metasurfaces.

1.7 THE ROAD TO HYBRID-2D METASURFACES

To harness the tunability of 2D excitons for active metasurfaces, the most direct approach is to pattern bare monolayers into optical elements—such as zone-plate lenses and binary blazed gratings—and integrate them with an electrochemical cell to modulate the carrier density.[25,148] In particular, the monolayer lens showed a promising 33% modulation of the focal intensity upon switching the monolayer from intrinsic to n-type doping. However, in absolute terms, the efficiency remained

[i] In multilayers, the valence-band maximum is located at the Γ point and the conduction-band minimum near the Q point of the hexagonal Brillouin zone. In contrast, the band structure evolves into a direct bandgap at the K and K' valleys in the monolayer limit.

[ii] Odd-layered 2H TMDCs lack inversion symmetry, which, combined with the strong spin–orbit coupling from the heavy transition metal atoms, gives rise to spin-split valence and conduction bands [228]. Consequently, these monolayers feature spin-split excitonic states labeled the A and B excitons, with the former denoting the lowest-energy transition.

below 1%, which is typical of atomically thin optical elements, where the light–exciton interaction is limited by the sub-nanometer optical interaction length of the material. Moreover, at room temperature, the excitonic quantum efficiency is plagued by rapid nonradiative decay processes, which typically occur an order of magnitude faster than radiative recombination. As a consequence, it has proven challenging to fully capitalize on the tunability of excitons in atomically thin semiconductors.

To progress exciton resonance tuning from a laboratory curiosity to a technologically viable platform for dynamic light control, new methods must be found that can reliably enhance the excitonic light–matter interaction. One approach is to leverage mutually synergistic effects between different van der Waals materials by combining them in heterostructures.[236,237] Because the crystalline layers of these materials are free from dangling bonds, they can be stacked vertically in almost any sequence and with arbitrary orientations (*i.e.* twist angles). This comes with the exciting prospect of assembling artificial crystals that integrate excitonic 2D semiconductors with materials that have complementary properties, including graphene (as transparent electrical contacts) and especially hBN. In particular, hBN encapsulation screens the active layer from the dielectric environment and reduces strain, thereby minimizing unwanted nonradiative decay processes.[227] In addition, hBN has a high dielectric breakdown strength, making it an ideal companion for electrically tunable devices,[238,239] as well as excellent chemical stability, providing protection against heat and chemicals encountered during fabrication and preventing degradation from exposure to atmospheric molecules.[240]

Pioneering works have leveraged hBN-encapsulated monolayers to achieve pristine excitonic properties at cryogenic temperatures by reducing exciton–phonon scattering. By combining low-temperature operation with electrostatic gating to neutralize the monolayers, most nonradiative decay pathways can be suppressed and linewidths approach the intrinsic limit.[227,241] When these tunable heterostructures are placed on mirrors to form vertical heterostructure cavities, their high exciton quantum efficiencies can be leveraged to achieve near-unity excitonic absorption[213] and reflection.[144,212] This platform has additionally enabled dynamic beam steering on nanosecond timescales by using spatially separated gate electrodes to locally modulate the excitonic response.[145,146] In simulation, it was even shown that, when all nonradiative decay and dephasing mechanisms are artificially removed, these materials exhibit tunable topological phase singularities that yield full and active control over the scattering amplitude and phase.[242] Unfortunately, none of these remarkable results has been replicated outside a helium cryostat, raising the question of how excitonic losses could be mitigated to enable room-temperature operation.

Recently, a free-space amplitude modulator was created by placing a monolayer semiconductor on a metallic subwavelength grating supporting surface plasmon

polaritons.[147] Utilizing the Purcell enhancement offered by the metasurface,[69] this device set a record with 10% reflectance modulation at room temperature (a ~ 20× improvement over the previous best[25]). Nevertheless, the device performance was still constrained by defects and disorder in the unprotected monolayer introduced during nanofabrication. In another recent work, a phase modulator was demonstrated based on a superlattice of three monolayers separated by dielectric spacers.[243] This structure leveraged coupling between the excitons and a cavity mode in an attempt to overcome the excitonic nonradiative decay.[244] By continuous electrostatic tuning of the exciton resonance, the modulator achieved full 0–2π phase modulation at 1–2% reflection, representing a ~ 10× improvement over a bare monolayer.[245] However, the device still showed undesirable cross-modulation of the reflected amplitude and phase, as well as requiring high operating voltages. Thus, despite the performance enhancements they offer, both metasurfaces and heterostructures still face severe challenges on their own. It is therefore tempting to explore whether these strategies could be merged to achieve the best of both worlds.

To achieve the strongest possible interaction of light with 2D excitons, it is appealing to leverage the long resonant lifetimes of *nonlocal* metasurfaces. Placing the 2D material near the electric-field hotspot of a nonlocal mode can enable rapid energy exchange between excitons and photons, leading to the formation of in-plane-propagating exciton–polaritons.[246–248] These nonlocal light–matter states inherit a geometrically tailorable lifetime from the photonic mode, while retaining the electrical tunability of the bare exciton resonance. So far, there have been a few encouraging demonstrations of strongly coupled exciton–polaritons in hybrid heterostructure–metasurfaces.[249–251] However, thus far these have remained entirely passive, neglecting the unique potential of 2D excitons for dynamic wavefront manipulation.

In this thesis, we take the next step by introducing a new platform for active meta-optics—ELECTRICALLY TUNABLE HYBRID-2D METASURFACES—that combines the pristine excitons supported by van der Waals heterostructures with the strong field enhancements offered by nonlocal metasurfaces (Fig. 1.3). At the interface of these two concepts, a range of fundamental research questions arise: How can the excessive losses of room-temperature excitons be mitigated using engineered dielectric environments and nonlocal resonances? How can exciton resonance tuning be harnessed to transform passive metasurfaces into active components with improved functionality and efficiency? How do free carriers influence exciton–photon coupling, and how can strong coupling be leveraged to actively manipulate the flow of light? What is the role of phase in excitonic light scattering, and can it be combined with active tuning of the amplitude to enable full dynamic control over light? What happens when nonlocal modes are confined within tightly confined spaces, and how

can finite-size nonlocal metasurfaces be modeled theoretically? Finding answers to these questions is the central aim of this thesis, ultimately motivating the research discussed in the following chapters.

1.8 OUTLINE OF THIS THESIS

In **Chapter 2**, we start by briefly introducing the design, fabrication, and characterization techniques used throughout this thesis to design, create, and study electrically tunable hybrid-2D metasurfaces. We first provide a short description of the methods used to model the tunable optical response of excitonic 2D materials, followed by an introduction of nonlocal guided-mode resonances. Next, we present the fabrication protocols employed to create our devices and elaborate on why we favored certain techniques over alternative approaches. We end the chapter with an overview of the custom experimental setups used to study the optoelectronic response and characterize the performance of our devices.

In **Chapter 3**, we present active metasurfaces for free-space optical amplitude modulation (Fig. 1.3a). The dynamic operation is based on electrostatic gating of excitons in atomically thin WS_2, which is heterostructured with hBN and functionalized with a dielectric subwavelength grating. The grating enables coupling of incident light to the fundamental guided mode supported by the structure, producing strong nonlocal field enhancements at the monolayer position. As a result, when the WS_2 is intrinsically doped, excitons hybridize with guided photons to form exciton–polaritons. Using electrostatic gating to switch between the strong- and weak-coupling regimes, we demonstrate 9.9 dB of reflectance modulation and a 48.9% absolute reflectance change at room temperature, which is a fivefold improvement over the previous best achieved with excitonic 2D materials. We reveal that the continuous transition from strong to weak exciton–photon coupling is governed by the effect of gating-induced free carriers on the rate of nonradiative exciton decay.

In **Chapter 4**, we numerically demonstrate a hybrid-2D metasurface for reflection-mode complex-amplitude modulation at visible wavelengths (Fig. 1.3b). Crucially, all simulations are grounded in experimentally measured material properties. To achieve independent control over the scattered amplitude and phase, the device requires two separate control voltages and must operate near critical coupling, which requires a delicate balance of radiative and nonradiative decay channels. We develop an inverse-design pipeline to deal with the high dimensionality of the design space and the intricate interdependence of geometrical and material parameters. We then design metasurfaces for π-phase modulation at a constant amplitude, full 0–2π complex-amplitude modulation, and diffractive beam steering. The results are additionally interpreted with temporal coupled-mode theory

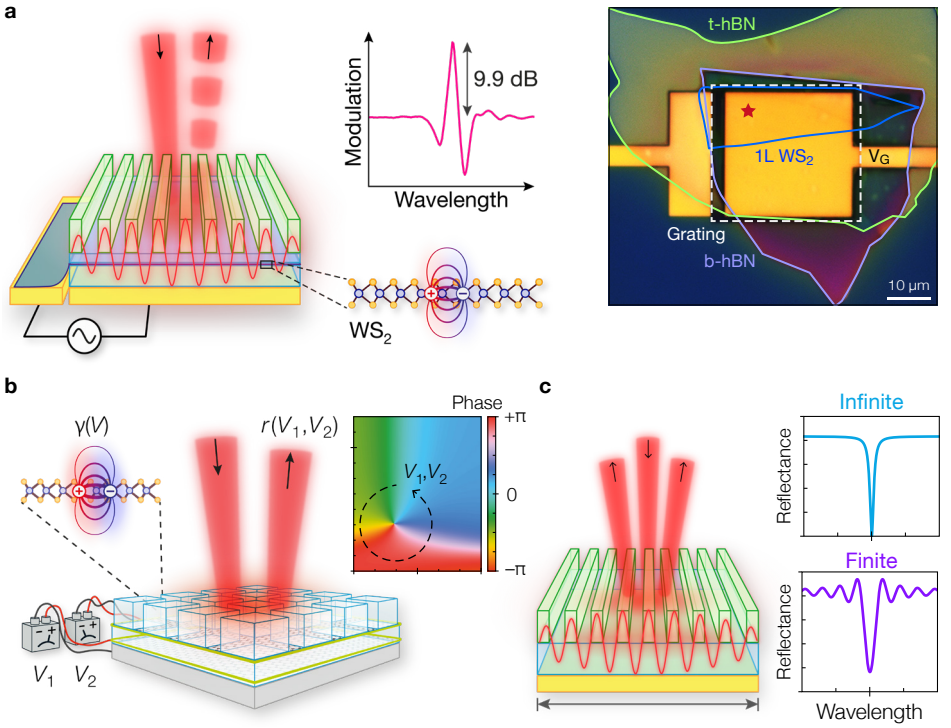

Figure 1.3: Electrically tunable hybrid-2D metasurfaces. **(a)** Chapter 3: The combined merits of a tunable van der Waals heterostructure cavity with the strong light-matter interaction of a nonlocal dielectric metasurface enable 9.9 dB optical amplitude modulation at room temperature. **(b)** Chapter 4: Two independently gated monolayers enable decoupling of the scattering amplitude and phase while covering the full 0–2π phase range. **(c)** Chapter 5: Spatiotemporal coupled-mode theory qualitatively and quantitatively captures the linewidth broadening and interference patterns observed in finite-size nonlocal metasurfaces.

to elucidate the underlying physics and establish the generality of our approach.

In this thesis, we envision that nonlocal resonances such as exciton–polaritons can be leveraged to create highly miniaturized active meta-optical elements. However, the lateral confinement of spatially extended modes can degrade the optical performance, a drawback that was already realized soon after the first guided-mode resonant gratings were demonstrated. Despite this, today, nonlocal metasurfaces are still typically simulated as infinitely periodic, resulting in unpredictable finite-size effects in fabricated devices, as observed in Chapter 3. This has created a need for a broadly applicable modeling framework that can predict the impact of finite size.

In **Chapter 5**, we develop a spatiotemporal coupled-mode theory (STCMT) to intuitively and quantitatively capture how finite lateral footprints reshape the scattering response of nonlocal hybrid-2D metasurfaces (Fig. 1.3c). We show that when the physical metasurface size becomes comparable to the modal propagation

length, finite-size effects fundamentally modify the optical response, giving rise to interference fringes and linewidth broadening. Crucially, we derive an expression for the Q factor that incorporates an additional dissipation channel due to edge losses, demonstrating that the stored energy and effective lifetime scale exponentially with the interaction length of the nonlocal mode. We validate the model experimentally by performing position- and momentum-resolved reflectance spectroscopy on a 30-μm-wide hybrid-2D metasurface. The measurements show remarkable agreement with the theory, directly confirming the predicted size effects and enabling quantitative separation of the intrinsic, radiative, and edge-induced loss rates, establishing STCMT as an invaluable tool for designing and interpreting the optical response of footprint-restricted hybrid-2D metasurfaces.

Altogether, the results presented in this thesis demonstrate that, by leveraging the combined merits of nonlocal dielectric metasurfaces and excitonic van der Waals heterostructures, ELECTRICALLY TUNABLE HYBRID-2D METASURFACES hold the key to realizing ultracompact optoelectronic devices for dynamic manipulation of visible light.

2

Modeling, fabrication and characterization

In this chapter, we discuss the key methods employed to model, manufacture and measure hybrid-2D metasurfaces. In Section 2.1, we first describe the various numerical tools employed to design the desired tunable optical response. Next, in Section 2.2 we outline the procedures used to fabricate the designed hybrid-2D metasurfaces. Finally, in Section 2.3 we detail the modular experimental setup used to characterize the devices' optical responses.

2.1 Modeling

2.1.1 Dielectric permittivity

The contribution of excitonic resonances to the dielectric permittivity of 2D semiconductors is most commonly described using the Lorentz oscillator model[252–255], although more refined descriptions such as the Tauc–Lorentz model[256,257] and the Elliott model[258] exist, which incorporate additional features including band-edge absorption and the continuum of unbound electron–hole states. In this framework, the bulk permittivity generally takes the form

$$\varepsilon(\omega) = \varepsilon_{\mathrm{bg}} + \sum_j \frac{f_j}{\omega_j^2 - \omega^2 - i\omega\gamma_j}, \tag{2.1}$$

where $\varepsilon_{\mathrm{bg}}$ is the background permittivity accounting for higher-frequency transitions, ω_j is the resonant frequency of the j^{th} oscillator (*i.e.*, exciton), and f_j is its oscillator strength. The total decay rate $\gamma_j = \gamma_{j,\mathrm{r}} + \gamma_{j,\mathrm{nr}}$ is the sum of radiative recombination ($\gamma_{j,\mathrm{r}}$) and nonradiative relaxation ($\gamma_{j,\mathrm{nr}}$) pathways.

Due to quantum confinement within an atomically thin layer, the excitonic polarization is effectively two-dimensional. To nevertheless describe the 2D sheet response with a 3D permittivity (which is often necessary or convenient within optical

simulation frameworks), the 2D sheet response can be homogenized over the layer thickness d as[259,260]

$$\varepsilon(\omega) = \varepsilon_{\mathrm{bg}} + \frac{c}{d}\sum_j \frac{\gamma_{j,\mathrm{r}}}{\omega_j^2 - \omega^2 - i\omega\gamma_j}. \tag{2.2}$$

Importantly, the optical response of monolayers is fundamentally governed by the sheet susceptibility,[261] and Eq. (2.2) should be viewed as a convenient phenomenological model. In addition, the excitonic linewidth is broadened by pure dephasing (*i.e.* decoherence) arising from random fluctuations in the exciton transition energy and dipole phase.[131,213,262] Although pure dephasing does not change the exciton population, it broadens the optical linewidth and is commonly absorbed into an effective nonradiative linewidth $\gamma_{j,\mathrm{nr}}$, and we adopt this approach throughout this thesis. Furthermore, we note that the symbol Γ denotes the amplitude decay rate, which appears as the half-width-at-half-maximum linewidth in optical spectra, whereas $\gamma = 2\Gamma$ denotes the intensity decay rate and corresponds to the full-width-at-half-maximum (FWHM).[i]

In this thesis, we focus primarily on monolayer WS_2 rather than other TMDCs because of its particularly pronounced A-exciton resonance, arising from a large oscillator strength and a comparatively low nonradiative decay rate,[254,255] which can be actively and reversibly quenched via electrostatic gating.[263] Moreover, the A-exciton lies well within the visible spectral range (around 615 nm at room temperature) and is well separated from the B-exciton (around 515 nm), making monolayer WS_2 a particularly promising platform for active metasurfaces based on exciton resonance tuning. In the next section, we discuss how the A-exciton can be modulated through electrostatic gating.

2.1.2 Exciton resonance tuning

We model the electrical tunability of the A-exciton resonance by expressing the decay rate in terms of the 2D free-electron density (n_e, typically in units of cm^{-2}). To determine the doping dependence of the decay rate, we follow the optical rate-equation framework used in prior works to describe the interplay between free electrons and excitons in monolayer TMDCs, ignoring hole-assisted scattering for simplicity. In the steady state, linear excitation regime (pump fluences $\lesssim 1\ \mu\mathrm{J/cm}^{-2}$),[233] the A-exciton population density (n_{A}) obeys an optical rate equation of the form[147,241]

$$G_{\mathrm{A}} = n_{\mathrm{A}}\gamma_{\mathrm{A}} = n_{\mathrm{A}}\left(\gamma_{\mathrm{A,r}} + \gamma_{\mathrm{A,ph}} + \gamma_{\mathrm{A,e}} + \gamma_{\mathrm{A,T}}\right), \tag{2.3}$$

[i] Strictly speaking, decay rates carry units of inverse time, but can equally be expressed in energy units as $\hbar\gamma$. In the literature, the factor $\hbar$ is often left implicit for notational clarity, and we adopt this convention here as well.

where G_A is the exciton generation rate, $\gamma_{A,ph}$ is the phonon-assisted nonradiative decay, $\gamma_{A,e}$ is the electron-assisted nonradiative decay, and $\gamma_{A,T}$ accounts for conversion from neutral to charged excitons (*i.e.* trions, denoted by subscript 'T'). In a charge-neutral monolayer, the overall nonradiative decay is set by phonon-assisted mechanisms, including exciton dissociation and scattering into "dark" (optically inactive) excitonic states.[264] When the monolayer is electrostatically doped, the presence of free electrons increases the exciton–electron scattering rate, which can be modeled as

$$\gamma_{A,e} = A_e n_e \,, \tag{2.4}$$

where A_e is the rate coefficient for electron-assisted scattering processes. Free carriers additionally modify the efficiency of phonon-mediated processes by changing the electronic environment, for instance through screening of the Coulomb interaction between the electron–hole pair and modifications of the available states through Pauli blocking.[i] As a result, additional phonon-scattering channels can become accessible, and these contributions are generally nonlinear in n_e.[241,264,267] At the typical doping levels achieved through electrostatic gating ($\sim 10^{12}$ cm^{-2}), the phonon-assisted contribution can be expanded to second order in n_e as[147]

$$\gamma_{A,ph} = \gamma_{A,ph0} + A_{ph1} n_e + A_{ph2} n_e^2 + \dots \,, \tag{2.5}$$

where A_{ph1} and A_{ph2} are the rate coefficients.

At the same time, the population density of trions obeys the rate equation

$$G_T = n_T \gamma_T = n_A \gamma_{A,T} \,, \tag{2.6}$$

The trion density is linked to the exciton density via the trion formation coefficient T as

$$n_T = T n_A n_e, \tag{2.7}$$

which together with Eq. (2.6) implies

$$\gamma_{A,T} = T n_e \gamma_T \,. \tag{2.8}$$

Combining all decay channels, the total excitonic decay rate can be written as the sum

[i] By the same token, doping also modifies the radiative exciton dynamics through phase-space filling and electric-field screening, and bandgap renormalization at higher carrier densities.[265, 266] However, in our experiments, we cannot cleanly separate the influence of doping on both of these decay pathways, and in our model we therefore let only the nonradiative component vary with electron density.

of radiative and nonradiative pathways as

$$\gamma_{\mathrm{A}}(n_e) \approx \gamma_{\mathrm{A,r}} + \underbrace{\gamma_{\mathrm{A,ph0}} + \left(A_{\mathrm{ph1}} + A_e + \gamma_{\mathrm{T}} T\right) n_e + A_{\mathrm{ph2}} n_e^2}_{\gamma_{\mathrm{A,nr}}}. \tag{2.9}$$

This may be expressed compactly as

$$\gamma_{\mathrm{A}}(n_e) \approx \gamma_{\mathrm{A,r}} + \gamma_{\mathrm{A,ph0}} + B n_e + C n_e^2, \tag{2.10}$$

where $\gamma_{\mathrm{A,r}} + \gamma_{\mathrm{A,ph0}}$ is the intrinsic decay rate in the absence of free carriers and the coefficients B and C are parameters that absorb all the doping-dependent relaxation mechanisms. The linear coefficient B captures first-order carrier-assisted processes, including exciton–electron scattering and electron-enhanced phonon-assisted decay, and the quadratic coefficient C accounts for higher-order many-body effects.[227,264] While, microscopically, the interplay between free charges and excitons contains intricacies not captured here, we emphasize that in the regime of linear excitation and low electron density, this approach appropriately captures the experimentally observed trend that electron injection progressively broadens and suppresses the exciton resonance.[233,252,263]

Next, we need to consider the mechanism by which free electrons are induced in the monolayer material to tune the decay rate.

2.1.3 Electrostatic gating

In this section, we discuss the impact of electrostatic gating on the electron density and the exciton decay rate in a planar (parallel-plate-like) metal–oxide–semiconductor capacitor geometry. To express n_e in terms of the applied gate voltage V_{G}, we first note that electrons can bind to excitons to form trions. Charge conservation together with trion formation yields[147,241]

$$n_e + n_{\mathrm{T}} = n_e\,(1 + T\,n_{\mathrm{A}}) = n_{\mathrm{int}} + n_{\mathrm{ext}}(V_{\mathrm{G}}), \tag{2.11}$$

where n_{int} is the intrinsic doping level arising from crystalline defects (*e.g.* sulfur vacancies) and fabrication-induced disorder,[221,268] and $n_{\mathrm{ext}}(V_{\mathrm{G}})$ is extrinsic doping induced via electrostatic gating. In the low-excitation limit, trion formation does not significantly deplete the free-carrier reservoir, implying $1 + T\,n_{\mathrm{A}} \approx 1$ and therefore

$$n_e(V_{\mathrm{G}}) \approx n_{\mathrm{int}} + n_{\mathrm{ext}}(V_{\mathrm{G}}). \tag{2.12}$$

To connect V_{G} to n_{ext}, we start by considering a simple parallel-plate capacitor

geometry, in which the voltage drop V_{ox} across the gate "oxide" (dielectric) is[269]

$$V_{\mathrm{ox}}(n_e) = \frac{e\, n_e}{C_{\mathrm{geo}}}, \tag{2.13}$$

and the capacitance per unit area is

$$C_{\mathrm{geo}} = \frac{\varepsilon_0 \varepsilon}{d}, \tag{2.14}$$

with thickness d and static permittivity ε of the gate dielectric, and the elementary charge e. For 2D semiconductors, however, the finite density of states in the channel implies that a non-negligible part of the applied bias is spent on shifting the chemical potential.[270,271] This is commonly captured by the quantum capacitance, C_{q}, connected in series with C_{geo}, such that the overall capacitance per unit area is[272]

$$C = \left(\frac{1}{C_{\mathrm{geo}}} + \frac{1}{C_{\mathrm{q}}}\right)^{-1}. \tag{2.15}$$

To determine the voltage drop associated with the quantum capacitance, we employ the carrier statistics for a 2D parabolic band,[271]

$$n_e = g_{\mathrm{2D}} k_{\mathrm{B}} T \ln\left[1 + \exp\left(\frac{eV_{\mathrm{ch}} - E_0}{k_{\mathrm{B}} T}\right)\right], \tag{2.16}$$

where V_{ch} is the channel electrostatic potential (*i.e.* the Fermi level shift expressed as a voltage), $E_0 = E_{\mathrm{bg}}/2$ corresponds to midgap for a symmetric two-band picture, with bandgap energy E_{bg} and the 2D density of states

$$g_{\mathrm{2D}} = \frac{g_{\mathrm{s}} g_{\mathrm{v}} m^*}{\pi \hbar^2} \tag{2.17}$$

with effective mass m^* and spin/valley degeneracies g_{s} and g_{v}, respectively. Inverting Eq. (2.16) yields an explicit relation for the channel potential as a function of density,

$$V_{\mathrm{ch}}(n_e) = \frac{E_0}{e} + \frac{k_{\mathrm{B}} T}{e} \ln\left[\exp\left(\frac{n_e}{g_{\mathrm{2D}} k_{\mathrm{B}} T}\right) - 1\right]. \tag{2.18}$$

The applied gate voltage is then the sum of the dielectric drop and the channel potential shift,

$$V_{\mathrm{G}} - V_{\mathrm{CNP}} = V_{\mathrm{ox}}(n_e) + V_{\mathrm{ch}}(n_e) = \frac{e\, n_e}{C_{\mathrm{geo}}} + \frac{E_0}{e} + \frac{k_{\mathrm{B}} T}{e} \ln\left[\exp\left(\frac{n_e}{g_{\mathrm{2D}} k_{\mathrm{B}} T}\right) - 1\right], \tag{2.19}$$

where the charge neutrality point V_{CNP} is the gate-voltage offset required to bring the system to charge neutrality in the presence of a non-zero background doping n_{int}

(such that $n_e \approx 0$ when $V_G = V_{CNP}$). Overall, this procedure is equivalent to treating the quantum-capacitance effect as a series contribution to the gate response,[271,272] while retaining the full carrier statistics appropriate for 2D TMDC channels.[270] However, because Eq. (2.19) is transcendental in n_e, it cannot be inverted in closed form and must be evaluated numerically. We therefore compute the quantitative mapping $V_G \mapsto n_e$ in order to translate an applied gate bias into a carrier-density-dependent exciton decay rate $\gamma_A(n_e)$.

In sum, the previous sections established the control knob of our active metasurfaces: by applying a gate voltage, we induce free carriers in a 2D semiconductor to dynamically tune the exciton resonance. In the remainder of this section, we introduce the photonic resonance that we leverage to maximize the excitonic light-matter interaction.

2.1.4 Guided-mode resonances

Throughout this thesis, we harness nonlocal modes known as guided-mode resonances to enhance the excitonic light-matter interaction. These resonances arise from light scattering with a periodic perturbation introduced in or on a waveguiding layer, facilitating coupling of free-space radiation with a guided mode supported by the structure.[2,41,273,274]

To understand the mechanism, consider a one-dimensional, translationally invariant grating with period Λ and illumination from air with free-space wavevector $k_0 = 2\pi/\lambda_0$, which can be decomposed into in-plane ($k_\parallel$) and out-of-plane (k_z) components,

$$k_0^2 = k_\parallel^2 + k_z^2. \tag{2.20}$$

The in-plane component is set by the incidence angle θ with respect to the surface normal (in the plane perpendicular to the grating lines) as

$$k_\parallel = k_0 \sin\theta. \tag{2.21}$$

By way of scattering, a grating can add (or subtract) integer multiples m of the reciprocal lattice vector,

$$q = \frac{2\pi}{\Lambda}. \tag{2.22}$$

Hence, the m^{th} spatial harmonic of the scattered field has in-plane wavevector

$$k_\parallel^{(m)} = k_0 \sin\theta + m\frac{2\pi}{\Lambda}. \tag{2.23}$$

For a given excitation and grating structure, propagating diffraction orders exist in the superstrate if $|k_\parallel^{(m)}| \leq k_0$; otherwise no real-valued k_z can satisfy Eq. (2.20) and

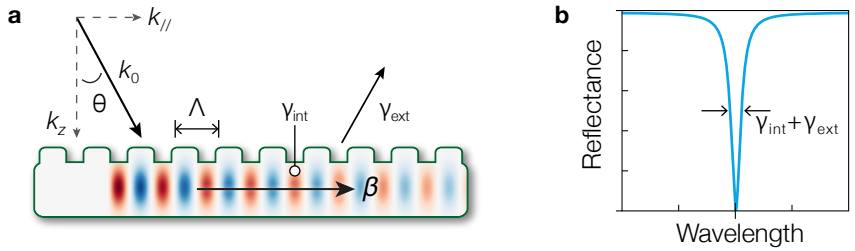

Figure 2.1: Guided-mode resonance. (a) Schematic of a guided-mode resonance in a subwavelength grating. The quasi-guided mode experiences internal (absorption) losses γ_{int} and external (radiative) losses γ_{ext}. **(b)** The resulting reflection spectrum shows a sharp resonant dip with a full-width-at-half-maximum linewidth of $\gamma_{int} + \gamma_{ext}$.

the order is purely evanescent. In Section 1.3, we introduced subwavelength gratings as the earliest optical metamaterials. These operate in the regime where $\Lambda < \lambda_0$ and therefore all orders except the specular 0^{th} order are evanescent, such that only the 0^{th} order appears in the far-field channel.

In this evanescent-order regime, the periodic perturbation can couple an incident plane wave to a guided mode supported by the structure (Fig. 2.1a). Since guided modes have a higher in-plane wavevector than free-space waves at the same frequency ($\beta > k_0$, with $n_{eff} = \beta/k_0$), a truly guided mode cannot be excited directly from free space, because phase matching requires $k_{\parallel}^{(m)} = \beta$. In a guided-mode resonant structure, the periodic pattern supplies the missing in-plane momentum (q). By reciprocity, the mode can also radiate out through the grating, becoming a leaky (quasi-guided) mode with a finite radiative lifetime, γ_{ext}, set by the grating geometry, manifesting in reflection or transmission spectra as a sharp guided-mode resonance (GMR; Fig. 2.1b). By confining light inside the structure for multiple optical cycles, GMRs yield strong near-field enhancements, and embedding a 2D semiconductor in the waveguiding region therefore leads to enhanced excitonic light–matter interactions. It is precisely this mechanism that we harness in our hybrid-2D metasurfaces. How we fabricate these structures is described in the next section.

2.2 FABRICATION

In this section, we detail the fabrication protocols for creating prepatterned substrates (Section 2.2.1), van der Waals heterostructures (2.2.2), and dielectric subwavelength gratings (2.2.3) used throughout this work. In addition, we discuss the rationale behind certain design choices.

2.2.1 Prepatterned substrates

In our metasurfaces, we employ electrostatic gating to control the charge density in monolayer 2D semiconductors. A common approach to realize electrical contacts starts by transferring the monolayer material, then creating a lithographic mask, and finally depositing electrodes directly onto the material. This increases the contact resistance by introducing defects, strain and atomic disorder in the contact region, as well as degrading the material quality during the various processing steps.[275] To circumvent this, we prepare chips with prepatterned gold (Au) electrodes and deterministically transfer the 2D material onto the electrodes (described in the next section). It should be noted that the devices presented in this thesis are designed to operate in reflection, and we therefore create double-purpose gold pads serving simultaneously as optical back-reflector and a localized electrical back-gate. Using this strategy, we find that our fabricated devices show excellent tunability at ambient conditions (Chapter 3).

Despite this, our strategy also has drawbacks. For instance, the surface roughness of the evaporated metal and potential surface contaminants (including atmospheric water and hydrocarbons) degrades the 2D semiconductor-metal interface, increasing the contact resistance and the resistive-capacitive time constant of the electrical circuits, thereby lowering the modulation bandwidth.[276] Fortunately, the interface cleanliness can be improved post-hoc by thermally annealing the structure in a vacuum environment (2.2.2).[277,278] Future work could employ several promising methods that have recently been demonstrated to lower the contact resistance. For instance, van der Waals contacts reduce process-induced damage[279], semimetallic contacts lower the Schottky barrier[280], and edge contacts facilitate direct in-plane carrier injection into the channel[281].

To create our prepatterned substrates, we use the following protocol:

1. We start from commercially obtained silicon wafers with 100 nm or 300 nm dry-grown thermal oxide[i], which are diced into 12 × 12 mm^2 substrates.

2. The substrates are thoroughly cleaned using base piranha (a 1:1 solution of NH_3:H_2O_2) at ~75 °C for ~10 min, followed by an isopropyl alcohol (IPA) rinse and nitrogen-gas (N_2) blow-dry.

3. We spin-coat a ~400 nm layer of positive-tone electron-beam resist (chemical semi-amplified resist, CSAR AR-P 6200, diluted 13% in anisole) at 4000 rpm using a spin coater[ii], and cure it on a hot plate for 2 minutes at 175 °C.

[i] University Wafer
[ii] Süss MicroTec Delta 80

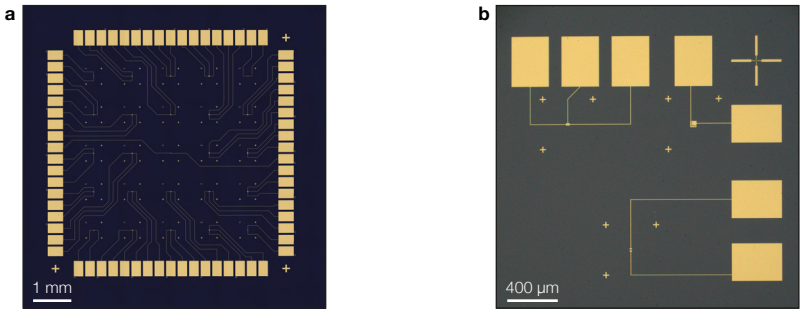

Figure 2.2: Prepatterned substrates. **(a)** Large-area stitched image of a 2nd-generation prepatterned substrate, and **(b)** close-up of several electrodes on a 3rd generation chip.

4. The electrode outlines are patterned by electron-beam lithography[i] (beam current 1.96 nA, dose ~150 µC/cm^2, dwell time 310 ns).

5. The resist is developed by immersing the sample for 60 s in n-amyl acetate, followed by 7 s in o-xylene, and finally 15 s in MIBK:IPA (9:1) to stop the development process. The samples are then rinsed with IPA and dried with N_2 gas.

6. Next, we mount the samples in a custom thermal evaporator, pump it down to ~ 10^{-6} mbar, and deposit a 3 nm chromium (Cr) adhesion layer at a rate of 0.5 Å/s, followed by a 100 nm Au layer at 1.0 Å/s.

7. The residual resist is removed by lift-off in anisole at elevated temperature (typically 70 °C for ~20 min), assisted by intermittently creating turbulence in the solvent using a syringe.

8. After lift-off, we thoroughly clean the substrate with the gold contacts using another base piranha step, followed by an IPA rinse and N_2 blow-dry.

9. Finally, we apply a short O_2/N_2 plasma treatment (~2 min at ~70 W)[ii] to remove residual organic contamination from the prepatterned substrates, before ultimately storing them in a N_2 atmosphere.

2.2.2 Van der Waals heterostructures

Since the first isolation of graphene in 2004,[216] the 2D materials community has made tremendous progress in improving the size and quality of atomically thin layers via top-down exfoliation.[282–286] as well as bottom-up growth.[287–290] Additionally, by now,

[i] Raith Voyager, 50 kV acceleration voltage
[ii] Diener Zepto

countless protocols exist for handling, transferring, and stacking various layered van der Waals materials to create heterostructures.[291–301] Since the aim of this thesis is to leverage 2D materials in active and nonlocal metasurfaces, the methods outlined below do not represent the latest advances, nor are they particularly well-suited for commercial manufacturing. Instead, the employed techniques enable straightforward and reliable fabrication of high-quality van der Waals heterostructures with precisely controlled geometries and active areas of tens of micrometers, making them very valuable for prototyping and proof-of-principle demonstrations in a laboratory setting.

Exfoliation

To start, we obtain bulk crystals of van der Waals layered materials commercially[i]. We then manually exfoliate the crystals to obtain "flakes" of the desired thickness with blue "surface protection" tape[ii] (polyvinylchloride film with an acrylic adhesive). For excitonic materials, such as tungsten disulfide (WS_2), this is typically the monolayer limit, whereas for other materials, *e.g.* hexagonal boron nitride (hBN), the thickness is often rather on the order of 10–100 nm, depending on the application. The exfoliation procedure is inherently stochastic, such that we need a method of identifying and selecting the flakes that match the size and thickness requirements of a particular heterostructure. For this reason, after exfoliating 4–8 times with the blue tape, depending on the thickness of the starting crystal,[302,303] we perform one final exfoliation onto a transparent carrier substrate ("stamp") cut from a sheet of ~ 150 µm thick polydimethylsiloxane (PDMS) with a polyester backing[iii].

In our experience, tape exfoliation should be performed slowly to prevent cracking and folding of the flakes, while the transfer onto PDMS should be performed rapidly to maximize the yield. The latter may be explained by the viscoelasticity of PDMS: it behaves like a viscous liquid on long time scales and as an elastic solid on short time scales, such that quick movements tend to promote adhesion. Oppositely, the viscous regime facilitates detachment from the PDMS surface, which is exploited for the deterministic transfer method outlined below. After the final exfoliation step, the PDMS substrate is covered with a large amount of flakes of varying shapes and sizes. We identify suitable flakes using our modular confocal microscope system[iv] (Section 2.3).

[i] HQ Graphene
[ii] Nitto SPV-224
[iii] Gel-Pak WF-30
[iv] WITec α-300

Identification

To identify potentially useful flakes of an exfoliated Van der Waals material, we employ different strategies depending on whether we are looking for a monolayer or a multilayer. For a given material, monolayers can typically be identified by measuring their Raman "signature", *i.e.* the unique pattern of inelastic scattering modes that characterize the material in question. Typically, Raman modes tend to be different for monolayers then their bulk counterparts, such that they can be identified by comparing the measured Raman response to a well-established reference, given that it exists. However, monolayers of strongly emissive excitonic materials such as WS_2 are much more rapidly identified by their photoluminescence, which is orders of magnitude stronger in the monolayer limit than it is for thicker flakes (Section 1.6).[224,225] For this, we employ direct photoluminescence imaging (see also Section 2.3.2) using widefield laser excitation[i] and a long-pass filter[ii] inserted before the camera. When the camera gain is sufficiently increased, the monolayer emission (~ 620 nm for WS_2 at room temperature) becomes clearly visible against an otherwise dark background, allowing for rapid identification of large monolayer regions.

Beyond the monolayer limit, the use of van der Waals materials in photonic designs generally calls for flakes with high thickness uniformity and precise knowledge of the layer thickness to tailor interference in the scattered light. As such, a fast and reliable technique is required to sift through large amounts flakes and determine their thicknesses. To this end, potentially useful multilayers are first identified by eye, after which their thicknesses are determined using reflectometry, which leverages thin-film interference and a fitting routine to extract the thickness, as discussed in Section 2.3.1. Although the throughput of this method is relatively low, an experienced user can visually identify flakes with thicknesses in the right ballpark (± 20 nm) based on their apparent color (arising from thin-film interference), which drastically speeds up the overall searching phase.

Transfer

When flakes of the desired size and thickness are identified, we use an all-dry deterministic stamping technique that leverages the viscoelasticity of PDMS to transfer flakes from the stamp onto the target substrate (Fig. 2.5). This approach was first demonstrated in 2014 and has since been refined.[304,305] Despite substantial advances in 2D-material handling—which now enable pick-up, rotation, flipping, and deposition with high precision and cleanliness[291–301]—all-dry PDMS stamping remains relevant by providing one of the simplest methods to reliably create high-quality heterostructures from tape-exfoliated flakes. In practice, this simplicity is often

[i] For instance, using a Becker & Hickl 405 nm diode laser.
[ii] Thorlabs

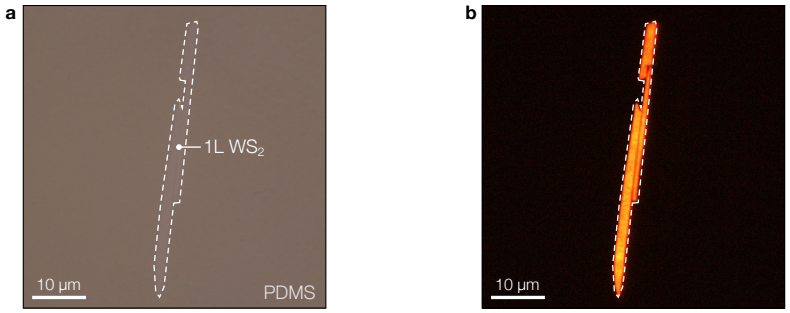

Figure 2.3: Monolayer identification. **(a)** Brightfield microscope image of a monolayer WS_2, barely visible against the PDMS substrate under LED illumination. **(b)** Direct photoluminescence imaging of the same monolayer. The illumination is switched to widefield excitation using a 405 nm laser, and a 550 nm long-pass filter is inserted in the detection arm to suppress the reflected laser light, leaving only the excitonic emission around $\lambda_A = 620$ nm visible on the camera.

beneficial in the prototyping stage, compared to elaborate transfer schemes that require specialized multilayer stamps or restrictive stacking routines, and whose reproducibility can be sensitive to hidden variables such as surface hydrophilicity, ambient humidity, and the precise polymer composition.

PDMS stamping is nonetheless subject to several limitations: (i) PDMS can leave uncrosslinked surface oligomers on contacted surfaces that are difficult to remove; (ii) the method is not selective, so nearby flakes are often transferred unintentionally; (iii) it is not well suited for pick-up; and (iv) it is sensitive to surface chemistry (including adsorbed water) and roughness, and tends to fail if adhesion between the flake and the target substrate is too weak.[i]

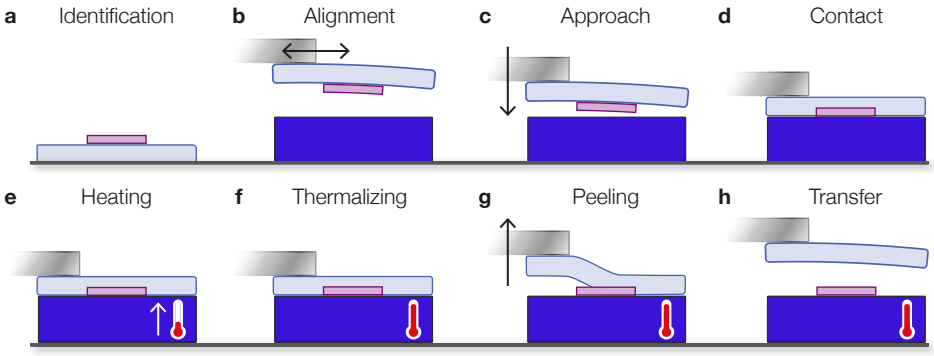

Figure 2.4: Deterministic transfer using PDMS. The general steps of PDMS transfer are: (1) identification of a suitable flake; (2) aligning the stamp, and (3) approaching the substrate, (4) to make contact. (5) The stack is heated, and (6) thermalized before (7) slowly peeling the stamp to (8) complete the transfer.

[i] To address these limitations, a new transfer method was recently developed in-house that employs common cling film to achieve selective pick-up and transfer onto low-adhesion substrates including metasurfaces [306].

The stamping setup is a self-built optical microscope[i] with long-working-distance objectives[ii], a sample platform comprising a hand-calibrated, PID-controlled heating element with a lateral translation stage that provides micrometer precision, and a stamping stage comprising a mechanical fixture for the stamp and three computer-controlled micro-actuators for lateral movement.

Figure 2.4 shows a schematic representation of the general stamping procedure broken down into eight steps, whereas Fig. 2.5 shows representative microscope images of some of these steps for a specific multilayer hBN flake being stamped onto prepatterned contacts. In the following, we describe the procedure in detail.

1. We mount the stamp in the stamping stage in a cantilever-like geometry. To this end, we first prepare a glass slide with a piece of double-sided tape at the edge, attaching the polyester backing on the side farthest from the target flake to the tape. By leaving the region containing the target flake overhanging (protruding beyond the glass slide), the semi-flexible stamp bends slightly under gravity, which helps to control the initial contact in a later step.[iii]

2. We mount the target substrate on the heating stage of the stamping microscope, keeping in mind the orientation of the flake on the stamp and the desired orientation on the substrate, as we have limited control over the rotation degree of freedom afterwards.

3. Next, we mount the glass slide in the stamping stage, *i.e.* with the stamp hanging upside down (flakes facing downward).

4. We align the stamp over the target substrate, and gently lower the stamp while continuously monitoring and fine-adjusting the alignment.

5. As the stamp comes into close proximity to the substrate, a thin air layer keeps them separated until they suddenly make contact at a nucleation point, producing a propagating contact front that expels the intervening air. Because the stamp is slightly bent, it typically makes first contact at the outer edge, with the contact front traveling inward toward the flake.[iv] If the stamp does not nucleate spontaneously, gentle pressure is applied using a polyester-tipped applicator[v] to initiate contact.

[i] Components obtained primarily from Thorlabs.
[ii] Nikon CFI Plan Fluor 4X, 10X, and 20X
[iii] It also helps to avoid trapped air pockets at the target location, which can otherwise prevent transfer, and ensures that no excessive downward force is exerted on the flake upon contact.
[iv] It is often possible to stop the contact front just beyond the flake by raising the glass slide slightly, preventing further unintended transfer beyond that point.
[v] Ted Pella, Inc.

6. Once the stamp and flake are fully in contact, we heat the stack from room temperature to 60–65 °C and let it thermalize for at least 5 minutes. This promotes conformal contact and helps trapped air escape.

7. Next, we raise the glass slide at a controlled rate of 0.1–0.5 µm/s to disengage the stamp from the substrate. As the stamp gradually detaches, the contact front moves from the outside in with a lateral speed of 0.5–1.5 µm/s.[i] By heating the PDMS (with the temperature chosen empirically), it becomes more viscous, which further lowers adhesion such that the flake is reliably transferred to the target substrate.

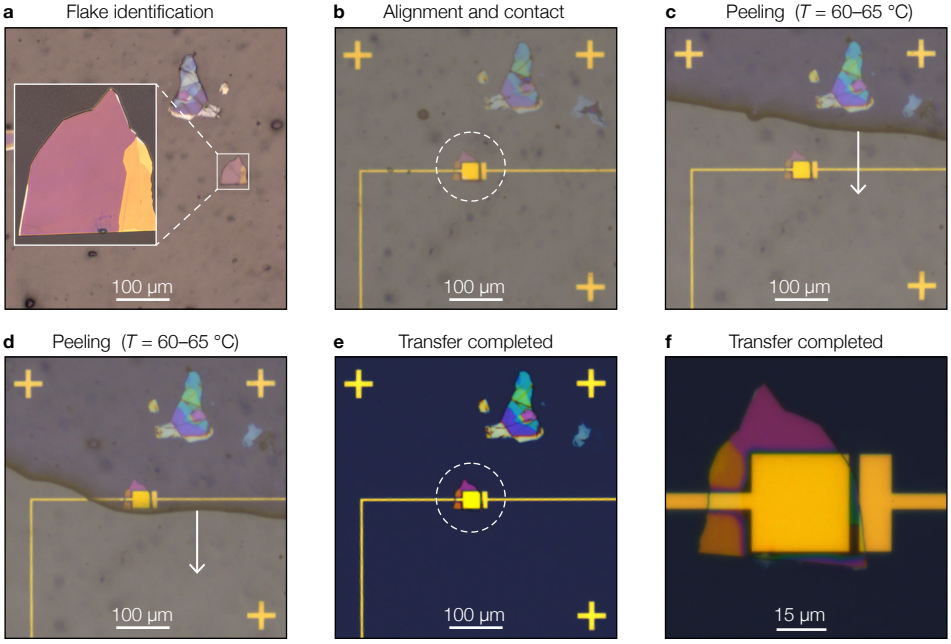

Figure 2.5: Stamping hBN on prepatterned contacts. **(a)** Identification of a hBN flake on PDMS. **(b)** After alignment of the flake over the prepatterned gold pad, the stamp is brought into contact. **(c)** When the stack has thermalized at 60–65 °C, the stamp is slowly peeled. The contact front propagates in the indicated direction. **(d)** The contact front passes the region of interest. **(e)** The flake is transferred successfully, **(f)** with no *visible* damage or residue.

Annealing

Vacuum thermal annealing is a simple but powerful post-transfer step to improve the interfacial quality of van der Waals heterostructures, reducing strain and promoting conformal contact by relaxing interfacial bubbles and wrinkles.[307] In addition,

[i] Since the vertical motion indirectly controls the lateral speed, we sometimes pause to ensure that peeling does not proceed too quickly.

vacuum annealing removes contamination from exposed surfaces as well as buried interfaces through diffusion, minimizing unwanted doping and improving electrical contacts.[278] Together, these effects make vacuum annealing an enabling step for achieving more stable performance in hybrid-2D metasurfaces.

Specifically, after each transfer step, we thermally anneal the sample in a tube furnace. We place the sample in a quartz boat, slide it into a quartz tube, and attach it to a turbomolecular pump[i] to reach $P \approx 10^{-6}$–10^{-7} mbar. The furnace temperature is set by a PID[ii] controller, and we calibrated the temperature inside the quartz tube by measuring it at various positions and setpoints using a thermocouple. Typically, we program a ramp rate of 1–3 °C/min, a set temperature of 100–300 °C, and a dwell time of 1–24 h.

We note that the variability in ramp rates and dwell times is mostly due to practical time constraints, and we generally aim for a slow ramp rate and a long dwell time. To choose an annealing temperature, we first inspect the sample optically for interfacial contamination.[iii] If the interface appears dirty, we typically use lower temperatures, as we have observed that harsh annealing can cause the stack to "explode", likely due to excessive pressure build-up resulting from the coalescence of interfacial contaminants into agglomerates.[294,309] Conversely, if the interface appears clean, we set the temperature to 300 °C, as WS_2 has been shown to safely withstand this temperature in a vacuum environment.[310]

The sample is then ready for another round of stamping, or for nanofabrication if the heterostructure is complete.

2.2.3 Subwavelength gratings

To create subwavelength gratings, two primary routes can be identified: either the structure can be shallow-etched into the topmost layer, or patterned in a spin-coated layer of low-index (electron-beam or photo-)resist.[250,311] The latter approach is especially useful in the prototyping stage because, if the patterning fails, the resist can simply be dissolved and re-applied for another attempt. Moreover, based on recent demonstrations of million-Q guided-mode resonators, it is clear that this approach can be leveraged to achieve structures with exceptionally low disorder. Together, these features make it an attractive approach for our hybrid-2D metasurfaces.

To fabricate the subwavelength grating on top of the encapsulated heterostructure, we use the following protocol.

1. Because the topmost layer is hBN, we can safely apply an oxygen plasma cleaning step to remove organic surface contamination and improve resist

[i] Pfeiffer Vacuum TSH 261
[ii] Eurotherm 2404
[iii] Note that hidden residues may be present as well, as revealed by atomic force microscopy [308].

adhesion, without directly exposing WS_2 to reactive chemistries. We apply a brief 30–60 s O_2 plasma[i] at 5 mTorr pressure (30 mTorr strike pressure), 25 sccm flow rate, and 50 W RF power. The typically observed DC bias is ~166 V.

2. Next, we let undiluted CSAR AR-P 62.09 electron-beam resist equilibrate to room temperature for ~15 min. To prevent resist from flowing underneath the chip during spin coating, we stick a square of blue polyester tape underneath the substrate. We then spin-coat the CSAR at 4000 rpm with 1500 rpm/s acceleration for 50 s, yielding a resist thickness of ~210–225 nm. We cure the resist for 120 s on a hot plate set to 150 °C. Finally, we make a small scratch in the bottom-right corner using a diamond pen, which is used as a height reference during pattern writing.

3. After spin coating, we determine the CSAR thickness using reflectometry in our confocal microscope setup[ii] and fit the reflectance with a transfer-matrix model (similar to the method in Section 2.3.1). To this end, we first determine the dielectric function of CSAR via spectroscopic ellipsometry of the material spin-coated on a Si chip.[iii] Using the measured resist thickness, we then refine the grating pitch and fill factor before finalizing the GDSII layout.

4. We expose the grating with electron-beam lithography[iv], aligning the pattern using a three-point adjustment—first with large alignment marks at the corners of the prepatterned substrate, followed by small marks near the stamped heterostructure (typical beam current 1.93 nA, dwell time 265 ns, and dose ~131 $\mu C/cm^2$).

5. The resist is developed by immersing the sample for 60 s in n-amyl acetate, 7 s in o-xylene, and 15 s in MIBK:IPA (9:1) to stop the development. We then rinse in IPA for > 15 s and dry with N_2 gas.

6. To verify that the fabricated dimensions match the design, we characterize the patterned grating by performing atomic force microscopy on a small, representative section of the grating.[v]

2.2.4 Electrical connections

To enable electrical contact and mounting in the optical microscope, we attach one of the sample chips to a custom printed circuit board (PCB) using double-sided tape. Using a manually operated wedge bonder (Fig. 2.6a),[vi] we wire-bond the gate and

[i] Oxford Instruments Plasma 80
[ii] WITec α-300
[iii] J.A. Woollam VB-400
[iv] Raith Voyager, 50 kV acceleration voltage
[v] Bruker Dimension FastScan
[vi] West.Bond 7KE

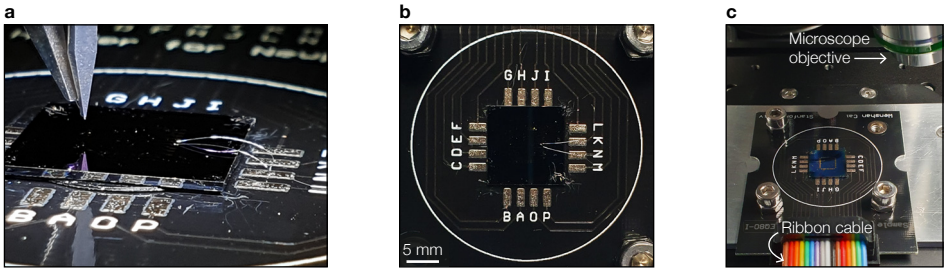

Figure 2.6: Electrical connections. **(a)** Wire-bonding the chip to a custom PCB, **(b)** yields a stable electrical interface. **(c)** The PCB is screwed onto the microscope stage for mechanical stability.

ground electrodes to the PCB with 25 µm diameter aluminium wires, yielding a stable electrical interface (Fig. 2.6b) to electronic instruments using a 16-pin ribbon cable (Fig. 2.6c). For mechanical stability, the PCB is mounted on a metal plate that can be screwed to the microscope's piezo-actuated translation stage. In sum, this completes the fabrication of a representative electrically tunable hybrid-2D metasurface.

2.3 CHARACTERIZATION

The primary experimental platform used throughout this thesis is *Hyperion*.[i] This highly customized, partially self-built setup is centered around a modular, diffraction-limited confocal microscope[ii] and integrates a range of light sources, detection schemes, and electronic instrumentation that collectively enable a wide variety of measurement configurations. In Chapter 4, we additionally use *Skaði*,[iii] an in-house-built 4f Köhler-illumination microscope integrated with a closed-cycle helium cryostat.[iv] In this section, we briefly describe the configurations and procedures used for the most important measurements throughout this thesis. For visual clarity, the setup schematics are not drawn to scale and do not strictly match the full experimental geometries, which are typically more convoluted due to practical constraints. Rather, they should be viewed as idealized representations that highlight only the components critical to each experiment.

2.3.1 Reflectometry

In general, Hyperion is well suited for various forms of optical spectroscopy, including reflection and photoluminescence (Section 2.3.2), both in real space and in momentum space (*i.e.*, angle-resolved). In this section, we describe the standard reflection configuration used for reflectometry experiments (Fig. 2.7).

[i] The Greek Titan of Heavenly Light.
[ii] WITec α-300
[iii] The Nordic Goddess of Winter.
[iv] Montana CryoAdvance-50

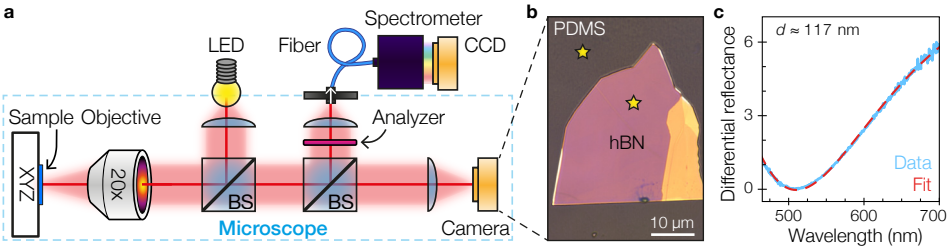

Figure 2.7: Reflectometry. (a) Schematic of Hyperion configured for regular (image-plane) reflection spectroscopy. Focused LED illumination is collected by the objective, chromatically dispersed by a fiber-coupled spectrometer and detected on a charge-coupled device (CCD) camera. XYZ: three-axis sample positioning stage, BS: beam splitter. **(b)** Image of a hBN flake on PDMS. The stars indicate the measurement positions. **(c)** Differential reflectance measured (light blue) and fitted (red, dashed) to a hBN thickness of $d = 117$ nm.

Determining a layer thickness using reflectometry relies on accurate thin-film interference measurements and subsequent comparison to the theoretical thickness-dependent response. Here, we use the microscope's LED[i] as the white-light source, which is directed onto the sample with a beam splitter (BS) and focused onto the sample with an objective lens.[ii] The sample itself is mounted on a stage that combines long-range lateral translation driven by a stepper stage with fine three-axis motion provided by a piezo stage. The reflected signal is collected by the same objective and directed either onto the camera or into the detection arm for spectroscopic measurements. The detection arm features a linear polarization analyzer, after which the light is out-coupled to a spectrometer[iii] that chromatically disperses the light onto a charge-coupled device (CCD) camera.[iv]

In general, there are two main methods to characterize the reflection, the absolute reflection (reflectance, or $R = |r|^2$, where r is the Fresnel reflection coefficient) and differential reflection (ΔR). Experimentally, the reflectance is typically calculated as

$$R = \frac{I - I_{\text{dark}}}{I_{\text{ref}} - I_{\text{dark}}} \times R_{\text{ref}}. \tag{2.24}$$

where I is the reflected intensity from the sample and I_{dark} denotes the dark counts measured on the CCD when the illumination is turned off, which in the diffraction-limited detection scheme is simply given by the thermal noise of the CCD camera. Moreover, I_{ref} is the reflected intensity from the chosen reference, and R_{ref} is its

[i] Alternatively, a halogen lamp can be used for a broader and more uniform illumination spectrum, but this comes with the disadvantage of long stabilization times and temperature-induced drift in the microscope's optical response.

[ii] Zeiss Epiplan 5x (NA = 0.13), 20x (NA = 0.4), 50x (NA = 0.75), 50x long working distance (NA = 0.55), or 100x (NA = 0.9).

[iii] WITec UHTS300 SMFC VIS spectrograph, with gratings of 150, 600, or 1800 lines/mm and center wavelength of 500 nm.

[iv] Andor Newton EMCCD camera, cooled to -60 °C

theoretical spectrum. Common normalization references such as coated silver mirrors can be obtained commercially[i] together with tabulated polarization-resolved spectral reflectance data. In practice, however, many different references can be used, provided that their theoretical response can be accurately established. It is generally beneficial to use a highly reflective surface, since low intensities in the denominator of Eq. 2.24 can strongly amplify the normalization error. In this thesis, we broadly use the (angle-resolved) intensity measured on an optically thick gold layer as the reference (an example of the normalization procedure is shown in Fig. 3.A8). We establish R_{ref} by taking the optical constants of thin-film gold from literature,[312] and use these to numerically calculate the corresponding thin-film reflectance.[2]

To determine the thickness of hBN flakes during the flake identification stage (Section 2.2.2), we typically measure the differential reflection by recording the reflected intensity I_{sub} of the PDMS substrate immediately next to the flake and calculate the differential reflectance as

$$\Delta R = \frac{I - I_{\mathrm{sub}}}{I_{\mathrm{sub}} - I_{\mathrm{dark}}}. \tag{2.25}$$

We then use a custom Python script that fits a transfer-matrix simulation of ΔR to the measured spectrum using the refractive-index dispersion of the constituent materials.[ii] Provided that the optical constants accurately represent the material under investigation, this procedure can determine the thickness with high accuracy. For instance, for the hBN flake shown in Fig. 2.5 and Fig. 2.7b, we find excellent agreement between the measured and fitted spectra and extract a thickness of d = 117 nm (Fig. 2.7c).[iii]

2.3.2 Photoluminescence

We perform photoluminescence spectroscopy and mapping with Hyperion in dark-field mode using a fiber-coupled 532 nm continuous-wave laser (Fig. 2.8). The laser is directed toward the sample with a holographic beam splitter (HBS) and focused into a diffraction-limited spot with a dark-field-supporting objective. The same objective collects the emitted light at high angles (relative to the surface normal) and directs it toward a fiber-coupled spectrograph, where the HBS filters out the laser; an analyzer can be inserted for polarization-resolved measurements. For spectrally

[i] Thorlabs

[ii] The optical constants are typically taken from literature as tabulated data, including hBN[313] and PDMS[314] or, in select cases such as CSAR, measured by spectroscopic ellipsometry.

[iii] It should be noted that, unlike ellipsometry, reflectometry as employed here does not uniquely determine both the thickness and refractive index, since an error in one can often be partially compensated by the other. Consequently, if the refractive index taken from literature does not accurately match the material in the lab, the fit may still appear very good while the extracted thickness is inaccurate. In practice, however, this is often not critical, provided that the same refractive index is also used in the simulations employed to design the structures and that the mismatch is not too large.

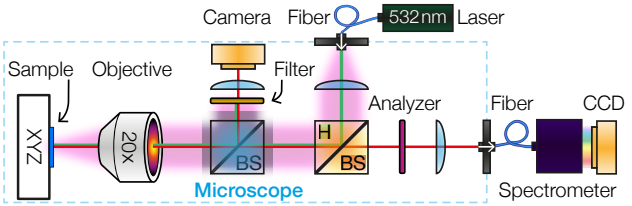

Figure 2.8: Photoluminescence spectroscopy. Schematic of Hyperion configured for photoluminescence spectroscopy and mapping. BS: beam splitter, HBS: holographic beam splitter, CCD: charge-coupled device, XYZ: three-axis sample positioning stage.

resolved spatial mapping, we control the sample position using the piezo-actuated stage. Light can also be directed onto the camera, where a long-pass filter suppresses the laser; under widefield excitation, this enables direct imaging of a monolayer's photoluminescence emission on the camera (Fig. 2.3b).

2.3.3 Angle-resolved reflection

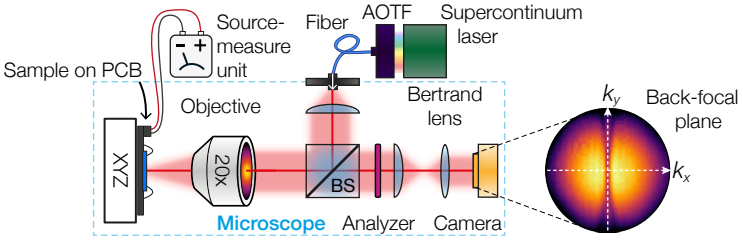

Figure 2.9: Angle-resolved reflection. Schematic of Hyperion configured for angle-resolved reflection measurements via back-focal (Fourier) plane imaging. BS: beam splitter, AOTF: acousto-optically tunable filter, $k_{x,y}$ in-plane wavevector components. XYZ: three-axis sample positioning stage.

The microscope cannot be configured to use white-light excitation for angle-resolved reflection measurements. Instead, we use a tunable laser system coupled into the microscope via a single-mode photonic crystal fiber[i] (Fig. 2.9). Linearly polarized coherent light is provided by a pulsed supercontinuum white-light source[ii], which is spectrally selected with an acousto-optically tunable filter[iii] (AOTF) to yield monochromatic light with a bandwidth of ~1 nm across the visible range. The collimated beam is directed to the entrance pupil (Fourier plane) of the 20× (NA = 0.4) objective, producing a diffraction-limited spot at the sample plane. For direct-current electrical gating measurements, the PCB-mounted sample can be connected to a source-measure unit controlled via a custom script that ramps the voltage from zero

[i] NKT Photonics SuperK, Connect FD7-PM
[ii] Extreme EXW-12; 78 MHz repetition rate, ~5 ps pulse width
[iii] Select VIS/1X

to the setpoint to avoid abrupt voltage steps and thereby limit transient current peaks that could lead to dielectric breakdown. Since the incident polarization is fixed by the microscope, we rotate the sample holder (PCB) by a quarter turn around the optical axis to switch between orthogonal linear polarizations.

The reflected signal is collected by the same objective and imaged onto a 14-bit monochromatic CMOS (complementary metal-oxide-semiconductor) camera[i]. A Bertrand lens can be inserted in the detection path to switch between real-space and momentum-space imaging. The incident power and camera exposure time are calibrated and adjusted slightly per wavelength to maximize the signal-to-noise ratio. For position-dependent dispersion measurements, we automate wavelength sweeps and piezo-stage scans using a custom Python control script. Two reference measurements are acquired: one without a sample mounted to account for internal reflections, and one normalization reference.

We extract the k_x and k_y dispersions from the back-focal plane images by carefully determining the center and radius in pixels of the back-focal plane in an over-exposed image, and performing a coordinate transformation between image pixels and the objective numerical aperture using the known back-focal plane radius in millimeter. A distinct dust particle visible on the Fourier plane helps to align the images and ensures a common center coordinate. We enhance the signal-to-noise ratio by integrating traces over a small angular region ($-3 \leq \theta \leq 3$ mrad, 11 pixels). By repeating this process at each wavelength, we construct the dispersion relation line-by-line.

2.3.4 Alternating current modulation

We perform frequency-dependent alternating-current modulation measurements by appropriately modifying the Hyperion setup (Fig. 2.10). We feed the tunable laser into the microscope via another fiber port with an added collimating lens to achieve wide-field excitation through the 20× objective. A square-wave modulation signal (up to 20 V peak-to-peak) is provided by a function generator[ii], which is interfaced with the PCB via connections to the appropriate pins on the ribbon cable (Fig. 2.6). The modulated beam is collected with the same objective, out-coupled into a fiber, and detected with a biased Si photodiode[iii]. We connect the photodiode output via BNC to a source-measure unit[iv] (operated at 0 V as a current monitor and convenient interface), and amplify the photogenerated current (responsivity ≈ 0.43 A/W) while converting it to a voltage (2 V/nA) with a transimpedance amplifier[v]. Finally, we

[i] Zeiss Axiocam 705 mono
[ii] Agilent HP 33120A
[iii] Thorlabs DET100A2
[iv] Keithley 2600B SourceMeter
[v] Stanford Research Systems SR-570

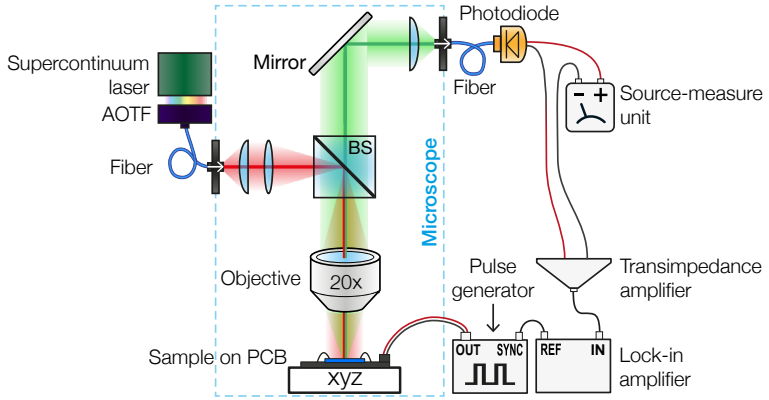

Figure 2.10: Alternating current modulation. Schematic of Hyperion configured for alternating current modulation measurements. BS: beam splitter. XYZ: three-axis sample positioning stage. REF: reference input. SYNC: synchronization output.

measure the signal using a lock-in amplifier[i] or an oscilloscope[ii] (not shown), synchronized to the function generator. For alternating-current reflection spectroscopy, we scan the laser wavelength and record the measured signal at each step. The signal is normalized similarly to regular reflection spectroscopy, according to Eq. (2.24), by additionally recording a bright reference and a dark noise measurement. The measurements are fully automated using custom Python programs.

2.3.5 Cryogenic reflection

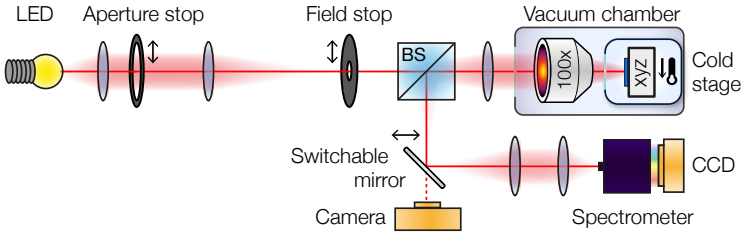

Figure 2.11: Cryogenic reflection. Schematic of Skaði configured for image-plane reflection spectroscopy. The sample, mounted on the cold stage, can be helium cooled down to $T = 3$ K. An aperture stop diaphragm controls the incident angle range, while a field stop diaphragm controls the part of the image plane that is illuminated. LED: light-emitting diode. BS: beam splitter, CCD: charge-coupled device.

We perform cryogenic reflectance measurements with Skaði by mounting the sample (using silver paint for thermal contact) in a closed-cycle helium cryostat

[i] Stanford Research Systems SR-830
[ii] Tektronix TDS 3032

that can be cooled down to 3 K and optically accessed with an objective[i] situated inside the vacuum chamber.[ii] We illuminate the sample with unpolarized white light, controlling the effective angular range with an aperture-stop diaphragm (in the Fourier plane) and the excitation area with a field-stop diaphragm (in the image plane). We capture the reflected signal by projecting the image plane onto the entrance slit of a spectrometer[iii], where it is chromatically dispersed and recorded on the CCD camera.[iv] The full CCD image retains spatial information along the vertical axis (parallel to the entrance slit), while the horizontal axis is spectrally dispersed by the grating, yielding an instantaneous position-wavelength map. To calibrate the spatial axis, we use a switchable mirror to direct the reflected light onto a camera and thereby map the vertical position on the sample to the vertical axis of the CCD image.

Altogether, in this chapter we have provided the necessary modeling frameworks, fabrication protocols, and measurement schemes to design, create, and characterize electrically tunable hybrid-2D metasurfaces. In the next chapter, we leverage these methods to realize a free-space optical modulator that shows nearly 50% reflection modulation by gate-tuning excitons in atomically thin WS_2.

[i] Zeiss Epiplan-Neofluar, 100× objective, NA = 0.9

[ii] The custom-built microscope is highly modular and can readily be configured for reflection and photoluminescence measurements in the image plane as well as the back-focal plane.

[iii] Princeton Instruments SpectraPro 2300i, 300 lines/mm grating

[iv] Pixis Si, cooled to –70 °C

3

FREE-SPACE OPTICAL MODULATION

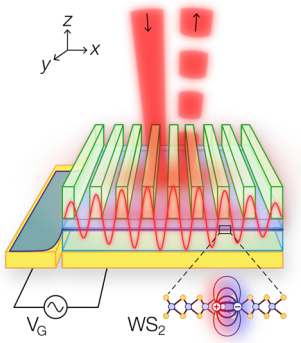

Figure 3.1: Concept of a hybrid-2D metasurface for optical modulation. The electrical tunability of a monolayer 2D semiconductor in a heterostructure cavity is combined with the strong light-matter interaction of a dielectric nonlocal metasurface to achieve strong intensity modulation of the reflected beam.

3.1 INTRODUCTION

IN THIS CHAPTER, we combine the pristine excitonic properties of a van der Waals heterostructure with the nanophotonic field enhancement offered by a nonlocal metasurface to demonstrate a dynamically tunable excitonic metasurface with high efficiencies. This hybrid-2D configuration enables strong exciton-photon interactions, which we harness for free-space optical modulation by electrically manipulating excitons in monolayer tungsten disulfide (WS_2). By switching between the weak and strong coupling regimes, we demonstrate 9.9 dB modulation of the reflected beam at room temperature, which is a fivefold improvement over the previous record reflection contrast achieved with excitonic 2D materials[147]. Furthermore, we show that the gating-induced free carrier density governs the exciton's nonradiative decay rate, providing a continuous transition from strong to weak exciton-photon

coupling. Altogether, these results demonstrate that, by leveraging the combined merits of dielectric metasurfaces and van der Waals heterostructures, electrically tunable hybrid-2D metasurfaces hold the key to realizing ultracompact optoelectronic devices for dynamic wavefront manipulation at ambient conditions.

3.2 HYBRID-2D METASURFACE

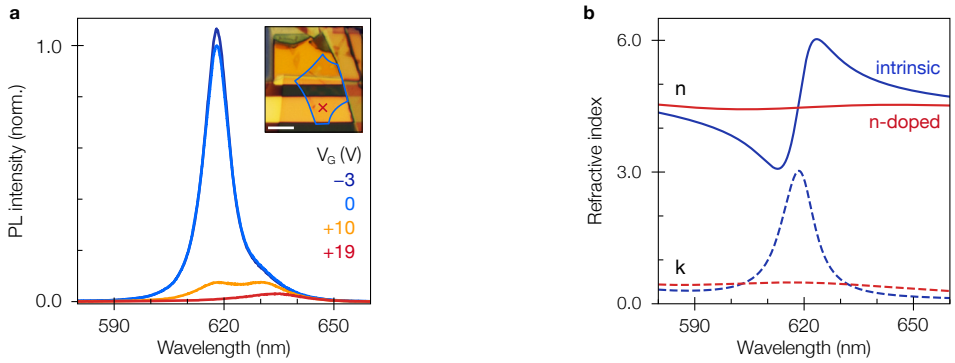

Figure 3.2: Electrical tunability of the A-exciton. **(a)** Experimentally measured photoluminescence intensity for a bare heterostructure cavity as a function of gate voltage (color). The inset shows a micrograph of the heterostructure, with the monolayer outlined in blue and the measurement position indicated by the red cross. Scalebar: 5 µm. **(b)** Modeled real (n, solid) and imaginary (k, dashed) components of the complex refractive index of monolayer WS_2 at intrinsic (blue) and strong n-type (red) doping.

Figure 3.1 illustrates a free-space optical modulator whose performance is derived from the combined merits of monolayer 2D semiconductors and dielectric metasurfaces. The hybrid-2D modulator achieves strong modulation of the input field through the electrical tunability of exciton resonances in atomically thin tungsten disulfide (WS_2) combined with the electromagnetic field enhancement offered by guided-mode resonances[39,147]. Applying a voltage between the gold (Au) back-gate and the monolayer results in strong electron-doping of the WS_2, which increases the exciton-electron (Coulomb) scattering rate and thereby efficiently quenches the so-called A-exciton transition[233,263]. To demonstrate this, we measure the excitonic photoluminescence emission in a flat reference device at room temperature and show a 108-fold reduction at λ_0 = 618 nm, while the charged exciton[229] (trion) peak at 635 nm remains mostly unaltered (Fig. 3.2a). Although electrical tuning of exciton emission is by now well-established, such efficient quenching has thus far mostly been limited to cryogenic temperatures[144,212,213].

The designed optical modulator combines several key elements to leverage the tunability of 2D excitons (Fig. 3.2b). First, the WS_2 monolayer is electrically connected to the ground electrode, but otherwise isolated through encapsulation with

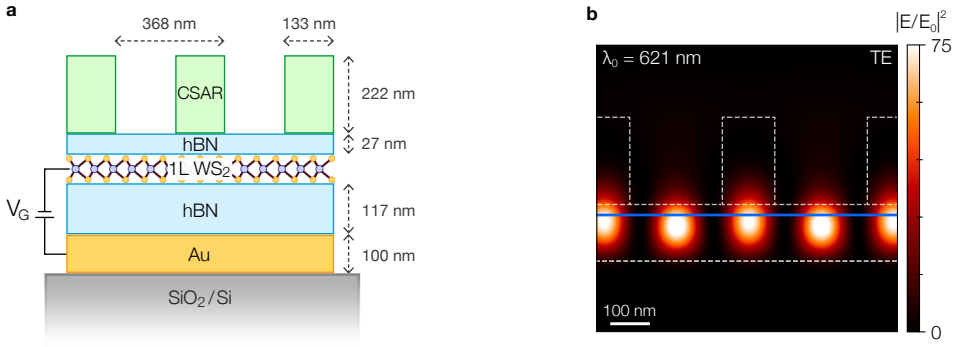

Figure 3.3: Field enhancement in the hybrid-2D metasurface. (a) Schematic of the detailed geometry of the modulator design (not to scale). **(b)** Electric field intensity enhancement for a transverse electric (TE) polarized normal-incident wave at free-space wavelength $\lambda_0 = 621$ nm. Blue line represents the monolayer.

hexagonal boron nitride (hBN; Fig. 3.3a). This provides screening from local charge fluctuations and defects in the dielectric environment, resulting in a narrow exciton linewidth[315]. At the same time, the resulting van der Waals heterostructure combined with the Au back-reflector functions as an asymmetric optical cavity to confine light inside the layer stack[213]. Second, to maximize the light-matter interaction we introduce a dielectric subwavelength grating on top of the heterostructure to enable resonant excitation of its fundamental TE_0 guided mode. The resulting guided mode resonance (GMR) provides a 74-fold electric field intensity enhancement and greatly increases the interaction length of light with the WS_2 monolayer (Fig. 3.3b). Finally, the back-reflector additionally serves as a local back-gate to the WS_2 layer, where the bottom hBN layer functions as the gate dielectric. As such, the back-gate enables electrical manipulation of the carrier concentration in the monolayer. In the strongly electron-doped (n-doped) regime, the exciton is effectively quenched, and the reflectance spectrum shows a single critically coupled resonance, splitting into two strongly coupled resonances when the monolayer is brought to intrinsic doping instead (Fig. 3.4a). Consequently, in simulation, the device exhibits an absolute reflectance contrast of $\Delta R = 47.5\%$ ($\lambda_0 = 627$ nm) when it is switched between these two states. We quantify the modulation depth as $10\log_{10}(R_i/R_n)$, where R_i and R_n are the reflectance in the intrinsic and n-doped regimes, respectively (Fig. 3.4b). Using this definition, our modulator achieves 25 dB peak signal modulation at the operating wavelength.

3.3 STRONG EXCITON-PHOTON COUPLING

Next, we outline our approach for maximizing the modulation efficiency by simultaneously designing for perfect absorption in the exciton-quenched state and strong

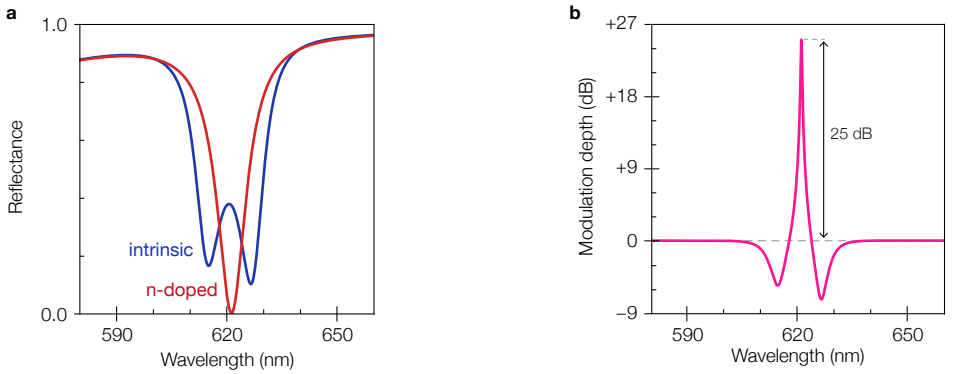

Figure 3.4: Simulated modulator performance. **(a)** Calculated reflectance spectra for the device with an intrinsic (R_i, blue) and n-doped (R_n, red) monolayer. **(b)** The corresponding modulation depth ($10\log_{10}(R_\mathrm{i}/R_\mathrm{n})$, magenta) extracted from (a).

exciton-photon coupling in the unquenched state. To this end, we use rigorous coupled-wave analysis (RCWA) simulations to optimize the dimensions of the heterostructure cavity as well as the grating's unit cell.[i] Here, we choose to design the modulator for operation around the A-exciton wavelength, $\lambda_A = 620$ nm, with normal-incident TE-polarized light, while retaining a mirror-like response for TM polarization.

To start, we tailor the bottom hBN thickness such that the monolayer is positioned at a $\lambda/2$ separation from the back-reflector (Fig. 3.5a). In concept, this is reminiscent of the famous Salisbury screen, in which a thin absorber is separated $\lambda/4$ from a mirror to enhance absorption through constructive interference. In contrast, placing the WS_2 at $\lambda/2$ instead minimizes absorption losses in the cavity due to destructive interference at the monolayer position. Since TM-polarized light cannot couple to the TE_0 guided mode supported by the structure, it is predominantly reflected from the cavity in this spectral and angular range (Fig. 3.5b). On the other hand, TE-polarized light can pick up first-order grating momentum (equal to $2\pi/\Lambda$, where Λ is the grating period) and thereby couple to the GMR, which enhances the interaction of light with the monolayer by confining the field inside the structure.

In our simulations, we phenomenologically capture the doping-dependent optical response of monolayer WS_2 (Fig. 3.2b) by allowing the A-exciton nonradiative decay rate, $\gamma_{\mathrm{A,nr}}$, to increase with electron density. In the presence of excess charge carriers, excitons can convert to trions, which exhibit a comparatively weak oscillator strength and decay mostly nonradiatively.[241,317] Consequently, the trion does not appear as a distinct resonance in reflection (Appendix A.2), and we treat trion formation as an additional nonradiative decay channel for the exciton. Accordingly, we

[i] Implemented using the Python interface of S^4 RCWA [316].

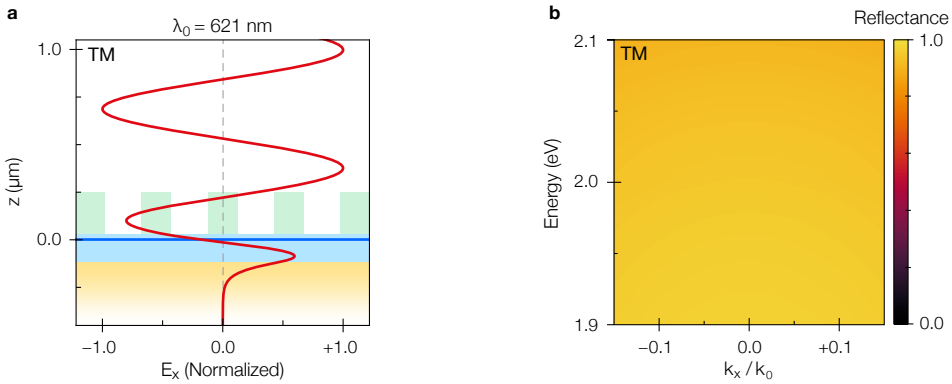

Figure 3.5: Mirror-like optical response under transverse magnetic polarization. (a) Standing wave profile of the electric field under normal-incidence transverse magnetic (TM)-polarized illumination showing minimal field overlap with the monolayer (blue line at $z = 0$ μm). **(b)** Numerically simulated angular (k_x) dispersion of the designed modulator under TM-polarized illumination showing mirror-like reflectance.

write $\gamma_{A,nr} = \gamma_{A,ph} + \gamma_{A,e} + \gamma_{A,T}$, where $\gamma_{A,ph}$ and $\gamma_{A,e}$ denote the phonon- and electron-assisted nonradiative decay rates and $\gamma_{A,T}$ corresponds to the exciton-to-trion conversion rate, as outlined in Section 2.1.2. In the intrinsic doping regime, phonon-assisted decay processes dominate, and we set the nonradiative decay to occur ten times faster than the radiative decay ($\gamma_{A,r}$), with characteristic values $\gamma_{A,r} = 2.7$ meV and $\gamma_{A,nr} = 27$ meV chosen to match the rates observed in preliminary experiments. At strong n-type doping, the exciton transition is severely broadened due to the increased exciton-electron scattering rate and the formation of trions,[233,263,317] which we model by artificially increasing the nonradiative decay rate to $\gamma_{A,nr} = 270$ meV. In this regime, absorptive losses in the cavity reduce to those suffered evanescently in the gold and by means of sub-bandgap absorption in monolayer WS_2 owing to impurities, defects and edge states.[318]

We optimize the grating periodicity such that the GMR coupling condition is satisfied at normal incidence for a photon energy matching the exciton energy, $E_A = 2.00$ eV, while the duty cycle is tailored to achieve perfect absorption when the monolayer is strongly n-doped (Fig. 3.6a). The resulting dispersion relation simply resembles the bare cavity dispersion with a slightly broader linewidth (Fig. 3.A2). Crucially, the n-doped dispersion is critically coupled such that the reflectance dips to $R \approx 0$, and the Γ-point is located near E_A. As a consequence, a gap opens in the dispersion around E_A when the monolayer is neutralized[319,320], indicative of strong exciton-photon interactions (Fig. 3.6b).

To evaluate the coupling strength, we additionally simulate the normal-incidence reflectance as function of grating period (Fig. 3.7a). This reveals the characteristic anti-crossing behavior associated with strong light-matter coupling.

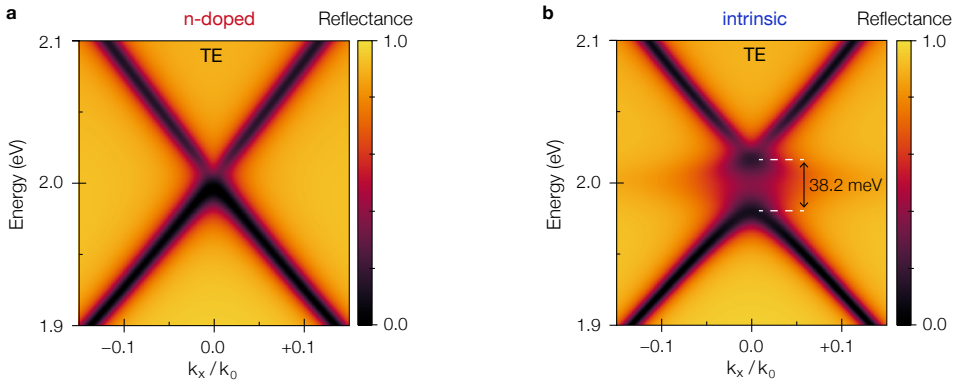

Figure 3.6: Simulated angular dispersion. (a) Angle-dependent reflectance of the designed modulator under TE-polarized illumination with monolayer WS_2 at strong n-type doping and **(b)** at intrinsic doping. In the latter case, the A-exciton is strongly coupled to the GMR, resulting in the formation of a 38.2 meV gap (indicated) at the exciton energy.

Two hybridized exciton-polariton branches emerge due to the rapid energy exchange between excitons and photons, leading to an energy separation proportional to the coupling strength $g \propto \mu \mathscr{E}$, where μ is the exciton dipole moment and $\mathscr{E}$ is the local electric field strength.[321,322] At resonance, a pair of coupled oscillators is said to be strongly coupled if the mode splitting, characterized by the Rabi energy Ω_R, is larger than the average decay rate of the uncoupled resonances, *i.e.*, $\Omega_R > (\gamma_A + \gamma_{GMR})/2$. From simulations of the cavity in absence of the exciton resonance, we determine $\gamma_{GMR} = 23.3$ meV for the bare GMR, in good agreement with the experimentally estimated value of 22.9 meV. We subsequently fit the dispersion at intrinsic doping using temporal coupled-mode theory (TCMT; Appendix A.1) to extract the complex eigenenergies of the polariton modes.[320] From this, we extract a Rabi splitting of $\Omega_R = 38.2$ meV and a corresponding coupling strength $g = 19.1$ meV, putting the system well into the regime of strong coupling ($(\gamma_A + \gamma_{GMR})/2 = 25.2$ meV). Instead, in the strongly n-doped regime (inset of Fig. 3.7a), the exciton decay rate is so large that Ω_R becomes purely imaginary and the gap closes, as expected for a weakly coupled system. Our metasurface leverages this tunability between strong and weak coupling to achieve > 12 dB reflectance modulation in a broad wavelength range around E_A (Fig. 3.7b). This highlights how integration of a 2D semiconductor in a hybrid metasurface configuration considerably enhances the excitonic modulation depth.

3.4 EXPERIMENTAL REFLECTANCE MODULATION

To demonstrate our approach experimentally, we fabricate the designed hybrid-2D metasurfaces following the general procedure outlined in Section 2.2. Specifically,

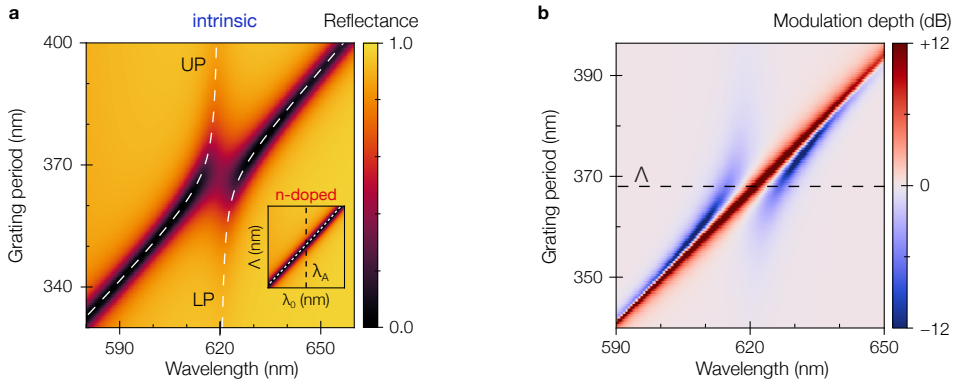

Figure 3.7: Grating period dependence of the optical performance. (a) Reflectance at intrinsic doping and strong n-type doping (inset). The calculated upper (UP) and lower polariton (LP) branches of the coupled mode analysis are represented by the white dashed lines. In the inset, the A-exciton wavelength λ_A is represented by the dashed line (black) and the GMR dispersion by the dotted line (white). **(b)** Modulation depth as function of grating period, with the designed period Λ indicated (dashed line). The color scale is capped at ± 12 dB for visibility.

we start by mounting a fresh prepatterned substrate in the stamping setup. After aligning the bottom hBN flake (117 nm thick) with the back-reflector and the ground electrode, we bring the stamp into contact and heat the stack to 60 °C for a minimum of 5 minutes. We peel the stamp to transfer the bottom hBN, followed by vacuum annealing at 150 °C for 8 hours. We repeat this process for the WS_2 monolayer (annealing at 90 °C for 8 hours) and the 27 nm thick top hBN layer (120 °C for 24 hours) to complete the heterostructure cavity.

For the subwavelength grating, we utilize an etch-free approach—where the grating is patterned in a low-index resist rather than shallow-etched in the waveguiding layer itself—to minimize fabrication imperfections and allow rapid prototyping[250,311,323]. To start, we clean the samples with a 30 second O_2 descum and then spin-coat a 222 nm thick layer of CSAR resist. The gratings are patterned in the resist with an electron dose of 130.8 $\mu C/cm^2$ and exposed upon chemical development (Fig. 3.8a). Atomic force microscopy[i] confirms that the gratings match the designed specifications and reveals excellent uniformity of the grating lines (Fig. 3.8b). We additionally verify that the exciton resonance is not detrimentally red-shifted or broadened during fabrication—by virtue of the heterostructure encapsulation—through photoluminescence mapping spectroscopy (Fig. 3.A3). Finally, we wire-bond the sample to a custom PCB to create a stable interface for electrostatic gating.

Moving on, we measure the voltage-dependent reflectance dispersion through back-focal-plane imaging spectroscopy with a tunable pulsed laser system (Fig. 2.9).[ii]

[i] Bruker Dimension FastScan

[ii] The incident power is adjusted per wavelength to maximize the signal-to-noise ratio and lies in the range

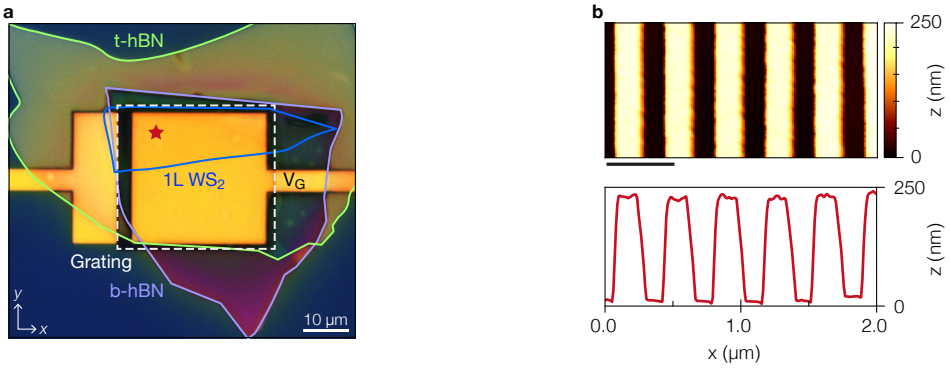

Figure 3.8: Fabricated hybrid-2D metasurface. **(a)** Optical microscope image of the device: a heterostructure comprised of monolayer WS_2 (blue) encapsulated by bottom (purple) and top (green) hBN layers is placed on a gold back-reflector, which doubles as the gate electrode (V_G), and integrated with a dielectric grating (white, dashed). The red star indicates the position of **(b)** the atomic force micrograph (top) and the horizontal cross-section through the center (bottom). Scalebar: 500 nm.

We first apply a +25 V gate bias to induce strong n-doping of the monolayer and thereby quench the exciton resonance. As shown in Fig. 3.9a, the dispersion relation in this state resembles that of the bare cavity (Fig. 3.A4). Critically, the Γ-point is located very close to E_A, such that when we neutralize the monolayer at -25 V, an energy gap of Ω_R = 36.0 meV opens in the dispersion due to strong exciton-photon coupling (Fig. 3.9b).

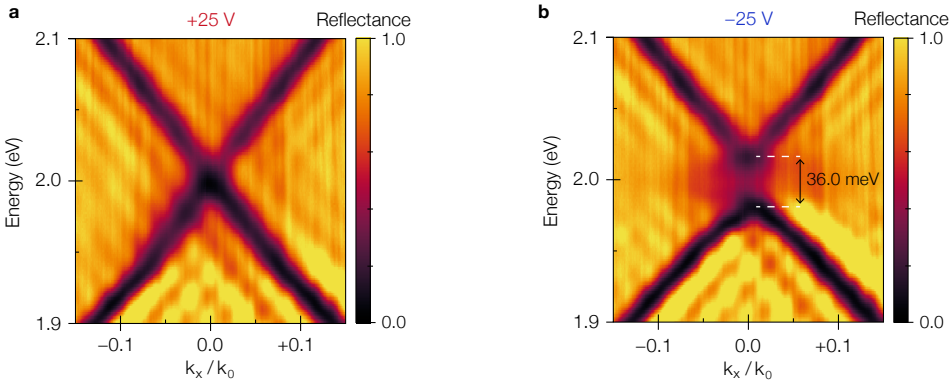

Figure 3.9: Measured angular dispersion. **(a)** Back-focal plane imaging spectroscopy of the angular dispersion at strong n-type doping (+25 V, red), and **(b)** intrinsic doping (–25 V, blue), with the latter exhibiting a Rabi splitting energy of Ω_R = 36.0 meV.

Before proceeding, we make two noteworthy observations about these results. First, to neutralize the WS_2, we reverse the bias from +25 V (electron injection) to

P = 36–80 nW, corresponding to fluences F = 7–16 nJ/cm^2, well within the linear excitation regime [265, 324].

-25 V (hole injection), indicating that the monolayer is significantly n-doped in the unbiased state. This is rationalized by the natural n-doping of exfoliated transition metal dichalcogenides due to chalcogen atom vacancies as well as extrinsic disorder incurred during (nano)fabrication[268,325,326]. Despite this, the device performance is not significantly impaired because the effects of unwanted doping are readily mitigated via electrostatic gating. Second, the fact that the absolute reflectance exceeds unity does not imply optical gain in this case. Instead, the lateral confinement of quasi-guided photons (exciton-polaritons) in the 30-µm-wide metasurface leads to pronounced finite-size effects, which are analyzed in detail in Chapter 5. For the present discussion, it suffices to note that these effects lead to broadening of the resonant linewidth and pronounced interference fringes which can exceed unity reflectance due to a redistribution of power in k-space. Apart from these deviations, the measured dispersion relations are in excellent agreement with the numerical simulations (Fig. 3.6).

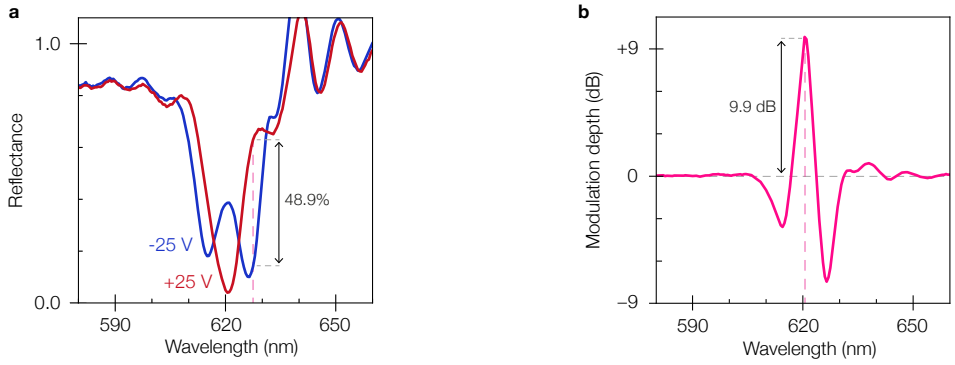

Figure 3.10: Measured modulator performance. (a) Normal-incidence TE-polarized reflectance spectra extracted from the dispersion relations at $k_x/k_0 = 0$, with a maximum reflectance contrast of 48.9% at $\lambda_0 = 627.5$ nm indicated. **(b)** Modulation depth obtained from the spectra in (a), revealing 9.9 dB peak signal modulation at $\lambda_0 = 620.5$ nm.

Next, we extract cross sections from the dispersion relations at $k_x = 0$ µm^{-1} (Fig. 3.10a). At +25 V, the exciton is suppressed, and the reflectance spectrum contains one near-critically coupled resonance that dips to a minimum of 4% at the operating wavelength $\lambda_0 = 620.5$ nm. Reversing the bias to -25 V neutralizes the monolayer, causing the spectrum to split into two strongly coupled polariton branches and thereby raising the reflectance to 39%. By switching between these two states, our modulator achieves a modulation depth of 9.9 dB ($\Delta R = 35\%$) at the operating wavelength (Fig. 3.10b) and a change in reflectance up to $\Delta R = 49\%$ at 627.5 nm. To our knowledge, the measured modulation ratio and reflectance contrast are 5 times greater than previously reported for excitonic metasurfaces at room

temperature[147], demonstrating the merits of our hybrid-2D approach.

We additionally assess the modulation frequency response of two more devices in alternating-current experiments (the setup and procedure are described in Section 2.3.4) and find that the −3 dB bandwidth is limited to $f_{-3\mathrm{dB}} = 26$ Hz (Figs. 3.A5 and 3.A6). We attribute this low bandwidth to a large resistor–capacitor time constant of the electrical circuit, arising from excessive contact resistance as well as the high sheet resistance of the 30 μm-long active WS_2 channel.[276] We emphasize this is merely a technological rather than a fundamental limitation, as bandwidths exceeding the megahertz regime have already been realized with optimized contact geometries in similar device architectures.[145,327,328]

3.5 ELECTRICALLY TUNABLE STRONG COUPLING

To gain insight into the voltage-dependence of the fundamental rates governing the metasurface's optical response, we measure the normal-incidence reflectance at gate voltages between ±25 V in intervals of 5 V (Fig. 3.11). With increasing voltage, the coupled modes gradually merge into a single resonance, continuously transitioning from strong to weak coupling.[246,319,327,329,330] In the following, we quantify the characteristic decay and coupling rates from our measurements by performing a comparative analysis using RCWA and TCMT.

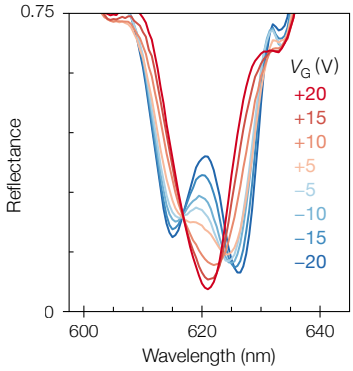

Figure 3.11: Continuous tunability of the optical response. Normal-incidence TE-polarized reflectance as function of gate voltage (color). The spectra measured at $V_G = 0$ V, ±25 V are omitted for clarity.

In the following, we first obtain the exciton decay rates by fitting the voltage-dependent reflectance spectra. To this end, we constrain the geometry and optical parameters of the fabricated device to replicate the system within RCWA. The refractive indices of Au[312] and hBN[313] are obtained from literature, while for CSAR we measure it using spectroscopic ellipsometry[i], and for monolayer WS_2 we use the Lorentz-

[i] J.A. Woollam VB-400

oscillator model introduced in Section 2.1.1. We approximate the A-exciton radiative rate $\gamma_{A,r}$ using values from literature[131,213,253] and determine the center energy E_A and total decay rate γ_A by fitting a spectrally resolved photoluminescence map (Fig. 3.A3). The exact geometry (Fig. 3.3) is further established by a combination of white-light reflectometry to measure the hBN thicknesses and atomic force microscopy to extract the CSAR grating dimensions. Throughout, we do not explicitly account for finite-size linewidth broadening (discussed in Chapter 5), and the extracted decay rates will therefore be slightly larger than those set by the intrinsic resonance linewidths.

We start by fitting the spectrum at $V_G = -25$ V (near-intrinsic doping) because the clearly distinguishable polariton branches allow for the most reliable determination of the constrained fitting parameters, and obtain $E_A = 2.00$ eV, $\gamma_{A,r} = 2.7$ meV, and $\gamma_{A,nr} = 26.7$ meV, closely matching the values used for our numerical simulations. Subsequently, we fix not only the geometry but also $\gamma_{A,r}$ (taking it to be voltage-independent) because allowing it to vary would over-parametrize the model in the exciton-quenched regime, while noting that this is a slight oversimplification.[252] We then continue the fitting procedure to extract $\gamma_{A,nr}$ and E_A at each voltage (Fig. 3.12). In the strongly n-doped regime (at +25 V), we find that the nonradiative decay rate increases fourfold to $\gamma_{A,nr} = 109.4$ meV, while the center energy redshifts to $E_A = 1.99$ eV. The observed redshift can be attributed to a doping-induced reduction of the exciton binding energy due to screening of the Coulomb interaction, and is consistent with earlier work.[233] Overall, the measurements are captured exceptionally well by the model, which reproduces two distinct exciton–polariton branches that gradually merge into a single resonance with increasing $\gamma_{A,nr}$, allowing us to directly overlay the fitting results on the simulated reflectance map (Fig. 3.12a). Notably, the RCWA model suggests that the modulator performance could be improved even further by operating at higher voltages (*i.e.* raising $\gamma_{A,nr}$) to bring the system closer to critical coupling.

Next, we determine the exciton–photon coupling strength by fitting the coupled exciton–GMR response as two Lorentzian reflectance dips superimposed on a non-resonant background (illustrated in Fig. 3.A7), which is modeled using the TM-polarized reflectance (Fig 3.5b).[i] The inverted Lorentzians are taken to represent the hybrid modes of the eigenvalue problem (Eq. (A.18) in Appendix A.1) and are parametrized using the previously extracted linewidths and center energies of the bare exciton and GMR, leaving only g and two weights w_A and w_{GMR} as free fitting parameters. By fitting the spectra at each voltage using a least-squares routine, we estimate a voltage-averaged value of $g = 16.6 \pm 1.0$ meV (inset of Fig. 3.12b), which implies that the excitonic and photonic modes remain strongly coupled up to a total

[i] Note that this is not a general approach; it applies here because, for TM-polarized illumination, no resonance is present in the relevant spectral window beyond the Fabry–P'erot background, as the monolayer is positioned in the heterostructure stack near an electric-field node of the standing-wave pattern.

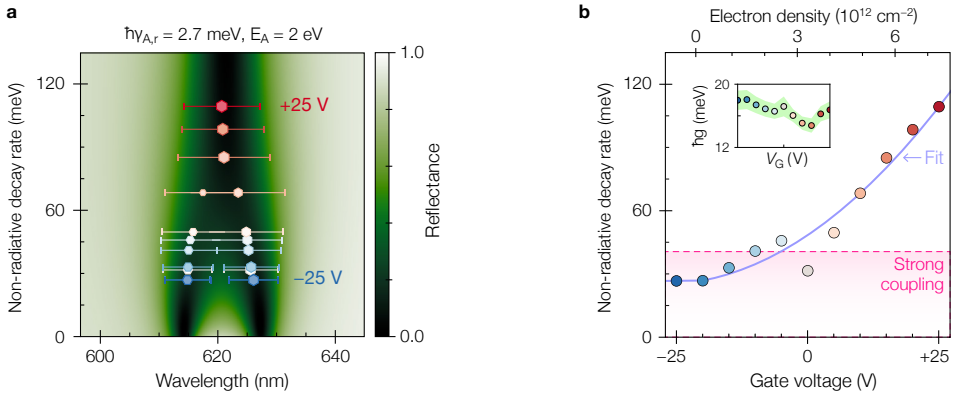

Figure 3.12: Electrically tunable strong coupling. **(a)** Spectral reflectance versus nonradiative decay rate of excitons in monolayer WS_2, simulated with the RCWA model for $\gamma_{A,r} = 2.7$ meV and $E_A = 2$ eV. The colored datapoints represent the fitted energies, relative amplitudes (position and size of hexagons, respectively) and linewidths (width of bars) of the coupled modes. **(b)** Exciton nonradiative decay rate as function of gate voltage (electron density) obtained from the RCWA fits (colored datapoints). Purple curve indicates the fitted optical rate equation, pink-shaded region represents the decay rates at which the system is strongly coupled. The coupling rates g obtained from the coupled-mode analysis are shown in the inset (fitting uncertainty in green).

exciton decay rate of $\gamma_{A,max} = 43.3$ meV.

Notably, the measurement at 0 V is also strongly coupled and appears to be a significant outlier. However, this is explained by hysteresis due to trapped charges[325] resulting from an imperfect measurement sequence, in which the monolayer was slightly p-doped (at −25 V) before sweeping the gate voltage from 0 to +25 V and finally from −5 back to −25 V. Because the described analysis does not account for coherent interference effects, the magnitude of g is underestimated and should be viewed as a conservative lower bound. Moreover, the trion resonance is excluded in this analysis, since we find it is only weakly coupled to the GMR and therefore negligibly impacts the fitted reflectance spectra (a full temporal coupled-mode analysis of the driven response, including trions, is included in Appendix A.2).

To gain insight into the gating-induced doping density $n_e(V_G)$ in the WS_2 monolayer, we describe our device as a parallel-plate capacitor modified to account for quantum capacitance effects, as described in Section 2.1.3. We fit the experimental decay rates by plugging the expression for n_e into the optical rate-equation model described in Section 2.1.2.[i] From the fit, we obtain an estimate of the charge neutrality point, $V_{CNP} = -21.3$ V, which enables us to calibrate n_e with respect to V_G (Fig. 3.12b). We estimate carrier concentrations ranging from $n_e \approx -0.4 \times 10^{12}$ cm^{-2} at $-25V$ up

[i]The free-electron density as function of gate voltage [270, 271] is computed numerically using the measured hBN thickness $d = 117$ nm, its static permittivity $\varepsilon \approx 3.4$ [239], and for monolayer WS_2 we take $E_{bg} \approx 2.15$ eV [331], $g_v = 2$, $g_s = 2$, and $m^* \approx 0.34 m_e$ [332]. We further obtain an estimate of the charge neutrality point by fitting the decay rate with the optical rate-equation model [175, 241].

to $n_e \approx 7.3 \times 10^{12}$ cm^{-2} at +25 V, with the maximum electron density up to which the device remains strongly coupled $n_{e,max} \approx 2.4 \times 10^{12}$ cm^{-2} (−5.2 V). Altogether, our results reveal that the metasurface's ability to electrically tune the hybrid-2D system in and out of the strong exciton-photon coupling regime fundamentally stems from doping-induced variations in the nonradiative decay rate of excitons in monolayer WS_2.

3.6 CONCLUSION

In this chapter, we introduced a hybrid-2D metasurface platform that combines the merits of a tunable van der Waals heterostructure cavity with the strong light-matter interaction of a nonlocal dielectric metasurface to achieve strong and tunable exciton-photon interactions at room temperature, which is leveraged for free-space optical modulation. The platform's simple yet versatile design readily accommodates other materials and is straightforwardly adapted to polarization-independent response and various optical functionalities, as will be discussed in the next chapter. More broadly, our platform highlights new opportunities for excitonic 2D metasurfaces for dynamic wavefront manipulation in ultra-compact metadevices.

3.7 ADDITIONAL FIGURES

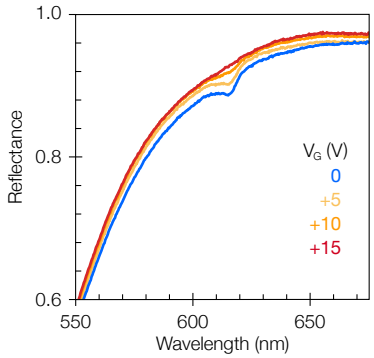

Figure 3.A1: Gate-dependent reflectance of a planar device. Experimentally measured reflectance spectra for a bare heterostructure cavity (*i.e.*, without subwavelength grating) as a function of gate voltage (color).

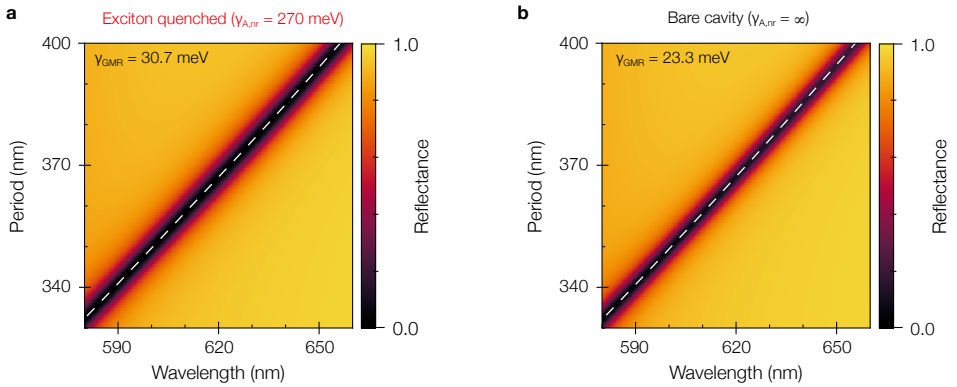

Figure 3.A2: Comparison of the modulator in the exciton-quenched state and the bare cavity. (a) Numerically simulated period dependence of the normal-incidence TE-polarized reflectance of the designed modulator in the exciton-quenched state, and **(b)** of the corresponding bare cavity. The fitted dispersion is overlaid on the colormaps (dashed) and the extracted damping rate of the guided-mode resonance (GMR) is indicated.

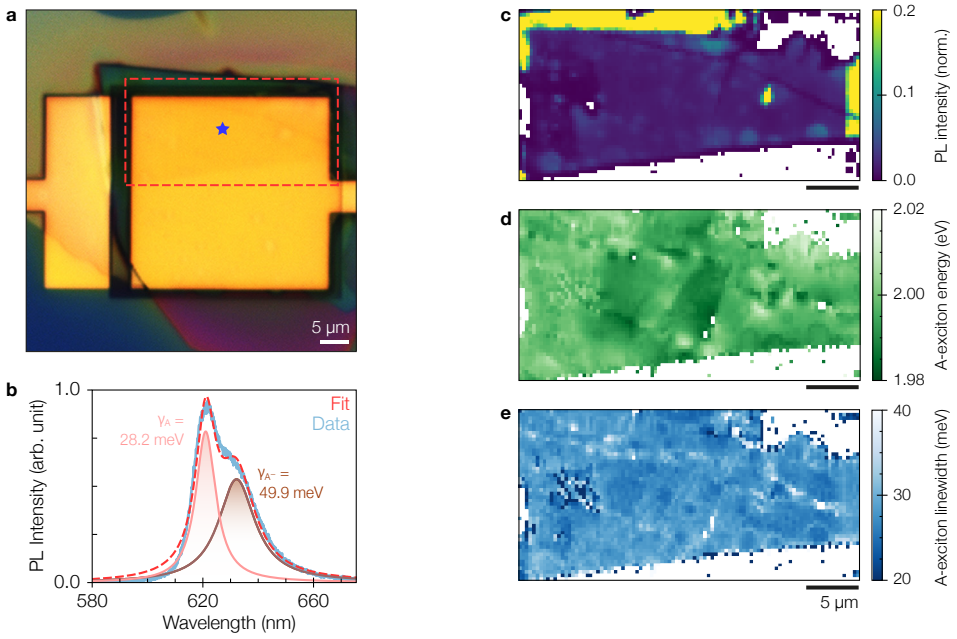

Figure 3.A3: Photoluminescence characterization. (a) Brightfield microscope image of the fabricated modulator. **(b)** Characteristic fluorescence spectrum (light blue) obtained by averaging a 1 μm^2 spot indicated by the blue star in (a). The data is fitted with a double Lorentzian function (red, dashed) and separated into A-exciton (pink) and negatively charged trion (A–, brown) contributions. **(c)** Spatially-resolved photoluminescence maps of the region (red, dashed) outlined in (a), showing the integrated intensity, **(d)** the fitted A-exciton energy, and **(e)** the fitted linewidth (total decay rate). Scalebars: 5 μm.

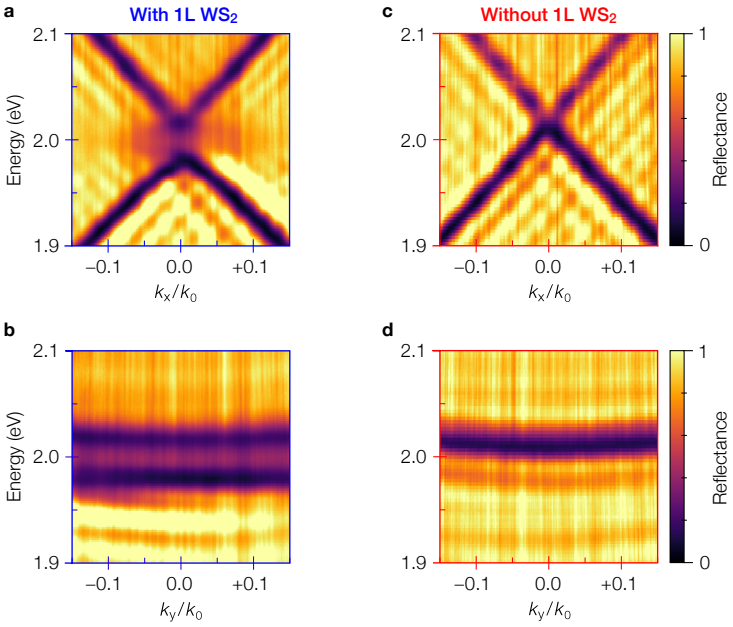

Figure 3.A4: Experimental dispersion of the cavity with and without monolayer WS_2. (a) k_x and **(b)** k_y dispersion of the fabricated modulator under TE-polarized illumination.**(c)** k_x and **(d)** k_y dispersion of the empty cavity, measured on a patch of the device that lacks the WS_2 monolayer.

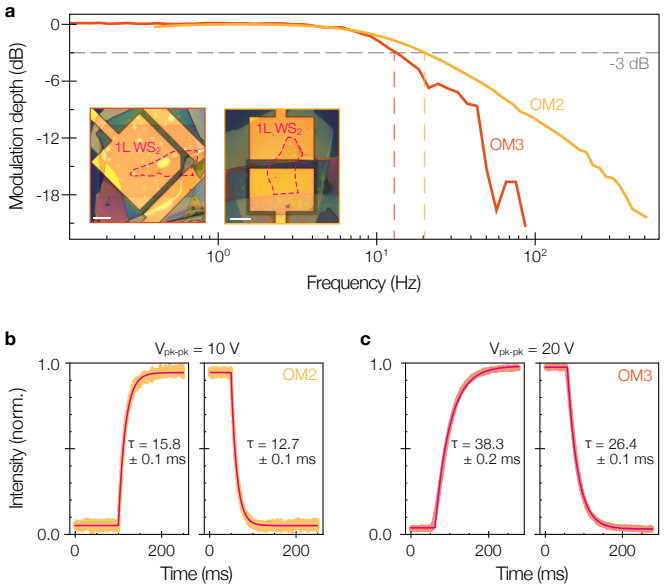

Figure 3.A5: AC modulation characteristics of two hybrid-2D modulators. (a) Modulation bandwidth of devices OM2 (yellow) at $\lambda_0 = 631$ nm with 3 dB cut-off at $f_{-3\mathrm{dB}} = 12.8$ Hz and OM3 (orange) at $\lambda_0 = 633$ nm with $f_{-3\mathrm{dB}} = 20.2$ Hz. Inset shows optical micrographs of OM2 and OM3 with monolayer (1L) WS_2 outlined in magenta. Scalebars: 10 µm. **(b, c)** Corresponding time traces of the rise (left) and fall (right) of the reflected intensity in response to a 1 Hz square-wave modulation signal for devices OM2 (b) and OM3 (c). The rise and fall times obtained by fitting (magenta) and the peak-to-peak driving voltage $V_{\mathrm{pk-pk}}$ are also shown.

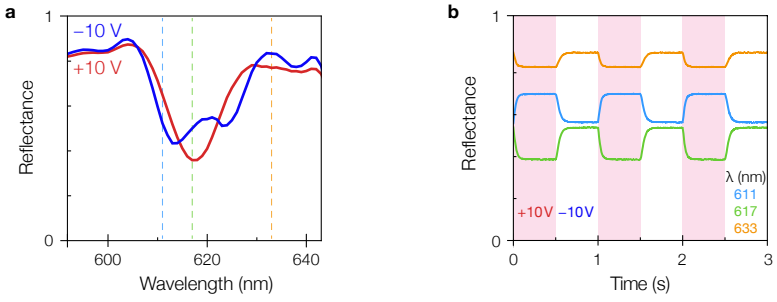

Figure 3.A6: Reflectance modulation of device OM3. (a) DC reflectance spectra of device at +10 V (red) and −10 V (blue), and **(b)** reflectance as function of time in response to a 1 Hz pulse at $\lambda_0 = 611$ nm (light blue), 617 nm (green) and 633 nm (orange). Colors correspond to the dotted lines in (a).

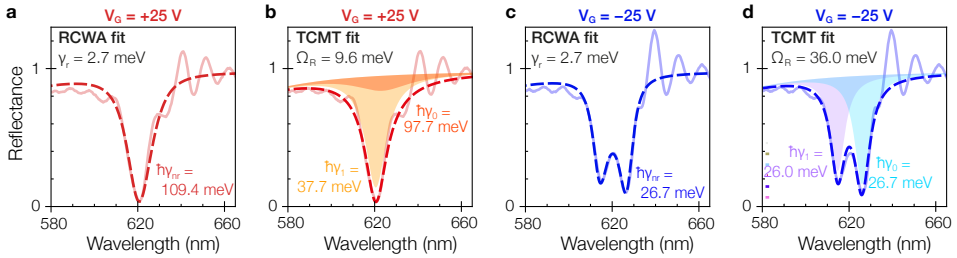

Figure 3.A7: Parameter extraction via reflectance fitting. **(a)** Fit (dashed) of the normal-incidence reflectance for an n-doped (+25 V) monolayer performed with rigorous coupled-wave analysis (RCWA), and **(b)** with temporal coupled mode theory (TCMT). **(c, d)** Similar to (a) and (b), but for a neutral (–25 V) monolayer. The RCWA fits are used to extract the A-exciton energy plus the radiative and nonradiative decay rates, γ_r and γ_{nr}, respectively, while the TCMT fits allow extraction of the exciton-photon coupling strength as well as the energies and linewidths (γ_0 and γ_1) of the coupled modes. The TCMT fits are offset by a non-resonant background reflectance obtained through RCWA simulations for TM-polarized illumination.

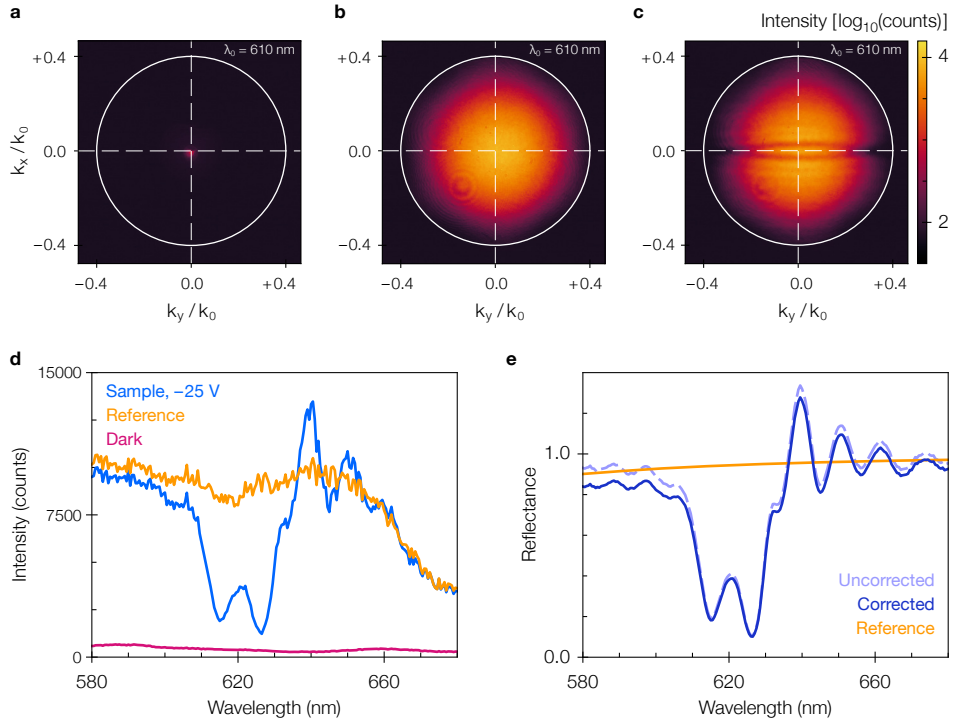

Figure 3.A8: Reflectance extraction from back-focal plane images. **(a)** Back-focal plane image at $\lambda_0 = 610$ nm in absence of a sample (I_{dark}), **(b)** of the gold reference ($I_{reference}$), and **(c)** of the sample at –25 V (I_{sample}). **(d)** The extracted spectral intensities I_{sample} (blue), $I_{reference}$ (yellow), and I_{dark} (magenta) at normal-incidence ($k_x = k_y = 0$). (e) Corresponding absolute reflectance of the sample before (dashed, light blue) and after (solid, dark blue) corrected using the RCWA-calculated reference spectrum $R_{reference}$ (yellow).

4

Complex amplitude modulation

4.1 Introduction

Dynamic wavefront manipulation calls for complex amplitude modulation: independent control over the amplitude and phase of scattered light over the full 0–2π phase range. Despite the tremendous advances harbored by passive metasurfaces to control the scattered field at the nanoscale, active metasurfaces are typically hindered by undesired cross-modulation of the amplitude and phase, because decoupling these parameters requires two independent control knobs.[154,242,333,334] At the same time, accessing the complete phase range necessitates a delicate balance of the metasurface's radiative and absorptive losses.[335] Due to these limitations, platforms for complete complex amplitude modulation have mostly been limited to the infrared spectral range where materials absorption is naturally lower[154,242,333].

Monolayer transition metal dichalcogenides are promising candidates to extend complex amplitude modulation into the visible regime. These materials exhibit strong exciton resonances that dominate the optical properties due to their large binding energies arising from quantum- and dielectric confinement in the atomically thin crystal[226]. Moreover, these excitons are highly tunable, with free-carrier injection emerging as a particularly attractive mechanism for ultrafast modulation and compatibility with existing electronic circuitry[233,252,263,317]. However, limited by their atomic thickness, metasurfaces patterned directly into bare monolayers typically reach efficiencies of only a few percent[25,148,253]. To enhance the light-matter interaction, monolayers have been placed in the vicinity of metasurfaces to leverage their strong Purcell enhancements[147]. Nevertheless, their performance remains constrained by defects and disorder introduced into the unprotected monolayer during nanofabrication.

Encapsulating the monolayer with hBN provides a robust route to preserve pristine excitonic properties, owing to its atomically smooth surface, wide bandgap, high dielectric strength, and chemical stability[213,238,336]. The merits of encapsulation are exemplified by experimental demonstrations of planar heterostructures achiev-

ing near-unity reflection modulation[144,212] and active beam steering[145,146], as well as full complex amplitude modulation in simulation[242]. Yet, the latter was only achieved by artificially eliminating the nonradiative losses that typically hamper excitonic systems. In practice, these unwanted decay channels can be mitigated by hybridizing planar heterostructures with metasurfaces to leverage strong coupling between excitons and a photonic mode[251]. While this strategy has already delivered record-high excitonic amplitude modulation at room temperature[337], independent phase control remains an important open challenge.

In this chapter, we numerically demonstrate a hybrid-2D metasurface platform for independent amplitude and phase modulation in the visible regime. The high dimensionality of the design space and the intricate interdependence of geometrical and material parameters limit the utility of conventional forward-design approaches. We therefore develop an inverse-design pipeline to optimize metasurface designs for π-phase modulation and full complex amplitude modulation. We further validate the platform's applicability by demonstrating a three-level programmable beam-steering metasurface. Crucially, all simulations are grounded in experimentally measured material properties and are interpreted using TCMT to elucidate the underlying physics and establish the generality of our approach.

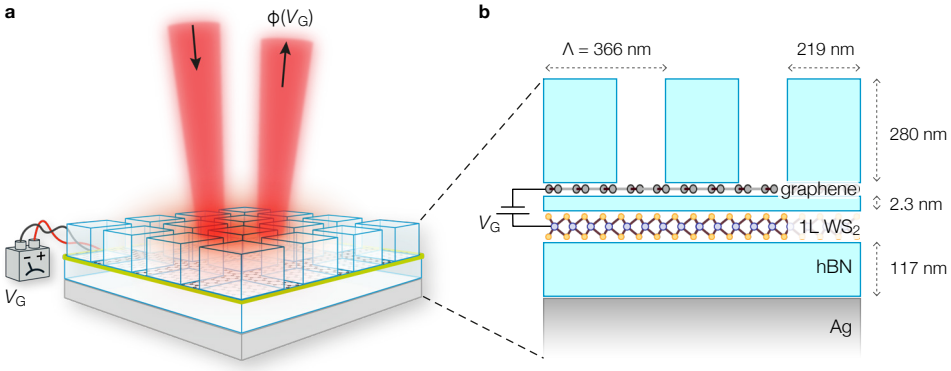

Figure 4.1: A hybrid-2D metasurface for free-space phase modulation. (a) Conceptual illustration of the phase modulator, in which the gate voltage (V_G) controls the phase (ϕ) of the reflected light. **(b)** Cross-sectional view of the metasurface design (not to scale), showing the hBN subwavelength grating, graphene gate electrode, monolayer (1L) WS_2 encapsulated by hBN and placed on the Ag mirror. The grating period (Λ) and other geometrical parameters are indicated.

4.2 π-PHASE MODULATION

Figure 4.1a shows an active hybrid-2D metasurface for free-space phase modulation, where the gate voltage (V_G) shifts the phase (ϕ) of a reflected beam while maintaining a constant amplitude. The device combines the tunability of excitons in monolayer

WS_2 and the field enhancement offered by a nonlocal dielectric metasurface (Fig. 4.1b). To maximize the phase modulation performance under realistic constraints, we design the metasurface architecture using full-wave RCWA[i] simulations, optimized using a custom inverse design routine which proceeds in two stages: an initial global search using Bayesian optimization[ii] followed by local refinement with the covariance matrix adaptation evolution strategy[iii] (Appendix A.3).

The designed modulator combines several key elements. First, a monolayer WS_2 is encapsulated between two multilayer slabs of hBN, which is known to reduce the linewidth of the exciton resonance by screening it from the dielectric environment[227,315]. The entire stack is situated on a silver (Ag) back-reflector to effectively trap light in the heterostructure cavity[213] and redirect it into the reflection channel. The heterostructure is then functionalized with a planar array of hBN subwavelength scatterers spaced with period $\Lambda = 366$ nm, enabling polarization-independent normal-incident resonant excitation of a GMR which provides a 36-fold enhancement of the incident field intensity (Fig. 4.2a). A single layer of graphene, situated beneath the grating, acts as an etch stop during dry etching of the hBN nanostructures[338] and serves as the gate electrode for modulation of the electron density (n_e) in the WS_2 monolayer. The thickness of the hBN gate dielectric is 7 atomic layers thick (2.33 nm) to provide a sufficiently high breakdown voltage[238,336] (Fig. 4.A1a) to enable significant amplitude and phase modulation at low-voltages (0–5 V). In this device, the tunability is inherited from the sensitivity of monolayer WS_2 to the presence of free carriers. Using electrostatic gating to control the doping level, the A-exciton resonance ($\lambda_A = 597$ nm) can be actively and reversibly quenched, modulating the material's permittivity and thereby the overall metasurface response.[233,252,263,317]

Throughout, we model the carrier density-dependent permittivity of WS_2 using the Lorentz-oscillator model introduced in Section 2.1.1.[iv] Although near-unity quantum yields have been reported for transition metal dichalcogenides at cryogenic temperatures in isolated cases,[144,341] such performance is not routinely observed under standard laboratory conditions. Instead, to ground the simulations in reality, we parametrize the model with experimentally established values for the A-exciton energy E_A and total decay rate γ_A (Fig. 4.2b).

To this end, we use deterministic stamping to create a hBN-encapsulated monolayer WS_2 using the protocol outlined in Section 2.2.2. Specifically, we sequentially stamp the bottom hBN, monolayer WS_2, and top hBN flakes on a 100 nm SiO_2/Si

[i] Implemented using the Python interface of S^4 with circular lattice truncation and 561 Fourier orders to provide convergence (mean absolute deviation < 0.1%) while maintaining reasonable computation times on a self-hosted 64-core computing cluster [316]

[ii] *scikit-optimize*

[iii] *pycma*

[iv] The frequency-dependent optical constants of Ag, hBN and graphene are obtained from literature as tabulated data [313, 339, 340].

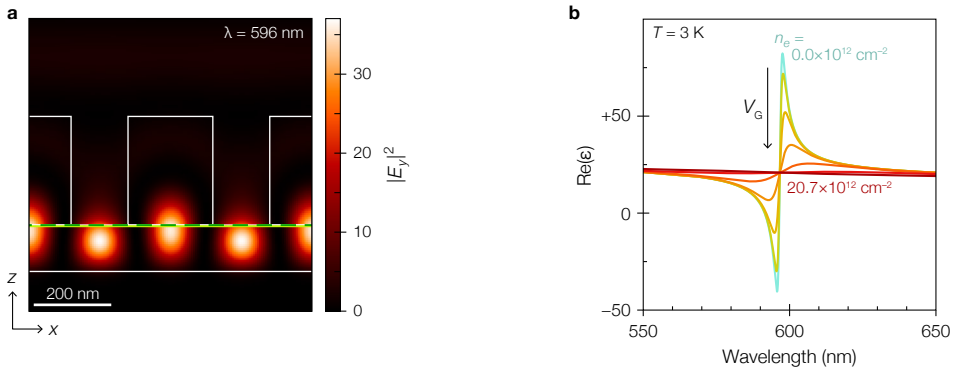

Figure 4.2: Resonant field enhancement and tunability. (a) Electric field intensity ($|E_y|^2$) enhancement offered by the guided mode resonance, simulated in absence of excitons for a TE-polarized normal-incident wave at $\lambda = 596$ nm. The positions of monolayer WS_2 (light green, solid) and graphene (dark green, dashed) are indicated. **(b)** Modeled permittivity of monolayer WS_2 at $T = 3$ K, showing the tunability of the A-exciton resonance as function of n_e (color).

substrate (Fig. 4.3a). At each step, we bring the stamp into contact at ambient conditions ($T = 21$ °C, R.H. ≈ 50 %), then set the stage heater to 65 °C and let it thermalize for at least 5 minutes, after which we peel the stamp at a controlled rate of 0.5 µm/s to complete the transfer. Once the full heterostructure is assembled, we anneal it at 200 °C in vacuum ($P \approx 10^{-6}$ mbar) for 2 hours to improve interface cleanliness.

We then mount the sample in the Skaði setup—a cryostat integrated with a 4f Köhler-illumination microscope, as detailed in Section 2.3—and helium-cool it to 3 K. We manually select a clean region of the sample and measure 13 spectra spanning ~ 3 µm to account for spatial inhomogeneity arising from natural variations in the local charge and strain landscapes—which are expected even in near-perfect samples. We calculate the average reflectance contrast (Fig. 4.3b), $(R_{WS_2}-R_{hBN})/R_{hBN}$, between the heterostructure stack with monolayer WS_2 (R_{WS_2}) and without it (R_{hBN}). By taking the numerical derivative with respect to energy, we can fit the Lorentzian resonance without precise knowledge of the hBN layer thicknesses (Fig. 4.3c). From this analysis, we obtain $E_A \approx 2.078$ eV and $\gamma_A \approx 6.5$ meV. Taking a conservative estimate of the effective radiative component, $\gamma_{A,r} \approx 2.6$ meV, based on literature[147,213,253,254] and the results presented in Section 3.5, we estimate a nonradiative rate of $\gamma_{A,nr} = \gamma_A - \gamma_{A,r} \approx 3.9$ meV. Based on this analysis, we establish that an excitonic quantum yield of $\gamma_{A,r}/\gamma_A = 0.4$ is realistically achievable in pristine, hBN-encapsulated monolayer WS_2, and we use this value throughout this chapter.

In this chapter, we use the rate-equation model outlined in Section 2.1.2 to model the doping dependence of the A-exciton as a quadratic dependence of $\gamma_{A,nr}$ on n_e. Here, we use the linear and quadratic coefficients obtained in Section 3.5

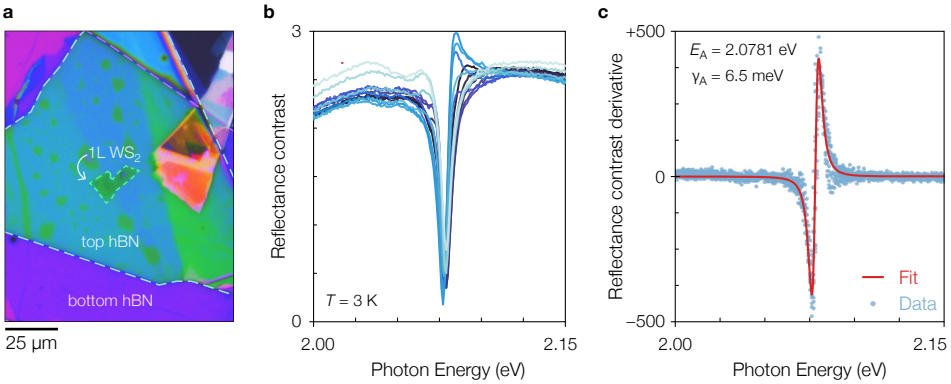

Figure 4.3: Experimental parametrization of the A-exciton. **(a)** Brightfield microscope image of the fabricated planar heterostructure sample, with monolayer (1L) WS_2 encapsulated between hBN. **(b)** Thirteen spectra (spanning ~ 3 μm) measured at $T = 3$ K, showing the reflectance contrast of the monolayer with respect to the hBN, $(R_{WS_2} - R_{hBN})/R_{hBN}$. **(c)** The calculated energy-derivatives of the different reflectance contrast spectra (pale blue dots) and Lorentzian fit (red line) used to extract the total linewidth $\gamma_A = 6.5$ meV and the A-exciton resonance energy $E_A = 2.0781$ eV.

to parametrize the model (Fig. 4.A1b). We note that the tunable range of $\gamma_{A,nr}$ is extrapolated to high carrier densities (~ 10^{13} cm^{-2}) where the approximations underlying the rate equation model break down.[147,241] It has been demonstrated, however, that the exciton resonance can be completely quenched at high carrier densities due to a concomitant collapse of the oscillator strength ($\gamma_{A,r}$) at high doping densities caused by Pauli blocking and screening of the Coulomb interaction.[252] As such, the quadratic extrapolation used here can be viewed as a phenomenological method to fully suppress the resonance in simulation.

By leveraging the tunability of the exciton resonance, the metasurface reflection coefficient at $\lambda = 596$ nm traces a path in the complex plane from $\varphi = 0$ rad to $\varphi = \pi$ rad (Fig. 4.4a). Thus, when the monolayer is switched between intrinsic and strong n-type doping ($n_e = 20.7 \times 10^{12}$ cm^{-2}), the device flips the phase of a reflected beam while maintaining a constant amplitude of $|r| = 0.58$ (Fig. 4.4b).

To understand how such a high modulation depth can arise from exciton resonance tuning in an atomically thin layer, we study how light interacts with the guided-mode and A-exciton resonances in our metasurface (Fig. 4.5a). Broadly, when the resonance condition is satisfied (matching of the in-plane wavevector by addition of grating momentum $q = 2\pi/\Lambda$), free-space radiation couples to the GMR with a coupling efficiency governed by the radiative rate $\gamma_{G,r}$. Since the grating period is subwavelength, coupling is entirely mediated by the direct 0th order reflection channel, making this a one-port system. The GMR, in turn, coherently excites excitons through optical coupling with strength g that is governed primarily by the field overlap between both resonances. By fitting the reflectance in absence of

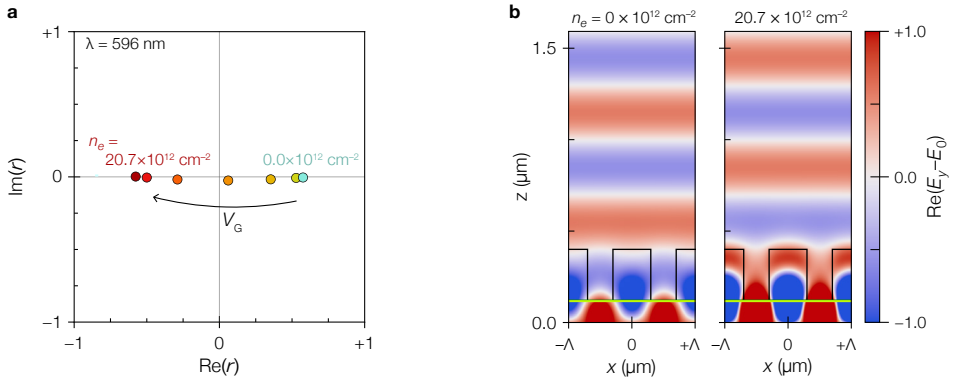

Figure 4.4: π-phase modulation. (a) Complex reflection coefficients of the metasurface at $\lambda = 596$ nm as function of n_e (color). **(b)** Corresponding electric field distributions of the reflected light (Re(E_y–E_0)) for intrinsic ($n_e = 0.0 \times 10^{12}$ cm^{-2}, left) and highly n-doped ($n_e = 20.7 \times 10^{12}$ cm^{-2}, right) monolayer WS_2 yielding the same amplitude but opposite phase.

excitons (setting $\gamma_{A,r} = 0$ meV), we determine the radiative coupling rate and the nonradiative loss rate of the GMR, $\gamma_{G,r} = 55.0$ meV and $\gamma_{G,nr} = 13.8$ meV, respectively. Since $\gamma_{G,r} \gg \gamma_{A,r}$, we consider direct coupling between excitons and free-space to be negligible, such that the GMR is entirely responsible for the coupling to and from free-space.

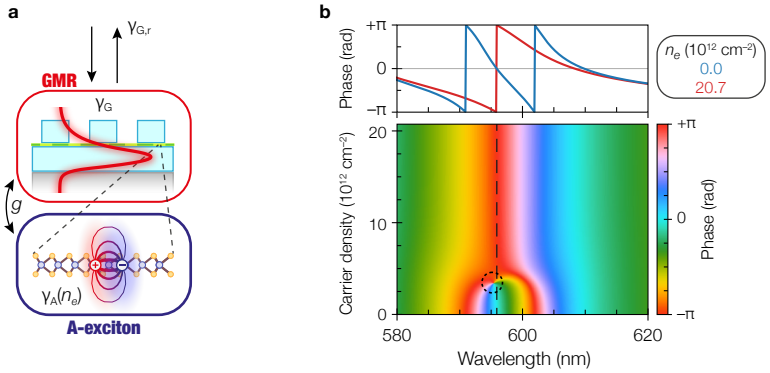

Figure 4.5: Operation near critical coupling enables π-phase modulation. (a) Schematic of the one-port coupled-resonator system. The GMR has intrinsic loss rate $\gamma_{G,nr}$ and facilitates free-space coupling with radiative rate $\gamma_{G,r}$. The A-exciton is coupled to the GMR with strength g, and its decay rate γ_A is modulated by gate-induced changes in n_e. **(b)** Top: reflection-phase spectra at intrinsic (blue) and strong n-doping (red). Bottom: Phase as function of n_e, with the operating wavelength indicated (dashed line). The dashed black circle indicates the phase singularity arising from critical coupling.

To achieve the π phase flip, it is necessary to operate around the critical coupling point ($|r| = 0$), where the phase is undefined and thus singular (Fig. 4.5b). In a one-port system, this condition occurs when the metasurface's radiative coupling

rate matches the overall loss rate[342,343]. Apart from the losses suffered in the Ag and graphene layers (characterized by $\gamma_{G,nr}$), excitonic absorption in monolayer WS_2 constitutes the primary other loss channel (characterized by $\gamma_{A,nr}$) and can be actively modulated via gate-induced changes in n_e. In our device, critical coupling is reached when the monolayer is at mild doping, $n_e = 3.5 \times 10^{12}$ cm^{-2} (Fig. 4.6a). At strong n-doping, the exciton resonance is quenched and the bare GMR produces a single reflectance minimum. On the other hand, at intrinsic doping, the exciton hybridizes with the GMR, leading to an avoided crossing in the dispersion that appears as two distinct reflectance minima. For both regimes, we plot the spectral evolution of the reflection amplitude and phase in a phasor diagram (Fig. 4.6b). In the n-doped case, the reflection coefficient traces a single loop in the complex plane (single photonic resonance), whereas at charge neutrality a double loop is traced due to the additional presence of the A-exciton (material resonance). At the design wavelength $\lambda = 596$ nm, perfect π-phase modulation is achieved with a constant amplitude of $|r| = 0.58$.

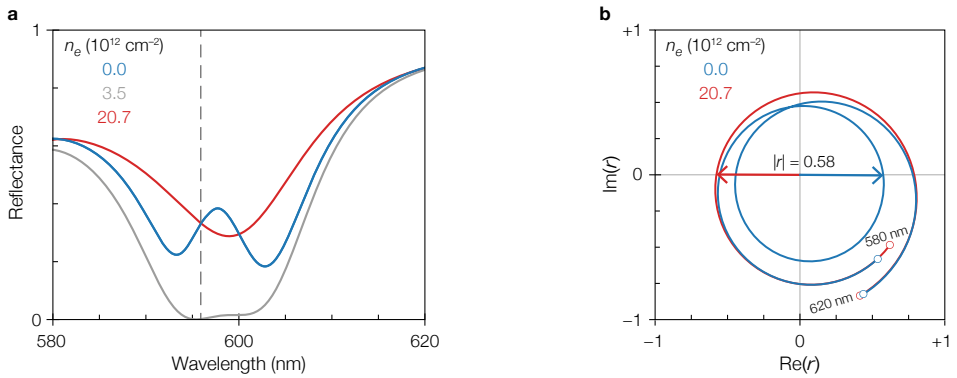

Figure 4.6: Gate-dependent reflection. **(a)** Reflectance spectra at different carrier concentrations showing the evolution from bare GMR at strong n-doping (red) to critical coupling at mild n-doping (gray) to exciton-GMR hybridization at intrinsic doping (blue). Dashed line indicates the operating wavelength. **(b)** Phasor diagram of the complex reflection coefficient, r, at intrinsic and strong n-doping. Vectors indicate r at the operating wavelength and show the perfect π phase flip.

Next, we probe the fundamental limits of a π-phase modulator by performing a TCMT analysis of a one-port two-resonator system (Fig. 4.A2 and Appendix A.4). We estimate $g \leq 20$ meV as a reasonable physical bound based on the work in Chapter 3, which we plug into our model together with the stated radiative and nonradiative rates. Using our inverse design framework, we find an upper bound on the reflection amplitude that allows π-phase modulation of $|r|_{max} = 0.62$, which highlights that our modulator design ($|r| = 0.58$) operates close to this fundamental limit. The TCMT model additionally allows us to quantify how changes in the metasurface's fundamental rates affect the achievable phase modulation depth (Fig. 4.A3). For

instance, increasing the radiative coupling rate of the GMR could be achieved by raising the index contrast of the subwavelength grating through duty cycle adjustments or by using a higher-index material. Reducing absorption losses may be achieved by minimizing losses in the electrical contacts and in the back-reflector (*e.g.* using a dielectric Bragg mirror). Moreover, the excitonic quantum yield could be further optimized by improving the material quality of WS_2 or via strain engineering[341]. Overall, we find that cutting the nonradiative losses provides the largest gain, with the maximum modulation amplitude increasing to $|r|_{\max} = 0.81$. Thus, eliminating parasitic absorption channels in the metasurface is the most fruitful avenue to further enhance the π-phase modulation depth.

Altogether, these results demonstrate a general strategy for achieving π-phase modulation by sweeping through critical coupling using a single control parameter[151]. Intriguingly, this concept can be extended to gain independent control over amplitude and phase—and thus achieve complete complex amplitude modulation—by introducing a second control parameter.

4.3 Complex amplitude modulation

The two-control-parameter approach has previously been demonstrated as an effective route to full complex-reflection control in the infrared spectral domain[154,242,333]. Here, we leverage the remarkable tunability of excitons in our hybrid-2D metasurface platform to extend this mechanism into the visible regime. To achieve this, we add a second monolayer at a different position in the heterostructure stack (Fig. 4.7a), which is independently addressable by applying a voltage (V_B) from the Ag back-reflector, while the original monolayer remains electrically connected to the graphene gate (V_T). Both monolayers are electrically insulated from each other by an extra multi-layer hBN slab. To enhance the modulation depth with this architecture, we choose to relax the maximum voltage constraint to $V_{\max} = 10$ V. Again, we optimize the metasurface geometry using our inverse design framework, updating the figure-of-merit to maximize the amplitude $|r|$ at which complex amplitude modulation is achievable over the full 0–2π phase range.

In the optimized design, both monolayers are separated by 102 nm of hBN and therefore experience different field overlaps with the GMR (Fig. 4.7b). The excitons in the top and bottom monolayers therefore couple to the GMR with unequal strengths, breaking the symmetry between both resonances (Fig. 4.A6 and Appendix A.4). Consequently, the complex $r(n_t, n_b)$ is uniquely affected by gate-modulation of the top and bottom carrier densities (n_t and n_b, respectively), with the extrema of n_t (0 to 25×10^{12} cm^{-2}) and n_b (0 to 6.8×10^{12} cm^{-2}) roughly defining the perimeter of the tunable range (Fig. 4.8a).

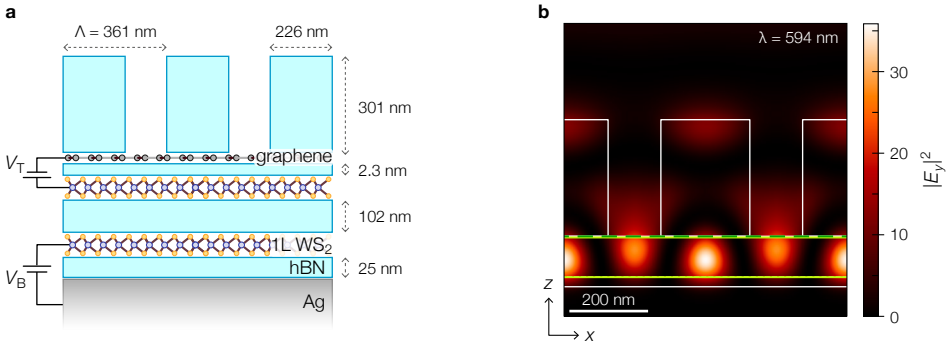

Figure 4.7: Double-gated metasurface design. (a) Cross-sectional view of the 2π phase modulator (not to scale). The WS_2 monolayers are independently addressable via the top (V_T) and bottom (V_B) gate voltages. The grating period and other geometrical parameters are indicated. **(b)** Electric field intensity ($|E_y|^2$) in absence of excitons, for a TE-polarized normal-incident wave at $\lambda = 594$ nm. The positions of 1L WS_2 (light green, solid) and graphene (dark green, dashed) are indicated.

To access the full 0–2π phase modulation range, the metasurface is designed to center r around the origin of the complex plane and thus operate in the vicinity of critical coupling (Fig. 4.8c,d; reflectance spectra shown in Fig. 4.A7). Whereas with a single control parameter it is only possible to trace a straight trajectory through the phase singularity, the two-control-parameter approach enables phase-only modulation by tracing a constant-reflectance path around a phase singularity (Fig. 4.8b). By judiciously selecting combinations of (n_t, n_b), we trace the largest constant-amplitude contour that sweeps the full 0–2π phase range at $|r| = 0.13$. We note that the maximum amplitude tunability extends beyond this cut-off with a limited phase range, which can be advantageous for applications including beam steering[344]. Notably, the same mechanism remains functional at room temperature, albeit it with a reduced constant-amplitude of $|r| = 0.06$ owing to the larger excitonic nonradiative decay rate (Fig. 4.A8).

Again, we use TCMT to assess whether the observed reflection amplitude approaches the theoretical maximum (details in Appendix A.4). First, we fit the reflectance without excitons to obtain the GMR loss rates, $\gamma_{G,r} = 55.0$ meV and $\gamma_{G,nr} = 18.6$ meV. Notably, the nonradiative rate is slightly higher than before due to the addition of another WS_2 monolayer in the heterostructure cavity. Even without excitons, the monolayers exhibit sub-bandgap absorption from impurities, edge states and defects[318], which increases the overall absorption losses. We consider a one-port resonator with three coupled oscillators (GMR and two exciton resonances) and optimize the exciton-photon coupling strengths, the metasurface's resonance wavelength, and the operating wavelength. The resulting TCMT system achieves full complex amplitude modulation at $|r| = 0.15$, indicating that our inverse-designed metasurface operates close to the fundamental limits of a reflection-phase modulator

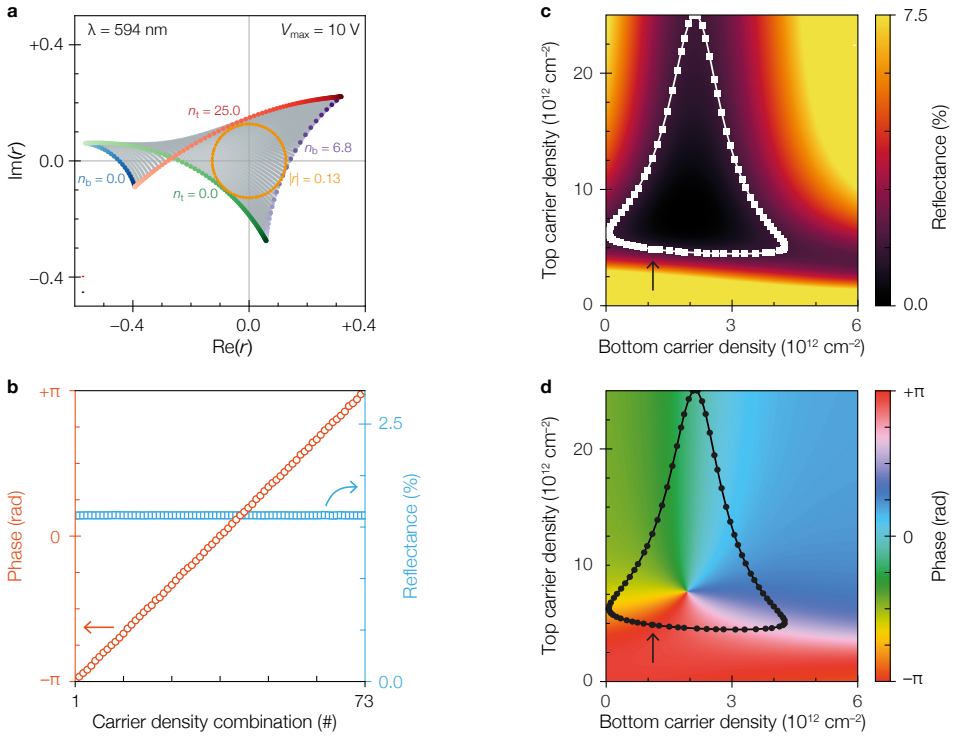

Figure 4.8: Full 2π complex amplitude modulation. (a) The reflection coefficients, r, which result from all possible combinations of carrier densities in the top (n_t) and bottom (n_b) monolayers (the extrema are color-marked, units: 10^{12} cm^{-2}). The metasurface achieves complete complex amplitude modulation up to $|r| = 0.13$ (orange circle), allowing for **(b)** continuous phase modulation from –π to π at a constant reflection amplitude. **(c)** Reflectance map and **(d)** reflection-phase map as function of top and bottom carrier densities. The carrier density combinations corresponding to $|r| = 0.13$ are indicated, where combination #1 is indicated with an arrow.

with the stated internal and external loss rates (Fig. 4.A4a). Naturally, the modulation depth is affected by modifying the fundamental rates that govern the metasurface's optical response. We again observe the strongest enhancement when absorption losses in the metasurface are eliminated ($\gamma_{G,nr} = 0$ meV), increasing the full-2π amplitude to $|r| = 0.22$ (Fig. 4.A4b). Beyond this, optimizing the radiative coupling rate, improving the excitonic quantum yield, or extending the modulation range of excitons in the bottom monolayer each yield only modest additional gains.

4.4 PROGRAMMABLE BEAM STEERING

To demonstrate the utility of complex amplitude modulation using our hybrid-2D metasurface platform, we design a three-level programmable beam steering device. Building on the double-gated design outlined above, we create a supercell with period $\Lambda = 1.08$ μm consisting of three geometrically identical unit cells (Fig. 4.9a). The

WS_2 monolayers are severed by carving 11-nm-wide slits along the y-axis to define individually addressable strips in the top and bottom monolayers (six gates in total). This segmentation lets us program the complex reflection coefficient of each unit cell (under TM illumination) and enables sculpting of the reflected wavefront across the supercell.

As a baseline, we design an intuitive forward-designed beam steering metasurface: a three-level electrically-blazed grating with a flat amplitude profile and a constant phase gradient, *i.e.*, a phased array (Fig. 4.A5a). Picking three carrier density combinations from Fig. 4.8 at the maximum amplitude of $|r| = 0.13$ with relative phases spaced $2\pi/3$ rad apart, we design the phase ramp to steer light into the –1 order (at an angle of $\theta = -33.3°$). The resulting phased array reaches a relative diffraction efficiency of 72.2% at $\lambda = 595$ nm, with the absolute reflected power capped at $R = 0.3\%$.

Next, we show how the diffraction efficiency can be increased by relaxing the constant-amplitude constraint and instead freely engineering both the phase and amplitude in each unit cell. This way, complex reflection coefficients with much larger amplitudes can be reached at the cost of a smaller overall phase ramp. It has been shown that these less intuitive configurations can be leveraged to enhance the performance, and that inverse design techniques are especially powerful to arrive at such unintuitive solutions.[344,345]. To this end, we utilize our optimization framework again (details in Appendix A.3) jointly optimizing the element width and the carrier densities in the top and bottom monolayers to generate a three-level (*i.e.* three unit cells) complex-amplitude pattern that steers light into the –1 order (Fig. 4.9a). Here, we kept all layer thicknesses from the preceding design but varied the grating-element width to enlarge the tuning range of the reflection amplitude (Fig. 4.9b). The grating's blazing is achieved by electrically configuring each unit cell to a unique carrier density combination (n_t,n_b; units of 10^{12} cm^{-2}), and we determine the optimal configuration to steer light into the -1 order as: I (0, 6.8), II (3.7, 1.3), III (25,6.8). This yields a marked improvement over the forward-designed structure, with the total reflected power at the operating wavelength ($\lambda = 595$ nm) rising to $R = 3.4\%$ (Fig. 4.9c), with 88.5% diffracted into the –1 order (Fig. 4.9d). Simply reprogramming the carrier densities to the mirror configuration, III-II-I, steers light into the +1 order instead (right-hand panel of Fig. 4.9d).

The same programmable architecture can be electrically reconfigured to enable other functionalities, such as perfect absorption or ~ 25% reflection in the 0^{th} order specular reflection channel. Naturally, increasing the number of independently tunable elements within the supercell would transform the system from a coarse three-level array into a fully programmable spatial light modulator. This comes with the practical limitation of our current design's reliance on a nonlocal resonance,

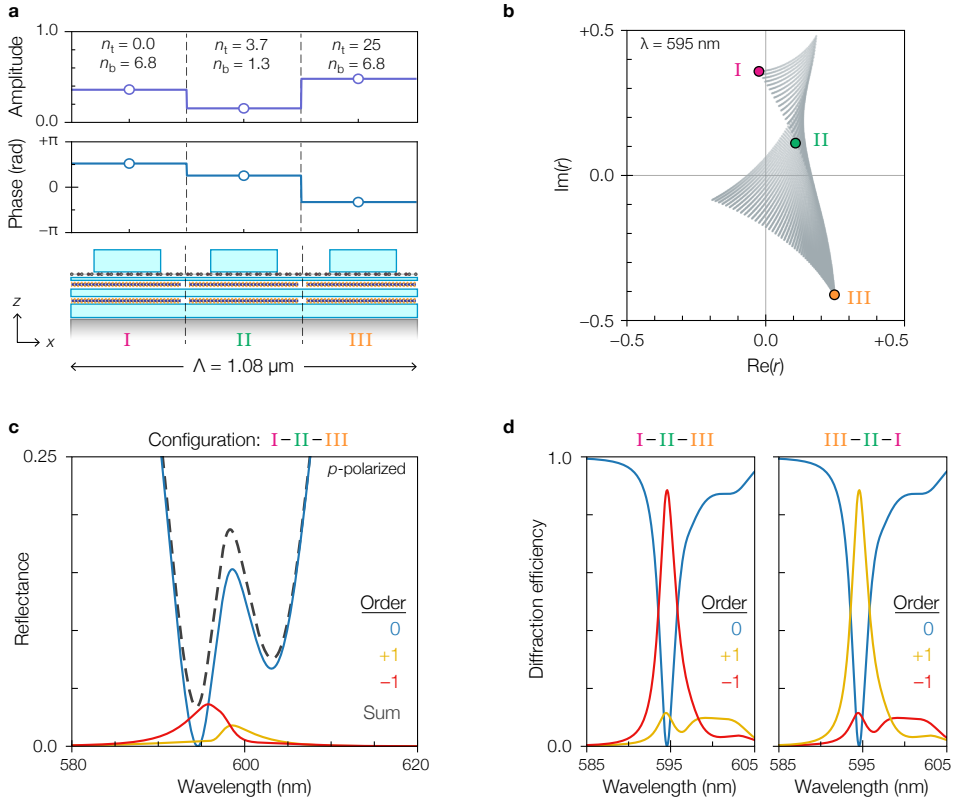

Figure 4.9: Beam steering with a three-level programmable metasurface. **(a)** Bottom: three-level programmable metasurface with supercell period $\Lambda = 1.08$ μm, designed to steer a normal-incident p-polarized beam into the –1 order. The phase (middle) and amplitude (top) of levels I, II, and III are programmed independently by tuning n_t and n_b to the indicated values (units: 10^{12} cm^{-2}). **(b)** Phasor diagram of the achievable complex amplitudes at each level, with the optimized values I (magenta), II (green), and III (orange) indicated. **(c)** Total reflectance (gray, dashed) and the –1 (red), 0 (blue), and +1 (yellow) diffraction orders for supercell configuration I-II-III. **(d)** The corresponding diffraction efficiency revealing that 88.5% of reflected power is redirected into the –1 order (left), or into the +1 order when the configuration is electrically switched III-II-I instead (right).

which imposes a larger unit-cell footprint than highly localized resonances would. Yet, a hybrid approach that leverages both local and nonlocal resonances within the same structure may mitigate this constraint while enabling multifunctional or multi-wavelength operation[100,346]. Overall, these results demonstrate the flexibility of our hybrid-2D platform for electrically reconfigurable metasurfaces.

4.5 CONCLUSION AND DISCUSSION

In this chapter, we have established hybrid-2D metasurfaces as a versatile platform for active wavefront shaping, enabled by the electrical tunability of excitons in van der Waals heterostructures combined with the field enhancement of a nonlocal

resonance. Inverse design is used throughout the chapter to maximize the performance within the physical constraints. With a single gate-tunable monolayer WS_2, sweeping through critical coupling enables a π phase flip at constant amplitude. The metasurface reaches an amplitude of $|r| = 0.58$ which closely tracks the upper bound of $|r| = 0.62$ retrieved from TCMT. Incorporating a second, independently gated monolayer WS_2 extends the phase coverage to $0–2\pi$ and decouples the amplitude to realize full complex amplitude modulation, which the optimized design achieves up to $|r| = 0.13$, agreeing well with the TCMT ceiling of $|r| = 0.15$. Finally, we demonstrate a three-level programmable metasurface for beam steering. The device redirects light with 88.5% efficiency into the ± 1 order at $\theta = \pm 33.3°$, with the 0^{th} order entirely suppressed, underscoring the applicability of our hybrid-2D platform.

The modest amplitudes associated with full complex-amplitude control reflect the need to operate near critical coupling to access the entire $0–2\pi$ phase range—a trend seen across other metasurface modulators. In an experimental realization[154], a conductive oxide plasmonic metasurface was capped at $|r| \approx 0.08$, while graphene plasmonic metamolecules reached $|r| \approx 0.19$ in simulation[333]. Crucially, both approaches remained restricted to polarization-dependent operation in the infrared spectral region. More recently, these limitations were overcome in simulation using an excitonic 2D materials heterostructure that enabled polarization-independent complex-amplitude control just beyond the visible regime[242]. However, this work relied on an assumed unity excitonic quantum yield—a condition rarely observed under standard laboratory conditions. Against this backdrop, achieving visible-wavelength, polarization-insensitive complex amplitude modulation with realistic material parameters is a meaningful advance for metasurface modulators.

As shown throughout this chapter, the efficiency of our modulator is ultimately constrained by the radiative and nonradiative channels within the metasurface. Improving the demonstrated design therefore hinges on reducing absorption or enhancing radiative coupling. The former may be achieved by minimizing Ohmic losses in the gate electrodes and suppressing sub-bandgap absorption in the excitonic materials by eliminating impurities and defects. The latter could be accomplished by replacing hBN in the grating layer with a higher-index, low-loss dielectric such as TiO_2 or Si.

In conclusion, the results presented in this chapter complement those of the previous chapter. We have demonstrated that meticulously designed hybrid-2D metasurfaces can be leveraged not only for active amplitude modulation, but also for independent phase control. Thus, our results establish excitonic 2D semiconductors as a promising platform for dynamic manipulation of free-space optical waves with exciting opportunities in up-and-coming optoelectronic applications.

4.6 ADDITIONAL FIGURES

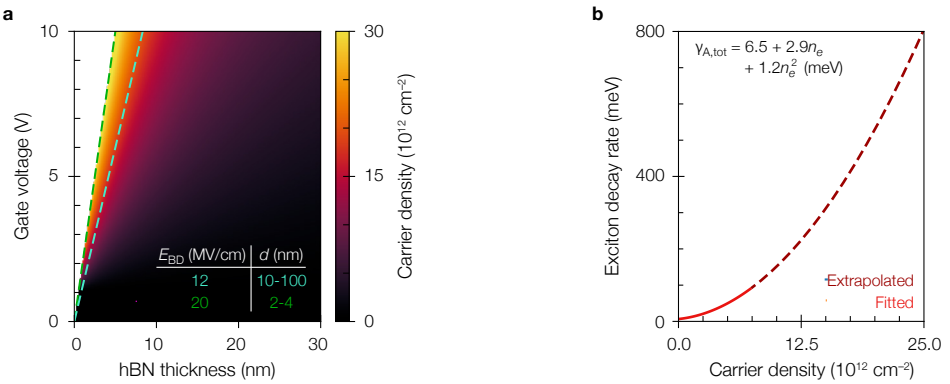

Figure 4.A1: Electrical tuning of exciton decay rate. **(a)** Gate-induced carrier density n_e in monolayer WS_2 calculated with a parallel-plate capacitor model modified to include the quantum capacitance, using hBN as a gate dielectric. Two representative hBN breakdown field limits are indicated:[238,336] $E_{BD} = 12$ and 20 MV/cm for thicknesses $d = 10$–100 and 2–4 nm, respectively (green and cyan dashed lines). **(b)** Total A-exciton decay rate $\gamma_{A,tot}$ as function of n_e (fit: $\gamma_{A,tot} = 6.5 + 2.9n_e + 1.2n_e^2$ (meV) with n_e in units of 10^{12} cm^{-2}). The solid red curve is a fit to experimental data from Section 3.5 up to $n_e = 7.3 \times 10^{12}$ cm^{-2}, the dashed maroon curve is an extrapolation beyond this range.

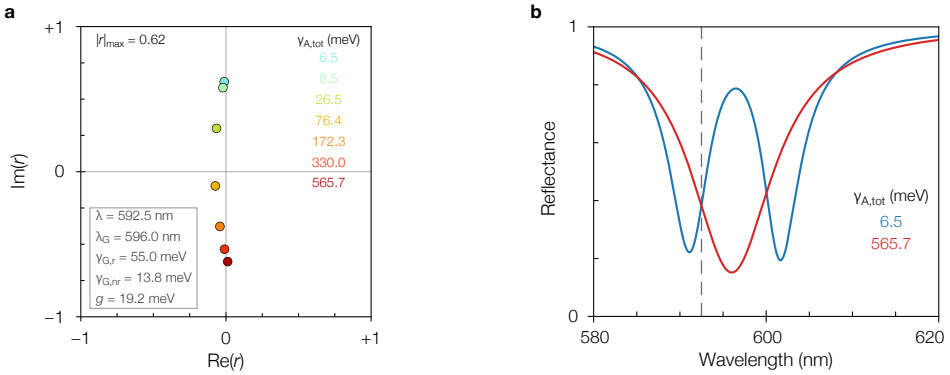

Figure 4.A2: Coupled mode theory analysis of a π-phase modulator. (a) Complex reflection coefficients of the optimized metasurface at operating wavelength $\lambda = 592.5$ nm for different values of the total exciton decay rate $\gamma_{A,\mathrm{tot}}$ (indicated by color), calculated using TCMT. The metasurface achieves π-phase modulation at $|r|_{\max} = 0.62$ at the optimized values of the resonance wavelength λ_G, radiative linewidth $\gamma_{G,r}$, nonradiative linewidth $\gamma_{G,nr}$, and exciton-photon coupling strength g listed in the lower left corner. **(b)** Reflectance spectra at intrinsic (blue) and strong n-type doping (red) indicated by their respective exciton decay rates of $\gamma_{A,\mathrm{tot}} = 6.5$ and 565.7 meV showing that the system transitions from strong to weak coupling. The dashed line indicates the operating wavelength.

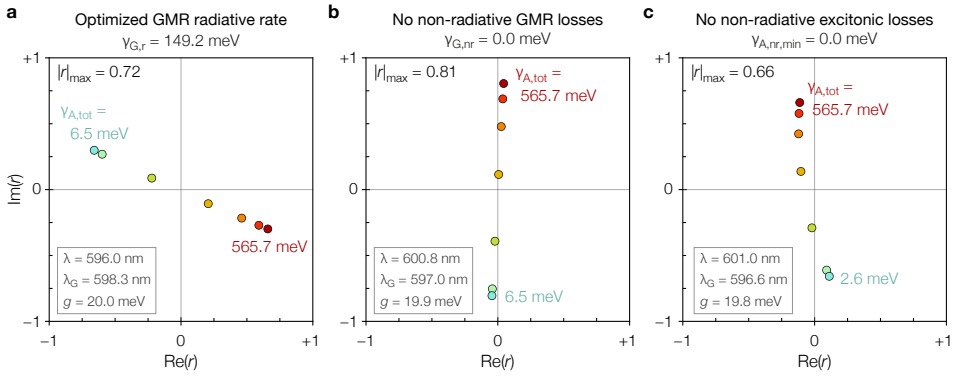

Figure 4.A3: Analysis of the limits to π-phase modulation. TCMT calculations of the complex reflection coefficients for different total exciton decay rates $\gamma_{A,\mathrm{tot}}$ (colored dots), with the optimized free parameters listed in the lower left corner of each diagram. The explored limiting cases are **(a)** optimized GMR radiative rate $\gamma_{G,r} = 149.2$ meV ($|r|_{\max} = 0.72$), **(b)** no nonradiative GMR losses $\gamma_{G,nr} = 0.0$ meV ($|r|_{\max} = 0.81$), and **(c)** no nonradiative excitonic losses, $\gamma_{A,nr,\min} = 0.0$ meV ($|r|_{\max} = 0.66$).

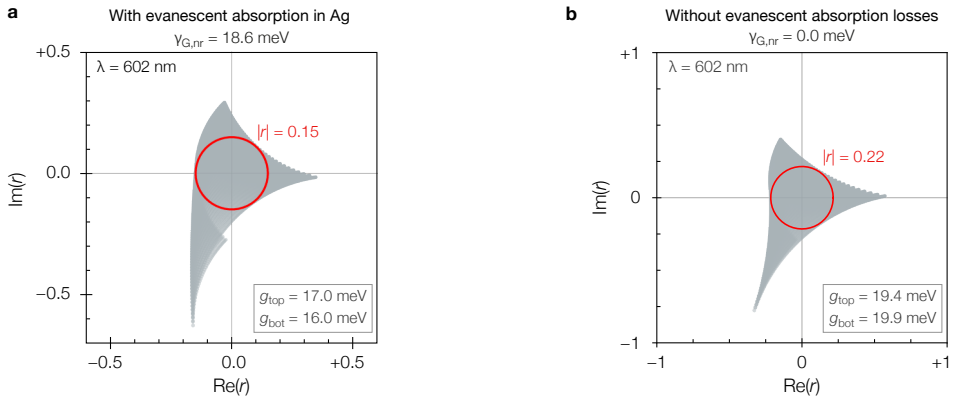

Figure 4.A4: Analysis of the limits to 2π-phase modulation. The complex reflection coefficients at λ = 602 nm for all allowed values of the exciton decay rates in the top ($\gamma_{A,top}$) and bottom ($\gamma_{A,bot}$) monolayers (gray dots), calculated with TCMT for two cases. The optimized coupling strengths g_{top} and g_{bot} for each case are listed in the lower right corner of each diagram. **(a)** The metasurface with the same exciton and GMR decay rates as the full-wave simulations, and **(b)** the same system with no nonradiative GMR losses ($\gamma_{G,nr}$ = 0 meV). Reducing these losses is identified as the most promising avenue to boost $|r|_{max}$.

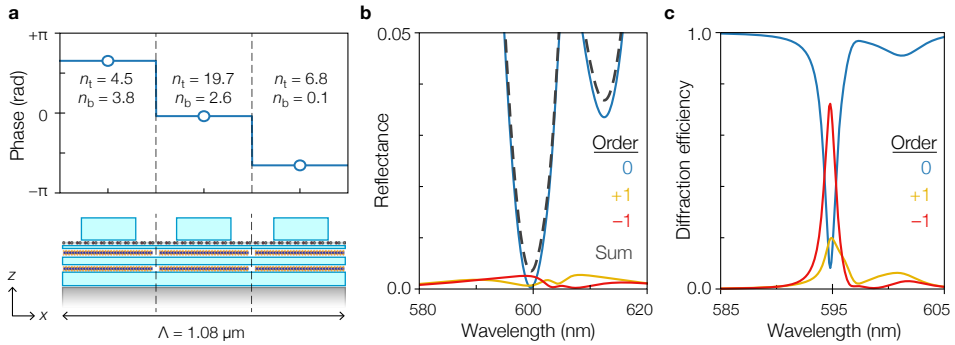

Figure 4.A5: Forward-designed beam steering metasurface. (a) Three-level programmable metasurface with supercell period Λ = 1.08 μm, designed for redirecting normal-incident p-polarized light at λ = 595 nm into the −1 order, with a constant phase gradient (top) and uniform amplitude of $|r|$ = 0.13 (not shown) achieved by tuning n_t and n_b to the indicated values (units: 10^{12} cm^{-2}). **(b)** Total reflected power (gray, dashed) and reflected power into the −1 (red), 0 (blue), and +1 (yellow) diffraction orders. **(c)** The corresponding diffraction efficiency reveals 72.2% of reflected power is redirected into the −1 order at λ = 595 nm.

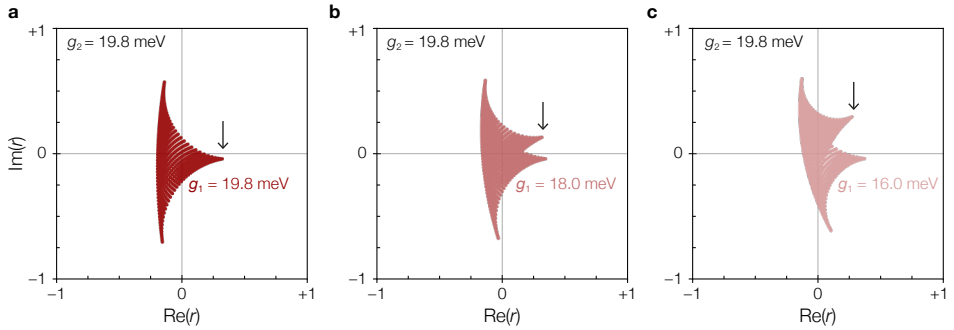

Figure 4.A6: Asymmetric reflection tunability through unequal coupling strengths. TCMT simulations of the reflection coefficients r of a complex amplitude modulator calculated for three different scenarios to elucidate the role played by the relative magnitudes of the coupling strengths g_1 and g_2 in shaping the available complex amplitudes. **(a)** When $g_1 = g_2$, the contribution of each exciton resonance is identical and their impact on r is fully symmetric. **(b)** Reducing the coupling strength of one exciton to $g_1 = 18.0$ meV, **(c)** down to $g_1 = 16.0$ meV, shows that the difference in coupling strengths leads to the appearance of two distinct lobes in the complex plane (corresponding to the tunable range provided by each exciton).

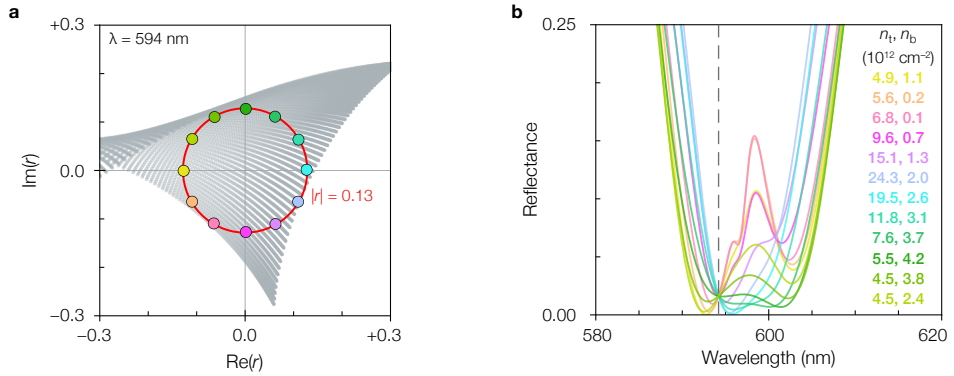

Figure 4.A7: Reflectance evolution of the complex amplitude modulator. (a) Phasor diagram of the reflection coefficients r at $\lambda = 594$ nm for all allowed combinations (n_t, n_b) (gray dots). The red circle with $|r| = 0.13$ indicates the maximum constant-amplitude contour along which the phase spans the full 0–2π range. Twelve evenly spaced points on this circle (colored dots) represent selected r values shown in **(b)** the corresponding reflectance spectra to highlight the evolution thereof, labeled with their respective (n_t, n_b) values. The operating wavelength is indicated (dashed, gray).

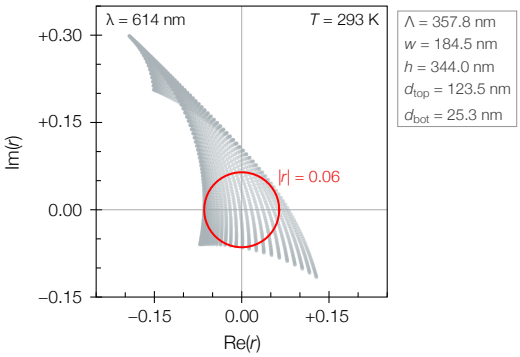

Figure 4.A8: Complex amplitude modulation at room temperature. Phasor diagram of the reflection coefficients r at $\lambda = 614$ nm for all allowed combinations of carrier densities in the top and bottom monolayers (gray dots), simulated at room temperature ($T = 293$ K). The optimized design achieves full 0–2π complex amplitude modulation at $|r| = 0.06$ (red circle) with the parameters indicated in the box.

5

Finite-size effects

5.1 Introduction

In the preceding chapters, we have demonstrated hybrid-2D metasurfaces that achieve electrical control over light by leveraging the combined merits of tunable excitons and nonlocal resonances supported by the structure. As discussed in the introduction (Chapter 1), nonlocal metasurfaces harnessing high-Q modes, including guided-mode resonances[91,347–349] and quasi-bound states in the continuum[350–352], have emerged as a promising alternative to local metasurfaces,[346] owing to their potential for realizing tremendous spectral resolution and strong near-field enhancements.[311,323,353] Recently, it was even shown that nonlocalities can be engineered with locally varying features to ameliorate the loss in spatial resolution compared to localized plasmonic or Mie-type resonances.[100,354,355] Together, these properties are broadly applicable in biomolecular sensing,[123–125] coherent light sources,[356–358] free-space modulators,[114,115,337] mixed-reality eyewear,[101,121] nonlinear optics,[116–118] optical image processing,[96,359] thermal metasurfaces,[119,120] and wavefront shaping.[111–113]. It is therefore compelling to embrace nonlocality in the move toward ultracompact meta-devices.

In the pursuit of miniaturization, however, the finite lateral extent of a metasurface may introduce unwanted effects. Whereas in local metasurfaces such finite-size effects could largely be ignored, with only select works investigating them,[87,88,360,361] the inherent delocalization of high-Q resonances means finite-size effects can no longer be neglected.[117,362,363] Indeed, not long after the introduction of guided-mode resonant gratings,[35,39], it was realized that finite sizes can degrade their performance.[364–370] Despite the importance of finite-size effects, nonlocal metasurfaces are typically simulated as infinitely periodic due to the computational cost of modeling finite arrays in full-wave solvers, and the inability to account for lattice truncation in temporal coupled-mode theory.[342,371–373] As a result, the resonant response of fabricated devices is often influenced by the unpredictable corollaries of finite size, such as those encountered in Chapter 3, prompting efforts to develop mitigation

strategies[362,374–376] and theoretical models.[377,378] Yet, so far, a broadly applicable predictive modeling framework has remained elusive.

Here, we develop a model that intuitively and quantitatively captures how a finite lateral footprint reshapes the scattering response of guided-mode resonant metasurfaces. We use spatiotemporal coupled-mode theory (STCMT), a recent extension of temporal coupled-mode theory that captures spatial inhomogeneity.[379–381] Our model explicitly accounts for excitation of a traveling wave that can re-radiate within a finite aperture due to the limited metasurface width. We show that when the physical interaction length becomes comparable to the modal propagation length, finite-size effects fundamentally modify the optical response, giving rise to excitation position-dependent interference fringes and linewidth broadening. Crucially, we derive an expression for the Q-factor that incorporates an additional dissipation channel due to edge losses, demonstrating that the stored energy and effective lifetime scale exponentially with the interaction length L, defined as the distance over which the nonlocal mode travels after excitation at x_0 before reaching the termination (Fig. 5.1a). We validate the model experimentally by performing position- and momentum-resolved reflectance spectroscopy on the 30-µm-wide hybrid-2D metasurface fabricated in Chapter 3. The measurements show remarkable agreement with the theory, directly confirming the predicted size effects and enabling quantitative separation of the intrinsic, radiative, and edge-induced loss rates. Finally, we provide concrete design guidelines for achieving the theoretical response and maximizing the light-matter interaction in finite-size guided-mode resonators, establishing STCMT as an invaluable tool for designing and interpreting footprint-limited hybrid-2D metasurfaces.

5.2 SEMI-INFINITE METASURFACE

In the following, we study the effects of finite size on the optical response of a reflective guided-mode resonator. Here, the structure consists of a truncated waveguide of width W patterned with a subwavelength grating of period Λ and backed by a reflector (Fig. 5.1a). The scattering problem is described in terms of a single modal parameter $a(x,t)$ that is excited from free-space by a spatially localized input field $s_+(x')$. Compared to an infinite metasurface, lattice truncation can fundamentally alter the scattered field $s_-(x)$ near the resonant frequency ω_0 or, equivalently, the in-plane wavevector $k_{x,\mathrm{res}}$, introducing fringes and broadening the resonance (Fig. 5.1b,c).

To determine the origin of the finite size effects observed in Fig. 5.1c, we first start with an infinitely periodic system. We consider a quasi-guided mode that is characterized by a dispersion that is linearized around a point (ω_0, β_0) as

$$\Omega(\beta) \simeq \omega_0 - i\Gamma + v_g(\beta - \beta_0) \tag{5.1}$$

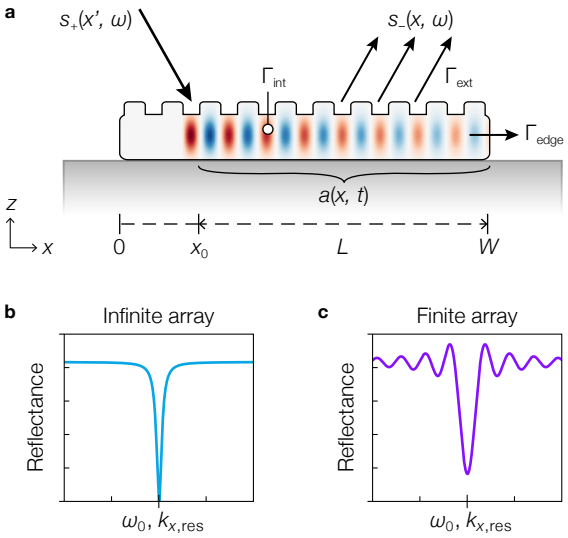

Figure 5.1: A nonlocal metasurface with finite-size effects. (a) An incident field $s_+(x', \omega)$ centered at x_0 excites a right-propagating quasi-guided mode with amplitude $a(x,t)$. The mode has an interaction length L, over which it decays through intrinsic loss (Γ_{int}) and re-radiation (Γ_{ext}). Power reaching the right edge, $x = W$, is irreversibly lost, giving rise to an additional edge loss channel Γ_{edge}. The scattered field is denoted $s_-(x, \omega)$. **(b)** Modeled reflectance for an infinite, and **(c)** a finite metasurface array, respectively, showing the impact of finite size on the scattering response near the resonant frequency ω_0 or in-plane wavevector $k_{x,res}$.

where β is the phase constant, v_g is the group velocity, and $\Gamma = \Gamma_{int} + \Gamma_{ext}$ is the rate at which the mode decays due to internal (nonradiative) and external (radiative) mechanisms, respectively (see also Appendix A.5.1). To achieve such dispersion, we design a dielectric hexagonal boron nitride (hBN) waveguide on a gold (Au) back-reflector that supports the fundamental TE_0 mode (Fig. 5.2a). The waveguide is capped with a low-index dielectric polymer, specifically chemically semi-amplified resist (CSAR), in which a subwavelength grating is patterned with period $\Lambda = 368$ nm and duty cycle of 36%. In this system, the duty cycle governs the radiative coupling (Γ_{ext}), while nonradiative losses (Γ_{int}) are incurred evanescently in the Au layer. We optimize the geometry to achieve mirror-like background reflection over the relevant bandwidth.

The periodic perturbation in the CSAR layer breaks the in-plane translational symmetry and folds the dispersion of the guided mode into the light cone (Fig. 5.2b). The subwavelength periodicity restricts scattering to the 0^{th}-order direct reflection channel, with the diffracted orders constituting both left- and right-propagating evanescent waves owing to the grating's symmetric design. From full-wave simulations (Fig. 5.2c), we find that the coupling between these modes is negligible except in the vicinity of $k_x = 0\ \mu m^{-1}$, and consequently we can treat them as independent linear modes over most of the relevant k_x range. This is not a general result, and a parabolic

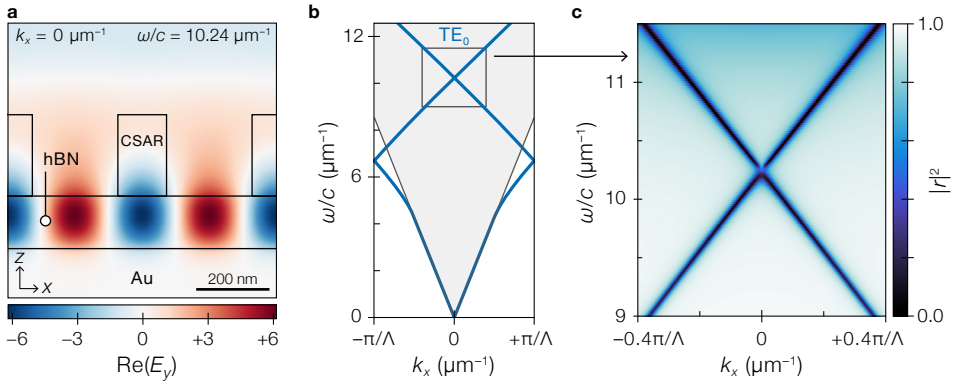

Figure 5.2: Semi-infinite guided-mode resonator. (a) Full-wave simulation of the electric-field profile $\mathrm{Re}(E_y)$ of the quasi-guided mode in a semi-infinite resonator comprised of a CSAR subwavelength grating on a hBN waveguide with an Au back-reflector. **(b)** Calculated TE_0 guided-mode dispersion, where the grating is modeled as an effective medium. The grating folds the dispersion into the first Brillouin zone ($-\pi/\Lambda$ to $+\pi/\Lambda$), shown by vertical dashed lines, with the portion that lies within the light cone indicated by the gray shaded region. **(c)** Simulated momentum-resolved reflectance ($|r|^2$) showing the corresponding dispersion.

dispersion arises at the band edge when the coupling between forward and backward propagating modes is non-negligible[379]. We attribute the minimal mode coupling to their predominant confinement in the continuous waveguide layer (Fig. 5.2a) and to the relatively weak scattering efficiency of the low-contrast grating.

To parametrize the dispersion within STCMT, *i.e.* Eq. (A.50), we obtain the guided mode dispersion numerically using a slab waveguide mode solver by modeling the grating as an effective medium.[382,383] This directly yields most of the physical parameters entering Eq. (5.1). However, since the eigenmode is computed for a closed system, we must obtain the radiative rate Γ_{ext} by other means. In this case, we use the full-wave simulations of the driven semi-infinite metasurface response (Fig. 5.2c) and fit it with the well-known TCMT expression for a system with a single mode and one external port.[371] From this analysis, we find that a constant value of $\Gamma_{\mathrm{ext}} = 7.4 \times 10^{12}\ \mathrm{s}^{-1}$ is sufficient to accurately reproduce the full-wave response over the bandwidth considered here (Fig. 5.A2), where the observed deviation at higher frequencies is due to increasing optical losses in the gold layer, which we do not explicitly account for in our model.

The decay rate sets the resonance lifetime and is closely related to the quality factor, which is formally defined as the ratio of stored energy U in the resonator to the rate of energy dissipation P_{loss},

$$Q \equiv \omega_0 \frac{U}{P_{\mathrm{loss}}} = \frac{\omega_0}{2\Gamma}, \tag{5.2}$$

as well as the modal propagation length,

$$L_p = \frac{v_g}{\Gamma}, \tag{5.3}$$

which governs the characteristic length scale over which nonlocality must be considered (*i.e.* the nonlocality length [380]). When an impinging wave launches a right-propagating mode at $x' = x_0$, the resulting excitation interacts with the structure over a finite length $L = W - x_0$. In the semi-infinite limit, $L/L_p \to \infty$, the array size negligibly perturbs the resonant response (Fig. 5.1b). Conversely, in the short-grating limit, $L \lesssim L_p$, finite-size effects critically impair the theoretical performance (Fig. 5.1c). At $\omega/c = 9\ \mu\text{m}^{-1}$, we find $L_p = 11.9\ \mu$m and $Q = 132$, which reduces to $L_p = 6.4\ \mu$m and $Q = 96$ at $\omega/c = 11.5\ \mu\text{m}^{-1}$ due to increased optical losses in the Au layer at higher frequencies[312].

The infinitely periodic limit discussed so far is typically the starting point of metasurface design, but it is clear that if the lateral dimensions of the metasurface are close to the propagation length L_p, we may expect significant finite-size effects. In the following, we will discuss how to take those finite-size effects into consideration using STCMT.

5.3 FINITE-SIZE EFFECTS

Generally, the spatiotemporal equation of motion for a system with one input port and a locally linear dispersion is written as[380]

$$\begin{aligned} \frac{\partial a(x,t)}{\partial t} + v_g \frac{\partial a(x,t)}{\partial x} + i\Big(\omega_0 - i\Gamma - v_g\beta_0\Big)\, a(x,t) \\ = \int \kappa(x,x')\, s_+(x',t)\, \mathrm{d}x'. \end{aligned} \tag{5.4}$$

This equation describes the propagation of a single modal amplitude $a(x,t)$ that is excited from free-space by an incident wave $s_+(x',t)$ with coupling coefficient κ. The parameter $a(x,t)$ is normalized such that its absolute value squared gives the instantaneous stored energy in the nonlocal mode per unit area, while $|s_+|^2$ captures the input power density. As the mode propagates along the structure, it radiates to free space (described by d) to build up the scattered field $s_-(x,t)$ (also normalized such that $|s_-|^2$ is the outgoing power density) in interference with the non-resonant background, described by $C\,s_+(x',t)$ (additional details in Appendix A.5):

$$s_-(x) = \int \Big(C(x,x')\, s_+(x') + d(x,x')\, a(x')\Big)\mathrm{d}x'. \tag{5.5}$$

Although the mode has a nonlocal spatial distribution, we assume scattering is

purely localized[380]. As a result, the scattering coefficients become proportional to $\delta(x-x')$ (Appendix A.5.4). In the steady state, Eqs. (5.4) and (5.5) then reduce to

$$v_g\left(\frac{\partial}{\partial x}-i\tilde{\beta}\right)a(x)=\kappa(x)s_+(x), \tag{5.6}$$

$$s_-(x)=-s_+(x)+d(x)a(x), \tag{5.7}$$

where we introduced the complex propagation constant $\tilde{\beta}=\beta+i\alpha$ with attenuation rate $\alpha=\Gamma/v_g$ in the standard waveguide form. In addition, we assumed a perfectly reflective off-resonant response over the bandwidth of interest, *i.e.* $C=-1$.

To apply STCMT to a metasurface of width of W, we simply take the coupling coefficients to be non-zero only over the interval $x\in[0,W]$,

$$\kappa(x)=d(x)^*=\sqrt{2\Gamma_{\text{ext}}}\,e^{iqx}\Theta(x)\Theta(W-x), \tag{5.8}$$

where $\sqrt{2\Gamma_{\text{ext}}}$ is the familiar radiative coupling term from temporal coupled-mode theory[371] and the phase factor (e^{iqx}, with $q=2\pi/\Lambda$) encodes in-plane momentum matching between the guided mode and free-space radiation. Crucially, the Heaviside functions (Θ) restrict coupling to the finite interval $x\in[0,W]$. Note that while we have the standard TCMT identity $|\kappa|^2=|d|^2=2\Gamma_{\text{ext}}$, we also have the unusual relationship $\kappa=d^*$, which is a consequence of the in- and out-coupling coefficients carrying opposite grating momentum.

To capture the essential physics of interest here, we find that it is sufficient to model *only* a single, right-propagating mode,

$$a(x)=\frac{\sqrt{2\Gamma_{\text{ext}}}}{v_g}\int_0^x e^{i\tilde{\beta}(x-x')}e^{iqx'}\,s_+(x')\,\mathrm{d}x'. \tag{5.9}$$

While this simplification strictly speaking violates reciprocity (due to the absence of a backward propagating mode), we find this approach justified in the regime where the interaction between the forward and backward modes is negligible. We note that, in principle, the theory can readily account for coupled, counter-propagating modes at the cost of increased complexity.[379]

The preceding equations provide us with a method to solve the reflected field from a finite nonlocal metasurface. In general, the easiest way to solve for the reflection involves numerically integrating Eq. (5.9) to find the mode amplitude, and then inserting this into Eq. 5.5. In certain cases, however, these equations can readily be solved analytically: for example, when the resonance linewidth is much narrower than the NA of excitation ($\alpha\ll k_{x,\text{max}}$), we can approximate the diffraction-limited input field as a point source (*i.e.* a δ-function; the validity of this approximation is

confirmed below. This collapses the reflection coefficient to a compact closed form,

$$r(k_x) = -1 + \frac{2\Gamma_{\text{ext}}}{v_g\,(\alpha + i\Delta_k)}\left(1 - e^{-(\alpha+i\Delta_k)L}\right), \tag{5.10}$$

or similarly in terms of ω (full derivation in Appendix A.5.5). Here, the first factor recovers the familiar Lorentzian dependence on detuning $\Delta_k = k_x - k_{x,\text{res}}$, while the exponential term encodes the effects of finite size via the interaction length L. The prevalence of these effects is governed by the relative magnitudes of L and L_p. In the short-grating limit, $L \lesssim L_p$, the finite aperture produces oscillatory spectral features and apparent resonance broadening, whereas in the long-grating limit, $L \gg L_p$, the finite-size term vanishes and Eq. (5.10) reduces to the standard one-port TCMT expression.[371]

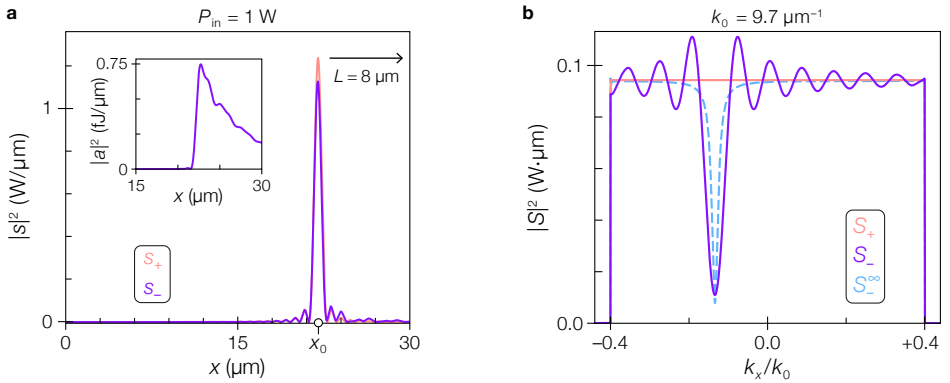

Figure 5.3: Scattering response of a finite-size guided-mode resonator. (a) STCMT simulations of the real-space input field $|s_+(x')|^2$ (salmon) and the corresponding scattered field $|s_-(x)|^2$ (purple), calculated for a $P_{\text{in}} = 1$ W excitation at $x_0 = 22$ μm ($L = 8$ μm) and NA $= k_{x,\text{max}}/k_0 = 0.4$. The inset shows the abrupt truncation of the mode amplitude $a(x)$ at $x = W$. **(b)** The corresponding transverse-momentum representation of the input field $|S_+(k_x)|^2$. The resulting scattered field $|S_-(k_x)|^2$ shows broadening and fringes arising from edge truncation when compared to the semi-infinite response $|S_-^\infty|^2$ (blue, dashed).

In the following, we apply the model to a finite metasurface with width $W = 30$ μm illuminated by a coherent, diffraction-limited input field arising from the Fourier transform of a one-dimensional entrance pupil with numerical aperture NA $= k_{x,\text{max}}/k_0 = 0.4$. The excitation launches a right-propagating quasi-guided mode that decays through absorption and radiation. As the mode reaches the termination of the metasurface at $x = W$, we assume that any remaining power is irreversibly lost. The finite width W thus restricts the mode's interaction length, or scattering aperture, to $L = W - x_0$. Figure 5.3a shows the input and output fields at frequency $k_0 = \omega/c = 9.7$ μm^{-1} and centered at $x_0 = 22$ μm, corresponding to an interaction length $L = 8$ μm. We observe strongly localized excitation with characteristic sinc

fringes (in salmon), and a reflected field that is only slightly reduced in amplitude (in purple), since most of the incident power is distributed among non-resonant k-vectors. However, when looking at the mode amplitude, we clearly observe an excitation that is launched at x_0, right-propagates and exponentially decays (Fig. 5.3a, inset). At this frequency, the propagation length is $L_p = 10.6$ µm such that the mode amplitude only reduces to $e^{-L/L_p} \approx 0.47$ before reaching the termination at $x = W$, and finite-size effects cannot be ignored.

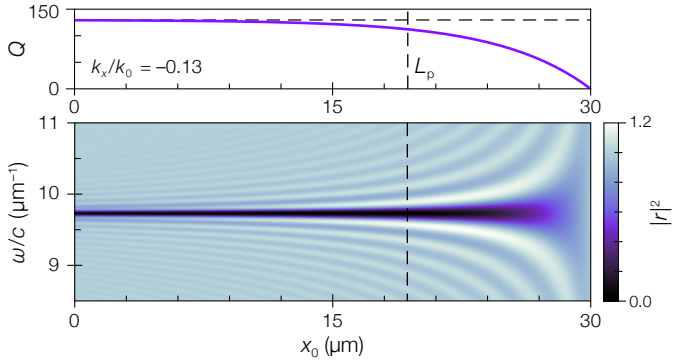

Figure 5.4: Position-dependent spectral response. STCMT-simulated evolution of the Q-factor (top) and reflectance (bottom) as a function of x_0, for fixed $k_x/k_0 = -0.13$, with the propagation length L_p indicated with respect to the edge of the resonator (vertical, dashed). The Q-factor tends to the semi-infinite limit (horizontal, dashed) as L increases.

While, in real space, the effects of lattice truncation appear to be mild, the same cannot be said about Fourier space (Fig. 5.3b). The angular scattering response still exhibits a resonant dip at $k_x/k_0 = -0.13$ (in purple), consistent with the semi-infinite structure (in dashed blue), but the overall response deviates strongly from a simple Lorentzian lineshape. Instead, the resonant feature is modulated by a sinc-like envelope set by the finite scattering aperture, with pronounced fringes arising from coherent interference between radiation emitted from different positions along the grating. We note that the scattered field $|S_-(k_x)|^2$ can locally exceed unity due to a redistribution of power within the angular spectrum and does not imply optical gain; the total scattered power is limited by the incident power minus the power dissipated through absorption and edge losses.

Moving the point of excitation along the sample changes L and systematically reshapes the spectral (Fig. 5.4) and angular response (Fig. 5.5a–e). As the beam approaches the right edge ($x_0 \to W$), the interference pattern becomes more pronounced and the fringe spacing increases as $\Delta k_{\text{fringe}} = 2\pi/L$, in direct analogy with Fraunhofer diffraction from a rectangular aperture. Conversely, moving x_0 farther away from the right edge reduces the fringe spacing. Ultimately, at $L = 29$ µm ($L/L_p =$

2.7) the response appears indistinguishable from the infinite array. In this case, the mode decays to $e^{-L/L_p} \approx 0.06$ before reaching $x = W$—providing an indication of the relative sizes required to obtain unperturbed performance.

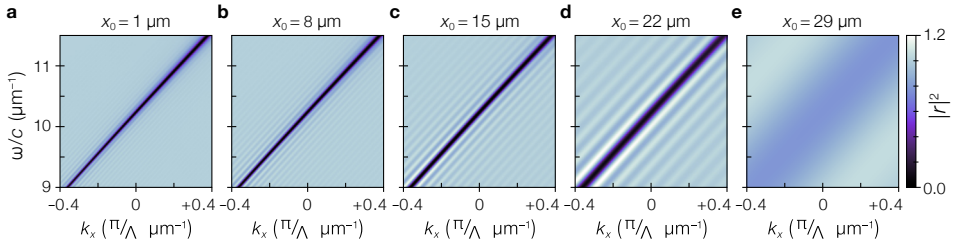

Figure 5.5: Position-dependent angular response. (a–e) STCMT-simulated reflectance dispersion at various positions x_0 showing position-dependent variation in interference fringes and linewidths.

Before proceeding, we briefly assess the validity of the point-source approximation for this system, with $\alpha/k_0 \approx 0.01$ and NA = 0.4. Figures 5.A3a,b show the resonant scattered field in real space and momentum space, respectively, calculated under δ-excitation and sinc illumination. While the real-space scattered fields differ, with the sinc beam producing oscillatory fringes, in momentum space the fields overlap almost perfectly: the mean relative error (calculated over the full NA range) remains well below 1%, confirming that the point-source approximation is valid for this system. We further quantify the regime in which the approximation holds by varying the NA and computing the mean relative error between the reflectance $|r(k_x)|^2$ under effectively infinite-NA excitation and finite-NA excitation (Fig. 5.A3c). From this analysis, we find that the error remains below 1% when the NA exceeds the normalized resonance linewidth by roughly a factor of 16, *i.e.* when NA $\gtrsim 16\,\alpha/k_0$.

Having established the validity of the point-source approximation, we now use the closed-form expression of Eq. 5.10 to derive an expression for the L-dependent Q-factor. This is necessary because, in a finite metasurface, the apparent spectral width of the resonant feature is not, in general, a direct measure of the stored energy and power dissipation of the guided mode, and the Q-factor therefore cannot be directly inferred from the spectrum. To capture the influence of edge losses, we introduce an effective decay rate $\Gamma_{\text{tot}}(L) = \Gamma + \Gamma_{\text{edge}}(L)$ where Γ_{edge} is the L-dependent edge loss rate. We can then rewrite Eq. (5.2) as

$$Q(L) = \frac{\omega_0}{2\Gamma_{\text{tot}}(L)} = \frac{\omega_0}{2\Gamma}\left(1 - e^{-2L/L_p}\right) \tag{5.11}$$

which yields a lifetime-based Q that formalizes the dependence on the interaction length and the propagation length, vanishing as $L \to 0$ while approaching the semi-infinite limit ($Q \to 130$ at $k_0 = 9.7\ \mu\text{m}^{-1}$) as $L \gg L_p$ (Fig. 5.4). Together, these findings

underscore the detrimental impact that finite size can have, even at a moderate Q-factor.

5.4 EXPERIMENTAL VALIDATION

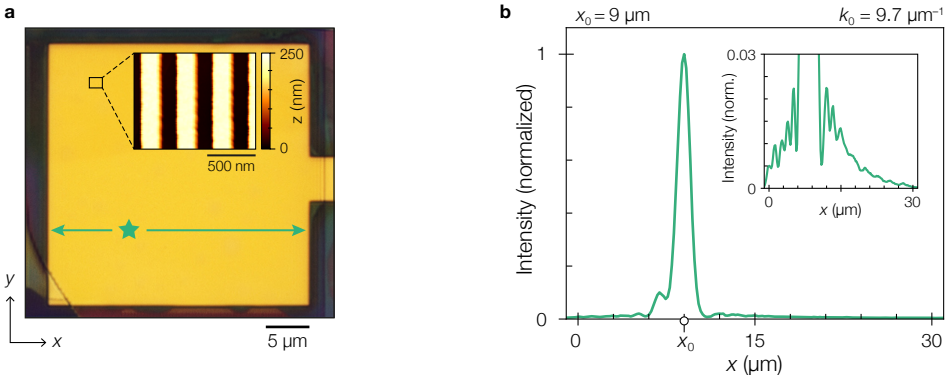

Figure 5.6: Fabricated metasurface. (a) Optical image of the resonator. Inset: atomic force micrograph of the subwavelength grating. The green star marks the excitation position (x_0 = 9 μm). **(b)** Horizontal linecut through the center of the reflected beam imaged in real-space. Inset: the same image recorded with a longer exposure to reveal the low-intensity features, scaled to match the intensity in the main panel.

To test the model experimentally, we use a region of the hybrid-2D metasurface fabricated in Chapter 3 that does not contain monolayer WS_2. This section of the device consists of 143 nm-thick mechanically exfoliated hBN on top of a 30 μm-wide Au back-reflector, which is capped with a subwavelength grating patterned in a 222-nm-thick layer of CSAR resist with Λ = 368 nm. Using atomic force microscopy, we established that the grating is patterned with excellent uniformity and matches the design parameters (Fig. 5.6a).

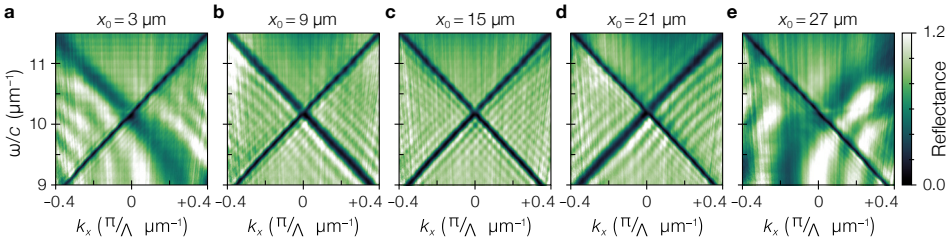

Figure 5.7: Position-dependent angular response. (a–e) Measured momentum-resolved reflectance at different incident positions x_0, confirming the predicted interference fringes and linewidth variation.

We mount the sample in our diffraction-limited optical microscope setup and illuminate it with a focused monochromatic laser beam (20× objective, NA = 0.4) at

$k_0 = 9.7\ \mu\text{m}^{-1}$, centered at coordinate $x_0 = 9\ \mu\text{m}$. In contrast to the STCMT model, the symmetry of the grating leads to the excitation of two counter-propagating guided waves from the illumination spot. Figure 5.6b shows a horizontal linecut through the real-space reflected intensity profile imaged on the camera. When recorded with a longer exposure time, a delocalized radiation pattern and exponential decay away from x_0 become apparent, characteristic of a leaky guided resonance (inset of Fig. 5.6b).

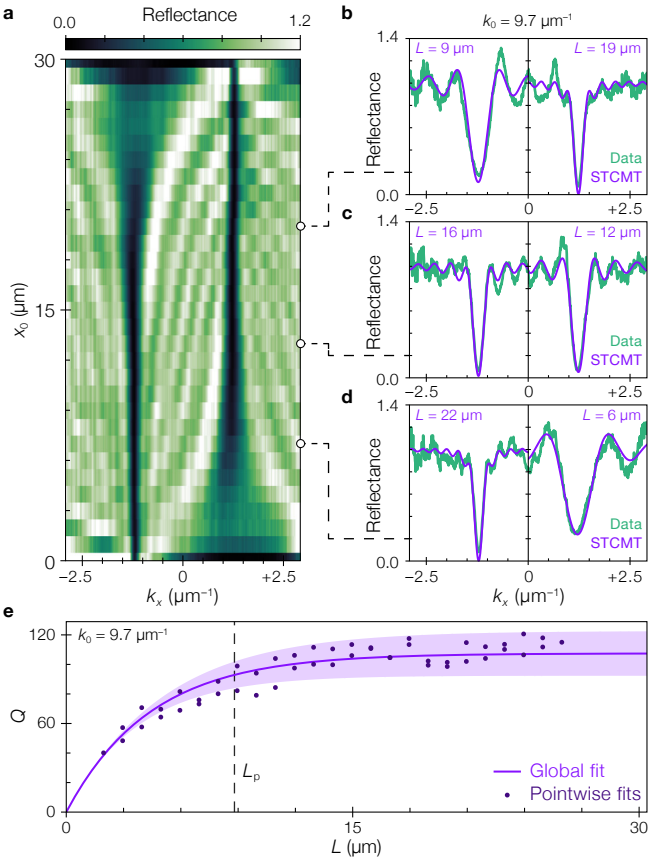

Figure 5.8: Comparison between model and experiment. **(a)** Measured reflectance versus excitation position x_0 and transverse momentum k_x, at $k_0 = 9.7\ \mu\text{m}^{-1}$. **(b–d)** Representative momentum-resolved reflectance linecuts (green) at selected x_0, overlaid with the global STCMT fit (purple). The fitted lengths L are indicated. **(e)** Quality factor $Q(L)$ inferred from the global STCMT fit, with the extracted propagation length L_p indicated (dashed line). Points represent fits performed independently at each linecut; the shaded band indicates the corresponding model discrepancy (one standard deviation) relative to these pointwise fits.

By inserting a Bertrand lens, we image the back-focal (Fourier) plane of the microscope objective to obtain the scattered field in momentum space (Fig. 5.A1).

Two resonant features are observed as dips in the reflectance at $k_x/k_0 \approx \pm 0.13$. Because the excitation is off-center, the left- and right-propagating guided waves experience different interaction lengths. From the phase-matching condition of the forward mode, $k_x + q = \beta$, we obtain $k_x/k_0 = -0.13$ and we therefore identify the feature at negative k_x as right-propagating. This assessment is directly corroborated by the back-focal plane image, where this branch exhibits a narrower resonance than the branch at $k_x/k_0 = +0.13$, owing to its longer interaction length L.

To study the position dependence of the resonant lineshapes in more detail, we scan the laser spot over the metasurface from $x = 0$ µm to $x = W = 30$ µm in 1 µm steps. At each position, we sweep the laser frequency and record the momentum-resolved reflectance. Figures 5.7a–e show the measured dispersion at five representative incident positions. When the metasurface is illuminated near its center (Fig. 5.7c), the response is symmetric and both counter-propagating modes exhibit a narrow resonance while already showing an interference pattern indicating that the finite sample size affects the response. As the spot is moved toward the left (Fig. 5.7b), this symmetry is broken: the right-propagating branch narrows (due to a longer L) while the left-propagating branch broadens, eventually becoming barely discernible near the edge (Fig. 5.7a). This trend reverses when moving to the right edge (Fig. 5.7d,e), consistent with the swapped interaction lengths experienced by the two guided waves. To further illustrate this modal evolution, we plot the position-dependent angular reflectance at a fixed $k_0 = 9.7$ µm^{-1} (Fig. 5.8a), emphasizing how both the resonance lineshape and the interference fringes vary with the excitation position. Overall, these observations are in excellent agreement with the STCMT predictions (Fig. 5.5).

Motivated by this qualitative correspondence, we next extract the intrinsic decay rates, Γ_{int} and Γ_{ext} by fitting the measured reflectance. To reduce the parameter space, we fix β and v_g from the eigenmode dispersion (Fig. 5.2b) and capture experimental deviations by a small Δk_x offset. In addition, we introduce an effective width correction, ΔW, to account for a systematic reduction of L due to edge apodization in the fabricated metasurface. Figures 5.8b–d show representative linecuts at three excitation positions x_0, with the STCMT fitted separately to the left- and right-propagating branches (since the STCMT was developed for a single mode only). The model accurately reproduces the reflectance data across the scanned range for $\Delta k_x \approx 0.08$ µm^{-1} and $\Delta W \approx -2.1$ µm, including many of the smaller fringes around the resonant dips. From these fits, we obtain $\Gamma_{\text{ext}} \approx 7.1 \times 10^{12}$ s^{-1} and $\Gamma_{\text{int}} \approx 6.5 \times 10^{12}$ s^{-1}, corresponding to a propagation length $L_p \approx 8.8$ µm. Via Eq. (5.11), we then retrieve the experimental $Q(L)$ curve with $Q \to 107$ as $L \gg L_p$ (Fig. 5.8e). Although the extracted radiative rate agrees closely with the modeled value $\Gamma_{\text{ext}}^{\text{sim}} = 7.4 \times 10^{12}$ s^{-1}, the nonradiative rate exceeds the modeled $\Gamma_{\text{int}}^{\text{sim}} = 3.9 \times 10^{12}$ s^{-1}

by almost a factor of two, which we attribute to additional dissipation due to surface roughness, polymer residues and other forms of spatial inhomogeneity. As a result, the experimental L_p and Q are smaller than the modeled values. To nevertheless assess the model discrepancy, we re-fit Q independently at each x_0 (data points in Fig. 5.8e) and use this to define an uncertainty range on Q (shaded region). These pointwise fits reproduce the same overall trend, further supporting the validity of our model.

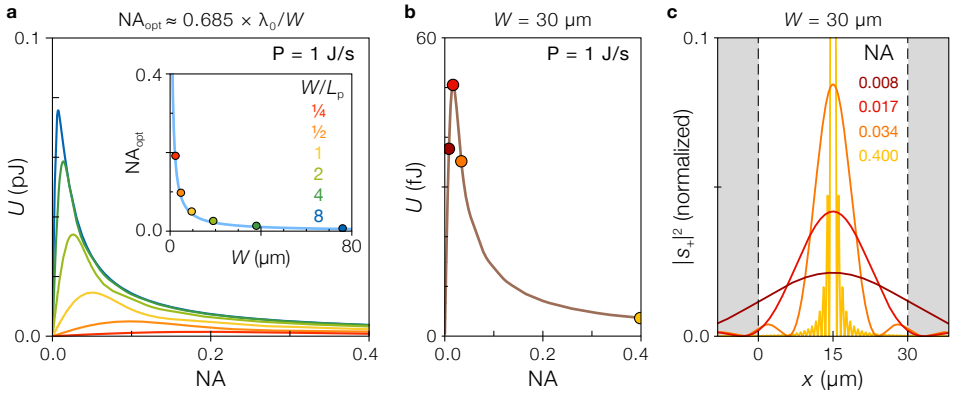

Figure 5.9: Maximizing stored energy by matching illumination width to the grating. (a) Stored energy (U) as a function of incident NA, calculated for varying grating widths W/L_p (color) under sinc excitation in the center ($L = W/2$) with constant total incident power $P = 1$ W. Inset: the optimal NA extracted at each width (colored datapoints) is well approximated by $\mathrm{NA}_{\mathrm{opt}} \approx 0.685\,\lambda_0/W$ (light blue curve). **(b)** Stored energy versus NA (brown curve) for the $W = 30$ μm grating discussed in the main text, with four highlighted datapoints corresponding to **(c)** the normalized incident intensity profiles $|s_+(x)|^2$ for the same four NA values. The grating boundaries are indicated (dashed lines); incident field outside the grating (gray shaded region) does not contribute to resonant energy build-up.

5.5 DESIGN PRINCIPLES

Although this work focused on a specific guided-mode resonant metasurface with a moderate Q-factor to demonstrate the impact of finite size, we stress that our observations apply more broadly. In principle, any propagating nonlocal mode that can be described by a locally linear dispersion will feature a Q-factor approaching the semi-infinite limit as $1 - e^{-2L/L_p}$. Concretely, our design advice for reaching the long-grating regime, in which finite-size effects can mostly be neglected, is to fabricate a metasurface with a physical width of 5× the modal propagation length. This ensures that a mode excited in the center of the structure ($L/L_p = 2.5$), decays to about 8% of its original amplitude and the lifetime-based Q-factor reaches 99.3% of the theoretical value. Of course, it may be interesting to operate in the limit of a size-constrained grating. Remarkably, in this regime the quality factor is primarily

governed by the mode's transit time to the edge (Appendix A.5.6). This implies that, for strongly footprint-constrained devices, high-Q requires increasing the interaction time within the fixed footprint by engineering flat bands, *i.e.* slow light.[362,384]

Another aspect that we have not examined so far is the impact of the NA (spot size) of the driving field, which relates to the experimental design rather than the sample size. In general, for an infinite grating, it is favorable to minimize the angular bandwidth such that all the incident power is concentrated at $k_{x,\mathrm{res}}$. This can be particularly important for applications requiring the highest possible light-matter interactions such as nonlinear optics.

In the following, we consider a finite-NA sinc-beam to explore how the stored energy U in the resonator is maximized by matching the spot size to the grating width (details in Appendix A.5.6). Keeping the total incident power fixed at an arbitrary value of $P_{\mathrm{inc}} = 1\ W$, we vary the NA to control the diffraction-limited spot size. We then evaluate

$$U \equiv \int_0^W |a(x)|^2 \,\mathrm{d}x, \tag{5.12}$$

by plugging the solution of the mode amplitude, Eq. (5.9) for various normalized widths W/L_p (Fig. 5.9a), observing a pronounced maximum that is captured well by the simple coherent aperture-overlap,

$$\int w(x) s_+(x) \,\mathrm{d}x, \tag{5.13}$$

Note that U does not vary monotonically with NA, but rather features a maximum at some optimal NA value. For a sinc beam centered on the grating ($L = W/2$), we find the optimum to be NAopt $\approx 0.685\lambda_0/W$. While the numerical prefactor depends on the specific excitation conditions assumed here, the overall scaling $\mathrm{NA}_{\mathrm{opt}} \propto \lambda_0/W$ holds generally.

To explore the origin of this maximum, let us again consider the 30-µm-wide metasurface discussed throughout this work (Fig. 5.9b). We choose four representative numerical apertures to show that for a finite grating, as NA $\to$ 0 the illumination profile $s_+(x)$ starts to extend well beyond the grating window $[0, W]$, and an increasing fraction of the incident power cannot excite the resonant mode (Fig. 5.9c). On the other hand, if the NA increases, an increasing fraction of the incident power is at wavenumbers outside of the resonant wavenumber, increasing reflection and reducing power coupled into the resonance. As a result, U is maximized when the spot size is matched to the grating width, or vice versa, reflecting the trade-off between matching the real-space footprint and matching the resonance in momentum-space.

In sum, we have formalized the relations between the modal propagation length,

physical metasurface footprint, excitation spot size, and critical performance metrics of nonlocal metasurfaces, which is especially relevant amid the recent push toward ultrahigh Q-factors. Our work provides practicable design guidelines that can be leveraged to reach the theoretical linewidth and maximize the light-matter interaction: i) to achieve a Q-factor close to that of the infinite array, the metasurface needs to be over five propagation lengths long, and ii) to maximize the stored energy in the resonator, the array size must be matched to the central lobe of the incident beam.

5.6 Conclusion and discussion

In this chapter, we presented the effects of finite lateral extent on the optical properties of leaky-wave metasurfaces. In particular, we leveraged the STCMT framework to derive approximate analytic expressions for the spectro-spatial scattering response of a truncated guided-mode resonator. This reveals that, when the interaction length is on the order of, or shorter than the guided wave's propagation length, the scattered field shows strong interference fringes that can exceed unity reflectance due to a redistribution of spectral weight in momentum space, as well as a reduction of the effective lifetime and therefore the energy stored in the resonator. To test the model's predictions, we employed the guided-mode resonant metasurface fabricated in Chapter 3 to measure position- and momentum-resolved reflectance spectra. These measurements accurately reproduce the predicted finite-size effects and thereby validate our model. In general, the framework presented here offers a straightforward method to predict the impact of finite sizes on many relevant physical parameters—including the stored energy and quality factor—given only the theoretical dispersion of the guided wave. This further establishes STCMT as a valuable technique to both qualitatively and quantitatively capture the scattering response of real-world nonlocal meta-optical elements.

The broad applicability of STCMT leaves many promising directions for further inquiry. For instance, future work could investigate the use of in-plane reflectors to increase the effective interaction length by trapping light within a finite scattering aperture[374,375]. Other directions include metasurfaces exhibiting a quadratic dispersion arising from quasi-bound states in the continuum or strongly coupled counter-propagating leaky waves, as well as two-port systems to model transmission-based meta-optics[96,346,362,379]. Altogether, the framework presented here provides fundamental insight into how finite size reshapes the resonant response of these emerging photonic systems and establishes concrete design guidelines to mitigate these effects.

5.7 ADDITIONAL FIGURES

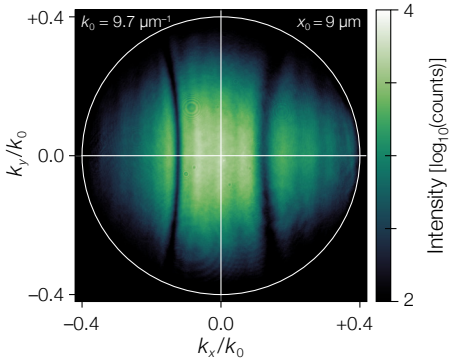

Figure 5.A1: Back-focal plane reflection. Image of the Fourier plane (logarithmic intensity scale, unnormalized) recorded at free-space wavevector $k_0 = 9.7\ \mu m^{-1}$ and position $x_0 = 9\ \mu m$ on the fabricated metasurface.

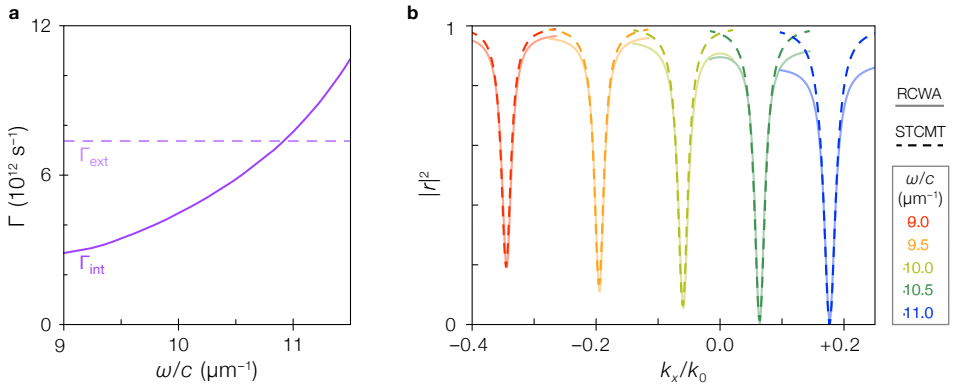

Figure 5.A2: Comparison of STCMT and RCWA simulations. **(a)** Loss rates used in STCMT: the eigenmode-solver decay rate is taken as the internal (nonradiative) loss rate Γ_{int} (purple, solid), while the external (radiative) loss rate Γ_{ext} is treated as approximately constant over the relevant frequency band and extracted by fitting to full-wave RCWA simulations (pink, dashed; $\Gamma_{\text{ext}} = 7.4 \times 10^{12}\,\text{s}^{-1}$). **(b)** Momentum-resolved reflectance $|r(k_x)|^2$ from full-wave RCWA at selected frequencies (solid), overlaid with the corresponding STCMT prediction (dashed) evaluated in the long-grating limit. Colors indicate the frequencies ω/c as labeled.

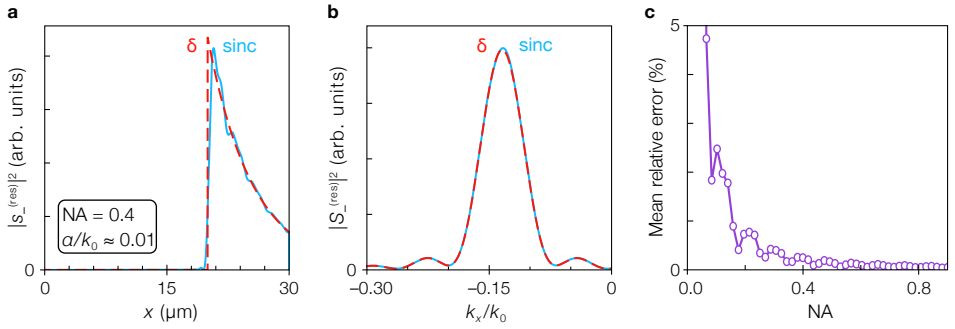

Figure 5.A3: Evaluating the point-source approximation. Comparison of the NA = 0.4 sinc excitation (blue, solid) and the closed-form expressions of the infinite-NA δ-function excitation (red, dashed). **(a)** Resonant scattered field in real space, and **(b)** in momentum space evaluated at $k_0 = 9.7\ \mu\text{m}^{-1}$ and $L = 10\ \mu\text{m}$, where $\alpha/k_0 \approx 0.01$ **(c)** The mean relative error between $R(k_x)$ calculated using the sinc and δ-function excitations, as function of NA, shows that the error diverges as $\text{NA} \to \alpha/k_0$.

6

Outlook

Excitonic 2D semiconductors provide the key asset that conventional passive metasurfaces lack: a strong, electrically tunable resonance. At this point, the central obstacle to technological feasibility is no longer whether 2D excitons can be harnessed to modulate light efficiently and rapidly, as demonstrated by femtojoule switching energies and gigahertz-rate operation in simulations and cryogenic experiments,[145,328] and now also by ~ 50 % reflection modulation at room temperature (Chapter 3).[337] Rather, the primary obstacle lies in the reproducible manufacturing of van der Waals materials and their heterostructures at useful scales. For TMDCs, a realistic near-term path will likely rely on top-down manufacturing methods, including improved high-throughput exfoliation,[284] macroscopic gold-assisted exfoliation,[285,286] robotic heterostructure assembly,[385] and cleaner transfer protocols,[300] and may become commercially relevant in specialized, lower-throughput applications (*e.g.*, scientific and medical equipment), where performance per device matters more than overall cost. Nevertheless, for large-scale integration and broad deployment, the long-term goal remains bottom-up methods such as wafer-scale vapor-phase growth, by virtue of their higher throughput and compatibility with existing semiconductor processing pipelines.[287,288]

For hybrid-2D metasurfaces, the scalability of hBN is another point of debate. As an encapsulating layer, it crucially protects 2D semiconductors against contamination, degradation, and disorder, thereby preserving pristine excitonic quality. At the same time, hBN can be nanopatterned to realize high-Q resonances across the visible spectrum and into the near-infrared,[386] while also featuring a high breakdown strength that makes it especially valuable in electrically tunable devices.[238,336] Nevertheless, the use of hBN in photonic metasurfaces and van der Waals heterostructures remains closely tied to mechanically exfoliated flakes,[386] whereas growth methods for high-quality, optically uniform films with accurate thickness control, as well as scalable heterostructure fabrication workflows, remain underdeveloped.[287,387,388]

Electrical interfacing is a crucial factor that will likely determine whether active

metasurfaces leveraging van der Waals materials remain a laboratory curiosity or become a practical technology. This calls for thorough research into materials and methods that can achieve low-resistance Ohmic contacts, overcome high sheet resistances, and mitigate dielectric disorder.[276,279,280,389,390] A second challenge is the routing architecture across many active metasurface "pixels" that emerges when devices are scaled from proof-of-concept demonstrations, such as our three-level programmable beam steerer (Chapter 4), to large-scale, high-pixel-density electro-optic technologies.[110,214] The femtojoule and nanosecond electrical switching scales already demonstrated with 2D semiconductors are encouraging proofs of feasibility,[145,328] but future work should continue pushing in this direction.

In parallel, the strong light–matter interactions enabled by nonlocal resonances open up exciting opportunities. For instance, strongly coupled exciton–polaritons can preserve partial coherence over tens of micrometers, even in systems where dielectric disorder limits excitonic transport,[248,391] and can be switched between the strong and weak coupling regimes at ultrafast speeds.[392] At the same time, harnessing nonlocal resonances in ultracompact devices comes with practical challenges. Compared to plasmonic or Mie-type nano-resonators, nonlocal modes exhibit inherently lower spatial resolution. However, it has been pointed out that diffractive nonlocal metasurfaces—in which nonlocal modes are combined with local resonances or perturbations—can mitigate this resolution loss.[346,354,355] Moreover, as we have seen in Chapter 5, confining nonlocal modes in tiny structures leads to finite-size broadening, which becomes especially punishing at high Q-factors. Fortunately, several mitigation strategies have already emerged, including in-plane photonic mirrors,[374,375] topologically miniaturized modes,[352,353] and slow-light dispersion,[362,384] and research in this direction will only accelerate as spatiotemporal coupled-mode theory evolves into a mainstream predictive modeling tool.

Fundamental questions remain at the interface of electrical tuning and strong light–matter interactions. While it is known that doping can modify the excitonic oscillator strength through phase-space filling, screening, and other many-body effects,[241,265,266] it remains unclear how these changes translate to the exciton–photon coupling strength in realistic devices. Intuitively, doping should attenuate the interaction because the coupling strength scales with the exciton dipole moment (*i.e.* the oscillator strength), yet this dependence has not been mapped systematically across gate bias and temperature. Because the achievable modulation depth with an excitonic metasurface can depend sensitively on the Rabi splitting, photonic design should also account for the lifetime mismatch between the exciton and photonic resonance[248,393] (Appendix A.1.4) as well as exciton decoherence (pure dephasing).[131,262] In this sense, maximizing the Q-factor in isolation is rarely optimal. Instead, the goal is to balance field enhancement, disorder tolerance, finite-size robustness, and

electrical control simultaneously. This makes designing hybrid-2D devices a dynamic co-optimization problem, for which computational methods such as inverse design and machine learning are likely to play an enabling role.[344,394]

Altogether, ELECTRICALLY TUNABLE HYBRID-2D METASURFACES could find use in optoelectronic technologies requiring active control over visible light. While many emerging application areas have been identified—including analog optical computing, light detection and ranging, free-space optical communications, quantum photonics, and augmented-reality lenses—there is still a lack of a truly compelling "killer" application that creates real market pull.[214] For technological integration, the largest obstacle for excitonic 2D semiconductors has been low optical efficiency at room temperature, driven by excessive nonradiative loss and limited light–matter interaction, but it is now clear that these constraints can be mitigated through nanophotonic designs. The primary challenges are now on the fronts of electrical engineering—to reliably achieve high modulation speeds at low switching energies—and bottom-up, industrially compatible manufacturing routines. Addressing them will require tight integration of materials growth and transfer, nanofabrication, contact and device engineering, and computational modeling approaches. If these pieces mature in parallel, hybrid-2D metasurfaces are poised to move beyond lab-scale prototypes toward scalable technologies.

Appendix

A.1 Temporal coupled-mode theory

Many optical systems can be described as a small set of interacting resonant degrees of freedom that exchange energy among themselves and with free-space radiation. A convenient and widely used approach to do this is temporal coupled-mode theory (TCMT),[342,371,372] in which the internal dynamics of a resonant system are represented by a vector of complex amplitudes,

$$\mathbf{a} = \begin{pmatrix} a_1 \\ a_2 \\ \vdots \\ a_N \end{pmatrix}, \tag{A.1}$$

in which each amplitude a_j represents an oscillator such as an exciton or a photonic mode.

The metasurfaces treated in this thesis typically exhibit only a single scattering port that facilitates the interaction between the internal modes and the external radiation continuum, *i.e.*, the zeroth order reflection channel. The dynamical equations for such a one-port system can be written as

$$\dot{\mathbf{a}}(t) = -i\,\mathbf{H}_{\text{eff}}\,\mathbf{a}(t) + \mathbf{K}\,s_{\text{in}}(t), \tag{A.2}$$

where $\mathbf{K}$ is the coupling vector from the input wave into the internal resonances, $s_{\text{in}}(t)$ denotes the complex amplitude of the incoming wave in the external port, and $\mathbf{H}_{\text{eff}}$ is an effective non-Hermitian Hamiltonian,

$$\mathbf{H}_{\text{eff}} = \boldsymbol{\Omega} - i\boldsymbol{\Gamma}. \tag{A.3}$$

Here, $\boldsymbol{\Omega}$ is a Hermitian matrix containing the resonance frequencies on the diagonal and coherent coupling rates off-diagonally. The matrix $\boldsymbol{\Gamma}$ contains the internal (non-radiative/absorptive) and external (radiative) decay processes; in the simplest case it is diagonal, but cross-terms can be included when needed.[147] In the sign convention

used here, passivity corresponds to $\mathbf{\Gamma} \succeq 0$ such that the undriven amplitudes decay in time. Throughout, we adopt the standard time-harmonic convention for steady-state solutions,

$$\mathbf{a}(t) = \mathbf{a}(\omega)e^{-i\omega t}, \qquad s_{\text{in}}(t) = s_{\text{in}}(\omega)e^{-i\omega t}. \tag{A.4}$$

A.1.1 Eigenmodes

The hybrid modes intrinsic to the coupled system are obtained in the absence of a driving field, *i.e.* by setting $s_{\text{in}}(t) = 0$ in Eq. (A.2). For a mode with complex eigenfrequency $\tilde{\omega} = \omega - i\Gamma$, we seek time-harmonic solutions of the form

$$\mathbf{a}(t) = \mathbf{v}\, e^{-i\tilde{\omega}t}. \tag{A.5}$$

Substituting this ansatz into Eq. (A.2) yields the eigenproblem

$$\mathbf{H}_{\text{eff}}\mathbf{v} = \tilde{\omega}\,\mathbf{v}, \tag{A.6}$$

such that each hybrid mode is characterized by $\tilde{\omega}_m$, while the eigenvectors $\mathbf{v}_m$ quantify the composition of each hybrid mode in the original basis of uncoupled resonances.

A.1.2 One-port scattering

In the frequency domain, inserting Eq. (A.4) into Eq. (A.2) gives

$$(-i\omega\mathbf{I} + i\mathbf{H}_{\text{eff}})\mathbf{a}(\omega) = \mathbf{K}\, s_{\text{in}}(\omega), \tag{A.7}$$

which can be rewritten as

$$(\omega\mathbf{I} - \mathbf{H}_{\text{eff}})\mathbf{a}(\omega) = i\,\mathbf{K}\, s_{\text{in}}(\omega). \tag{A.8}$$

Solving for the modal amplitudes therefore requires matrix inversion of the operator $(\omega\mathbf{I} - \mathbf{H}_{\text{eff}})$,

$$\mathbf{a}(\omega) = i\,(\omega\mathbf{I} - \mathbf{H}_{\text{eff}})^{-1}\mathbf{K}\, s_{\text{in}}(\omega), \tag{A.9}$$

The input–output relation for the one-port system reads

$$s_{\text{out}}(\omega) = C\, s_{\text{in}}(\omega) + \mathbf{D}^{\dagger}\mathbf{a}(\omega), \tag{A.10}$$

where C describes the direct (non-resonant) background pathway and $\mathbf{D}^{\dagger}$ is the conjugate transpose of the out-coupling vector describing radiation from internal modes into the external port. Substituting Eq. (A.9) into Eq. (A.10) yields the reflection

coefficient

$$r(\omega) \equiv \frac{s_{\text{out}}(\omega)}{s_{\text{in}}(\omega)} = C + i\,\mathbf{D}^{\dagger}(\omega\mathbf{I} - \mathbf{H}_{\text{eff}})^{-1}\mathbf{K}. \tag{A.11}$$

This expression describes the resonant scattering process and includes coherent mode coupling, energy dissipation, and interference with a background channel. In physically constrained models, the quantities $\boldsymbol{\Gamma}$, $\mathbf{K}$, and $\mathbf{D}$ are not independent, but constrained by time-reversal symmetry, reciprocity, and energy conservation.

A.1.3 Physical constraints

For a passive, reciprocal (time-reversal invariant) one-port resonator, energy conservation and time-reversal symmetry impose fixed relations between the radiative decay rate and the coupling constants.[342] In the general multi-mode formulation, this condition is expressed as

$$\mathbf{D}^{\dagger}\mathbf{D} = 2\Gamma_{\text{r}}, \tag{A.12}$$

where Γ_{r} is the total radiative decay rate into the external port. Time-reversal invariance further relates the in-coupling and out-coupling amplitudes,

$$\mathbf{K} = \mathbf{D}, \tag{A.13}$$

i.e., the same coefficient governs excitation of the resonance from the port and radiation back into the port. Finally, time-reversal symmetry constrains the phase of the direct (non-resonant) pathway relative to the resonant channel as

$$C\,\mathbf{D}^{*} = -\mathbf{D}. \tag{A.14}$$

Together, these relations ensure that the scattering matrix remains unitary in the absence of internal loss.

A.1.4 Rabi splitting

In this section, we demonstrate how the strong coupling condition can be evaluated by computing the complex eigenfrequencies using Eq. (A.6).[321,322,395] In the following, we consider a simple system with two coupled modes—a photonic resonance (G) and an exciton resonance (A)—for which the effective non-Hermitian Hamiltonian of Eq. (A.3) becomes

$$\mathbf{H}_{\text{eff}} = \begin{pmatrix} \tilde{\omega}_{\text{G}} & g \\ g & \tilde{\omega}_{\text{A}} \end{pmatrix}, \tag{A.15}$$

where g is the coherent coupling rate. The hybrid eigenfrequencies follow from Eq. (A.6) by solving the characteristic equation

$$\det(\mathbf{H}_{\text{eff}} - \tilde{\omega}\mathbf{I}) = 0, \tag{A.16}$$

$$(\tilde{\omega}_{\text{G}} - \tilde{\omega})(\tilde{\omega}_{\text{A}} - \tilde{\omega}) - g^2 = 0, \tag{A.17}$$

which yields

$$\tilde{\omega}_{\pm} = \frac{\tilde{\omega}_{\text{G}} + \tilde{\omega}_{\text{A}}}{2} \pm \sqrt{g^2 + \left(\frac{\tilde{\omega}_{\text{G}} - \tilde{\omega}_{\text{A}}}{2}\right)^2}. \tag{A.18}$$

The complex Rabi (mode) splitting is then $\Omega_{\text{R}} \equiv \tilde{\omega}_{+} - \tilde{\omega}_{-}$, whose real part corresponds to the observable frequency splitting. When the uncoupled resonances are exactly degenerate in frequency ($\omega_{\text{G}} = \omega_{\text{A}}$, and thus $\tilde{\omega}_{\text{G}} - \tilde{\omega}_{\text{A}} = -i(\Gamma_{\text{G}} - \Gamma_{\text{A}})$), the splitting reduces to

$$\Omega_{\text{R}} = \sqrt{4g^2 - (\Gamma_{\text{G}} - \Gamma_{\text{A}})^2}, \tag{A.19}$$

which highlights that, all else being equal, the Rabi splitting is maximized when the decay rates of the uncoupled modes are matched.

Although multiple definitions of strong coupling exist in the literature, in this thesis we use the criterion[393]

$$\Omega_{\text{R}} > \Gamma_{\text{G}} + \Gamma_{\text{A}}, \tag{A.20}$$

i.e. the system is strongly coupled if coherent energy exchange between the modes occurs faster than dissipation of the uncoupled resonances.

A.2 ANALYSIS OF THE OPTICAL COUPLING WITH TRIONS

To investigate the impact of optical coupling between trions (charged excitons) and guided photons on the exciton-photon coupling strength and the reflectivity of the hybrid-2D metasurface of Chapter 3, we additionally model the system using temporal coupled mode theory (TCMT).[342,371] The model includes three oscillators representing the guided-mode, A-exciton and trion resonances (denoted with subscripts 'G', 'A', and 'T', respectively). Since this is a one-port system and the coupling from free-space directly to excitons and trions is negligible due to destructive interference of free-space radiation at the monolayer position (Fig. 3.5a), the coupled equations are written as

$$\frac{\mathrm{d}}{\mathrm{d}t}\begin{pmatrix} a_\mathrm{G} \\ a_\mathrm{A} \\ a_\mathrm{T} \end{pmatrix} = -i\begin{pmatrix} \Delta_\mathrm{G} - i\Gamma_\mathrm{G} & g_\mathrm{A} & g_\mathrm{T} \\ g_\mathrm{A} & \Delta_\mathrm{A} - i\Gamma_\mathrm{A} & 0 \\ g_\mathrm{T} & 0 & \Delta_\mathrm{T} - i\Gamma_\mathrm{T} \end{pmatrix}\begin{pmatrix} a_\mathrm{G} \\ a_\mathrm{A} \\ a_\mathrm{T} \end{pmatrix} + \begin{pmatrix} \sqrt{2\Gamma_{\mathrm{G,r}}} \\ 0 \\ 0 \end{pmatrix} s_\mathrm{in}. \tag{A.21}$$

Here, a, $\Delta_\mathrm{j} = E_\mathrm{j} - E$, Γ, and g denote the mode amplitude, energy detuning, damping rate, and coherent coupling strength, respectively, and s_in is the free-space input field.

The reflected signal follows from the one-port input–output relation,

$$s_\mathrm{out} = C\, s_\mathrm{in} + \sqrt{2\Gamma_\mathrm{c,r}}\, a_\mathrm{G}\,, \tag{A.22}$$

such that the reflection coefficient becomes

$$r = C + \frac{\sqrt{2\Gamma_\mathrm{c,r}}\, a_\mathrm{G}}{s_\mathrm{in}} \tag{A.23}$$

which yields:

$$r = C + \frac{2\Gamma_\mathrm{c,r}}{-i\Delta_\mathrm{G} + \Gamma_\mathrm{G} + \frac{g_\mathrm{A}^2}{-i\Delta_\mathrm{A}+\Gamma_\mathrm{A}} + \frac{g_\mathrm{T}^2}{-i\Delta_\mathrm{T}+\Gamma_\mathrm{T}}}. \tag{A.24}$$

To account for a slowly varying Fabry–Pérot interference component, we introduce an approximate background reflection $C \simeq r_\mathrm{bg}$ where $r_\mathrm{bg} \approx 1$ over the relevant spectral range.

To analyze the impact of trions on r and g_A, we first fit the model in absence of trions (*i.e.*, the two-oscillator TCMT model) by setting the trion-photon coupling strength, $g_\mathrm{T} = 0$ meV. Plugging all the extracted values from our RCWA fits (described in the manuscript, see also Fig. 3.A7a, b) into the model leaves only g_A and $\Gamma_\mathrm{c,r}$ as free parameters. Using a least-squares fitting routine, we fit the optical response at all voltages (–25 to +25 V in 5 V steps) and find $g_\mathrm{A} = 21.01$ meV and $\Gamma_\mathrm{c,r} = 7.45$ meV (Fig. A.1). Here, we note that this value is considerably higher than the one extracted in Chapter 3, reflecting the fundamental differences between TCMT, which captures

the full scattering response including interference effects, and the coupled-oscillator model, which extracts the complex eigenenergies of the hybrid modes. While the latter is, strictly speaking, most accurate for closed systems with fully guided modes, it is nevertheless commonly employed in the literature to report polariton properties.

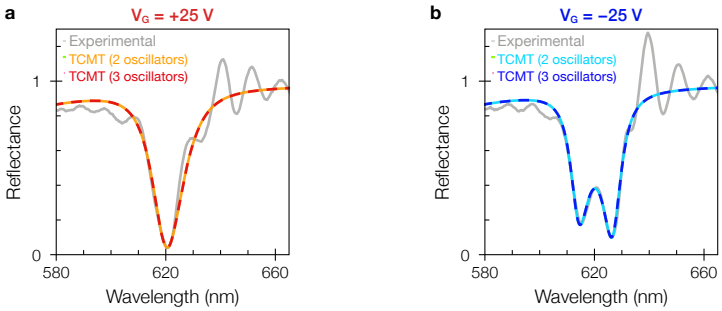

Figure A.1: Comparison of two- and three-oscillator coupled mode theory models. (a) Fits of the experimental normal-incidence reflectance (grey solid line) for an n-doped (+25 V) monolayer using two-oscillator coupled mode theory (TCMT, orange solid line) and three-oscillator TCMT (red dashed line). **(b)** Similarly, two-oscillator TCMT (light blue solid line) and three-oscillator TCMT (dark blue dashed line) fits for a neutral (−25 V) monolayer. These fits are used to confirm that the two-oscillator TCMT model with only the guided-mode and excitonic resonances is justified, and the contribution from a third trionic oscillator to the reflectance is negligible (mean relative difference of 0.1%).

Next, we reintroduce the trion resonance with a characteristic energy E_T = 1.9630 eV and a total decay rate of Γ_T = 23.6 meV obtained from the photoluminescence data (Fig. 3.A3). To evaluate the impact of trions coupling to the guided photons, we need to estimate the coupling strength g_T, which is proportional to the transition dipole moment μ_T and the local electric field strength $\mathscr{E}$ at the trion energy E_T. Since the transition dipole moment is proportional to the square root of the oscillator strength $\mu_T \propto \sqrt{f_T}$, we can write $g_T \propto \sqrt{f_T}\mathscr{E}(E_T)$ and similarly for the exciton resonance: $g_A \propto \sqrt{f_A}\mathscr{E}(E_A)$. We may use this to estimate the trion-photon coupling strength:

$$\frac{g_T}{g_A} \propto \sqrt{\frac{f_T}{f_A}}\frac{\mathscr{E}(E_T)}{\mathscr{E}(E_A)}, \tag{A.25}$$

$$g_T \approx g_A\sqrt{\frac{f_T}{f_A}}\frac{\mathscr{E}(E_T)}{\mathscr{E}(E_A)}. \tag{A.26}$$

Lien *et al.*[241] show that in WS_2 the trion's oscillator strength is 16× smaller than the neutral exciton, such that $\sqrt{f_T/f_A} = 1/4$. Furthermore, we know, from *e.g.* Novotny & Hecht[1], that the energy-dependent local electric field strength of the guided mode

resonance can be expressed using a Lorentzian as:

$$|\mathscr{E}(E)| \propto \sqrt{\frac{\Gamma_G^2}{\Delta_G^2 + \Gamma_G^2}}. \tag{A.27}$$

Putting it all together, we evaluate the voltage-averaged ratio $\mathscr{E}(E_T)/\mathscr{E}(E_A) = 0.351$ and $g_T = 1/4 \times 0.351 \times 21.01 = 1.84$ meV. Clearly, the optical coupling between guided photons and trions is an order of magnitude weaker than with excitons, due to the smaller oscillator strength and decreased spectral overlap with the guided mode resonance.

Finally, to quantify the impact on the metasurface reflectivity and g_A, we now fit the reflectance spectra with the three-oscillator TCMT model by setting $g_T = 1.84$ meV and leaving g_A as free fitting parameter (Fig. A.1). From this, we extract $g_A = 20.93$ meV, corresponding to a relative change in exciton-photon coupling strength of 0.2% compared to the two-oscillator model. At the same time, the mean relative difference in the reflectance across the spectral range of interest and all voltages is only 0.1%. Hence, in this scenario, the use of a two-oscillator TCMT model with just the excitonic and photonic modes is clearly justified. We emphasize that this is largely due to the fact that excitons and trions are predominantly excited by guided photons instead of being directly excited from free-space. As such, it is not necessary to include the trion as a third oscillator in the TCMT analysis, except if the trion oscillator strength would be much stronger and/or the spectral overlap with the guided mode resonance much larger.

A.3 Inverse design of hybrid-2D metasurfaces

Throughout Chapter 4, optimization of the metasurface designs is achieved using an inverse design framework implemented in custom Python scripts. In this section, we describe the basic procedure used to create metasurfaces for π-phase modulation, complex amplitude modulation and programmable beam steering. Generally, the target optical response is encoded in an objective function, *i.e.*, the figure-of-merit (FOM), and the optimization seeks the set of parameters that minimizes the FOM. This requires computationally efficient algorithms to navigate high-dimensional parameter spaces and accommodate multiple objectives. Broadly, optimization strategies fall into two categories: gradient-based and gradient-free.[396] Because the S^4 implementation of RCWA does not provide direct access to analytical gradients, we employ derivative-free techniques in this study.

Gradient-free optimization is well suited for electromagnetic design with a modest number of parameters. Although the absence of gradients typically slows convergence relative to gradient-based methods, these approaches are less sensitive to initialization. Here, we combine two complementary schemes: Bayesian optimization[i] for sample-efficient global exploration, followed by covariance matrix adaptation evolution strategy[ii] (CMA-ES) for local refinement. Bayesian optimization constructs a Gaussian-process surrogate of the objective and focuses expensive evaluations on promising regions of parameter space. This is particularly beneficial for 2D periodic RCWA simulations where convergence requires many Fourier orders N and the simulation time scales as N^3. Once a promising region in parameter space is identified, CMA-ES is employed to refine the solution. CMA-ES is a stochastic, population-based evolutionary algorithm that iteratively adapts a Gaussian distribution over design candidates, requiring minimal manual hyper-parameter tuning which makes it straightforward to deploy.

A.3.1 π-phase modulation

For the π-phase modulation metasurface with one monolayer, two complex reflection coefficients, r_i and r_n, are calculated at intrinsic and strong n-type doping, respectively. The optimization minimizes both the deviation from a perfect π-phase shift and amplitude variation, while maximizing the mean amplitude:

$$\mathrm{FOM} = w_1 \frac{|\Delta\phi - \pi|}{\pi} + w_2 \, ||r_\mathrm{i}| - |r_\mathrm{n}|| - w_3 \frac{|r_\mathrm{i}| + |r_\mathrm{n}|}{2} \,, \tag{A.28}$$

$$\Delta\phi = |\arg(r_\mathrm{i}) - \arg(r_\mathrm{n})| \,. \tag{A.29}$$

[i] *scikit-optimize*
[ii] *pycma*

Here, $w_1 = 9$, $w_2 = 3$, and $w_3 = 1$ are the weights given to each sub-objective. For the RCWA optimization, the free parameters are the grating period Λ, grating element width w, grating height h, hBN thickness d, operating wavelength λ and carrier density in the n-doped state n_e. On the other hand, for the TCMT analysis, the free parameters are the operating energy E, GMR energy E_G, and coupling strength g.

A.3.2 Complex amplitude modulation

Next, for the complex-amplitude modulation metasurface with two monolayers, the complex reflection coefficient is sampled over the 2D carrier density space $(n_\mathrm{t}, n_\mathrm{b})$ in the top and bottom monolayers:

$$r_{ij} \equiv r\left(n_\mathrm{t}^i, n_\mathrm{b}^j\right). \tag{A.30}$$

The FOM aims to reward uniform phase coverage and maximize the amplitude over all phases. To quantify phase coverage in the complex plane, we partition the interval $[-\pi, \pi]$ into M uniform angular bins ϕ_m with:

$$\phi_m = -\pi + m\Delta\phi\ , \tag{A.31}$$

$$\Delta\phi = \frac{2\pi}{M}. \tag{A.32}$$

For each bin, we define a set $\mathcal{K}_m$ containing all grid points $\phi_{ij} = \arg(r_{ij})$ whose phase lies in that bin and whose amplitude exceeds a fixed threshold $|r|_{\min}$:

$$\mathcal{K}_m = \left\{(i,j)\middle|\ \phi_{m-1} < \phi_{ij} < \phi_m,\ |r_{ij}| \geq |r|_{\min}\right\}. \tag{A.33}$$

We then define the maximum achievable amplitude in bin m as:

$$A_m = \begin{cases} \max\limits_{(i,j)\in\mathcal{K}_m} |r_{ij}|, & \text{if } \mathcal{K}_m \neq \emptyset, \\ 0, & \text{if } \mathcal{K}_m = \emptyset. \end{cases} \tag{A.34}$$

Finally, a scalar metric is extracted to describe the phase coverage:

$$C = \frac{1}{M}\sum_{m=1}^{M} \Theta(A_m), \tag{A.35}$$

where Θ is the Heaviside step function (a bin is "covered" if $A_m > 0$).

In addition, we maximize the minimum achievable amplitude across all phases:

$$A_{\min}^* = \min_{1\leq m\leq M} A_m\ . \tag{A.36}$$

Crucially, this definition of A^*_{min} ensures full phase coverage before optimizing the amplitude, because if at least one bin remains unpopulated, $A^*_{\text{min}} = 0$. In other words, this definition treats the lowest achievable amplitude across the full 0–2π phase range as the limiting factor. This ensures that the metasurface maintains a usable reflection amplitude for all phases, which is a prerequisite for complex amplitude modulation.

With these definitions, we calculate the FOM as:

$$\text{FOM} = -w_1 C - w_2 A^*_{\text{min}} , \tag{A.37}$$

where we choose weights $w_1 = w_2 = 1$. In the RCWA simulations, we optimize this FOM for the following free parameters: grating period Λ, grating element width w, grating height h, top hBN thickness d_{T}, bottom hBN thickness d_{b}, and operating wavelength λ. In the TCMT analysis, the free parameters are the operating energy E, GMR energy E_{G}, and coupling strengths with excitons in the top and bottom monolayer g_t and g_b, respectively.

A.3.3 Beam steering

Lastly, we leverage the complex amplitude modulator to demonstrate a three-level programmable beam steering metasurface. Here, we denote with R_k the reflected power (normalized to incident power) in diffraction order k, and R_{tot} is the total reflected power. For beam-steering design 'Configuration A', we target the –1 diffraction order, and define the diffraction efficiency as:

$$\eta_{-1} = \frac{R_{-1}}{R_{\text{tot}}} . \tag{A.38}$$

The objective function is given by:

$$\text{FOM} = -w_1 \eta_{-1} - w_2 R_{-1} , \tag{A.39}$$

with weights $w_1 = 1$ and $w_2 = 3$. This favors both a high fraction of power into the steered order as well as a large absolute value of that power, preventing the optimizer from converging to trivial solutions with high relative efficiency but negligible absolute power. In our RCWA simulations, the grating element width w is the only geometric parameter that is re-optimized. We further optimize the operating wavelength λ, and a pair of $(n_{\text{t}}, n_{\text{b}})$ for each of the three unit cells within the supercell.

A.4 FUNDAMENTAL LIMITS OF PHASE MODULATION

In this section, we employ a TCMT analysis to study the fundamental limits of π-phase and complex-amplitude modulation with hybrid-2D metasurfaces (as described in Chapter 4). To achieve this, we first obtain the loss rates of the GMR (denoted by subscript 'G') by performing RCWA simulations of the metasurfaces without excitons. Since the metasurfaces can only be addressed from the top side, we describe this system with a one-port one-oscillator TCMT model. The temporal evolution of the mode amplitude, a_G, driven by the incident field s_{in}, is given by:

$$\frac{da_G}{dt} = -i\left(\Delta_G - i\Gamma_G\right)a_G + \sqrt{2\Gamma_{G,r}}s_{in}, \tag{A.40}$$

where $\Delta_G = E_G - E$ is the detuning between photon energy E and resonance energy E_G, and $\Gamma_G = \gamma_G/2$ is the damping rate. The corresponding input-output relation for a one-port resonator is given by:

$$s_{out} = r_{bg}s_{in} + \sqrt{2\Gamma_{G,r}}\,a_G, \tag{A.41}$$

where r_{bg} is a constant that accounts for a slowly varying background reflection term. In the steady state, solving the coupled equations for a_G and substituting into the input-output relation yields the reflection coefficient, defined as $r = s_{out}/s_{in}$:

$$a_G = \left(\frac{\sqrt{2\Gamma_{G,r}}}{-i\Delta_G + \Gamma_G}\right)s_{in}, \tag{A.42}$$

$$r(E) = r_{bg} + \frac{2\Gamma_{G,r}}{-i\Delta_G + \Gamma_G}\,. \tag{A.43}$$

From this procedure, for the metasurface with one monolayer, we find $\Gamma_{G,r} = 22.5$ meV and $\Gamma_{G,nr} = 6.9$ meV for the radiative and non-radiative components, respectively. For the metasurface with two monolayers, the non-radiative damping rate increases to $\Gamma_{G,nr} = 9.3$ meV.

With these rates locked in, we now add the excitons back into the model. We first consider the metasurface with one monolayer and thus a single exciton resonance (denoted with subscript 'A') coupled to the GMR (Fig. 4.A2). The intrinsic exciton resonance energy E_A and damping rate Γ_A are obtained by fitting the reflectance of hBN-encapsulated WS_2 measured at 3 K (Fig. 4.3). The evolution of Γ_A with the carrier density n_e in monolayer WS_2 is taken from the section 3.5 in the previous chapter. Since, in our system, $\Gamma_{G,r} \gg \Gamma_{A,r}$ and the exciton-GMR coupling strength g typically exceeds $\Gamma_{A,r}$ by roughly an order of magnitude, we assume that optical coupling from free space is mediated entirely by the metasurface, and therefore neglect direct coupling between excitons and free-space[147,337]. In the steady state, the coupled

equations are then written as:

$$\frac{\mathrm{d}}{\mathrm{d}t}\begin{pmatrix} a_\mathrm{G} \\ a_\mathrm{A} \end{pmatrix} = -i\begin{pmatrix} \Delta_\mathrm{G} - i\Gamma_\mathrm{G} & g \\ g & \Delta_\mathrm{A} - i\Gamma_\mathrm{A}(n_\mathrm{e}) \end{pmatrix}\begin{pmatrix} a_\mathrm{G} \\ a_\mathrm{A} \end{pmatrix} + \begin{pmatrix} \sqrt{2\Gamma_{\mathrm{G,r}}} \\ 0 \end{pmatrix} s_\mathrm{in}. \tag{A.44}$$

Solving this system, we find that the reflection coefficient is described as:

$$r = r_\mathrm{bg} + \frac{2\Gamma_{\mathrm{G,r}}}{-i\Delta_\mathrm{G} + \Gamma_\mathrm{G} + \frac{g^2}{-i\Delta_\mathrm{A} + \Gamma_\mathrm{A}(n_\mathrm{e})}}. \tag{A.45}$$

Finally, we consider the metasurface with two monolayers (Fig. 4.A4a), top (subscript 't') and bottom (subscript 'b'), with exciton resonances described by the same resonance energy E_A, but unique decay rates $\Gamma_\mathrm{T}(n_\mathrm{t})$ and $\Gamma_\mathrm{b}(n_\mathrm{b})$, as well as coupling rates g_T and g_b. Since, in practice, both monolayers are separated by a tens-of-nanometers-thick hBN layer, the coupling between the two exciton resonances can be ignored. This gives a three-oscillator TCMT model with the following coupled equations:

$$\frac{\mathrm{d}}{\mathrm{d}t}\begin{pmatrix} a_\mathrm{G} \\ a_\mathrm{t} \\ a_\mathrm{b} \end{pmatrix} = -i\begin{pmatrix} \Delta_\mathrm{G} - i\Gamma_\mathrm{G} & g_\mathrm{t} & g_\mathrm{b} \\ g_\mathrm{t} & \Delta_\mathrm{A} - i\Gamma_\mathrm{t}(n_\mathrm{t}) & 0 \\ g_\mathrm{b} & 0 & \Delta_\mathrm{A} - i\Gamma_\mathrm{b}(n_\mathrm{b}) \end{pmatrix}\begin{pmatrix} a_\mathrm{G} \\ a_\mathrm{t} \\ a_\mathrm{b} \end{pmatrix} + \begin{pmatrix} \sqrt{2\Gamma_{\mathrm{G,r}}} \\ 0 \\ 0 \end{pmatrix} s_\mathrm{in}. \tag{A.46}$$

and the reflection coefficient is:

$$r = r_\mathrm{bg} + \frac{2\Gamma_{\mathrm{G,r}}}{-i\Delta_\mathrm{G} + \Gamma_\mathrm{G} + \frac{g_\mathrm{T}^2}{-i\Delta_\mathrm{A} + \Gamma_\mathrm{t}(n_\mathrm{t})} + \frac{g_\mathrm{b}^2}{-i\Delta_\mathrm{A} + \Gamma_\mathrm{b}(n_\mathrm{b})}}. \tag{A.47}$$

The closed-form analytic expressions for r of the two- and three-oscillator TCMT models provide valuable insight into the principles governing phase modulation, without relying on specific device geometries. In particular, for complex amplitude modulation it is not self-evident why two degenerate exciton resonances should uniquely impact the complex reflection amplitude. However, from the equation above it is clear that the symmetry between both resonances is broken when $g_\mathrm{T} \neq g_\mathrm{b}$ (Fig. 4.A6). In addition, by modifying the fitted radiative and non-radiative rates, we can assess the ultimate limits of both π-phase modulation (Fig. 4.A3) and complex amplitude modulation (Fig. 4.A4b).

A.5 SPATIOTEMPORAL COUPLED-MODE THEORY

In this section, we present the detailed derivations of the spatiotemporal coupled-mode theory (STCMT) discussed in Chapter 5. We start by introducing the linear dispersion relation in Section A.5.1 and the equation of motion in Section A.5.2. Next, in Section A.5.3 we use the Green's function formalism to derive the mode amplitude, and we establish the free-space coupling to and from this mode in Section A.5.4. Next, in Section A.5.5 we make the point-source approximation to derive a closed-form expression for the reflection coefficient. Finally, in Section A.5.6 we use this expression to evaluate several physical consequences arising from confinement of a nonlocal mode in a finite-size metasurface.

A.5.1 Dispersion relation

Consider a quasi-guided mode propagating in the positive x-direction described by the modal parameter $a(x,t)$, which evolves as

$$a(x,t) \propto e^{i\beta x - i\omega t} \tag{A.48}$$

with phase constant β and frequency ω. Throughout, we approximate the dispersion as locally linear (Fig. A.2), by expanding the complex propagation constant to first-order near a reference point (β_0,ω_0) as

$$\tilde{\beta}(\omega) = \beta + i\alpha \simeq \beta_0 + \frac{\omega-\omega_0}{v_g} + i\alpha, \qquad v_g \equiv \left.\frac{d\omega}{d\beta}\right|_{\beta_0}, \tag{A.49}$$

where α is the spatial attenuation rate. Equivalently, in the momentum-domain picture we can write the complex frequency

$$\Omega(\beta) \equiv \omega - i\Gamma \simeq \omega_0 - i\Gamma + v_g(\beta-\beta_0), \tag{A.50}$$

where $\Gamma \equiv \Gamma_{\text{ext}} + \Gamma_{\text{int}} = v_g\alpha$ is the temporal decay rate comprising the external (radiative) decay rate Γ_{ext} associated with coupling of the guided mode to the far field via the grating, and the intrinsic, non-radiative loss rate Γ_{int}. A closely related parameter is the modal propagation length,

$$L_p = \frac{1}{\alpha} = \frac{v_g}{\Gamma}, \tag{A.51}$$

i.e., the distance over which the mode amplitude decays to $1/e$. This parameter is particularly important because it governs the characteristic length scale over which finite-size effects cannot be ignored.

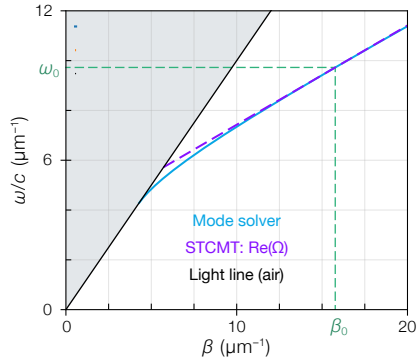

Figure A.2: Locally linear dispersion relation. Fundamental TE_0 eigenmode dispersion obtained with a slab waveguide mode solver by treating the grating as an effective medium (blue). Overlaid is the approximate STCMT dispersion Ω (purple, dashed) which is linearized around the point ω_0, β_0 (green, dashed). For reference, the light cone (shaded gray) and light line in air (black) are shown.

A.5.2 Equation of motion

The spatiotemporal dynamical equation for a system with a single mode $a(x,t)$ may be written as

$$\frac{\partial a(x,t)}{\partial t} + i\Omega a(x,t) = \int \kappa(x,x')\, s_+(x',t)\, \mathrm{d}x', \tag{A.52}$$

where κ is the in-coupling parameter that couples the external driving field s_+ to the internal mode. Specifically, under the locally linear dispersion of Eq. (A.50), this becomes

$$\frac{\partial a(x,t)}{\partial t} + i\Big(\omega_0 - i\Gamma + v_g(\beta-\beta_0)\Big)\, a(x,t) = \int \kappa(x,x')\, s_+(x',t)\, \mathrm{d}x'. \tag{A.53}$$

Realizing the space-harmonic $\beta \to -i\partial_x$, this can be rewritten in the form presented in the main text:

$$\frac{\partial a(x,t)}{\partial t} + v_g \frac{\partial a(x,t)}{\partial x} + i\Big(\omega_0 - i\Gamma - v_g\beta_0\Big)\, a(x,t) = \int \kappa(x,x')\, s_+(x',t)\, \mathrm{d}x'. \tag{A.54}$$

Instead realizing the time-harmonic $\partial_t \to -i\omega$, we can write the expression for the steady-state as a purely spatial differential equation:

$$v_g \frac{\partial a(x)}{\partial x} + i\Big(\omega_0 - \omega - i\Gamma - v_g\beta_0\Big)\, a(x) = \int \kappa(x,x')\, s_+(x')\, \mathrm{d}x'. \tag{A.55}$$

We can rewrite the left-hand side as

$$\left(-i(\omega-\omega_0) + v_g\frac{\partial}{\partial x} + \Gamma - i v_g\beta_0\right) a(x) = v_g\left(\frac{\partial}{\partial x} - i\tilde{\beta}\right) a(x). \tag{A.56}$$

Introducing the spatial operator $\mathscr{L}$,

$$\mathscr{L}a(x) = v_g\left(\frac{\partial}{\partial x} - i\tilde{\beta}\right)a(x), \tag{A.57}$$

we finally obtain the compact form

$$\mathscr{L}a(x) = \int \kappa(x,x')\, s_+(x')\,\mathrm{d}x'. \tag{A.58}$$

A.5.3 Mode amplitude

To solve Eq. (A.58), we introduce the Green's function $G(x;x')$, defined by,

$$\mathscr{L}G(x;x') = \delta(x-x'). \tag{A.59}$$

For $x \neq x'$, the Green's function satisfies

$$\mathscr{L}G(x;x') = 0, \tag{A.60}$$

which implies,

$$\frac{\partial}{\partial x}G(x;x') = i\left(\beta_0 + \frac{\omega-\omega_0}{v_g} + i\frac{\Gamma}{v_g}\right)G(x;x') = i\tilde{\beta}\,G(x;x'). \tag{A.61}$$

The solution away from the source point therefore takes the form

$$G(x;x') = A\, e^{i\tilde{\beta}(x-x')}, \qquad \text{for } x \neq x'. \tag{A.62}$$

To determine the prefactor and the causal structure, we integrate Eq. (A.59) over an infinitesimal interval around x',

$$\int_{x'-\epsilon}^{x'+\epsilon} \mathscr{L}G\,\mathrm{d}x = v_g\big[G(x'+0;x') - G(x'-0;x')\big] = 1, \tag{A.63}$$

where only the derivative term contributes to the discontinuity. Restricting to a right-propagating solution enforces causality, $G(x<x')=0$, such that $G(x'-0;x')=0$. This yields $G(x'+0;x') = 1/v_g$. The Green's function can therefore be written as

$$G(x;x') = \begin{cases} \dfrac{1}{v_g}\, e^{i\tilde{\beta}(x-x')} & \text{for } x > x', \\ 0 & \text{for } x < x'. \end{cases} \tag{A.64}$$

Equivalently, this can be expressed in compact form using the Heaviside step function Θ,

$$G(x;x') = \frac{1}{v_g} e^{i\tilde{\beta}(x-x')}\,\Theta(x-x'). \tag{A.65}$$

The mode amplitude follows from convolution of the Green's function with the driving term,

$$a(x) = \int_{-\infty}^{+\infty} \kappa(x')\,G(x;x')\,s_+(x')\,\mathrm{d}x', \tag{A.66}$$

Finally, inserting Eq. (A.65), the mode amplitude is found as:

$$a(x) = \frac{1}{v_g}\int_0^x e^{i\tilde{\beta}(x-x')}\,\kappa(x')\,s_+(x')\mathrm{d}x'. \tag{A.67}$$

A.5.4 Input-output relation

The general form of the scattered field is written as

$$s_-(x,t) = \int \big(C(x,x')\,s_+(x',t) + d(x,x')\,a(x',t)\big)\mathrm{d}x', \tag{A.68}$$

where C denotes the contribution from non-resonant (background) scattering and $d(x,x')$ is a out-coupling parameter which mediates coupling from the internal mode to external radiation. In this work, we assume spatially invariant background scattering and spatially instantaneous in- and out-coupling, such that

$$C(x,x') = C\delta(x-x'), \tag{A.69}$$

$$\kappa(x,x') = \kappa(x)\delta(x-x'), \tag{A.70}$$

$$d(x,x') = d(x)\delta(x-x'). \tag{A.71}$$

Under these assumptions, in the steady state, the input–output relation takes the form

$$s_-(x) = C\,s_+(x) + d(x)\,a(x). \tag{A.72}$$

The resonant contribution is generated by out-coupling of the guided mode back to the external channel. We write

$$s_-^{(\mathrm{res})}(x) = d(x)\,a(x). \tag{A.73}$$

Coupling between the external field and the guided mode is enabled by a subwavelength grating of period Λ, which provides the grating momentum $q = 2\pi/\Lambda$. In addition, coupling is restricted to a finite grating region of width W, which we

represent by a window function

$$w(x) = \Theta(x)\Theta(W - x), \tag{A.74}$$

so that both in- and out-coupling vanish outside $x \in [0, W]$. Adopting this description, we model the in-coupling as

$$\kappa(x) = \kappa_0\, w(x)\, e^{iqx}, \tag{A.75}$$

and the out-coupling as

$$d(x) = d_0\, w(x)\, e^{-iqx}. \tag{A.76}$$

The factors $e^{\pm iqx}$ enforce grating-assisted momentum matching: the external field acquires grating momentum upon coupling into the guided mode, and the opposite phase factor appears upon re-radiation to the external channel. The overall coupling strength is constrained by energy conservation [342, 380], such that $\kappa_0 = d_0 = \sqrt{2\Gamma_{\text{ext}}}$, and

$$\kappa(x) = d(x)^* = \sqrt{2\Gamma_{\text{ext}}}\, e^{iqx}\, w(x). \tag{A.77}$$

Finally, by plugging Eq. (A.77) in Eq. (A.67), we obtain the general expression for the mode amplitude for the metasurface under consideration:

$$a(x) = \frac{\sqrt{2\Gamma_{\text{ext}}}}{v_g} \int_0^x e^{i\tilde{\beta}(x-x')} e^{iqx'}\, w(x')\, s_+(x')\, \mathrm{d}x'. \tag{A.78}$$

Input field

In general, the incident field is modeled as a diffraction-limited spot centered at position x_0, which is represented in momentum-space as

$$S_+(k_x) = S_0\, e^{-ik_x x_0}, \quad \text{for } |k_x/k_0| \le \text{NA}, \tag{A.79}$$

where $|S_0|^2$ represents the incident power per unit k_x. Here, the in-plane wavevector is $k_x = k_0 \sin\theta$ with free-space wavevector $k_0 = \omega/c$ and incidence angle θ. The numerical aperture $\text{NA} = k_{x,\max}/k_0$ sets the excitation bandwidth.

In real space, this aperture-limited momentum-space distribution produces a sinc illumination profile,

$$s_+(x') \propto \text{sinc}\big(k_{x,\max}(x' - x_0)\big). \tag{A.80}$$

This is analogous to a diffraction-limited optical system, where an Airy disk is produced by uniform illumination of the circular entrance pupil of a microscope objective. Crucially, when the width of the resonance in k-space (governed by α)

is sufficiently narrow compared to the numerical-aperture window ($\alpha / k_0 \ll \mathrm{NA}$), the incident field can be approximated as a point excitation localized at x_0,

$$s_+(x') \approx S_0\, \delta(x' - x_0), \quad \text{with } x_0 \in [0, W]. \tag{A.81}$$

This approximation enables the derivation of closed-form expressions for many relevant physical quantities within our framework.

A.5.5 Point-source approximation

In the following, we first derive a closed-form expression for the resonant contribution $S_-^{(\mathrm{res})}(k_x)$. We start from the formal solution of the mode amplitude, Eq. (A.78), which, for the point-excitation approximation introduced above evaluates straightforwardly to

$$a(x) = \frac{\sqrt{2\Gamma_{\mathrm{ext}}}\, S_0}{v_g}\, e^{i\tilde{\beta}(x-x_0)}\, e^{iqx_0}\, \Theta(x - x_0), \tag{A.82}$$

with the understanding that scattering is restricted to the grating region by $w(x)$. Plugging this into Eq. (A.73), we obtain

$$s_-^{(\mathrm{res})}(x) = \frac{2\Gamma_{\mathrm{ext}}\, S_0}{v_g}\, e^{i(\tilde{\beta}-q)(x-x_0)} \Theta(x - x_0). \tag{A.83}$$

To compute the resonant scattering contribution in k-space, we integrate from x_0 to the right edge W, *i.e.*, over the modal interaction length $L = W - x_0$,

$$S_-^{(\mathrm{res})}(k_x) = \int_{x_0}^{W} s_-^{(\mathrm{res})}(x)\, e^{-ik_x x}\, \mathrm{d}x. \tag{A.84}$$

Substituting $u = x - x_0$ and rewriting yields

$$S_-^{(\mathrm{res})}(k_x) = \frac{2\Gamma_{\mathrm{ext}}\, S_0}{v_g}\, e^{-ik_x x_0} \int_0^L e^{i\tilde{\beta}u}\, e^{-i(k_x+q)u}\, \mathrm{d}u. \tag{A.85}$$

It is useful to define the detuning between the guided-mode wavevector and the input wave's in-plane momentum (for the $m = +1$ order) as

$$\Delta_k = (k_x + q) - \beta = k_x - k_{x,\mathrm{res}}, \tag{A.86}$$

where we additionally defined the resonant in-plane wavevector in free-space $k_{x,\mathrm{res}} = \beta - q$. Using this notation, we can write

$$S_-^{(\mathrm{res})}(k_x) = \frac{2\Gamma_{\mathrm{ext}}\, S_0}{v_g}\, e^{-ik_x x_0} \int_0^L e^{-(\alpha + i\Delta_k)u} \mathrm{d}u, \tag{A.87}$$

which evaluates to

$$S_{-}^{(\mathrm{res})}(k_x) = \frac{2\Gamma_{\mathrm{ext}} S_0}{v_g}\, e^{-ik_x x_0}\, \frac{1 - e^{-(\alpha + i\Delta_k)L}}{\alpha + i\Delta_k}. \tag{A.88}$$

Reflection coefficient

The input-output relation in k-space is written as

$$S_{-}(k_x) = C S_{+}(k_x) + S_{-}^{(\mathrm{res})}(k_x), \tag{A.89}$$

and the reflection coefficient is defined as

$$r(k_x) \equiv \frac{S_{-}(k_x)}{S_{+}(k_x)}. \tag{A.90}$$

For the metasurfaces considered here, the off-resonant response is mirror-like, such that $C \approx -1$ over the bandwidth of interest. The reflection coefficient is then readily obtained by plugging Eqs. (A.79) and (A.88) in Eq. (A.90):

$$r(k_x) = -1 + \frac{2\Gamma_{\mathrm{ext}}}{v_g\,(\alpha + i\Delta_k)} \left(1 - e^{-(\alpha + i\Delta_k)L}\right). \tag{A.91}$$

Under a linear dispersion, $\Delta_\omega = v_g \Delta_k$, such that we can equivalently express the reflection coefficient in frequency-space for an ultrashort pulse as

$$r(\omega) = -1 + \frac{2\Gamma_{\mathrm{ext}}}{\Gamma + i\Delta_\omega} \left(1 - e^{-(\Gamma + i\Delta_\omega)L/v_g}\right). \tag{A.92}$$

In both representations, the response consists of the familiar Lorentzian dependence on the detuning as well as an exponential term which encodes the effects of a finite interaction length L. This length scale should be compared to the propagation length L_p of the quasi-guided mode. When $L \lesssim L_p$, the finite aperture produces oscillatory spectral features and effective broadening of the resonance. On the other hand, in the long-grating limit $L \gg L_p$, the finite-size factor tends to unity and the reflection coefficient reduces to the well-known one-port TCMT expression [371],

$$r_\infty(\omega) = -1 + \frac{2\Gamma_{\mathrm{ext}}}{\Gamma + i\Delta_\omega}, \tag{A.93}$$

and equivalently in k-space,

$$r_\infty(k_x) = -1 + \frac{2\Gamma_{\mathrm{ext}}}{v_g(\alpha + i\Delta_k)}. \tag{A.94}$$

A.5.6 Finite-size effects

Resonant anti-reflection

A vanishing reflectance ($R = |r|^2 = 0$) corresponds to a destructive-interference condition in the output channel, which is modified by finite size. At resonance ($\Delta_k = 0$), the finite interaction length L introduces the factor $1 - e^{-\alpha L}$ in the resonant scattering amplitude, and the well-known critical coupling criterion $\Gamma_{\text{ext}} = \Gamma_{\text{int}}$ no longer corresponds to $R = 0$. Instead, the anti-reflection condition becomes

$$\frac{\Gamma_{\text{ext}}}{\Gamma} = \frac{1}{2(1 - e^{-\alpha L})}, \tag{A.95}$$

which generally requires stronger external coupling (more over-coupling) than the infinite-length case.

Solving Eq. (A.95) for L yields

$$L = -\frac{v_g}{\Gamma} \ln\left(1 - \frac{\Gamma}{2\Gamma_{\text{ext}}}\right). \tag{A.96}$$

Given $\Gamma \geq 0$, a necessary condition for a real, positive solution of (A.96) is that $\Gamma_{\text{ext}} > \Gamma/2$ (equivalently $\Gamma_{\text{ext}} > \Gamma_{\text{int}}$), otherwise no finite L can produce $R = 0$. It should be noted that, contrary to the infinite-length limit, the combination of parameters that yields perfect anti-reflection need not coincide with that which maximizes the stored energy U in the resonator.

Stored energy

We next derive a closed-form expression for the stored energy

$$U \equiv \int |a(x)|^2 \, \mathrm{d}x, \tag{A.97}$$

for $x \in [0, W]$. Using the definition of $a(x)$ (Eq. (A.82)), we have

$$|a(x)|^2 = 2\Gamma_{\text{ext}} \left(\frac{S_0}{v_g}\right)^2 e^{-2\alpha(x - x_0)} \Theta(x - x_0). \tag{A.98}$$

Since the excitation point lies within the grating ($x_0 \in [0, W]$), the integral reduces to the interval $x \in [x_0, W]$:

$$U = 2\Gamma_{\text{ext}} \left(\frac{S_0}{v_g}\right)^2 \int_{x_0}^{W} e^{-2\alpha(x - x_0)} \, \mathrm{d}x. \tag{A.99}$$

Substituting $u = x - x_0$ and defining $L = W - x_0$ gives

$$U = 2\Gamma_{\text{ext}} \left(\frac{S_0}{v_g} \right)^2 \int_0^L e^{-2\alpha u} \, \mathrm{d}u = 2\Gamma_{\text{ext}} \left(\frac{S_0}{v_g} \right)^2 \frac{1 - e^{-2\alpha L}}{2\alpha}. \tag{A.100}$$

Therefore, the stored energy is

$$U = \frac{S_0^2}{v_g} \frac{\Gamma_{\text{ext}}}{\Gamma} \left(1 - e^{-2\alpha L} \right). \tag{A.101}$$

In the long-grating limit $L \gg L_p$, the stored energy saturates to

$$U \to \frac{S_0^2}{v_g} \frac{\Gamma_{\text{ext}}}{\Gamma}. \tag{A.102}$$

Edge loss

The finite grating length introduces an additional loss channel associated with leakage of the quasi-guided wave at the grating edge. We assume that the guided mode propagates only in the positive x-direction and that any power reaching the right edge $x = W$ is irreversibly lost, with no reflection back into the guided mode.

The guided power flux at position x is proportional to

$$P(x) \propto v_g \, |a(x)|^2 . \tag{A.103}$$

Using the expression for the mode amplitude derived above (Eq. (A.98)), the power reaching the right edge is therefore

$$P_{\text{edge}} \propto v_g \, |a(W)|^2 = 2\Gamma_{\text{ext}} \frac{S_0^2}{v_g} e^{-2\alpha L}, \tag{A.104}$$

where $L = W - x_0$ is the distance from the excitation point to the right edge.

It is convenient to express this edge loss in terms of an effective decay rate Γ_{edge}, defined via the standard coupled-mode relation

$$P_{\text{edge}} = 2\Gamma_{\text{edge}} U, \tag{A.105}$$

with U the stored energy obtained in the previous section (Eq. (A.101)). Substituting the closed-form expressions for P_{edge} and U yields

$$\Gamma_{\text{edge}} = \Gamma \frac{e^{-2\alpha L}}{1 - e^{-2\alpha L}} = \frac{\Gamma}{e^{2\alpha L} - 1}. \tag{A.106}$$

This expression highlights the exponential suppression of edge loss with increas-

ing grating length. In the long-grating limit ($L \gg L_p$), the edge contribution becomes negligible, whereas in the short-grating limit ($L \ll L_p$) the edge loss is dominated by the transit time to the boundary. Within this picture, edge loss constitutes an additional, geometry-induced decay channel that is distinct from intrinsic and radiative losses.

Quality factor

While the finite grating length gives rise to sinc-like broadening in the k-space reflectance spectrum, this effect is geometric in origin and does not correspond to an intrinsic energy-decay process. A physically meaningful quality factor must therefore be defined in terms of the energy lifetime of the guided mode rather than the apparent spectral width of $|r(k_x)|^2$.

The quality factor of a resonance at angular frequency ω_0 is defined as

$$Q \equiv \omega_0 \frac{U}{P_{\text{loss}}} = \frac{\omega_0}{2\Gamma_{\text{tot}}}, \tag{A.107}$$

where U is the stored energy, P_{loss} is the rate of energy dissipation, and Γ_{tot} is the total energy-decay rate.

For an infinitely long grating, the total decay rate is simply $\Gamma = \Gamma_{\text{ext}} + \Gamma_{\text{int}}$. For a finite grating of length L, however, we must include the additional edge loss channel. As shown above, this edge-induced loss can be expressed as an effective decay rate (Eq. (A.106)), such that the total decay rate becomes

$$\Gamma_{\text{tot}}(L) = \Gamma + \Gamma_{\text{edge}}(L) = \frac{\Gamma}{1 - e^{-2\alpha L}}. \tag{A.108}$$

The corresponding quality factor is therefore given by the closed-form expression

$$Q(L) = \frac{\omega_0}{2\Gamma_{\text{tot}}(L)} = \frac{\omega_0}{2\Gamma}\left(1 - e^{-2L/L_p}\right). \tag{A.109}$$

This definition yields a lifetime-based quality factor that is not affected by apparent linewidth broadening arising from the finite scattering aperture.

In the long-grating limit ($L \gg L_p$), the edge contribution vanishes and the quality factor approaches its intrinsic value

$$Q \to \frac{\omega_0}{2\Gamma}. \tag{A.110}$$

In the opposite limit of a size-constrained grating ($L \ll L_p$), the exponential may

be Taylor-expanded to yield

$$Q(L) \simeq \frac{\omega_0}{2\Gamma} 2\frac{\Gamma}{v_g} L = \frac{\omega_0 L}{v_g} = \frac{\omega_0}{\Gamma}\frac{L}{L_p}. \tag{A.111}$$

Remarkably, in this regime the quality factor is primarily governed by the mode's transit time to the edge, $t = L/v_g$. This implies that, for strongly footprint-constrained devices, high-Q requires increasing the interaction time within the fixed footprint by engineering a reduced group velocity (slow light).

Interference fringes

In addition to setting the resonance lineshape, the finite grating length also gives rise to oscillatory fringes in the k-space reflectance. Specifically, the region over which the guided mode can couple out to the far field is defined by the effective length $L = W - x_0$, and the resulting fringes arise from coherent interference between contributions emitted from different positions along the grating. This corresponds to multiplication of the real-space field by a rectangular window, whose Fourier transform produces a sinc-like modulation in k-space. As a result, the reflected intensity exhibits an interference pattern with characteristic fringe spacing

$$\Delta k_{\text{fringe}} = \frac{2\pi}{L}. \tag{A.112}$$

Owing to redistribution of spectral weight in k-space by this finite-aperture interference, the reflectance can locally exceed unity without implying optical gain; the scattered power remains constrained by the input power minus the dissipated power.

Bibliography

1. Novotny, L. & Hecht, B. *Principles of nano-optics* Second edition (Cambridge University Press, Cambridge New York Melbourne, 2012).
2. Hecht, E. *Optics* 4th ed (Pearson, Harlow, 2014).
3. Born, M., Wolf, E. & Knight, P. *Principles of optics* 60th Anniversary Edition. 1 p. (Cambridge University Press, Cambridge, 2019).
4. Lindberg, D. C. *Theories of Vision from Al-kindi to Kepler* 331 pp. (University of Chicago Press, Chicago, IL, 1996).
5. Darrigol, O. *A history of optics: from Greek antiquity to the nineteenth century* (Oxford university press, Oxford, 2012).
6. Smith, A. M. *From Sight to Light: The Passage from Ancient to Modern Optics* 470 pp. (University of Chicago Press, 2017).
7. Enoch, J. "History of Mirrors Dating Back 8000 Years". *Optometry and Vision Science* **83,** 775–781 (2006).
8. Enoch, J. M. "Archeological optics: the very first known mirrors and lenses". *Journal of Modern Optics* **54,** 1221–1239 (2007).
9. Plantzos, D. "Crystals and Lenses in the Graeco-Roman World". *American Journal of Archaeology* **101,** 451–464 (1997).
10. Tsouvala, G., Brice, L. L., Papen, A. & Papen, G. "Quantitative characterization of archaic magnifying lenses from Ialysos, Rhodes". *Journal of Archaeological Science: Reports* **53,** 104320 (2024).
11. Barber, D. J. & Freestone, I. C. "An Investigation of the Origin of the Colour of the Lycurgus Cup by Analytical Transmission Electron Microscopy". *Archaeometry* **32,** 33–45 (1990).
12. Einstein, A. "Über einem die Erzeugung und Verwandlung des Lichtes betreffenden heuristischen Gesichtspunkt". *Annalen der Physik* **vol. 4, t. 17** (1905).
13. Einstein, A. "Zur Elektrodynamik bewegter Körper". *Annalen der Physik* **322,** 891–921 (1905).
14. Dirac, P. A. M. "The quantum theory of dispersion". *Proceedings of the Royal Society of London. Series A, Containing Papers of a Mathematical and Physical Character* **114,** 710–728 (1927).
15. Lewis, G. N. "The Conservation of Photons". *Nature* **118,** 874–875 (1926).
16. Dyson, F. J. "Tomonaga, Schwinger, and Feynman Awarded Nobel Prize for Physics". *Science* **150,** 588–589 (1965).
17. Feynman, R. P. *QED: the strange theory of light and matter* 158 pp. (Penguin Books, London, 1990).
18. Bose, J. C. "On the rotation of plane of polarisation of electric wave by a twisted structure". *Proceedings of the Royal Society of London* **63,** 146–152 (1898).

19. Kock, W. "Metal-Lens Antennas". *Proceedings of the IRE* **34,** 828–836 (1946).
20. Kock, W. E. "Metallic Delay Lenses". *Bell System Technical Journal* **27,** 58–82 (1948).
21. Shamonina, E. & Solymar, L. "Metamaterials: How the subject started". *Metamaterials* **1,** 12–18 (2007).
22. Iyer, A. K., Alù, A. & Epstein, A. "Metamaterials and Metasurfaces—Historical Context, Recent Advances, and Future Directions". *IEEE Transactions on Antennas and Propagation* **68,** 1223–1231 (2020).
23. Maci, S. "Electromagnetic Metamaterials and Metasurfaces: A historical journey". *IEEE Antennas and Propagation Magazine* **66,** 84–101 (2024).
24. Alù, A., Maci, S. & Engheta, N. "Metasurfaces and Metamaterials for Electromagnetics". *IEEE Transactions on Antennas and Propagation* (2025).
25. Van de Groep, J., Song, J. H., Celano, U., Li, Q., Kik, P. G. & Brongersma, M. L. "Exciton resonance tuning of an atomically thin lens". *Nature Photonics* **14,** 426–430 (2020).
26. Maiman, T. H. "Stimulated Optical Radiation in Ruby". *Nature* **187,** 493–494 (1960).
27. Moore, S. K. "The node is nonsense". *IEEE Spectrum* **57,** 24–30 (2020).
28. Yen, A., Kaiser, W. & Suzuki, A. "Development of Photolithography for Semiconductor Manufacturing – a Review". *IEEE Electron Devices Reviews,* 1–47 (2026).
29. Gale, M. T., Knop, K. & Morf, R. H. "Zero-order diffractive microstructures for security applications". in *Optical Security and Anticounterfeiting Systems* **1210** (SPIE, 1990), 83–89.
30. Stork, W., Streibl, N., Haidner, H. & Kipfer, P. "Artificial distributed-index media fabricated by zero-order gratings". *Optics Letters* **16,** 1921 (1991).
31. Farn, M. W. "Binary gratings with increased efficiency". *Applied Optics* **31,** 4453 (1992).
32. Haidner, H., Sheridan, J., Schwider, J. & Streibl, N. "Design of a blazed grating consisting of metallic subwavelength binary grooves". *Optics Communications* **98,** 5–10 (1993).
33. Peng, S. & Morris, G. M. "Sub-nanometer linewidth resonant grating filters". in *Diffractive Optics and Micro-Optics* (Optica Publishing Group, 1996), DWA.4.
34. Kipfer, P., Collischon, M., Haidner, H., Sheridan, J. T., Schwider, J., Streibl, N. & Lindolf, J. "Infrared optical components based on a microrelief structure". *Optical Engineering* **33,** 79–84 (1994).
35. Wang, S. S., Moharam, M. G., Magnusson, R. & Bagby, J. S. "Guided-mode resonances in planar dielectric-layer diffraction gratings". *Journal of the Optical Society of America A* **7,** 1470 (1990).
36. Agranovič, V. M., Ginzburg, V. L., Weinstein, N. & Agranovič, V. M. *Crystal optics with spatial dispersion, and excitons* 2. corrected and updated ed. *Springer series in solid state sciences* **42.** 441 pp. (Springer, Berlin Heidelberg, 1984).
37. Belov, P. A., Marqués, R., Maslovski, S. I., Nefedov, I. S., Silveirinha, M., Simovski, C. R. & Tretyakov, S. A. "Strong spatial dispersion in wire media in the very large wavelength limit". *Physical Review B* **67,** 113103 (2003).
38. Silveirinha, M. G. "Generalized Lorentz-Lorenz formulas for microstructured materials". *Physical Review B* **76,** 245117 (2007).
39. Wang, S. S. & Magnusson, R. "Theory and applications of guided-mode resonance filters". *Applied Optics* **32,** 2606 (1993).
40. Yablonovitch, E. "Photonic band-gap structures". *JOSA B* **10,** 283–295 (1993).

41. Joannopoulos, J. D., Meade, R. D. & Winn, J. N. *Photonic crystals: molding the flow of light* 137 pp. (Princeton University Press, Lawrenceville, NJ, 1995).

42. Krauss, T. F., Rue, R. M. D. L. & Brand, S. "Two-dimensional photonic-bandgap structures operating at near-infrared wavelengths". *Nature* **383,** 699–702 (1996).

43. Ebbesen, T. W., Lezec, H. J., Ghaemi, H. F., Thio, T. & Wolff, P. A. "Extraordinary optical transmission through sub-wavelength hole arrays". *Nature* **391,** 667–669 (1998).

44. Pendry, J. "Playing Tricks with Light". *Science* **285,** 1687–1688 (1999).

45. Hooper, I. R. & Sambles, J. R. "Dispersion of surface plasmon polaritons on short-pitch metal gratings". *Physical Review B* **65,** 165432 (2002).

46. Barnes, W. L., Dereux, A. & Ebbesen, T. W. "Surface plasmon subwavelength optics". *Nature* **424,** 824–830 (2003).

47. Zentgraf, T., Meyrath, T. P., Seidel, A., Kaiser, S., Giessen, H., Rockstuhl, C. & Lederer, F. "Babinet's principle for optical frequency metamaterials and nanoantennas". *Physical Review B* **76,** 033407 (2007).

48. Dintinger, J., Klein, S. & Ebbesen, T. W. "Molecule–Surface Plasmon Interactions in Hole Arrays: Enhanced Absorption, Refractive Index Changes, and All-Optical Switching". *Advanced Materials* **18,** 1267–1270 (2006).

49. Vuckovic, J., Loncar, M. & Scherer, A. "Surface plasmon enhanced light-emitting diode". *IEEE Journal of Quantum Electronics* **36,** 1131–1144 (2000).

50. Bellessa, J., Bonnand, C., Plenet, J. C. & Mugnier, J. "Strong Coupling between Surface Plasmons and Excitons in an Organic Semiconductor". *Physical Review Letters* **93,** 036404 (2004).

51. Astilean, S., Lalanne, P., Chavel, P., Cambril, E. & Launois, H. "High-efficiency subwavelength diffractive element patterned in a high-refractive-index material for 633 nm". *Optics Letters* **23,** 552–554 (1998).

52. Lalanne, P., Astilean, S., Chavel, P., Cambril, E. & Launois, H. "Blazed binary subwavelength gratings with efficiencies larger than those of conventional échelette gratings". *Optics Letters* **23,** 1081 (1998).

53. Lalanne, P. "Waveguiding in blazed-binary diffractive elements". *JOSA A* **16,** 2517–2520 (1999).

54. Lalanne, P., Hugonin, J. & Chavel, P. "Optical properties of deep lamellar Gratings: A coupled Bloch-mode insight". *Journal of Lightwave Technology* **24,** 2442–2449 (2006).

55. Bomzon, Z., Kleiner, V. & Hasman, E. "Formation of radially and azimuthally polarized light using space-variant subwavelength metal stripe gratings". *Applied Physics Letters* **79,** 1587–1589 (2001).

56. Bomzon, Z., Kleiner, V. & Hasman, E. "Pancharatnam–Berry phase in space-variant polarization-state manipulations with subwavelength gratings". *Optics Letters* **26,** 1424 (2001).

57. Bomzon, Z., Biener, G., Kleiner, V. & Hasman, E. "Space-variant Pancharatnam–Berry phase optical elements with computer-generated subwavelength gratings". *Optics Letters* **27,** 1141–1143 (2002).

58. Hasman, E., Kleiner, V., Biener, G. & Niv, A. "Polarization dependent focusing lens by use of quantized Pancharatnam–Berry phase diffractive optics". *Applied Physics Letters* **82,** 328–330 (2003).

59. Veselago, V. G. "The Electrodynamics of Substances with Simultaneously Negative Values of μ and ε". *Soviet Physics Uspekhi* **10,** 509 (1968).

60. Pendry, J. B. "Negative Refraction Makes a Perfect Lens". *Physical Review Letters* **85,** 3966–3969 (2000).

61. Smith, D. R., Padilla, W. J., Vier, D. C., Nemat-Nasser, S. C. & Schultz, S. "Composite Medium with Simultaneously Negative Permeability and Permittivity". *Physical Review Letters* **84,** 4184–4187 (2000).

62. Shelby, R. A., Smith, D. R. & Schultz, S. "Experimental Verification of a Negative Index of Refraction". *Science* **292,** 77–79 (2001).

63. Shalaev, V. M., Cai, W., Chettiar, U. K., Yuan, H.-K., Sarychev, A. K., Drachev, V. P. & Kildishev, A. V. "Negative index of refraction in optical metamaterials". *Optics Letters* **30,** 3356–3358 (2005).

64. Zhang, S., Fan, W., Panoiu, N. C., Malloy, K. J., Osgood, R. M. & Brueck, S. R. J. "Experimental Demonstration of Near-Infrared Negative-Index Metamaterials". *Physical Review Letters* **95,** 137404 (2005).

65. Valentine, J., Zhang, S., Zentgraf, T., Ulin-Avila, E., Genov, D. A., Bartal, G. & Zhang, X. "Three-dimensional optical metamaterial with a negative refractive index". *Nature* **455,** 376–379 (2008).

66. Mühlschlegel, P., Eisler, H.-J., Martin, O. J. F., Hecht, B. & Pohl, D. W. "Resonant Optical Antennas". *Science* **308,** 1607–1609 (2005).

67. Oldenburg, S. J., Averitt, R. D., Westcott, S. L. & Halas, N. J. "Nanoengineering of optical resonances". *Chemical Physics Letters* **288,** 243–247 (1998).

68. Schuller, J. A., Zia, R., Taubner, T. & Brongersma, M. L. "Dielectric Metamaterials Based on Electric and Magnetic Resonances of Silicon Carbide Particles". *Physical Review Letters* **99,** 107401 (2007).

69. Purcell, E. M. "Spontaneous Emission Probabilities at Radio Frequencies". *Physical Review* **69,** 681 (1946).

70. Ruan, Z. & Fan, S. "Temporal coupled-mode theory for fano resonance in light scattering by a single obstacle". *Journal of Physical Chemistry C* **114,** 7324–7329 (2010).

71. Lynch, J., Guarneri, L., Jariwala, D. & Van De Groep, J. "Exciton resonances for atomically-thin optics". *Journal of Applied Physics* **132,** 091102 (2022).

72. Hutter, E. & Fendler, J. H. "Exploitation of Localized Surface Plasmon Resonance". *Advanced Materials* **16,** 1685–1706 (2004).

73. Mie, G. "Beiträge zur Optik trüber Medien, speziell kolloidaler Metallösungen". *Annalen der Physik* **330,** 377–445 (1908).

74. Ozbay, E. "Plasmonics: Merging Photonics and Electronics at Nanoscale Dimensions". *Science* **311,** 189–193 (2006).

75. Kuznetsov, A. I., Miroshnichenko, A. E., Fu, Y. H., Zhang, J. & Luk'yanchuk, B. "Magnetic light". *Scientific Reports* **2,** 492 (2012).

76. Decker, M., Staude, I., Falkner, M., Dominguez, J., Neshev, D. N., Brener, I., Pertsch, T. & Kivshar, Y. S. "High-Efficiency Dielectric Huygens' Surfaces". *Advanced Optical Materials* **3,** 813–820 (2015).

77. Kuznetsov, A. I., Miroshnichenko, A. E., Brongersma, M. L., Kivshar, Y. S. & Luk'yanchuk, B. "Optically resonant dielectric nanostructures". *Science* **354** (2016).

78. De Waele, R., Koenderink, A. F. & Polman, A. "Tunable Nanoscale Localization of Energy on Plasmon Particle Arrays". *Nano Letters* **7,** 2004–2008 (2007).

79. Liu, N., Langguth, L., Weiss, T., Kästel, J., Fleischhauer, M., Pfau, T. & Giessen, H. "Plasmonic analogue of electromagnetically induced transparency at the Drude damping limit". *Nature Materials* **8,** 758–762 (2009).

80. Kildishev, A. V., Boltasseva, A. & Shalaev, V. M. "Planar Photonics with Metasurfaces". *Science* **339,** 1232009 (2013).

81. Yu, N. & Capasso, F. "Flat optics with designer metasurfaces". *Nature Materials* **13,** 139–150 (2014).

82. Povinelli, M. L., Lončar, M., Ibanescu, M., Smythe, E. J., Johnson, S. G., Capasso, F. & Joannopoulos, J. D. "Evanescent-wave bonding between optical waveguides". *Optics Letters* **30,** 3042 (2005).

83. Cao, L., Fan, P. & Brongersma, M. L. "Optical coupling of deep-subwavelength semiconductor nanowires". *Nano Letters* **11,** 1463–1468 (2011).

84. Kottmann, J. P. & Martin, O. J. F. "Plasmon resonant coupling in metallic nanowires". *Optics Express* **8,** 655–663 (2001).

85. Sönnichsen, C., Franzl, T., Wilk, T., Von Plessen, G., Feldmann, J., Wilson, O. & Mulvaney, P. "Drastic Reduction of Plasmon Damping in Gold Nanorods". *Physical Review Letters* **88,** 077402 (2002).

86. Dahmen, C., Schmidt, B. & Von Plessen, G. "Radiation Damping in Metal Nanoparticle Pairs". *Nano Letters* **7,** 318–322 (2007).

87. Rodriguez, S. R. K., Schaafsma, M. C., Berrier, A. & Gómez Rivas, J. "Collective resonances in plasmonic crystals: Size matters". *Physica B: Condensed Matter. Proceedings of the conference - Wave Propagation: From Electrons to Photonic Crystals and Metamaterials* **407,** 4081–4085 (2012).

88. Yang, Y., Kravchenko, I. I., Briggs, D. P. & Valentine, J. "All-dielectric metasurface analogue of electromagnetically induced transparency". *Nature Communications* **5,** 5753 (2014).

89. Li, Q., van de Groep, J., Wang, Y., Kik, P. G. & Brongersma, M. L. "Transparent multispectral photodetectors mimicking the human visual system". *Nature Communications* **10,** 1–8 (2019).

90. Yu, J., Yao, W., Qiu, M. & Li, Q. "Free-space high-Q nanophotonics". *Light: Science & Applications* **14,** 174 (2025).

91. Bandiera, S., Jacob, D., Muller, T., Marquier, F., Laroche, M. & Greffet, J.-J. "Enhanced absorption by nanostructured silicon". *Applied Physics Letters* **93,** 193103 (2008).

92. Van de Groep, J. *Resonant Nanophotonic Structures for Photovoltaics* (2015). 255 pp.

93. Tavakoli, N., Spalding, R., Lambertz, A., Koppejan, P., Gkantzounis, G., Wan, C., Röhrich, R., Kontoleta, E., Koenderink, A. F., Sapienza, R., Florescu, M. & Alarcon-Llado, E. "Over 65% Sunlight Absorption in a 1 μm Si Slab with Hyperuniform Texture". *ACS Photonics* **9,** 1206–1217 (2022).

94. Pecora, E. F., Cordaro, A., Kik, P. G. & Brongersma, M. L. "Broadband Antireflection Coatings Employing Multiresonant Dielectric Metasurfaces". *ACS Photonics* **5,** 4456–4462 (2018).

95. Cordaro, A., Van De Groep, J., Raza, S., Pecora, E. F., Priolo, F. & Brongersma, M. L. "Antireflection High-Index Metasurfaces Combining Mie and Fabry-Pérot Resonances". *ACS Photonics* **6,** 453–459 (2019).

96. Cordaro, A., Kwon, H., Sounas, D., Koenderink, A. F., Alù, A. & Polman, A. "High-Index Dielectric Metasurfaces Performing Mathematical Operations". *Nano Letters* **19,** 8418–8423 (2019).

97. Cordaro, A. *Metasurfaces for analog optical processing: high-index dielectric metasurfaces performing mathematical operations* (Netherlands, 2022).

98. Dias, B. S. & Van De Groep, J. "High-NA 2D Image Edge Detection Using Tamm Plasmon Polaritons in Few-Layer Stratified Media". *ACS Photonics* **12,** 311–319 (2025).

99. Khorasaninejad, M. & Capasso, F. "Broadband Multifunctional Efficient Meta-Gratings Based on Dielectric Waveguide Phase Shifters". *Nano Letters* **15,** 6709–6715 (2015).

100. Overvig, A. C., Malek, S. C. & Yu, N. "Multifunctional Nonlocal Metasurfaces". *Physical Review Letters* **125,** 017402 (2020).

101. Malek, S. C., Overvig, A. C., Alù, A. & Yu, N. "Multifunctional resonant wavefront-shaping meta-optics based on multilayer and multi-perturbation nonlocal metasurfaces". *Light: Science & Applications* **11,** 246 (2022).

102. Ni, X., Kildishev, A. V. & Shalaev, V. M. "Metasurface holograms for visible light". *Nature Communications* **4,** 2807 (2013).

103. Zheng, G., Mühlenbernd, H., Kenney, M., Li, G., Zentgraf, T. & Zhang, S. "Metasurface holograms reaching 80% efficiency". *Nature Nanotechnology* **10,** 308–312 (2015).

104. Cai, W., Chettiar, U. K., Kildishev, A. V. & Shalaev, V. M. "Optical cloaking with metamaterials". *Nature Photonics* **1,** 224–227 (2007).

105. Liu, R., Ji, C., Mock, J. J., Chin, J. Y., Cui, T. J. & Smith, D. R. "Broadband Ground-Plane Cloak". *Science* **323,** 366–369 (2009).

106. Chen, P.-Y. & Alù, A. "Mantle cloaking using thin patterned metasurfaces". *Physical Review B* **84,** 205110 (2011).

107. Yu, N., Genevet, P., Kats, M. A., Aieta, F., Tetienne, J.-P., Capasso, F. & Gaburro, Z. "Light Propagation with Phase Discontinuities: Generalized Laws of Reflection and Refraction". *Science* **334,** 333–337 (2011).

108. Larouche, S. & Smith, D. R. "Reconciliation of generalized refraction with diffraction theory". *Optics Letters* **37,** 2391 (2012).

109. Paniagua-Domínguez, R., Yu, Y. F., Miroshnichenko, A. E., Krivitsky, L. A., Fu, Y. H., Valuckas, V., Gonzaga, L., Toh, Y. T., Kay, A. Y. S., Lukyanchuk, B. & Kuznetsov, A. I. "Generalized Brewster effect in dielectric metasurfaces". *Nature Communications* **7** (2016).

110. Miller, D. A. "Attojoule Optoelectronics for Low-Energy Information Processing and Communications". *Journal of Lightwave Technology* **35,** 346–396 (2017).

111. Klopfer, E., Dagli, S., Barton, D. I., Lawrence, M. & Dionne, J. A. "High-Quality-Factor Silicon-on-Lithium Niobate Metasurfaces for Electro-optically Reconfigurable Wavefront Shaping". *Nano Letters* **22,** 1703–1709 (2022).

112. Lin, L., Hu, J., Dagli, S., Dionne, J. A. & Lawrence, M. "Universal Narrowband Wavefront Shaping with High Quality Factor Meta-Reflect-Arrays". *Nano Letters* **23,** 1355–1362 (2023).

113. Hail, C. U., Foley, M., Sokhoyan, R., Michaeli, L. & Atwater, H. A. "High quality factor metasurfaces for two-dimensional wavefront manipulation". *Nature Communications* **14,** 8476 (2023).

114. Benea-Chelmus, I. C., Mason, S., Meretska, M. L., Elder, D. L., Kazakov, D., Shams-Ansari, A., Dalton, L. R. & Capasso, F. "Gigahertz free-space electro-optic modulators based on Mie resonances". *Nature Communications* **13,** 3170 (2022).

115. Damgaard-Carstensen, C., Yezekyan, T., Brongersma, M. L. & Bozhevolnyi, S. I. "Highly Efficient, Tunable, Electro-Optic, Reflective Metasurfaces Based on Quasi-Bound States in the Continuum". *ACS Nano* **19,** 11999–12006 (2025).

116. Koshelev, K., Tang, Y., Li, K., Choi, D.-Y., Li, G. & Kivshar, Y. "Nonlinear Metasurfaces Governed by Bound States in the Continuum". *ACS Photonics* **6,** 1639–1644 (2019).

117. Liu, Z., Xu, Y., Lin, Y., Xiang, J., Feng, T., Cao, Q., Li, J., Lan, S. & Liu, J. "High-Q Quasibound States in the Continuum for Nonlinear Metasurfaces". *Physical Review Letters* **123,** 253901 (2019).

118. Zograf, G., Koshelev, K., Zalogina, A., Korolev, V., Hollinger, R., Choi, D.-Y., Zuerch, M., Spielmann, C., Luther-Davies, B., Kartashov, D., Makarov, S. V., Kruk, S. S. & Kivshar, Y. "High-Harmonic Generation from Resonant Dielectric Metasurfaces Empowered by Bound States in the Continuum". *ACS Photonics* **9,** 567–574 (2022).

119. Overvig, A. C., Mann, S. A. & Alù, A. "Thermal Metasurfaces: Complete Emission Control by Combining Local and Nonlocal Light-Matter Interactions". *Physical Review X* **11,** 021050 (2021).

120. De Luca, F., Guddala, S., Cotrufo, M., Touma, J., Overvig, A. & Alù, A. "Nonlocal Metasurface Lens for Long-Wavelength Infrared Radiation". *Advanced Materials* **37,** e07848 (2025).

121. Song, J. H., van de Groep, J., Kim, S. J. & Brongersma, M. L. "Non-local metasurfaces for spectrally decoupled wavefront manipulation and eye tracking". *Nature Nanotechnology* **16,** 1224–1230 (2021).

122. Yesilkoy, F., Arvelo, E. R., Jahani, Y., Liu, M., Tittl, A., Cevher, V., Kivshar, Y. & Altug, H. "Ultrasensitive hyperspectral imaging and biodetection enabled by dielectric metasurfaces". *Nature Photonics* **13,** 390–396 (2019).

123. Wang, J., Kühne, J., Karamanos, T., Rockstuhl, C., Maier, S. A. & Tittl, A. "All-Dielectric Crescent Metasurface Sensor Driven by Bound States in the Continuum". *Advanced Functional Materials* **31,** 2104652 (2021).

124. Kühner, L., Sortino, L., Berté, R., Wang, J., Ren, H., Maier, S. A., Kivshar, Y. & Tittl, A. "Radial bound states in the continuum for polarization-invariant nanophotonics". *Nature Communications* **13,** 4992 (2022).

125. Hu, J., Safir, F., Chang, K., Dagli, S., Balch, H. B., Abendroth, J. M., Dixon, J., Moradifar, P., Dolia, V., Sahoo, M. K., Pinsky, B. A., Jeffrey, S. S., Lawrence, M. & Dionne, J. A. "Rapid genetic screening with high quality factor metasurfaces". *Nature Communications* **14,** 4486 (2023).

126. Wang, G., Chen, X., Liu, S., Wong, C. & Chu, S. "Mechanical Chameleon through Dynamic Real-Time Plasmonic Tuning". *ACS Nano* **10,** 1788–1794 (2016).

127. Yu, P., Li, J., Zhang, S., Jin, Z., Schütz, G., Qiu, C.-W., Hirscher, M. & Liu, N. "Dynamic Janus Metasurfaces in the Visible Spectral Region". *Nano Letters* **18,** 4584–4589 (2018).

128. Duan, X. & Liu, N. "Magnesium for Dynamic Nanoplasmonics". *Accounts of Chemical Research* **52,** 1979–1989 (2019).

129. Huang, M., Jun Tan, A., Büttner, F., Liu, H., Ruan, Q., Hu, W., Mazzoli, C., Wilkins, S., Duan, C., Yang, J. K. W. & Beach, G. S. D. "Voltage-gated optics and plasmonics enabled by solid-state proton pumping". *Nature Communications* **10,** 5030 (2019).

130. Li, Q., Van De Groep, J., White, A. K., Song, J.-H., Longwell, S. A., Fordyce, P. M., Quake, S. R., Kik, P. G. & Brongersma, M. L. "Metasurface optofluidics for dynamic control of light fields". *Nature Nanotechnology* **17,** 1097–1103 (2022).

131. Van de Groep, J., Li, Q., Song, J.-H., Kik, P. G. & Brongersma, M. L. "Impact of substrates and quantum effects on exciton line shapes of 2D semiconductors at room temperature". *Nanophotonics* **12,** 3291–3300 (2023).

132. Doshi, S., Ji, A., Mahdi, A. I., Keene, S. T., Selvin, S. P., Lalanne, P., Appel, E. A., Melosh, N. A. & Brongersma, M. L. "Electrochemically mutable soft metasurfaces". *Nature Materials* **24,** 205–211 (2025).

133. Xiong, K., Olsson, O., Svirelis, J., Palasingh, C., Baumberg, J. & Dahlin, A. "Video Speed Switching of Plasmonic Structural Colors with High Contrast and Superior Lifetime". *Advanced Materials* **33,** 2103217 (2021).

134. Kaissner, R., Li, J., Lu, W., Li, X., Neubrech, F., Wang, J. & Liu, N. "Electrochemically controlled metasurfaces with high-contrast switching at visible frequencies". *Science Advances* **7,** eabd9450 (2021).

135. Wu, W., Wang, M., Ma, J., Cao, Y. & Deng, Y. "Electrochromic Metal Oxides: Recent Progress and Prospect". *Advanced Electronic Materials* **4,** 1800185 (2018).

136. Li, Y., van de Groep, J., Talin, A. A. & Brongersma, M. L. "Dynamic Tuning of Gap Plasmon Resonances Using a Solid-State Electrochromic Device". *Nano Letters* **19,** 7988–7995 (2019).

137. Hopmann, E. & Elezzabi, A. Y. "Plasmochromic Nanocavity Dynamic Light Color Switching". *Nano Letters* **20,** 1876–1882 (2020).

138. Eaves-Rathert, J., Kovalik, E., Ugwu, C. F., Rogers, B. R., Pint, C. L. & Valentine, J. G. "Dynamic Color Tuning with Electrochemically Actuated TiO_2 Metasurfaces". *Nano Letters* **22,** 1626–1632 (2022).

139. Zhang, J., Yang, A., Wu, X., Van De Groep, J., Tang, P., Li, S., Liu, B., Shi, F., Wan, J., Li, Q., Sun, Y., Lu, Z., Zheng, X., Zhou, G., Wu, C.-L., Zhang, S.-C., Brongersma, M. L., Li, J. & Cui, Y. "Reversible and selective ion intercalation through the top surface of few-layer MoS2". *Nature Communications* **9,** 5289 (2018).

140. Gong, Y., Yuan, H., Wu, C.-L., Tang, P., Yang, S.-Z., Yang, A., Li, G., Liu, B., Van De Groep, J., Brongersma, M. L., Chisholm, M. F., Zhang, S.-C., Zhou, W. & Cui, Y. "Spatially controlled doping of two-dimensional SnS_2 through intercalation for electronics". *Nature Nanotechnology* **13,** 294–299 (2018).

141. Zhou, J., Lin, Z., Ren, H., Duan, X., Shakir, I., Huang, Y. & Duan, X. "Layered Intercalation Materials". *Advanced Materials* **33,** 2004557 (2021).

142. Salary, M. M. & Mosallaei, H. "Tunable All-Dielectric Metasurfaces for Phase-Only Modulation of Transmitted Light Based on Quasi-bound States in the Continuum". *ACS Photonics* **7,** 1813–1829 (2020).

143. Yu, R., Pruneri, V. & García De Abajo, F. J. "Resonant Visible Light Modulation with Graphene". *ACS Photonics* **2,** 550–558 (2015).

144. Back, P., Zeytinoglu, S., Ijaz, A., Kroner, M. & Imamoğlu, A. "Realization of an Electrically Tunable Narrow-Bandwidth Atomically Thin Mirror Using Monolayer $MoSe_2$". *Physical Review Letters* **120,** 03740 (2018).

145. Andersen, T. I., Gelly, R. J., Scuri, G., Dwyer, B. L., Wild, D. S., Bekenstein, R., Sushko, A., Sung, J., Zhou, Y., Zibrov, A. A., Liu, X., Joe, A. Y., Watanabe, K., Taniguchi, T., Yelin, S. F., Kim, P., Park, H. & Lukin, M. D. "Beam steering at the nanosecond time scale with an atomically thin reflector". *Nature Communications* **13,** 3431 (2022).

146. Li, M., Hail, C. U., Biswas, S. & Atwater, H. A. "Excitonic Beam Steering in an Active van der Waals Metasurface". *Nano Letters* **23,** 2771–2777 (2023).

147. Li, Q., Song, J.-H., Xu, F., Van De Groep, J., Hong, J., Daus, A., Lee, Y. J., Johnson, A. C., Pop, E., Liu, F. & Brongersma, M. L. "A Purcell-enabled monolayer semiconductor free-space optical modulator". *Nature Photonics* **17,** 897–903 (2023).

148. Guarneri, L., Bauer, T., Li, Q., Song, J.-H., Selvin, S., Saunders, A. P., Liu, F., Brongersma, M. L. & Van De Groep, J. "Dynamic Excitonic Beam Switching with Atomically-Thin Binary Blazed Gratings". *Advanced Optical Materials,* 2403257 (2025).

149. Seah, S. K. W., Biswas, S., Hail, C. U., Jang, M. S. & Atwater, H. A. "Efficient, Polarization-Diverse State Generation with Tunable Black Phosphorus Cavity Heterostructures and Active Metasurfaces". *ACS Photonics* **12,** 1409–1417 (2025).

150. Huang, Y.-W., Lee, H. W. H., Sokhoyan, R., Pala, R. A., Thyagarajan, K., Han, S., Tsai, D. P. & Atwater, H. A. "Gate-Tunable Conducting Oxide Metasurfaces". *Nano Letters* **16,** 5319–5325 (2016).

151. Park, J., Kang, J.-H., Kim, S. J., Liu, X. & Brongersma, M. L. "Dynamic Reflection Phase and Polarization Control in Metasurfaces". *Nano Letters* **17,** 407–413 (2017).

152. Kafaie Shirmanesh, G., Sokhoyan, R., Pala, R. A. & Atwater, H. A. "Dual-Gated Active Metasurface at 1550 nm with Wide (>300°) Phase Tunability". *Nano Letters* **18,** 2957–2963 (2018).

153. Shirmanesh, G. K., Sokhoyan, R., Wu, P. C. & Atwater, H. A. "Electro-optically Tunable Multifunctional Metasurfaces". *ACS Nano* **14,** 6912–6920 (2020).

154. Park, J., Jeong, B. G., Kim, S. I., Lee, D., Kim, J., Shin, C., Lee, C. B., Otsuka, T., Kyoung, J., Kim, S., Yang, K.-Y., Park, Y.-Y., Lee, J., Hwang, I., Jang, J., Song, S. H., Brongersma, M. L., Ha, K., Hwang, S.-W., Choo, H. & Choi, B. L. "All-solid-state spatial light modulator with independent phase and amplitude control for three-dimensional LiDAR applications". *Nature Nanotechnology* **16,** 69–76 (2021).

155. Wu, P. C., Sokhoyan, R., Shirmanesh, G. K., Cheng, W.-H. & Atwater, H. A. "Near-Infrared Active Metasurface for Dynamic Polarization Conversion". *Advanced Optical Materials* **9,** 2100230 (2021).

156. Damgaard-Carstensen, C. & Bozhevolnyi, S. I. "Nonlocal electro-optic metasurfaces for free-space light modulation". *Nanophotonics* **12,** 2953–2962 (2023).

157. Komar, A., Fang, Z., Bohn, J., Sautter, J., Decker, M., Miroshnichenko, A., Pertsch, T., Brener, I., Kivshar, Y. S., Staude, I. & Neshev, D. N. "Electrically tunable all-dielectric optical metasurfaces based on liquid crystals". *Applied Physics Letters* **110,** 071109 (2017).

158. Li, S.-Q., Xu, X., Maruthiyodan Veetil, R., Valuckas, V., Paniagua-Domínguez, R. & Kuznetsov, A. I. "Phase-only transmissive spatial light modulator based on tunable dielectric metasurface". *Science* **364,** 1087–1090 (2019).

159. Hu, Y., Ou, X., Zeng, T., Lai, J., Zhang, J., Li, X., Luo, X., Li, L., Fan, F. & Duan, H. "Electrically Tunable Multifunctional Polarization-Dependent Metasurfaces Integrated with Liquid Crystals in the Visible Region". *Nano Letters* **21,** 4554–4562 (2021).

160. Bosch, M., Shcherbakov, M. R., Won, K., Lee, H.-S., Kim, Y. & Shvets, G. "Electrically Actuated Varifocal Lens Based on Liquid-Crystal-Embedded Dielectric Metasurfaces". *Nano Letters* **21,** 3849–3856 (2021).

161. Wu, P. C., Pala, R. A., Kafaie Shirmanesh, G., Cheng, W.-H., Sokhoyan, R., Grajower, M., Alam, M. Z., Lee, D. & Atwater, H. A. "Dynamic beam steering with all-dielectric electro-optic III–V multiple-quantum-well metasurfaces". *Nature Communications* **10,** 3654 (2019).

162. Yao, E., Su, Z., Bi, Y., Wang, Y. & Huang, L. "Tunable quasi-bound states in the continuum in magneto-optical metasurfaces". *Journal of Physics D: Applied Physics* **57,** 375104 (2024).

163. Bi, Y., Huang, L., Li, T., Wang, C., Zou, X., Zhou, L. & Kang, G. "Active metasurface via magnetic control for tri-channel polarization multiplexing holography". *Chinese Optics Letters* **22,** 043601 (2024).

164. Gutruf, P., Zou, C., Withayachumnankul, W., Bhaskaran, M., Sriram, S. & Fumeaux, C. "Mechanically Tunable Dielectric Resonator Metasurfaces at Visible Frequencies". *ACS Nano* **10,** 133–141 (2016).

165. Malek, S. C., Ee, H.-S. & Agarwal, R. "Strain Multiplexed Metasurface Holograms on a Stretchable Substrate". *Nano Letters* **17,** 3641–3645 (2017).

166. Chen, W., Liu, W., Jiang, Y., Zhang, M., Song, N., Greybush, N. J., Guo, J., Estep, A. K., Turner, K. T., Agarwal, R. & Kagan, C. R. "Ultrasensitive, Mechanically Responsive Optical Metasurfaces *via* Strain Amplification". *ACS Nano* **12,** 10683–10692 (2018).

167. Tao, W., Haas, J., Wu, Y., Simo, P. C., d'Orsonnens, W., Hmima, A., Laible, F., Meyer, J., Maurer, T. & Fleischer, M. "Dynamic tuning of surface lattice resonances via mechano-optical coupling in flexible nanoring metasurfaces". *Applied Physics Letters* **126,** 201707 (2025).

168. Arbabi, E., Arbabi, A., Kamali, S. M., Horie, Y., Faraji-Dana, M. & Faraon, A. "MEMS-tunable dielectric metasurface lens". *Nature Communications* **9,** 812 (2018).

169. Holsteen, A. L., Cihan, A. F. & Brongersma, M. L. "Temporal color mixing and dynamic beam shaping with silicon metasurfaces". *Science* **365,** 257–260 (2019).

170. Han, Z., Colburn, S., Majumdar, A. & Böhringer, K. F. "MEMS-actuated metasurface Alvarez lens". *Microsystems & Nanoengineering* **6,** 79 (2020).

171. Chen, S., Wei, W., Liu, Z., Liu, X., Feng, S., Guo, H. & Li, J. "Reconfigurable nano-kirigami metasurfaces by pneumatic pressure". *Photonics Research* **8,** 1177–1182 (2020).

172. Van Gorp, F., Liu, W., Coulais, C. & van de Groep, J. "Nonlocal Mechano-Optical Metasurfaces". *ACS Photonics* **12,** 5978–5984 (2025).

173. Liu, J., Zeng, H., Cheng, M., Wang, Z., Wang, J., Cen, M., Luo, D., Priimagi, A. & Liu, Y. J. "Photoelastic plasmonic metasurfaces with ultra-large near infrared spectral tuning". *Materials Horizons* **9,** 942–951 (2022).

174. Smalley, D. E., Smithwick, Q. Y. J., Bove, V. M., Barabas, J. & Jolly, S. "Anisotropic leaky-mode modulator for holographic video displays". *Nature* **498,** 313–317 (2013).

175. Li, B., Lin, Q. & Li, M. "Frequency–angular resolving LiDAR using chip-scale acousto-optic beam steering". *Nature* **620,** 316–322 (2023).

176. Yuan, J., Li, P., Song, J., Yang, S., Lu, C., Zhang, X., Feng, T. & Li, Z. "Enhancing Brillouin Scattering with Chalcogenide Metasurfaces of Optical Bound States in the Continuum and Mechanical Resonances". *Laser & Photonics Reviews* **18,** 2400763 (2024).

177. Lloyd, D., Liu, X., Christopher, J. W., Cantley, L., Wadehra, A., Kim, B. L., Goldberg, B. B., Swan, A. K. & Bunch, J. S. "Band Gap Engineering with Ultralarge Biaxial Strains in Suspended Monolayer MoS2". *Nano Letters* **16,** 5836–5841 (2016).

178. Carrascoso, F., Lin, D. Y., Frisenda, R. & Castellanos-Gomez, A. "Biaxial strain tuning of interlayer excitons in bilayer MoS_2". *JPhys Materials* **3** (2020).

179. Peng, Z., Chen, X., Fan, Y., Srolovitz, D. J. & Lei, D. "Strain engineering of 2D semiconductors and graphene: from strain fields to band-structure tuning and photonic applications". *Light: Science & Applications* **9,** 190 (2020).

180. Aslan, B., Yule, C., Yu, Y., Lee, Y. J., Heinz, T. F., Cao, L. & Brongersma, M. L. "Excitons in strained and suspended monolayer WSe_2". *2D Materials* **9,** 015002 (2022).

181. Alam, M. Z., De Leon, I. & Boyd, R. W. "Large optical nonlinearity of indium tin oxide in its epsilon-near-zero region". *Science* **352,** 795–797 (2016).

182. Shcherbakov, M. R., Vabishchevich, P. P., Shorokhov, A. S., Chong, K. E., Choi, D.-Y., Staude, I., Miroshnichenko, A. E., Neshev, D. N., Fedyanin, A. A. & Kivshar, Y. S. "Ultrafast All-Optical Switching with Magnetic Resonances in Nonlinear Dielectric Nanostructures". *Nano Letters* **15,** 6985–6990 (2015).

183. Yang, Y., Wang, W., Boulesbaa, A., Kravchenko, I. I., Briggs, D. P., Puretzky, A., Geohegan, D. & Valentine, J. "Nonlinear Fano-Resonant Dielectric Metasurfaces". *Nano Letters* **15,** 7388–7393 (2015).

184. Della Valle, G., Hopkins, B., Ganzer, L., Stoll, T., Rahmani, M., Longhi, S., Kivshar, Y. S., De Angelis, C., Neshev, D. N. & Cerullo, G. "Nonlinear Anisotropic Dielectric Metasurfaces for Ultrafast Nanophotonics". *ACS Photonics* **4,** 2129–2136 (2017).

185. Bijloo, F., Murzyn, K., Van Emmerik, F., Den Boef, A. J., Kraus, P. M. & Koenderink, A. F. "Near-Unity All-Optical Modulation of Third-Harmonic Generation with a Fano-Resonant Dielectric Metasurface". *Nano Letters,* acs.nanolett.4c03536 (2024).

186. Bijloo, F., Ogienko, M., Den Boef, A. J., Kraus, P. M. & Koenderink, A. F. "All-Optical Nonlinear Real and Fourier-Space Shaping with All-Dielectric Fano Resonant Metasurfaces". *ACS Nano* **20,** 4845–4854 (2026).

187. Baranov, D. G., Makarov, S. V., Milichko, V. A., Kudryashov, S. I., Krasnok, A. E. & Belov, P. A. "Nonlinear Transient Dynamics of Photoexcited Resonant Silicon Nanostructures". *ACS Photonics* **3,** 1546–1551 (2016).

188. Shcherbakov, M. R., Liu, S., Zubyuk, V. V., Vaskin, A., Vabishchevich, P. P., Keeler, G., Pertsch, T., Dolgova, T. V., Staude, I., Brener, I. & Fedyanin, A. A. "Ultrafast all-optical tuning of direct-gap semiconductor metasurfaces". *Nature Communications* **8,** 17 (2017).

189. Cheng, Y., Hong, H., Zhao, H., Wu, C., Pan, Y., Liu, C., Zuo, Y., Zhang, Z., Xie, J., Wang, J., Yu, D., Ye, Y., Meng, S. & Liu, K. "Ultrafast Optical Modulation of Harmonic Generation in Two-Dimensional Materials". *Nano Letters* **20,** 8053–8058 (2020).

190. Taghinejad, M., Xu, Z., Wang, H., Taghinejad, H., Lee, K.-T., Rodrigues, S. P., Adibi, A., Qian, X., Lian, T. & Cai, W. "Photocarrier-Induced Active Control of Second-Order Optical Nonlinearity in Monolayer MoS2". *Small* **16,** 1906347 (2020).

191. Klimmer, S., Ghaebi, O., Gan, Z., George, A., Turchanin, A., Cerullo, G. & Soavi, G. "All-optical polarization and amplitude modulation of second-harmonic generation in atomically thin semiconductors". *Nature Photonics* **15,** 837–842 (2021).

192. Li, Z., Zhou, Y., Qi, H., Pan, Q., Zhang, Z., Shi, N. N., Lu, M., Stein, A., Li, C. Y., Ramanathan, S. & Yu, N. "Correlated Perovskites as a New Platform for Super-Broadband-Tunable Photonics". *Advanced Materials* **28,** 9117–9125 (2016).

193. Zhu, Z., Evans, P. G., Haglund, R. F. & Valentine, J. G. "Dynamically Reconfigurable Metadevice Employing Nanostructured Phase-Change Materials". *Nano Letters* **17,** 4881–4885 (2017).

194. Kang, T., Ma, Z., Qin, J., Peng, Z., Yang, W., Huang, T., Xian, S., Xia, S., Yan, W., Yang, Y., Sheng, Z., Shen, J., Li, C., Deng, L. & Bi, L. "Large-scale, power-efficient Au/VO_2 active metasurfaces for ultrafast optical modulation". *Nanophotonics* **10,** 909–918 (2021).

195. Kim, Y., Wu, P. C., Sokhoyan, R., Mauser, K., Glaudell, R., Kafaie Shirmanesh, G. & Atwater, H. A. "Phase Modulation with Electrically Tunable Vanadium Dioxide Phase-Change Metasurfaces". *Nano Letters* **19,** 3961–3968 (2019).

196. Wang, Y., Landreman, P., Schoen, D., Okabe, K., Marshall, A., Celano, U., Wong, H.-S. P., Park, J. & Brongersma, M. L. "Electrical tuning of phase-change antennas and metasurfaces". *Nature Nanotechnology* **16,** 667–672 (2021).

197. Abdollahramezani, S., Hemmatyar, O., Taghinejad, M., Taghinejad, H., Kiarashinejad, Y., Zandehshahvar, M., Fan, T., Deshmukh, S., Eftekhar, A. A., Cai, W., Pop, E., El-Sayed, M. A. & Adibi, A. "Dynamic Hybrid Metasurfaces". *Nano Letters* **21,** 1238–1245 (2021).

198. Liu, T., Zhang, D., Liu, W., Yu, T., Wu, F., Xiao, S., Huang, L. & Miroshnichenko, A. E. "Phase-change nonlocal metasurfaces for dynamic wave-front manipulation". *Physical Review Applied* **21,** 044004 (2024).

199. Popescu, C. C., Aryana, K., Garud, P., Dao, K. P., Vitale, S., Liberman, V., Bae, H.-B., Lee, T.-W., Kang, M., Richardson, K. A., Julian, M., Ocampo, C. A. R., Zhang, Y., Gu, T., Hu, J. & Kim, H. J. "Electrically Reconfigurable Phase-Change Transmissive Metasurface". *Advanced Materials* **36,** 2400627 (2024).

200. Bohn, J., Bucher, T., Chong, K. E., Komar, A., Choi, D.-Y., Neshev, D. N., Kivshar, Y. S., Pertsch, T. & Staude, I. "Active Tuning of Spontaneous Emission by Mie-Resonant Dielectric Metasurfaces". *Nano Letters* **18,** 3461–3465 (2018).

201. Komar, A., Paniagua-Domínguez, R., Miroshnichenko, A., Yu, Y. F., Kivshar, Y. S., Kuznetsov, A. I. & Neshev, D. "Dynamic Beam Switching by Liquid Crystal Tunable Dielectric Metasurfaces". *ACS Photonics* **5,** 1742–1748 (2018).

202. Iyer, P. P., Pendharkar, M., Palmstrøm, C. J. & Schuller, J. A. "Ultrawide thermal free-carrier tuning of dielectric antennas coupled to epsilon-near-zero substrates". *Nature Communications* **8,** 472 (2017).

203. Rahmani, M., Xu, L., Miroshnichenko, A. E., Komar, A., Camacho-Morales, R., Chen, H., Zárate, Y., Kruk, S., Zhang, G., Neshev, D. N. & Kivshar, Y. S. "Reversible Thermal Tuning of All-Dielectric Metasurfaces". *Advanced Functional Materials* **27,** 1700580 (2017).

204. Horie, Y., Arbabi, A., Arbabi, E., Kamali, S. M. & Faraon, A. "High-Speed, Phase-Dominant Spatial Light Modulation with Silicon-Based Active Resonant Antennas". *ACS Photonics* **5,** 1711–1717 (2018).

205. Sokhoyan, R., Hail, C. U., Foley, M., Grajower, M. Y. & Atwater, H. A. "All-Dielectric High-Q Dynamically Tunable Transmissive Metasurfaces". *Laser & Photonics Reviews* **18,** 2300980 (2024).

206. Yang, S. & Ndukaife, J. C. "Optofluidic transport and assembly of nanoparticles using an all-dielectric quasi-BIC metasurface". *Light: Science & Applications* **12,** 188 (2023).

207. Kollipara, P. S., Chen, Z. & Zheng, Y. "Optical Manipulation Heats up: Present and Future of Optothermal Manipulation". *ACS Nano* **17,** 7051–7063 (2023).

208. Zheludev, N. I. & Kivshar, Y. S. "From metamaterials to metadevices". *Nature Materials* **11,** 917–924 (2012).

209. Brongersma, M. L. "The road to atomically thin metasurface optics". *Nanophotonics* **10,** 643–654 (2020).

210. Gu, T., Kim, H. J., Rivero-Baleine, C. & Hu, J. "Reconfigurable metasurfaces towards commercial success". *Nature Photonics* **17,** 48–58 (2023).

211. Jung, C., Lee, E. & Rho, J. "The rise of electrically tunable metasurfaces". *Science Advances* **10,** eado8964 (2024).

212. Scuri, G., Zhou, Y., High, A. A., Wild, D. S., Shu, C., De Greve, K., Jauregui, L. A., Taniguchi, T., Watanabe, K., Kim, P., Lukin, M. D. & Park, H. "Large Excitonic Reflectivity of Monolayer $MoSe_2$ Encapsulated in Hexagonal Boron Nitride". *Physical Review Letters* **120,** 037402 (2018).

213. Epstein, I., Terrés, B., Chaves, A. J., Pusapati, V. V., Rhodes, D. A., Frank, B., Zimmermann, V., Qin, Y., Watanabe, K., Taniguchi, T., Giessen, H., Tongay, S., Hone, J. C., Peres, N. M. & Koppens, F. H. "Near-unity light absorption in a monolayer WS_2 van der Waals heterostructure cavity". *Nano Letters* **20,** 3545–3552 (2020).

214. Azimi, A., Barrier, J., Barreda, A., Bauer, T., Bouzari, F., Brokkelkamp, A., Buatier de Mongeot, F., Parsons, T., Christianen, P., Conesa-Boj, S., Curto, A. G., Das, S., Dias, B., Epstein, I., Fedorova, Z., García de Abajo, F. J., Goykhman, I., Greten, L., Grönqvist, J., Guarneri, L., Guo, Y., Hoekstra, T., Hu, X., Laudert, B., Lynch, J., Meyer, S., Munkhbat, B., Neshev, D., Ogienko, M., Papadopoulos, S., Parappurath, A., Sangers, J., Soubelet, P., Soukaras, C., Soavi, G., Staude, I., Sun, Z., Tielrooij, K.-J., Uddin, M. G., Ustinov, A., van de Groep, J., van Wezel, J., Vermeulen, N., Wang, H., Wang, Y., Xiao, S., You, B. & Zambrana-Puyalto, X. "Photonics in Flatland: challenges and opportunities for nanophotonics with 2D semiconductors". *npj Nanophotonics* **2,** 44 (2025).

215. Geim, A. K. & Novoselov, K. S. "The rise of graphene". *Nature Materials* **6,** 183–191 (2007).

216. Novoselov, K. S., Geim, A. K., Morozov, S. V., Jiang, D., Zhang, Y., Dubonos, S. V., Grigorieva, I. V. & Firsov, A. A. "Electric Field Effect in Atomically Thin Carbon Films". *Science* **306,** 666–669 (2004).

217. Novoselov, K. S., Jiang, D., Schedin, F., Booth, T. J., Khotkevich, V. V., Morozov, S. V. & Geim, A. K. "Two-dimensional atomic crystals". *Proceedings of the National Academy of Sciences of the United States of America* **102,** 10451–10453 (2005).

218. Haastrup, S., Strange, M., Pandey, M., Deilmann, T., Schmidt, P. S., Hinsche, N. F., Gjerding, M. N., Torelli, D., Larsen, P. M., Riis-Jensen, A. C., Gath, J., Jacobsen, K. W., Jørgen Mortensen, J., Olsen, T. & Thygesen, K. S. "The Computational 2D Materials Database: high-throughput modeling and discovery of atomically thin crystals". *2D Materials* **5,** 042002 (2018).

219. Zhou, J., Shen, L., Costa, M. D., Persson, K. A., Ong, S. P., Huck, P., Lu, Y., Ma, X., Chen, Y., Tang, H. & Feng, Y. P. "2DMatPedia, an open computational database of two-dimensional materials from top-down and bottom-up approaches". *Scientific Data* **6,** 86 (2019).

220. Choudhary, K., Garrity, K. F., Reid, A. C. E., DeCost, B., Biacchi, A. J., Hight Walker, A. R., Trautt, Z., Hattrick-Simpers, J., Kusne, A. G., Centrone, A., Davydov, A., Jiang, J., Pachter, R., Cheon, G., Reed, E., Agrawal, A., Qian, X., Sharma, V., Zhuang, H., Kalinin, S. V., Sumpter, B. G., Pilania, G., Acar, P., Mandal, S., Haule, K., Vanderbilt, D., Rabe, K. & Tavazza, F. "The joint automated repository for various integrated simulations (JARVIS) for data-driven materials design". *npj Computational Materials* **6,** 173 (2020).

221. Chhowalla, M., Shin, H. S., Eda, G., Li, L. J., Loh, K. P. & Zhang, H. "The chemistry of two-dimensional layered transition metal dichalcogenide nanosheets". *Nature Chemistry* **5,** 263–275 (2013).

222. Mak, K. F. & Shan, J. "Photonics and optoelectronics of 2D semiconductor transition metal dichalcogenides". *Nature Photonics* **10,** 216–226 (2016).

223. Manzeli, S., Ovchinnikov, D., Pasquier, D., Yazyev, O. V. & Kis, A. "2D transition metal dichalcogenides". *Nature Reviews Materials* **2,** 17033 (2017).

224. Mak, K. F., Lee, C., Hone, J., Shan, J. & Heinz, T. F. "Atomically thin MoS2: A new direct-gap semiconductor". *Physical Review Letters* **105,** 2–5 (2010).

225. Tonndorf, P., Schmidt, R., Böttger, P., Zhang, X., Börner, J., Liebig, A., Albrecht, M., Kloc, C., Gordan, O., Zahn, D. R. T., Vasconcellos, S. M. de & Bratschitsch, R. "Photoluminescence emission and Raman response of monolayer MoS_2, $MoSe_2$, and WSe_2". *Optics Express* **21,** 4908–4916 (2013).

226. Chernikov, A., Berkelbach, T. C., Hill, H. M., Rigosi, A., Li, Y., Aslan, O. B., Reichman, D. R., Hybertsen, M. S. & Heinz, T. F. "Exciton Binding Energy and Nonhydrogenic Rydberg Series in Monolayer WS_2". *Physical Review Letters* **113,** 076802 (2014).

227. Moody, G., Kavir Dass, C., Hao, K., Chen, C.-H., Li, L.-J., Singh, A., Tran, K., Clark, G., Xu, X., Berghäuser, G., Malic, E., Knorr, A. & Li, X. "Intrinsic homogeneous linewidth and broadening mechanisms of excitons in monolayer transition metal dichalcogenides". *Nature Communications* **6,** 8315 (2015).

228. Xiao, D., Liu, G. B., Feng, W., Xu, X. & Yao, W. "Coupled spin and valley physics in monolayers of MoS_2 and other group-VI dichalcogenides". *Physical Review Letters* **108,** 1–5 (2012).

229. Mak, K. F., He, K., Lee, C., Lee, G. H., Hone, J., Heinz, T. F. & Shan, J. "Tightly bound trions in monolayer MoS_2". *Nature Materials* **12,** 207–211 (2013).

230. Arora, A., Deilmann, T., Reichenauer, T., Kern, J., Michaelis De Vasconcellos, S., Rohlfing, M. & Bratschitsch, R. "Excited-State Trions in Monolayer WS_2". *Physical Review Letters* **123,** 167401 (2019).

231. Lu, X. & Yang, L. "Stark effect of doped two-dimensional transition metal dichalcogenides". *Applied Physics Letters* **111,** 193104 (2017).

232. Rostami, H. & Asgari, R. "Valley Zeeman effect and spin-valley polarized conductance in monolayer MoS_2 in a perpendicular magnetic field". *Physical Review B* **91,** 075433 (2015).

233. Chernikov, A., Van Der Zande, A. M., Hill, H. M., Rigosi, A. F., Velauthapillai, A., Hone, J. & Heinz, T. F. "Electrical Tuning of Exciton Binding Energies in Monolayer WS_2". *Physical Review Letters* **115,** 126802 (2015).

234. Anichini, C., Czepa, W., Pakulski, D., Aliprandi, A., Ciesielski, A. & Samorì, P. "Chemical sensing with 2D materials". *Chemical Society Reviews* **47,** 4860–4908 (2018).

235. Ryu, Y. K., Carrascoso, F., López-Nebreda, R., Agraït, N., Frisenda, R. & Castellanos-Gomez, A. "Microheater Actuators as a Versatile Platform for Strain Engineering in 2D Materials". *Nano Letters* **20,** 5339–5345 (2020).

236. Geim, A. K. & Grigorieva, I. V. "Van der Waals heterostructures". *Nature* **499,** 419–425 (2013).

237. Novoselov, K. S., Mishchenko, A., Carvalho, A. & Castro Neto, A. H. "2D materials and van der Waals heterostructures". *Science* **353,** aac9439 (2016).

238. Hattori, Y., Taniguchi, T., Watanabe, K. & Nagashio, K. "Anisotropic Dielectric Breakdown Strength of Single Crystal Hexagonal Boron Nitride". *ACS Applied Materials & Interfaces* **8,** 27877–27884 (2016).

239. Pierret, A., Mele, D., Graef, H., Palomo, J., Taniguchi, T., Watanabe, K., Li, Y., Toury, B., Journet, C., Steyer, P., Garnier, V., Loiseau, A., Berroir, J.-M., Bocquillon, E., Fève, G., Voisin, C., Baudin, E., Rosticher, M. & Plaçais, B. "Dielectric permittivity, conductivity and breakdown field of hexagonal boron nitride". *Materials Research Express* **9,** 065901 (2022).

240. Grimaldi, G., Schuringa, I., Geuchies, J. J., Rigter, S. A., Hoekstra, T., Versluis, J., Hidalgo, J., Correa-Baena, J.-P., Van De Groep, J., Kim, H., Bonn, M. & Ehrler, B. "Atmospheric Exposure Triggers Light-Induced Degradation in 2D Lead-Halide Perovskites". *ACS Energy Letters,* 5771–5779 (2024).

241. Lien, D. H., Uddin, S. Z., Yeh, M., Amani, M., Kim, H., Ager, J. W., Yablonovitch, E. & Javey, A. "Electrical suppression of all nonradiative recombination pathways in monolayer semiconductors". *Science* **364,** 468–471 (2019).

242. Li, M., Michaeli, L. & Atwater, H. A. "Electrically Tunable Topological Singularities in Excitonic Two-Dimensional Heterostructures for Wavefront Manipulation". *ACS Photonics* **11,** 3554–3562 (2024).

243. Lynch, J., Kumar, P., Chen, C., Trainor, N., Kumari, S., Peng, T.-Y., Chen, C. Y., Lu, Y.-J., Redwing, J. & Jariwala, D. "Full 2π phase modulation using exciton-polaritons in a two-dimensional superlattice". *Device* **3** (2025).

244. Yu, Y. & Cao, L. "Coupled leaky mode theory for light absorption in 2D, 1D, and 0D semiconductor nanostructures". *Optics Express* **20,** 13847 (2012).

245. Wang, Z., Sebek, M., Liang, X., Elbanna, A., Nemati, A., Zhang, N., Goh, C. H. K., Jiang, M., Pan, J., Shen, Z., Su, X., Thanh, N. T. K., Sun, H. & Teng, J. "Greatly Enhanced Resonant Exciton-Trion Conversion in Electrically Modulated Atomically Thin WS_2 at Room Temperature". *Advanced Materials* **35,** 2302248 (2023).

246. Fernandez, H. A., Withers, F., Russo, S. & Barnes, W. L. "Electrically Tuneable Exciton-Polaritons through Free Electron Doping in Monolayer WS_2 Microcavities". *Advanced Optical Materials* **7,** 1900484 (2019).

247. Chen, Y., Miao, S., Wang, T., Zhong, D., Saxena, A., Chow, C., Whitehead, J., Gerace, D., Xu, X., Shi, S. F. & Majumdar, A. "Metasurface Integrated Monolayer Exciton Polariton". *Nano Letters* **20,** 5292–5300 (2020).

248. Liu, B., Lynch, J., Zhao, H., Conran, B. R., McAleese, C., Jariwala, D. & Forrest, S. R. "Long-Range Propagation of Exciton-Polaritons in Large-Area 2D Semiconductor Monolayers". *ACS Nano* **17,** 14442–14448 (2023).

249. Zhang, H., Abhiraman, B., Zhang, Q., Miao, J., Jo, K., Roccasecca, S., Knight, M. W., Davoyan, A. R. & Jariwala, D. "Hybrid exciton-plasmon-polaritons in van der Waals semiconductor gratings". *Nature Communications* **11,** 3552 (2020).

250. Shen, F., Liu, D., Chen, Z., Zhu, J., Jin, S., Zhao, X., Ma, Y., Lei, D. & Xu, J. "Manipulating the intrinsic light–matter interaction with high-Q resonances in an etch-free van der Waals metasurface". *Optica* **12,** 1702 (2025).

251. Sortino, L., Biechteler, J., Lafeta, L., Kühner, L., Hartschuh, A., Menezes, L. d. S., Maier, S. A. & Tittl, A. "Atomic-layer assembly of ultrathin optical cavities in van der Waals heterostructure metasurfaces". *Nature Photonics* **19,** 825–832 (2025).

252. Li, M., Biswas, S., Hail, C. U. & Atwater, H. A. "Refractive Index Modulation in Monolayer Molybdenum Diselenide". *Nano Letters* **21,** 7602–7608 (2021).

253. Guarneri, L., Li, Q., Bauer, T., Song, J.-H., Saunders, A. P., Liu, F., Brongersma, M. L. & van de Groep, J. "Temperature-Dependent Excitonic Light Manipulation with Atomically Thin Optical Elements". *Nano Letters* **24,** 6240–6246 (2024).

254. Li, Y., Chernikov, A., Zhang, X., Rigosi, A., Hill, H. M., Van Der Zande, A. M., Chenet, D. A., Shih, E. M., Hone, J. & Heinz, T. F. "Measurement of the optical dielectric function of monolayer transition-metal dichalcogenides: MoS_2, $MoSe_2$, WS_2, and WSe_2". *Physical Review B* **90,** 205422 (2014).

255. Hsu, C., Frisenda, R., Schmidt, R., Arora, A., de Vasconcellos, S. M., Bratschitsch, R., van der Zant, H. S. & Castellanos-Gomez, A. "Thickness-Dependent Refractive Index of 1L, 2L, and 3L MoS_2, $MoSe_2$, WS_2, and WSe_2". *Advanced Optical Materials* **7,** 1900239 (2019).

256. Tauc, J., Grigorovici, R. & Vancu, A. "Optical Properties and Electronic Structure of Amorphous Germanium". *physica status solidi (b)* **15,** 627–637 (1966).

257. Ermolaev, G. A., Yakubovsky, D. I., Stebunov, Y. V., Arsenin, A. V. & Volkov, V. S. "Spectral ellipsometry of monolayer transition metal dichalcogenides: Analysis of excitonic peaks in dispersion". *Journal of Vacuum Science & Technology B* **38,** 014002 (2019).

258. Lizárraga, K., Villegas, C. E. P., Lira, R., Serquen, E., Liu, H.-L., Guerra, J. A., Rocha, A. R. & Venezuela, P. "Dispersion model for the optical absorption of two-dimensional materials". *Physical Review B* **113,** 045410 (2026).

259. Andreani, L. C., Tassone, F. & Bassani, F. "Radiative lifetime of free excitons in quantum wells". *Solid State Communications* **77,** 641–645 (1991).

260. Ivčenko, E. L. & Ivčenko, E. L. *Optical spectroscopy of semiconductor nanostructures* 427 pp. (Alpha Science International Ltd, Harrow, UK, 2005).

261. Li, Y. & Heinz, T. F. "Two-dimensional models for the optical response of thin films". *2D Materials* **5,** 025021 (2018).

262. Atash Kahlon, A., Meshulam, M., Eini, T., Poirier, T., Edgar, J. H., Tongay, S. A. & Epstein, I. "Importance of pure dephasing in the optical response of excitons in high-quality van der Waals heterostructures". *Physical Review B* **112,** L041402 (2025).

263. Yu, Y., Yu, Y., Huang, L., Peng, H., Xiong, L. & Cao, L. "Giant Gating Tunability of Optical Refractive Index in Transition Metal Dichalcogenide Monolayers". *Nano Letters* **17,** 3613–3618 (2017).

264. Selig, M., Berghäuser, G., Raja, A., Nagler, P., Schüller, C., Heinz, T. F., Korn, T., Chernikov, A., Malic, E. & Knorr, A. "Excitonic linewidth and coherence lifetime in monolayer transition metal dichalcogenides". *Nature Communications* **7,** 13279 (2016).

265. Chernikov, A., Ruppert, C., Hill, H. M., Rigosi, A. F. & Heinz, T. F. "Population inversion and giant bandgap renormalization in atomically thin WS_2 layers". *Nature Photonics* **9,** 466–470 (2015).

266. Moody, G., Schaibley, J. & Xu, X. "Exciton dynamics in monolayer transition metal dichalcogenides". *Journal of the Optical Society of America B* **33,** C39 (2016).

267. Katsch, F. & Knorr, A. "Excitonic theory of doping-dependent optical response in atomically thin semiconductors". *Physical Review B* **105,** 045301 (2022).

268. Rhodes, D., Chae, S. H., Ribeiro-Palau, R. & Hone, J. "Disorder in van der Waals heterostructures of 2D materials". *Nature Materials* **18,** 541–549 (2019).

269. Sze, S. M. & Ng, K. K. *Physics of semiconductor devices* 3rd ed. 815 pp. (Wiley-Interscience, Hoboken, N.J, 2007).

270. Brumme, T., Calandra, M. & Mauri, F. "First-principles theory of field-effect doping in transition-metal dichalcogenides: Structural properties, electronic structure, Hall coefficient, and electrical conductivity". *Physical Review B* **91,** 155436 (2015).

271. Ma, N. & Jena, D. "Carrier statistics and quantum capacitance effects on mobility extraction in two-dimensional crystal semiconductor field-effect transistors". *2D Materials* **2,** 015003 (2015).

272. Luryi, S. "Quantum capacitance devices". *Applied Physics Letters* **52,** 501–503 (1988).

273. Snyder, A. W. & Love, J. D. *Optical waveguide theory* **190.** 734 pp. (Chapman and Hall, London ; New York, 1983).

274. Benisty, H., Greffet, J.-J. & Lalanne, P. *Introduction to nanophotonics* 655 pp. (Oxford University Press, 2022).

275. Liu, Y., Guo, J., Zhu, E., Liao, L., Lee, S.-J., Ding, M., Shakir, I., Gambin, V., Huang, Y. & Duan, X. "Approaching the Schottky–Mott limit in van der Waals metal–semiconductor junctions". *Nature* **557,** 696–700 (2018).

276. Allain, A., Kang, J., Banerjee, K. & Kis, A. "Electrical contacts to two-dimensional semiconductors". *Nature Materials* **14,** 1195–1205 (2015).

277. Bandyopadhyay, A. S., Saenz, G. A. & Kaul, A. B. "Role of metal contacts and effect of annealing in high performance 2D WSe_2 field-effect transistors". *Surface and Coatings Technology* **381** (August 2019 2020).

278. Bastante, P., Pucher, T. & Castellanos-Gomez, A. "Influence of vacuum thermal annealing and air exposure on the performance of single-layer MoS_2 devices". *Nanotechnology* **35,** 485201 (2024).

279. Wang, Y., Kim, J. C., Wu, R. J., Martinez, J., Song, X., Yang, J., Zhao, F., Mkhoyan, A., Jeong, H. Y. & Chhowalla, M. "Van der Waals contacts between three-dimensional metals and two-dimensional semiconductors". *Nature* **568,** 70–74 (2019).

280. Shen, P.-C., Su, C., Lin, Y., Chou, A.-S., Cheng, C.-C., Park, J.-H., Chiu, M.-H., Lu, A.-Y., Tang, H.-L., Tavakoli, M. M., Pitner, G., Ji, X., Cai, Z., Mao, N., Wang, J., Tung, V., Li, J., Bokor, J., Zettl, A., Wu, C.-I., Palacios, T., Li, L.-J. & Kong, J. "Ultralow contact resistance between semimetal and monolayer semiconductors". *Nature* **593,** 211–217 (2021).

281. Cheng, Z., Yu, Y., Singh, S., Price, K., Noyce, S. G., Lin, Y.-C., Cao, L. & Franklin, A. D. "Immunity to Contact Scaling in MoS_2 Transistors Using in Situ Edge Contacts". *Nano Letters* **19,** 5077–5085 (2019).

282. Huang, Y., Pan, Y.-H., Yang, R., Bao, L.-H., Meng, L., Luo, H.-L., Cai, Y.-Q., Liu, G.-D., Zhao, W.-J., Zhou, Z., Wu, L.-M., Zhu, Z.-L., Huang, M., Liu, L.-W., Liu, L., Cheng, P., Wu, K.-H., Tian, S.-B., Gu, C.-Z., Shi, Y.-G., Guo, Y.-F., Cheng, Z. G., Hu, J.-P., Zhao, L., Yang, G.-H., Sutter, E., Sutter, P., Wang, Y.-L., Ji, W., Zhou, X.-J. & Gao, H.-J. "Universal mechanical exfoliation of large-area 2D crystals". *Nature Communications* **11,** 2453 (2020).

283. Liu, F., Wu, W., Bai, Y., Chae, S. H., Li, Q., Wang, J., Hone, J. & Zhu, X.-Y. "Disassembling 2D van der Waals crystals into macroscopic monolayers and reassembling into artificial lattices". *Science* **367,** 903–906 (2020).

284. Sozen, Y., Riquelme, J. J., Xie, Y., Munuera, C. & Castellanos-Gomez, A. "High-Throughput Mechanical Exfoliation for Low-Cost Production of van der Waals Nanosheets". *Small Methods,* 2300326 (2023).

285. Wu, W., Luo, S., Li, T., Zhai, E., Wang, Z., Li, X., Han, Y., Lin, Y. C., Zhao, Y., Kono, J. & Huang, S. "Manufacturing Chip-Scale 2D Monolayer Single Crystals through Wafer-Bonder-Assisted Transfer". *Nano Letters* **25,** 14395–14403 (2025).

286. Olsen, N., Yoon, S., Holbrook, M., Thinel, M., Holtzman, L. N., Liu, Y., Hsieh, V., Li, Y., Xu, D. D., Rojas-Gatjens, E., Gavilanes, D., Handa, T., Arsenault, E. A., Huang, C.-Y., Guo, Y., Dean, C. R., Barmak, K., Pasupathy, A. N., Hone, J. C. & Zhu, X. "Macroscopic Transition Metal Dichalcogenide Monolayers from Gold-Tape Exfoliation Retain Intrinsic Properties". *Nano Letters* **25,** 15198–15205 (2025).

287. Xu, X., Guo, T., Kim, H., Hota, M. K., Alsaadi, R. S., Lanza, M., Zhang, X. & Alshareef, H. N. "Growth of 2D Materials at the Wafer Scale". *Advanced Materials* **34,** 2108258 (2022).

288. Zhang, T., Wang, J., Wu, P., Lu, A.-Y. & Kong, J. "Vapour-phase deposition of two-dimensional layered chalcogenides". *Nature Reviews Materials* **8,** 799–821 (2023).

289. Ambrozaite, O., Dziobek-Garrett, R. & Kempa, T. J. "Tailoring Light–Matter Interactions in 2D Semiconductors". *Accounts of Chemical Research* **58,** 2216–2228 (2025).

290. Zhang, X., Trainor, N., Mc Knight, T. V., Graves, A. R., Wu, Z., Xu, L., Zheng, X., Zhang, T., Zhu, J., Palacios, T., Kong, J., Groven, B., Tian, B., Duan, C., Chu, J. & Redwing, J. M. "Metal–organic chemical vapour deposition for 2D chalcogenides". *Nature Reviews Methods Primers* **5,** 57 (2025).

291. Wang, L., Meric, I., Huang, P. Y., Gao, Q., Gao, Y., Tran, H., Taniguchi, T., Watanabe, K., Campos, L. M., Muller, D. A., Guo, J., Kim, P., Hone, J., Shepard, K. L. & Dean, C. R. "One-Dimensional Electrical Contact to a Two-Dimensional Material". *Science* **342,** 614–617 (2013).

292. Zomer, P. J., Guimarães, M. H., Brant, J. C., Tombros, N. & Van Wees, B. J. "Fast pick up technique for high quality heterostructures of bilayer graphene and hexagonal boron nitride". *Applied Physics Letters* **105** (2014).

293. Pizzocchero, F., Gammelgaard, L., Jessen, B. S., Caridad, J. M., Wang, L., Hone, J., Bøggild, P. & Booth, T. J. "The hot pick-up technique for batch assembly of van der Waals heterostructures". *Nature Communications* **7** (May 2016).

294. Purdie, D. G., Pugno, N. M., Taniguchi, T., Watanabe, K., Ferrari, A. C. & Lombardo, A. "Cleaning interfaces in layered materials heterostructures". *Nature Communications* **9,** 5387 (2018).

295. Toyoda, S., Uwanno, T., Taniguchi, T., Watanabe, K. & Nagashio, K. "Pinpoint pick-up and bubble-free assembly of 2D materials using PDMS/PMMA polymers with lens shapes". *Applied Physics Express* **12,** 055008 (2019).

296. Martanov, S. G., Zhurbina, N. K., Pugachev, M. V., Duleba, A. I., Akmaev, M. A., Belykh, V. V. & Kuntsevich, A. Y. "Making van der Waals Heterostructures Assembly Accessible to Everyone". *Nanomaterials* **10,** 2305 (2020).

297. Wakafuji, Y., Moriya, R., Masubuchi, S., Watanabe, K., Taniguchi, T. & Machida, T. "3D Manipulation of 2D Materials Using Microdome Polymer". *Nano Letters* **20,** 2486–2492 (2020).

298. Iwasaki, T., Endo, K., Watanabe, E., Tsuya, D., Morita, Y., Nakaharai, S., Noguchi, Y., Wakayama, Y., Watanabe, K., Taniguchi, T. & Moriyama, S. "Bubble-Free Transfer Technique for High-Quality Graphene/Hexagonal Boron Nitride van der Waals Heterostructures". *ACS Applied Materials & Interfaces* **12,** 8533–8538 (2020).

299. Onodera, M., Wakafuji, Y., Hashimoto, T., Masubuchi, S., Moriya, R., Zhang, Y., Watanabe, K., Taniguchi, T. & Machida, T. "All-dry flip-over stacking of van der Waals junctions of 2D materials using polyvinyl chloride". *Scientific Reports* **12,** 21963 (2022).

300. Wang, W., Clark, N., Hamer, M., Carl, A., Tovari, E., Sullivan-Allsop, S., Tillotson, E., Gao, Y., de Latour, H., Selles, F., Howarth, J., Castanon, E. G., Zhou, M., Bai, H., Li, X., Weston, A., Watanabe, K., Taniguchi, T., Mattevi, C., Bointon, T. H., Wiper, P. V., Strudwick, A. J., Ponomarenko, L. A., Kretinin, A. V., Haigh, S. J., Summerfield, A. & Gorbachev, R. "Clean assembly of van der Waals heterostructures using silicon nitride membranes". *Nature Electronics* **6,** 981–990 (2023).

301. Jin, K., Wichmann, T., Wenzel, S., Samuely, T., Onufriienko, O., Szabó, P., Watanabe, K., Taniguchi, T., Yan, J., Tautz, F. S., Lüpke, F., Ternes, M. & Martinez-Castro, J. "Assembly of Arbitrary Designer Heterostructures with Atomically Clean Interfaces". *Advanced Materials Interfaces* **11,** 2300658 (2024).

302. Ottaviano, L., Palleschi, S., Perrozzi, F., D'Olimpio, G., Priante, F., Donarelli, M., Benassi, P., Nardone, M., Gonchigsuren, M., Gombosuren, M., Lucia, A., Moccia, G. & Cacioppo, O. A. "Mechanical exfoliation and layer number identification of MoS_2 revisited". *2D Materials* **4** (2017).

303. Hoekstra, T. *2D WS_2 Photodetectors for Excitonic Light Absorption* MSc thesis (University of Amsterdam, Amsterdam, 2021). 82 pp.

304. Castellanos-Gomez, A., Buscema, M., Molenaar, R., Singh, V., Janssen, L., Van Der Zant, H. S. & Steele, G. A. "Deterministic transfer of two-dimensional materials by all-dry viscoelastic stamping". *2D Materials* **1,** 011002 (2014).

305. Zhao, Q., Wang, T., Ryu, Y. K., Frisenda, R. & Castellanos-Gomez, A. "An inexpensive system for the deterministic transfer of 2D materials". *Journal of Physics: Materials* **3,** 016001 (2020).

306. Mentasti Meza, G. *Dissociation in 2D Material Photovoltaic Devices: The Role of Intralayer and Interlayer Excitons* MSc thesis (University of Amsterdam, Amsterdam, 2025). 51 pp.

307. Jain, A., Bharadwaj, P., Heeg, S., Parzefall, M., Taniguchi, T., Watanabe, K. & Novotny, L. "Minimizing residues and strain in 2D materials transferred from PDMS". *Nanotechnology* **29** (2018).

308. Gasparutti, I., Song, S. H., Neumann, M., Wei, X., Watanabe, K., Taniguchi, T. & Lee, Y. H. "How Clean Is Clean? Recipes for van der Waals Heterostructure Cleanliness Assessment". *ACS Applied Materials and Interfaces* **12,** 7701–7709 (2020).

309. Fan, S., Vu, Q. A., Tran, M. D., Adhikari, S. & Lee, Y. H. "Transfer assembly for two-dimensional van der Waals heterostructures". *2D Materials* **7** (2020).

310. Pace, S., Ferrera, M., Convertino, D., Piccinini, G., Magnozzi, M., Mishra, N., Forti, S., Bisio, F., Canepa, M., Fabbri, F. & Coletti, C. "Thermal stability of monolayer WS_2 in BEOL conditions". *Journal of Physics: Materials* **4,** 024002 (2021).

311. Fang, J., Chen, R., Sharp, D., Renzi, E. M., Manna, A., Kala, A., Mann, S. A., Yao, K., Munley, C., Rarick, H., Tang, A., Pumulo, S., Zheng, Y., Menon, V. M., Alù, A. & Majumdar, A. "Million-Q free space meta-optical resonator at near-visible wavelengths". *Nature Communications* **15,** 10341 (2024).

312. Yakubovsky, D. I., Arsenin, A. V., Stebunov, Y. V., Fedyanin, D. Y. & Volkov, V. S. "Optical constants and structural properties of thin gold films". *Optics Express* **25,** 25574 (2017).

313. Lee, S. Y., Jeong, T. Y., Jung, S. & Yee, K. J. "Refractive Index Dispersion of Hexagonal Boron Nitride in the Visible and Near-Infrared". *Physica Status Solidi B* **256,** 1800417 (2019).

314. Gupta, V., Probst, P. T., Goßler, F. R., Steiner, A. M., Schubert, J., Brasse, Y., König, T. A. F. & Fery, A. "Mechanotunable Surface Lattice Resonances in the Visible Optical Range by Soft Lithography Templates and Directed Self-Assembly". *ACS Applied Materials & Interfaces* **11,** 28189–28196 (2019).

315. Cadiz, F., Courtade, E., Robert, C., Wang, G., Shen, Y., Cai, H., Taniguchi, T., Watanabe, K., Carrere, H., Lagarde, D., Manca, M., Amand, T., Renucci, P., Tongay, S., Marie, X. & Urbaszek, B. "Excitonic linewidth approaching the homogeneous limit in MoS_2-based van der Waals heterostructures". *Physical Review X* **7,** 021026 (2017).

316. Liu, V. & Fan, S. "S^4: A free electromagnetic solver for layered periodic structures". *Computer Physics Communications* **183,** 2233–2244 (2012).

317. Ross, J. S., Wu, S., Yu, H., Ghimire, N. J., Jones, A. M., Aivazian, G., Yan, J., Mandrus, D. G., Xiao, D., Yao, W. & Xu, X. "Electrical control of neutral and charged excitons in a monolayer semiconductor". *Nature Communications* **4,** 1474 (2013).

318. Das, S., Wang, Y., Dai, Y., Li, S. & Sun, Z. "Ultrafast transient sub-bandgap absorption of monolayer MoS_2". *Light: Science & Applications* **10,** 27 (2021).

319. Chakraborty, B., Gu, J., Sun, Z., Khatoniar, M., Bushati, R., Boehmke, A. L., Koots, R. & Menon, V. M. "Control of Strong Light–Matter Interaction in Monolayer WS_2 through Electric Field Gating". *Nano Letters* **18,** 6455–6460 (2018).

320. Liu, X., Galfsky, T., Sun, Z., Xia, F., Lin, E.-c., Lee, Y.-H., Kéna-Cohen, S. & Menon, V. M. "Strong light–matter coupling in two-dimensional atomic crystals". *Nature Photonics* **9,** 30–34 (2015).

321. Shore, B. W. & Knight, P. L. "The Jaynes-Cummings Model". *Journal of Modern Optics* **40,** 1195–1238 (1993).

322. Dovzhenko, D. S., Ryabchuk, S. V., Rakovich, Y. P. & Nabiev, I. R. "Light-matter interaction in the strong coupling regime: Configurations, conditions, and applications". *Nanoscale* **10,** 3589–3605 (2018).

323. Huang, L., Jin, R., Zhou, C., Li, G., Xu, L., Overvig, A., Deng, F., Chen, X., Lu, W., Alù, A. & Miroshnichenko, A. E. "Ultrahigh-Q guided mode resonances in an All-dielectric metasurface". *Nature Communications* **14,** 3433 (2023).

324. Yu, Y., Yu, Y., Xu, C., Barrette, A., Gundogdu, K. & Cao, L. "Fundamental limits of exciton-exciton annihilation for light emission in transition metal dichalcogenide monolayers". *Physical Review B* **93,** 201111 (2016).

325. Mitta, S. B., Choi, M. S., Nipane, A., Ali, F., Kim, C., Teherani, J. T., Hone, J. & Yoo, W. J. "Electrical characterization of 2D materials-based field-effect transistors". *2D Materials* **8,** 012002 (2021).

326. Daus, A., Vaziri, S., Chen, V., Köroğlu, Ç., Grady, R. W., Bailey, C. S., Lee, H. R., Schauble, K., Brenner, K. & Pop, E. "High-performance flexible nanoscale transistors based on transition metal dichalcogenides". *Nature Electronics* **4,** 495–501 (2021).

327. Dibos, A. M., Zhou, Y., Jauregui, L. A., Scuri, G., Wild, D. S., High, A. A., Taniguchi, T., Watanabe, K., Lukin, M. D., Kim, P. & Park, H. "Electrically Tunable Exciton–Plasmon Coupling in a WSe_2 Monolayer Embedded in a Plasmonic Crystal Cavity". *Nano Letters* **19,** 3543–3547 (2019).

328. Yuan, R., Lynch, J. & Jariwala, D. "Ultra-compact plexcitonic electro-absorption modulator". *Device* **1,** 100002 (2023).

329. Lee, B., Liu, W., Naylor, C. H., Park, J., Malek, S. C., Berger, J. S., Johnson, A. T. C. & Agarwal, R. "Electrical Tuning of Exciton–Plasmon Polariton Coupling in Monolayer MoS_2 Integrated with Plasmonic Nanoantenna Lattice". *Nano Letters* **17,** 4541–4547 (2017).

330. Zhang, L., Gogna, R., Burg, W., Tutuc, E. & Deng, H. "Photonic-crystal exciton-polaritons in monolayer semiconductors". *Nature Communications* **9,** 713 (2018).

331. Roy, S. & Bermel, P. "Electronic and optical properties of ultra-thin 2D tungsten disulfide for photovoltaic applications". *Solar Energy Materials and Solar Cells* **174,** 370–379 (2018).

332. Liu, L., Kumar, S. B., Ouyang, Y. & Guo, J. "Performance Limits of Monolayer Transition Metal Dichalcogenide Transistors". *IEEE Transactions on Electron Devices* **58,** 3042–3047 (2011).

333. Han, S., Kim, S., Kim, S., Low, T., Brar, V. W. & Jang, M. S. "Complete Complex Amplitude Modulation with Electronically Tunable Graphene Plasmonic Metamolecules". *ACS Nano* **14,** 1166–1175 (2020).

334. Overvig, A. C., Shrestha, S., Malek, S. C., Lu, M., Stein, A., Zheng, C. & Yu, N. "Dielectric metasurfaces for complete and independent control of the optical amplitude and phase". *Light: Science & Applications* **8,** 92 (2019).

335. Kim, J. Y., Park, J., Holdman, G. R., Heiden, J. T., Kim, S., Brar, V. W. & Jang, M. S. "Full 2π tunable phase modulation using avoided crossing of resonances". *Nature Communications* **13,** 2103 (2022).

336. Ranjan, A., Raghavan, N., Holwill, M., Watanabe, K., Taniguchi, T., Novoselov, K. S., Pey, K. L. & O'Shea, S. J. "Dielectric Breakdown in Single-Crystal Hexagonal Boron Nitride". *ACS Applied Electronic Materials* **3,** 3547–3554 (2021).

337. Hoekstra, T. & van de Groep, J. "Electrically tunable strong coupling in a hybrid-2D excitonic metasurface for optical modulation". *Light: Science & Applications* **15,** 28 (2026).

338. Danielsen, D. R., Lyksborg-Andersen, A., Nielsen, K. E. S., Jessen, B. S., Booth, T. J., Doan, M.-H., Zhou, Y., Bøggild, P. & Gammelgaard, L. "Super-Resolution Nanolithography of Two-Dimensional Materials by Anisotropic Etching". *ACS Applied Materials & Interfaces* **13,** 41886–41894 (2021).

339. Ciesielski, A., Skowronski, L., Trzcinski, M. & Szoplik, T. "Controlling the optical parameters of self-assembled silver films with wetting layers and annealing". *Applied Surface Science. 7th International Conference on Spectroscopic Ellipsometry* **421,** 349–356 (2017).

340. El-Sayed, M. A., Ermolaev, G. A., Voronin, K. V., Romanov, R. I., Tselikov, G. I., Yakubovsky, D. I., Doroshina, N. V., Nemtsov, A. B., Solovey, V. R., Voronov, A. A., Novikov, S. M., Vyshnevyy, A. A., Markeev, A. M., Arsenin, A. V. & Volkov, V. S. "Optical Constants of Chemical Vapor Deposited Graphene for Photonic Applications". *Nanomaterials* **11,** 1230 (2021).

341. Kim, H., Uddin, S. Z., Higashitarumizu, N., Rabani, E. & Javey, A. "Inhibited nonradiative decay at all exciton densities in monolayer semiconductors". *Science* **373,** 448–452 (2021).

342. Fan, S., Suh, W. & Joannopoulos, J. D. "Temporal coupled-mode theory for the Fano resonance in optical resonators". *Journal of the Optical Society of America A* **20,** 569 (2003).

343. Piper, J. R. & Fan, S. "Total Absorption in a Graphene Monolayer in the Optical Regime by Critical Coupling with a Photonic Crystal Guided Resonance". *ACS Photonics* **1,** 347–353 (2014).

344. Thureja, P., Shirmanesh, G. K., Fountaine, K. T., Sokhoyan, R., Grajower, M. & Atwater, H. A. "Array-level inverse design of beam steering active metasurfaces". *ACS Nano* **14,** 15042–15055 (2020).

345. Mohammadi Estakhri, N. & Alù, A. "Wave-front Transformation with Gradient Metasurfaces". *Physical Review X* **6,** 041008 (2016).

346. Shastri, K. & Monticone, F. "Nonlocal flat optics". *Nature Photonics* **17,** 36–47 (2023).

347. Magnusson, R. & Ko, Y. H. "Guided-mode resonance nanophotonics: fundamentals and applications". in *Nanoengineering: Fabrication, Properties, Optics, and Devices XIII* **9927** (SPIE, 2016), 992702.

348. Kim, S. J. & Brongersma, M. L. "Active flat optics using a guided mode resonance". *Optics Letters* **42,** 5 (2017).

349. Lawrence, M., Barton, D. R., Dixon, J., Song, J.-H., Van De Groep, J., Brongersma, M. L. & Dionne, J. A. "High quality factor phase gradient metasurfaces". *Nature Nanotechnology* **15,** 956–961 (2020).

350. Hsu, C. W., Zhen, B., Lee, J., Chua, S.-L., Johnson, S. G., Joannopoulos, J. D. & Soljačić, M. "Observation of trapped light within the radiation continuum". *Nature* **499,** 188–191 (2013).

351. Koshelev, K., Lepeshov, S., Liu, M., Bogdanov, A. & Kivshar, Y. "Asymmetric Metasurfaces with High-Q Resonances Governed by Bound States in the Continuum". *Physical Review Letters* **121,** 193903 (2018).

352. Jin, J., Yin, X., Ni, L., Soljačić, M., Zhen, B. & Peng, C. "Topologically enabled ultrahigh-Q guided resonances robust to out-of-plane scattering". *Nature* **574,** 501–504 (2019).

353. Chen, Z., Yin, X., Jin, J., Zheng, Z., Zhang, Z., Wang, F., He, L., Zhen, B. & Peng, C. "Observation of miniaturized bound states in the continuum with ultra-high quality factors". *Science Bulletin* **67,** 359–366 (2022).

354. Overvig, A. & Alù, A. "Diffractive Nonlocal Metasurfaces". *Laser & Photonics Reviews* **16,** 2100633 (2022).

355. Chai, R., Liu, Q., Liu, W., Li, Z., Cheng, H., Tian, J. & Chen, S. "Emerging Planar Nanostructures Involving Both Local and Nonlocal Modes". *ACS Photonics* **10,** 2031–2044 (2023).

356. Kodigala, A., Lepetit, T., Gu, Q., Bahari, B., Fainman, Y. & Kanté, B. "Lasing action from photonic bound states in continuum". *Nature* **541,** 196–199 (2017).

357. Ha, S. T., Fu, Y. H., Emani, N. K., Pan, Z., Bakker, R. M., Paniagua-Domínguez, R. & Kuznetsov, A. I. "Directional lasing in resonant semiconductor nanoantenna arrays". *Nature Nanotechnology* **13,** 1042–1047 (2018).

358. Hwang, M.-S., Lee, H.-C., Kim, K.-H., Jeong, K.-Y., Kwon, S.-H., Koshelev, K., Kivshar, Y. & Park, H.-G. "Ultralow-threshold laser using super-bound states in the continuum". *Nature Communications* **12,** 4135 (2021).

359. Kwon, H., Sounas, D., Cordaro, A., Polman, A. & Alù, A. "Nonlocal Metasurfaces for Optical Signal Processing". *Physical Review Letters* **121,** 173004 (2018).

360. Grepstad, J. O., Greve, M. M., Holst, B., Johansen, I.-R., Solgaard, O. & Sudbø, A. "Finite-size limitations on Quality Factor of guided resonance modes in 2D Photonic Crystals". *Optics Express* **21,** 23640 (2013).

361. Zundel, L. & Manjavacas, A. "Finite-size effects on periodic arrays of nanostructures". *Journal of Physics: Photonics* **1,** 015004 (2018).

362. Taghizadeh, A. & Chung, I.-S. "Quasi bound states in the continuum with few unit cells of photonic crystal slab". *Applied Physics Letters* **111,** 031114 (2017).

363. Droulias, S., Koschny, T. & Soukoulis, C. M. "Finite-Size Effects in Metasurface Lasers Based on Resonant Dark States". *ACS Photonics* **5,** 3788–3793 (2018).

364. Brazas, J. C. & Li, L. "Analysis of input-grating couplers having finite lengths". *Applied Optics* **34,** 3786 (1995).

365. Saarinen, J., Noponen, E. & Turunen, J. P. "Guided-mode resonance filters of finite aperture". *Optical Engineering* **34,** 2560–2566 (1995).

366. Boye, R. R. & Kostuk, R. K. "Investigation of the effect of finite grating size on the performance of guided-mode resonance filters". *Applied Optics* **39,** 3649 (2000).

367. Jacob, D. K., Dunn, S. C. & Moharam, M. G. "Design considerations for narrow-band dielectric resonant grating reflection filters of finite length". *Journal of the Optical Society of America A* **17,** 1241 (2000).

368. Bendickson, J. M., Glytsis, E. N., Gaylord, T. K. & Brundrett, D. L. "Guided-mode resonant subwavelength gratings: effects of finite beams and finite gratings". *Journal of the Optical Society of America A* **18,** 1912 (2001).

369. Jeong, D.-Y., Ye, Y. H. & Zhang, Q. M. "Effective optical properties associated with wave propagation in photonic crystals of finite length along the propagation direction". *Journal of Applied Physics* **92,** 4194–4200 (2002).

370. Peters, D. W., Kemme, S. A. & Hadley, G. R. "Effect of finite grating, waveguide width, and end-facet geometry on resonant subwavelength grating reflectivity". *Journal of the Optical Society of America A* **21,** 981 (2004).

371. Haus, H. A. *Waves and fields in optoelectronics* 402 pp. (Prentice-Hall, Englewood Cliffs, NJ, 1984).

372. Haus, H. & Huang, W. "Coupled-mode theory". *Proceedings of the IEEE* **79,** 1505–1518 (1991).

373. Paddon, P. & Young, J. F. "Two-dimensional vector-coupled-mode theory for textured planar waveguides". *Physical Review B* **61,** 2090–2101 (2000).

374. Kintaka, K., Majima, T., Hatanaka, K., Inoue, J. & Ura, S. "Polarization-independent guided-mode resonance filter with cross-integrated waveguide resonators". *Optics Letters* **37,** 3264–3266 (2012).

375. Dolia, V., Balch, H. B., Dagli, S., Abdollahramezani, S., Carr Delgado, H., Moradifar, P., Chang, K., Stiber, A., Safir, F., Lawrence, M., Hu, J. & Dionne, J. A. "Very-large-scale-integrated high quality factor nanoantenna pixels". *Nature Nanotechnology* **19,** 1290–1298 (2024).

376. Hao, R., Ye, B., Xu, J. & Zou, Y. "Performance optimization of planar photonic crystal bound states in the continuum cavities: mitigating finite-size effects". *Frontiers of Optoelectronics* **18,** 3 (2025).

377. Ustimenko, N., Rockstuhl, C. & Evlyukhin, A. B. "Resonances in finite-size all-dielectric metasurfaces for light trapping and propagation control". *Physical Review B* **109,** 115436 (2024).

378. Hoang, T. X., Leykam, D., Chu, H.-S., Png, C. E., García-Vidal, F. J. & Kivshar, Y. S. "Collective nature of high-Q resonances in finite-size photonic metastructures". *Physical Review Research* **7,** 013316 (2025).

379. Bykov, D. A. & Doskolovich, L. L. "Spatiotemporal coupled-mode theory of guided-mode resonant gratings". *Optics Express* **23,** 19234 (2015).

380. Overvig, A., Mann, S. A. & Alù, A. "Spatio-temporal coupled mode theory for nonlocal metasurfaces". *Light: Science & Applications* **13,** 28 (2024).

381. Jeon, D., Kim, H. & Rho, J. "Leaky Guided Mode-Induced Large-Angle Nonlocal Metasurfaces". *ACS Photonics* **12,** 375–383 (2025).

382. Lalanne, P. & Lemercier-lalanne, D. "On the effective medium theory of subwavelength periodic structures". *Journal of Modern Optics* **43,** 2063–2085 (1996).

383. Lalanne, P. & Hugonin, J.-P. "High-order effective-medium theory of subwavelength gratings in classical mounting: application to volume holograms". *Journal of the Optical Society of America A* **15,** 1843 (1998).

384. Barton, D., Hu, J., Dixon, J., Klopfer, E., Dagli, S., Lawrence, M. & Dionne, J. "High-Q nanophotonics: sculpting wavefronts with slow light". *Nanophotonics* **10,** 83–88 (2021).

385. Mannix, A. J., Ye, A., Sung, S. H., Ray, A., Mujid, F., Park, C., Lee, M., Kang, J.-H., Shreiner, R., High, A. A., Muller, D. A., Hovden, R. & Park, J. "Robotic four-dimensional pixel assembly of van der Waals solids". *Nature Nanotechnology* **17,** 361–366 (2022).

386. Kühner, L., Sortino, L., Tilmann, B., Weber, T., Watanabe, K., Taniguchi, T., Maier, S. A. & Tittl, A. "High-Q Nanophotonics over the Full Visible Spectrum Enabled by Hexagonal Boron Nitride Metasurfaces". *Advanced Materials* **35,** 2209688 (2023).

387. Sutter, P., Lahiri, J., Zahl, P., Wang, B. & Sutter, E. "Scalable Synthesis of Uniform Few-Layer Hexagonal Boron Nitride Dielectric Films". *Nano Letters* **13,** 276–281 (2013).

388. Naclerio, A. E. & Kidambi, P. R. "A Review of Scalable Hexagonal Boron Nitride (h -BN) Synthesis for Present and Future Applications". *Advanced Materials* **35,** 2207374 (2023).

389. Tebbe, D., Schütte, M., Watanabe, K., Taniguchi, T., Stampfer, C., Beschoten, B. & Waldecker, L. "Tailoring the dielectric screening in WS_2–graphene heterostructures". *npj 2D Materials and Applications* **7,** 1–7 (2023).

390. Mondal, A., Biswas, C., Park, S., Cha, W., Kang, S.-H., Yoon, M., Choi, S. H., Kim, K. K. & Lee, Y. H. "Low Ohmic contact resistance and high on/off ratio in transition metal dichalcogenides field-effect transistors via residue-free transfer". *Nature Nanotechnology* **19,** 34–43 (2024).

391. Wurdack, M., Estrecho, E., Todd, S., Yun, T., Pieczarka, M., Earl, S. K., Davis, J. A., Schneider, C., Truscott, A. G. & Ostrovskaya, E. A. "Motional narrowing, ballistic transport, and trapping of room-temperature exciton polaritons in an atomically-thin semiconductor". *Nature Communications* **12,** 5366 (2021).

392. Genco, A., Louca, C., Cruciano, C., Song, K. W., Trovatello, C., Di Blasio, G., Sansone, G., Randerson, S. A., Claronino, P., Georgiou, K., Jayaprakash, R., Watanabe, K., Taniguchi, T., Lidzey, D. G., Kyriienko, O., Dal Conte, S., Tartakovskii, A. I. & Cerullo, G. "Femtosecond switching of strong light-matter interactions in microcavities with two-dimensional semiconductors". *Nature Communications* **16,** 6490 (2025).

393. Weber, T., Kühner, L., Sortino, L., Ben Mhenni, A., Wilson, N. P., Kühne, J., Finley, J. J., Maier, S. A. & Tittl, A. "Intrinsic strong light-matter coupling with self-hybridized bound states in the continuum in van der Waals metasurfaces". *Nature Materials* **22,** 970–976 (2023).

394. Tian, S., Zhou, K., Yin, W. & Liu, Y. "Machine learning enables the discovery of 2D Invar and anti-Invar monolayers". *Nature Communications* **15,** 6977 (2024).

395. Khitrova, G., Gibbs, H. M., Kira, M., Koch, S. W. & Scherer, A. “Vacuum Rabi splitting in semiconductors”. *Nature Physics* **2,** 81–90 (2006).

396. Elsawy, M. M. R., Lanteri, S., Duvigneau, R., Fan, J. A. & Genevet, P. “Numerical Optimization Methods for Metasurfaces”. *Laser & Photonics Reviews* **14,** 1900445 (2020).

Summary

Today, building on the rapid progress in nano-engineering in recent decades, visible light can be controlled at the subwavelength scale using optically resonant nano-antennas and metasurfaces. Although these structures provide unprecedented new ways to control light, the functionality of optical metasurfaces has largely remained passive due to the weakly tunable optical properties of most natural materials. To this end, monolayer semiconductors have emerged as an exciting class of materials with efficiently tunable excitons that dominate their optical properties. However, their application in active optoelectronic devices is limited by the excessive nonradiative losses at room temperature and the short interaction length of light with the atomically thin material. In this thesis, we introduce a new platform to overcome both of these problems simultaneously: ELECTRICALLY TUNABLE HYBRID-2D METASURFACES. By combining the pristine excitons supported by van der Waals heterostructures with the strong field enhancements offered by nonlocal metasurfaces, our metasurfaces achieve strong and dynamic modulation of the amplitude and phase of visible light at room temperature.

Chapter 2 outlines the design, fabrication, and characterization techniques underpinning the thesis. We first describe the modeling of the electrically tunable optical response of excitonic 2D materials. Next, the chapter details the fabrication protocols as well as the rationale behind selected techniques. The chapter concludes with an overview of the custom experimental setups that were used to probe the optoelectronic response of the metasurfaces.

Chapter 3 demonstrates active metasurfaces for free-space optical amplitude modulation. The devices consist of atomically thin WS_2 encapsulated with hBN and integrated with a dielectric subwavelength grating that couples incident light to a guided mode resonance, producing strong nonlocal field enhancement at the monolayer. In the intrinsically doped regime, excitons hybridize with guided photons to form exciton-polaritons. By electrostatically doping the monolayer to suppress the exciton by increasing its nonradiative decay rate, the metasurface is continuously tuned between the strong and the weak coupling regimes. Leveraging this mechanism, we achieve 9.9 dB reflectance modulation and a 48.9% absolute reflectance change at room temperature, representing a fivefold improvement over previous best achieved with excitonic 2D semiconductors.

In **Chapter 4**, we numerically extend the hybrid-2D metasurface concept to complex-amplitude modulation at visible wavelengths. We achieve independent control over the amplitude and phase of reflected light using two electrical control channels and operation near critical coupling, where radiative and nonradiative decay are delicately balanced. To navigate the high-dimensional design space and the interdependence of geometry and material response, we develop an inverse-design pipeline. We realize metasurfaces capable of π-phase modulation at constant amplitude, full 0–2π complex-amplitude control, and diffractive beam steering. We interpret the results using temporal coupled-mode theory to elucidate the underlying physical mechanisms and fundamental limitations.

A central theme of the thesis is that nonlocal resonances enable ultracompact active meta-optical elements. However, the large propagation lengths associated with nonlocal modes render them sensitive to finite-size effects. This calls for a predictive framework that can be used to understand and predict the impact of finite size on the optical properties of footprint-limited nonlocal metasurfaces. In **Chapter 5**, we develop such a framework using spatiotemporal coupled-mode theory. We show that, when the metasurface width approaches the modal propagation length, finite-size effects fundamentally reshape the scattering response, producing interference fringes and linewidth broadening. An analytical expression for the Q-factor is derived that incorporates an additional dissipation channel due to edge losses, revealing that stored energy and effective lifetime scale exponentially with the interaction length of the nonlocal mode. Position- and momentum-resolved reflectance spectroscopy on a 30-µm-wide hybrid-2D metasurface confirms the theoretical predictions and enables quantitative separation of intrinsic, radiative, and edge-induced loss rates. The intuitive and quantitative insights offered by our results establish spatiotemporal coupled-mode theory as a powerful tool for the design of highly compact hybrid-2D metasurfaces.

Taken together, this thesis shows that, by uniting nonlocal dielectric resonances with excitonic van der Waals heterostructures, ELECTRICALLY TUNABLE HYBRID-2D METASURFACES provide a uniquely versatile platform for achieving strong and tunable light–matter interactions in 2D quantum materials, which can be leveraged to study and control light at the nanoscale.

Samenvatting

Dankzij de snelle vooruitgang in de nanotechnologie van de afgelopen decennia, kan zichtbaar licht tegenwoordig beheersd worden met optisch resonante metaoppervlakken op een schaal kleiner dan de golflengte van het licht. Hoewel deze structuren ongekende mogelijkheden bieden om licht te manipuleren, is hun functionaliteit tot nu toe grotendeels passief gebleven, doordat de optische eigenschappen van de meeste natuurlijke materialen nauwelijks verstelbaar zijn. In dat opzicht zijn monolaag-halfgeleiders veelbelovend, omdat hun optische eigenschappen worden gedomineerd door efficiënt verstelbare excitonen. Hun toepassing in actieve opto-elektronische componenten wordt echter beperkt door grote niet-stralende verliezen bij kamertemperatuur en door de korte interactielengte van licht met een atomair dun materiaal. In dit proefschrift introduceren wij een nieuw platform dat beide beperkingen tegelijk ondervangt: ELEKTRISCH VERSTELBARE HYBRIDE-2D METAOPPERVLAKKEN. Door de hoogwaardige excitonen in Van der Waals-heterostructuren te combineren met de sterke veldversterking van niet-lokale metaoppervlakken, wordt sterke en dynamische modulatie van de amplitude en fase van zichtbaar licht mogelijk.

Hoofdstuk 2 beschrijft de ontwerp-, fabricage- en meettechnieken die aan dit proefschrift ten grondslag liggen. Eerst bespreken we hoe de invloed van vrije ladingsdragers op de optische eigenschappen van excitonische 2D-materialen wordt gemodelleerd. Vervolgens behandelen we de fabricageprotocollen en de overwegingen die aan de gekozen technieken ten grondslag liggen. Tot slot geven we een overzicht van de op maat gemaakte experimentele opstellingen die zijn gebruikt om de opto-elektronische respons van de metaoppervlakken te onderzoeken.

Hoofdstuk 3 demonstreert actieve metaoppervlakken voor optische amplitude-modulatie. De structuren bestaan uit een monolaag WS_2, ingekapseld in hBN en geïntegreerd met een diëlektrisch subgolflengterooster dat invallend licht koppelt aan een geleide-modusresonantie. Hierdoor ontstaat een sterke, over het oppervlak uitgespreide veldversterking in de monolaag. In het intrinsiek gedoteerde regime hybridiseren excitonen met geleide fotonen tot zogeheten exciton-polaritonen. Door de monolaag elektrostatisch te doteren worden de excitonen onderdrukt doordat hun niet-stralende vervalsnelheid toeneemt, waardoor het metaoppervlak continu kan worden versteld tussen het regime van sterke koppeling en dat van zwakke

koppeling tussen excitonen en fotonen. Met behulp van dit mechanisme bereiken we bij kamertemperatuur een reflectiemodulatie van 9,9 dB en een absolute verandering in reflectie van 48,9%, wat neerkomt op een vijfvoudige verbetering ten opzichte van de beste eerdere resultaten die met excitonische 2D-halfgeleiders zijn behaald.

In **Hoofdstuk 4** breiden we het concept numeriek uit naar modulatie van de complexe amplitude bij zichtbare golflengten. We bereiken onafhankelijke controle over de amplitude en fase van gereflecteerd licht met behulp van twee elektrische stuurkanalen. Daarbij werkt de modulator nabij kritische koppeling, waar stralende en niet-stralende verliezen zorgvuldig met elkaar in evenwicht zijn gebracht. Om de weg te vinden in deze hoog-dimensionale ontwerpruimte, waarin geometrie en materiaalrespons sterk met elkaar verweven zijn, ontwikkelen we een inverse-ontwerpmethode. Daarmee realiseren we metaoppervlakken die in staat zijn tot π-fasemodulatie bij constante amplitude, volledige controle over de complexe amplitude in het fasebereik van 0–2π, en diffractieve bundelsturing. We interpreteren de resultaten met temporele gekoppelde-modustheorie om de onderliggende fysische mechanismen en fundamentele beperkingen te verhelderen.

Een centraal thema van dit proefschrift is dat gedelokaliseerde resonanties het mogelijk maken om ultracompacte actieve meta-optische elementen te realiseren. Juist doordat zulke modi zich over relatief grote afstanden uitstrekken, zijn zij echter gevoelig voor eindige-afmetingseffecten. In **Hoofdstuk 5** ontwikkelen we een voorspellend model met ruimtelijk-temporele gekoppelde-modustheorie waarmee de invloed van een eindige afmeting op de optische eigenschappen van compacte metaoppervlakken begrepen en voorspeld kan worden. We laten zien dat, wanneer de breedte van het metaoppervlak in de buurt komt van de voortplantingslengte van de modus, eindige-afmetingseffecten de optische respons fundamenteel hervormen: er ontstaat een interferentiepatroon en de lijnbreedte neemt toe. We leiden een analytische uitdrukking af voor de Q-factor, waarin een extra dissipatiekanaal door randverliezen is opgenomen. Daaruit blijkt dat de opgeslagen energie en de effectieve levensduur exponentieel schalen met de interactielengte van de gedelokaliseerde modus. Door op een 30 µm breed hybride-2D-metaoppervlak plaats- en invalshoek-opgeloste reflectiespectroscopie uit te voeren, bevestigen we de theoretische voorspellingen en kunnen we de intrinsieke, extrinsieke en randverlieskanalen kwantitatief van elkaar scheiden. De inzichten die uit onze resultaten voortkomen, vestigen ruimtelijk-temporele gekoppelde-modustheorie als een krachtig raamwerk voor het ontwerp van uiterst compacte hybride-2D-metaoppervlakken.

Al met al laat dit proefschrift zien dat de hybridisatie van diëlektrische metaoppervlakken met excitonische Van der Waals-heterostructuren unieke kansen biedt om sterke en verstelbare interacties tussen licht en tweedimensionale kwantummaterialen te realiseren.

Gearfetting

Tsjintwurdich kin sichtber ljocht, troch de flugge foarútgong yn nanotechnology fan de ôfrûne desennia, stjoerd wurde op in skaal lytser as de golflingte fan ljocht mei optysk resonante nanoantennes en metaopperflakken. Hoewol't dy struktueren ûnkende mooglikheden biede om ljocht te behearskjen, is de funksjonaliteit fan optyske metaopperflakken oant no ta foar in grut part passyf bleaun. Dat komt trochdat de optyske eigenskippen fan de measte materialen harren mar beheind ferstelle litte. Monolaach-healgelieders foarmje dêrom in beloftefolle klasse fan materialen, om't harren optyske eigenskippen dominearre wurde troch ferstelbere eksitoanen. Harren tapassing yn aktive opto-elektroanyske komponinten wurdt lykwols beheind troch grutte net-strieljende ferliezen by keamertemperatuer en troch de koarte ynteraksjelingte fan ljocht mei in atomêr tin materiaal. Yn dit proefskrift yntrodusearje wy in nij platfoarm dat beide beheiningen ûnderfangt: elektrysk ferstelbere hybride-2D metaopperflakken. Troch de heechweardige eksitoanen yn Van der Waals-heterostruktueren te kombinearjen mei de sterke fjildfersterking fan net-lokale metaopperflakken, wurdt dynamyske modulaasje fan de amplitude en faze fan sichtber ljocht mooglik.

Haadstik 2 beskriuwt de ûntwerp-, fabrikaazje- en mjittechniken dy't oan dit proefskrift te 'n grûnslach lizze. Earst beprate wy hoe't de ynfloed fan frije ladingsdragers op de optyske eigenskippen fan eksitoanyske 2D-materialen modellearre wurdt. Dêrnei behannelje wy de fabrikaazjeprotokollen en de oerwagings dy't oan de keazen techniken te 'n grûnslach lizze. As lêste jouwe wy in oersjoch fan de eksperimintele opstellingen dy't brûkt binne om de opto-elektroanyske respons fan de metaopperflakken te ûndersykjen.

Haadstik 3 demonstrearret aktive metaopperflakken foar optyske amplitudemodulaasje. De struktueren bestean út in monolaach WS_2, ynkapsele yn hBN en yntegrearre mei in diëlektrysk subgolflingteroaster dat ynfallend ljocht keppelet oan in geliede-modusresonânsje. Dêrtroch ûntstiet in sterke, oer it oerflak útsprate fjildfersterking yn de monolaach. Yn it yntrinsyk dotearre rezjym hybridisearje eksitoanen mei liede fotoanen ta saneamde eksiton-polaritoanen. Troch de monolaach elektrostatysk te dotearjen wurde de eksitoanen ûnderdrukt trochdat harren net-strieljende ferfalsnelheid tanimt, wêrtroch't it metaopperflak kontinu fersteld wurde kin tusken it rezjym fan sterke keppeling en dat fan swakke keppeling tusken

eksitoanen en fotoanen. Mei help fan dit meganisme berikke wy by keamertemperatuer in refleksjemodulaasje fan 9,9 dB en in absolute feroaring yn refleksje fan 48,9%, wat delkomt op in fiiffâldige ferbettering neffens eardere resultaten mei eksitoanyske 2D-healgelieders.

Yn **Haadstik 4** wreidzje wy it konsept numeryk út nei modulaasje fan de komplekse amplitude by sichtbere golflingten. Wy berikke ûnôfhinklike kontrôle oer de amplitude en faze fan reflektearre ljocht mei help fan twa elektryske stjoerkanalen. Dêrby wurket de modulator tichtby krityske keppeling, dêr't strieljende en net-strieljende ferliezen yn lykwicht brocht binne. Om it paad te finen yn dizze heech-diminsjonale ûntwerpromte, dêr't geometry en materiaalrespons sterk mei-inoar ferweve binne, ûntwikkelje wy in ynverse-ûntwerpmetoade. Dêrmei realisearje wy metaopperflakken dy't by steat binne ta π-fazemodulaasje by konstante amplitude, folsleine kontrôle oer de komplekse amplitude yn it fazeberik fan 0–2π en diffraktive bondelstjoering. Wy ynterpretearje de resultaten mei help fan de tydlik keppele-modusteory om de ûnderlizzende fysyske meganismen en beheiningen te ferdúdlikjen.

In sintraal tema fan dit proefskrift is dat delokalisearre resonânsjes it mooglik meitsje om ultrakompakte aktive meta-optyske eleminten te realisearjen. Krekt trochdat sokke modi har oer relatyf grutte ôfstannen útstrekke, binne hja lykwols gefoelich foar einige-ôfmjittingseffekten. Dat freget om in model dêr't de ynfloed fan in einige ôfmjitting op de optyske eigenskippen fan kompakte metaopperflakken mei begrepen wurde kin. Yn **Haadstik 5** ûntwikkelje wy sa'n model mei help fan romtlik-tydlike keppele-modusteory. Wy litte sjen dat, as de breedte fan it metaopperflak yn'e buert komt fan de fuortplantingslingte fan de modus, einige-ôfmjittingseffekten de optyske respons herfoarmje: der ûntstiet in ynterferinsjepatroan en de linebreedte nimt ta. Wy liede in analytyske útdrukking ôf foar de Q-faktor, dêr't in ekstra dissipaasjekanaal troch râneferliezen opnommen is. Dêr docht út bliken dat de opsleine enerzjy en de effektive libbensdoer eksponinsjeel skale mei de ynteraksjelingte fan de delokalisearre modus. Troch op in 30 μm breed hybride-2D metaopperflak plakken ynfalshoeke-oploste refleksjespektroskopy út te fieren, befêstigje wy de teoretyske foarsizzingen en kinne wy de yntrinsike, ekstrinsike en râneferlieskanalen kwantitatyf faninoar skiede. De yntuïtive en kwantitative ynsichten ôflaat fan ús resultaten, fêstigje romtlik-tydlike keppele-modusteory as in krêftich ramtwurk foar it ûntwerp fan uterst kompakte hybride-2D metaopperflakken.

Al mei al lit dit proefskrift sjen dat de feriening fan diëlektryske metaopperflakken mei eksitoanyske Van der Waals-heterostruktueren, in unyk en alsidich platfoarm foarmje foar sterke en ferstelbere ynteraksjes tusken ljocht en twadiminsjonale kwantummaterialen.

Publications and author contributions

Related to this thesis

1. **T. Hoekstra** and J. van de Groep, "Electrically tunable strong coupling in a hybrid-2D excitonic metasurface for optical modulation". *Light: Science & Applications* **15**, 28 (2026). (**Chapter 3**)

   T.H. and J.v.d.G. conceived the concept behind this research. T.H. fabricated the samples, performed the simulations and measurements. T.H. and J.v.d.G. performed the data analysis and wrote the manuscript.

2. **T. Hoekstra**, M. L. Brongersma, and J. van de Groep, "Hybrid–2D Excitonic Metasurfaces for Complex Amplitude Modulation". Accepted for publication in *Nano Letters*. Preprint available at arXiv:2604.07619. (**Chapter 4**)

   T.H., J.v.d.G. conceived the concept behind this research. T.H. fabricated the sample, performed the measurements, and performed the RCWA and TCMT simulations with input from J.v.d.G. and M.L.B. All authors contributed to analyzing the results and writing the manuscript.

3. **T. Hoekstra**, S. A. Mann, and J. van de Groep, "Finite-Size Effects in Nonlocal Metasurfaces". Submitted to *ACS Photonics*. Preprint available at arXiv:2603.03552. (**Chapter 5**)

   T.H., J.v.d.G., and S.A.M. conceived the concept behind this research. S.A.M. and T.H. developed the STCMT model. T.H. fabricated the sample, and performed the measurements and simulations with input from J.v.d.G. and S.A.M. All authors contributed to analyzing the results and writing the manuscript.

Other publications

1. G. Grimaldi, I. Schuringa, J. J. Geuchies, S. A. Rigter, **T. Hoekstra**, J. Versluis, J. Hidalgo, J.-P. Correa-Baena, J. van de Groep, H. Kim, M. Bonn and B. Ehrler, Atmospheric Exposure Triggers Light-Induced Degradation in 2D Lead-Halide Perovskites. *ACS Energy Letters* **9**, 5771-5779 (2024).

2. A. Azimi, J. Barrier, A. Barreda, T. Bauer, F. Bouzari, A. Brokkelkamp, F. Buatier de Mongeot, T. Parsons, P. Christianen, S. Conesa-Boj, A. G. Curto, S. Das, B.

Dias, I. Epstein, Z. Fedorova, F. J. García de Abajo, I. Goykhman, L. Greten, J. Grönqvist, L. Guarneri, Y. Guo, **T. Hoekstra**, X. Hu, B. Laudert, J. Lynch, S. Meyer, B. Munkhbat, D. Neshev, M. Ogienko, S. Papadopoulos, A. Parappurath, J. Sangers, P. Soubelet, C. Soukaras, G. Soavi, I. Staude, Z. Sun, K.-J. Tielrooij, M. D. G. Uddin, A. Ustinov, J. van de Groep, J. van Wezel, N. Vermeulen, H. Wang, Y. Wang, S. Xiao, B. You, and X. Zambrana-Puyalto, Photonics in Flatland: challenges and opportunities for nanophotonics with 2D semiconductors. *npj Nanophotonics* **2**, 44 (2025).

CONFERENCE PRESENTATIONS

1. **T. Hoekstra** and J. van de Groep, "Active Exciton Resonance Tuning in Hybrid-2D Photodetectors". *2023 Conference on Lasers and Electro-Optics Europe & European Quantum Electronics Conference (CLEO/Europe-EQEC)*, Munich, Germany, June 2023.

2. **T. Hoekstra** and J. van de Groep, "Active Exciton Resonance Tuning for Ultra-thin Free-Space Optical Modulators". *2023 MRS Fall Meeting & Exhibit*, Boston, Massachusetts, United States, December 2023.

3. **T. Hoekstra** and J. van de Groep, "Hybrid-2D Optical Modulators Enabled by Strong Exciton-Photon Coupling". *2024 Gordon Research Seminar on Plasmonics and Nanophotonics (GRS)*, Newry, Maine, United States, July 2024.

4. **T. Hoekstra** and J. van de Groep, "Hybrid-2D Optical Modulators Enabled by Strong Exciton-Photon Coupling". *NWO Physics 2025*, Veldhoven, The Netherlands, January 2025.

5. **T. Hoekstra**, S. A. Mann, and J. van de Groep, "Impact of Finite Size Effects on the Response of Ultracompact Non-Local Metasurfaces". *The Nineteenth International Congress on Artificial Materials for Novel Wave Phenomena – Metamaterials 2025*, Amsterdam, The Netherlands, September 2025.

The author acknowledges the use of large language models during the preparation of this thesis. These tools were consulted during editing for suggestions on grammar and vocabulary, as well as for debugging and refining Python scripts used in numerical simulations and data analysis.

Acknowledgements

Although the work presented in this thesis was carried out almost entirely by myself, it would not have been possible without the generous support of many people over the years. Their support has given me the rare privilege of doing things in my own way—honest, intuitive, and unforced—and, for that, I am forever grateful.

First of all, I would like to express my gratitude to three excellent mentors who have guided my work. Jorik, woorden schieten tekort om uit te drukken hoe dankbaar ik ben voor alles wat je voor mij hebt betekend. Jouw inzichten en aanmoediging hebben mij verder gebracht dan ik had durven dromen en je mag ontzettend trots zijn op de groep die je hebt opgebouwd. Het is voor mij een grote verrijking geweest om daar vanaf het begin deel van uit te maken en te zien hoe die in de tussentijd is uitgegroeid tot een bloeiende groep. Daarnaast heb je mij de kans gegeven om een project te doen bij Stanford, in jouw oude groep, die van Mark Brongersma. Mark, bedankt dat ik zomaar een maand mocht meedraaien in jouw groep, en voor de openheid en generositeit waarmee je mij daar hebt ontvangen; onze samenwerking was mij een groot genoegen. Sander, jij hebt me uitgedaagd om mijn theoretische werk verder te trekken dan ik zelf voor mogelijk had gehouden. Ik heb onze samenwerking en discussies als bijzonder waardevol ervaren, en zij hebben me doen inzien dat ik niet alleen een experimentalist ben, maar ook een theoreticus.

In addition, this work would not have been possible without the support of a number of noteworthy people. Ludovica, you have been a wonderfully kind supervisor and colleague to work with. During my Master's project, you set an inspiring example and were always willing to help, which led me to pursue a PhD myself. Together with Marco, you taught me the basics of experimental optics and 2D materials science. Andrea, you taught me valuable first lessons in the cleanroom and in optical simulations. Gerrit, your help with all things coding and equipment interfacing has been invaluable; the experiment automation I eventually managed to set up would not have been possible without it. Speaking of things that might otherwise have been impossible, first setting up the Python interface for RCWA would surely have failed without the help of Thomas. Thank you for your unfailing willingness to help, and for the many genuinely helpful and inspiring discussions. Mark Golden, you already sparked my interest in condensed matter physics during my bachelor's, setting me on this path long before I fully realized it. Later, when I was

just starting out, your help in setting up vacuum annealing was greatly appreciated. Next, I would like to thank the technical staff at the workshop—Hans, Johan, Gertjan, and Tjeerd—for making and repairing several custom parts. I am also indebted to the lab technicians Grisha and Paul and cleanroom staff Bob, Igor, and Laura for teaching me to use many of the crucial facilities, tools, instruments, and techniques on which this work relied. I would further like to thank my committee members, Giancarlo, Ripalta, Esther, Femius, and Mark, as well as my co-promotor Peter, for taking the time to evaluate this thesis. Lastly, my time as a PhD candidate was further supported by Bart, my independent supervisor, Astrid at the secretariat, and Joost as head of the institute.

During my time as a PhD student, I have been fortunate to be surrounded by many people who, in one way or another, shaped my work or simply lifted my spirits through good conversations over a coffee or a beer. Inevitably, I am bound to forget some names; to those I have unintentionally omitted, I hope you will forgive me. From our own group, I want to acknowledge Alex, Alvaro, Anne Claude, Bernardo, David, Ershad, Eva, Freek, Johanna, Mehmet, and Reynolds, as well as our students Bas, Cian, Gaby, Juliette, Ruben, and Vera, and other students whom I have partially supervised: Sabyasachi, Sergio Salvía Fernández, Marcel, and Ferran. Next, I want to thank Susan, Abhishek, Ying Ying, Ina, and Bauke from Peter's group; Charly from Sander's group; Skyler, JP, Qitong, Juan, Nicholas, and Fenghao from Mark Brongersma's group; Sergio Barquero Pierantoni and Chrystal from Mark Golden's group; Marc and Jelle from Anne de Visser's group; Evelijn from Albert's group; Stephan and Esther from Erik's group; Falco, Nelson, Deba, Nick, and Masha from Femius' group; Daan from Corentin's group; Gianluca and Quynh.

I would also like to thank my friends, de Schaufelradmakkers, de Aardbeien, de Kerstgroep, de NNGO, and my family: Wessel, Baukje, and especially my parents. Heit, mem, mear as allinnich in lústerjend ear, binne jim myn grutste supporters. Ik hie it nea safier skoppe kind sûnder jim stipe troch de jierren hinne—en dêrfoar bin ik jim ivich tankber. Last but not least, Mathilda. Thillie, telkens als ik mijn gevoel probeer te verwoorden, merk ik dat woorden tekortschieten. Door de jaren heen heb jij me altijd gesteund en ik kan met zekerheid zeggen dat dit boekje er zonder jou nooit was geweest. Ik kijk uit naar alles wat hierna komt, samen met jou, nu het werk erop zit.

Sitting quietly, doing nothing;
Spring comes, and the grass grows by itself.

Matsuo Bashō